Application of deep learning techniques for exoplanet detection in high contrast imaging

by

Carles Cantero Mitjans

Montefiore Institute
Department of Electrical Engineering and Computer Science

STAR Institute
Planetary & Stellar system Imaging Laboratory (PSILab)

Supervised by
Prof. Marc Van Droogenbroeck
Dr. Olivier Absil

LIÈGE université

November 2023

Cover image credit : Image generated by San Francisco-based independent research lab Midjourney, Inc, Midjourney, with the prompt: *High resolution 3d perspective from deep and dark space of a distant glimpse star and an orbiting planet that is really small. The background color of the image is very dark and only a few background obscured stars are visible*

ABSTRACT

The direct imaging of exoplanets through 10-m class ground-based telescopes is now a reality of modern astrophysics. Reaching this milestone is the result of significant advances in the field of high-contrast imaging, marked by the development of dedicated telescope instrumentation, including extreme adaptive optics and advanced coronagraphy. However, despite these advancements, residual optical aberrations persist, generating quasi-static speckles in the image field of view, whose shape and intensity are similar to potential companions. Over the past two decades, numerous image post-processing techniques have been proposed to further eliminate this residual speckle noise and detect the planet signature. Among these techniques, supervised deep learning was introduced through the SODINN detection algorithm, a binary classifier that uses a convolutional neural network to learn a model that distinguishes between noise and the point-like source in the image. The recent *Exoplanet Imaging Data Challenge* (EIDC) served as a platform for benchmarking SODINN and other image post-processing techniques. The results revealed that SODINN tends to produce a notable number of false positives, while the most effective techniques rely on mechanisms to capture local image noise dependencies. Building upon these findings, this thesis aims to improve the detection performance of SODINN through capturing new local noise dependencies. Through the development of new statistical methods, we explore the possibility to identify different noise regimes across the angular differential imaging processed image and adapt the SODINN neural network, and its training process, to work under this stratification strategy. This model adaptation leads to the creation of a new detection algorithm, called NA-SODINN. Through ROC analyses, NA-SODINN undergoes rigorous testing against its predecessor, demonstrating an improved balance between sensitivity and specificity in detection. Furthermore, NA-SODINN is benchmarked against the full set of detection algorithms submitted in the EIDC. The results indicate that NA-SODINN either matches or exceeds the performance of the most powerful detection algorithms. NA-SODINN is finally used to reanalyze a filtered sample from the recent SHINE exoplanet survey, providing valuable insights and potential exoplanet candidates. Throughout the supervised machine learning case, this study illustrates and reinforces the importance of adapting the task of detection to the local content of processed images.

DOCTORAL COMMITEE

SUPERVISORS

Marc Van Droogenbroeck
Professor, Université de Liège (Belgium)

Olivier Absil
F.R.S.-FNRS Senior Research Associate, Université de Liège (Belgium)

JURY MEMBERS

Gaël Chauvin
CNRS Researcher, Laboratoire Lagrange, Observatoire de la Côte d'Azur (France)

Faustine Cantalloube
CNRS Researcher, Institut de Planétologie et d'Astrophysique de Grenoble (France)

Valentin Christiaens
Research Associate, Université de Liège & Katholieke Universiteit Leuven (Belgium)

Jean-Baptiste Ruffio
Assistant Research Scientist, University of California, San Diego (USA)

PRESIDENT

Louis Wehenkel
Professor, University of Liège (Belgium)

Where there is a will, there is a way.

ACKNOWLEDGEMENTS

Today, my dream comes true ...

It all began 27 years ago, when a misfortune led me to the hospital as a critical medical emergency. A brain injury due to a cranioencephalic trauma changed my life. While I could resist the ambulance ride and the long post-surgery, this incident left me with profound challenges, including the inability to walk, use my arms, and speak. However, it never stole my dreams.

In those early days, in my hospital room, my ambition to look up and know more about the Universe seemed like an unattainable possibility. But as time passed, I found the strength thanks to the love and dedication of my parents, family, and friends, and I could return to the primary school with a helmet on my head. I was very happy. I still remember my dad's constant encouragement, repeating me the sentence *heel-toe, heel-toe, ...*, to help me regain proper walking ability on our way to school. Likewise, I also recall my mum teaching me to speak again while talking to me about the solar planets.

Over the years, I gradually regained the skills of speech, walking, and substantial use of my affected arm due to persistent daily therapy. In parallel, I successfully completed primary, secondary, and high school education, and managed to pass the university entrance exams. With a clear determination of becoming an astronomer, I started my studies in Physics. However, the illusion was short-lived, as I suddenly started experiencing multiple seizures as a consequence of my prior head trauma. To manage these seizures, I underwent different medication changes, resulting in the loss of an entire year of university studies. Nonetheless, one of these changes was crucial to achieving stability and facilitating normal studies. Thanks to this adjustment, I successfully completed all the physics courses, recovering the lost time from my first year. Upon graduation, I pursued my master's degree and a traineeship in the European Space Agency, where I could gain expertise on Machine and Deep learning, three of the most rewarding years of my life, both in terms of professional growth and health stability.

Finally, the moment I had longed for arrived. I was selected for a Ph.D. position at Université de Liège to work in exoplanet direct imaging through deep learning. I still remember the day when I received Olivier's message, tears streaming down my face on a warm day at the French coast, alongside Nuria.

... today, my dream comes true.

Finding the words to express this arduous journey is almost an impossible task. However, I would like to sincerely thank all those people who, in one way or another, supported me in achieving my dream.

Academia and friends

Marc and **Olivier**, as supervisors, I would like to let you know that you represent the pinnacle of my dream's achievement. I will forever be grateful for believing in me, for your guidance, your patience, your effort, and above all, for making me happy. Thank you so much. **Rakesh, Maxime, Malavika, Lorenzo, Mariam, Jahanvi, Omer, Elena, Valentin, Agustina, Ardjun, Anusha** and **Carl**, you have been my second family here in Liège. Thank you very much for always supporting and encouraging me in the hardest moments, and bringing a smile to my face. Special thanks to the whole PSILab and Montefiore Institute team for offering help whenever I needed it. A very special and sincere memory to **Matt. Faustine**, I learned a lot from you during the EIDC. Thank you very much for trusting in me. **Iva**, thank you for your support, for inviting me to go to Paris, and encouraging me for the postdoc.

A very special thanks to **Héctor** for wishing me the best and giving me his support whenever I needed it. **Santi**, you were the first person to place trust in me and my work. Thank you so much. **Carme**, thank you for your teaching, and for introducing me into the Gaia mission. I also want to express my appreciation to **Juan** and **Carme**. I greatly enjoyed with both of you and learned invaluable lessons along the way.

To all my friends, **Irmina, Sergio, Laura, Sergi, Lluis, Oscar, Jaume, Roger, Charles, Cédric, Pablo** and **Mireia**. Thank you very much for your support. I also extend a big thank you to **Georgina** for helping me before starting the PhD. **Luigi**, thank you for your warm welcome and hospitality in Madrid.

To **Miguel**, for introducing me to another of my passions, chess, which has played a significant role in my recovery process. I thank all the members of the Sant Joan Despí Chess Club for the numerous regional and international tournaments we played together.

Medical support

To my neurologists, physiotherapists, and speech therapists from the Hospital Vall d'Hebron, Hospital Santa Creu i Sant Pau, and Institut Guttmann. I am deeply grateful to **Mónica, Jose, Lourdes, Gavi** and **Marisa**. A very special thanks to **Mercè**, for her love, for her professionalism, for so many things we

lived together, for her magic hands. **Begoña**, thank you for giving me the opportunity for introspection, for helping me discover my inner self, and for making the journey enjoyable.

A big thank you to **Javier Berché** and his foundation for their support, their courses, and for affording me the opportunity to study astronomy in the Johns Hopkins University.

Family

My profound gratitude and love go to my parents, to whom I dedicate this entire thesis, along with a few words in Catalan:

Papa, mama, tot i les dificultats, vaig jurar que arribaria el dia en què em dedicaria a buscar vida a l'univers, i ho he aconseguit. La veritat és que, a priori, no sé si la trobaré, però m'hi esforçaré, com sempre he fet. Però, si sé una cosa, un fet innegable que no necessita proves ni dades, ni estudis ni avaluacions, ni ciència ni religió, és que mai, absolutament mai, trobaré una vida com la que vosaltres m'heu donat a mi. Mama, papa, de tot cor us agraeixo tot l'esforç, dedicació, patiment, discussions i tristesa que heu hagut de suportar perquè jo avui compleixi un somni, un somni que un dia va ser una mera il·lusió. Gràcies per donar-me dues vides, estic aprofitant la segona al màxim. Us estimo molt.

Nuria, my friend, my travel companion, my *flipi*, my future. From the first moment, you accepted my dreams and made them your own. You accepted the distance and made it small, really small. You accepted my difficulties and turned them into advantages. This journey, known as a Ph.D., is not comprehensible without you and your support. I love you deeply. I would like to also thank to **Maria Dolors, Josep, Jaume, Maria, Pere, Pamela**, and **Oriol** for accepting me and loving me.

To all my family, **grandparents**, **aunts**, **uncles**, and **cousins**, I extend my gratitude for your love, support, actions, affection, and for turning moments of sadness into hope and fun.

Dear **Axel**, my best friend, the person who wanted to play with me in the hospital while I could not move. I consider myself fortunate to have you. Thank you immensely for everything you have done for me. **Esther** and **Fernando**, thank you for your support and love.

Dear **Montse**, thank you for giving me knowledge, for coming with me on different trips in search of my Ph.D., and for always supporting me in the hardest moments.

In loving memory to Margarita Salvador, Paco Mitjans, José Cantero, Glòria Bages, Roser Galitó, María de los Ángeles Vázquez, and Pedro Salvador.

Image generated by San Francisco-based independent research lab Midjourney, Inc, *Midjourney*.

PREFACE

In the boundless expanse of the Universe, a persistent question has stirred human curiosity: *do other worlds exist beyond ours?* This questioning, a part of human contemplation for millennia, has transcended epochs, from the speculative thoughts of antiquity to the modern astronomical observations.

The endeavour to detect exoplanets –planets orbiting other stars beyond ours– has unravelled an odyssey that connects the aspirations of philosophers and the innovations of astronomers. From the profound ponderings of ancient Greek philosophers like Epicurus and Democritus to the revolutionary ideas of Copernicus and Newton, the notion of distant worlds has been a constant companion on our intellectual journey. These visionaries dared to imagine Earth as not the only origin of life but as one among several. The advent of telescopes in the Renaissance illuminated this longing to explore. Galileo's research on Jupiter's moons and Saturn's rings rewrote the understanding of planetary motion, revealing previously unknown aspects of celestial movement. However, despite the use of telescopes, the mystery of exoplanets remained unresolved.

As theoretical insights merged with technological advancements, the approach to discovering other worlds began to crystallize. In 1992, the first exoplanets were finally discovered, and since then, thousands of them have been detected in the close vicinity of the Sun. Today, this exploration story continues, but it has seen remarkable progress, allowing us to accomplish what was once thought to be impossible: thanks to advancements in instrumentation, we are now equipped not only to detect, but also to capture the thermal emission of exoplanets in images.

In parallel with such a milestone, a transformative player has recently taken the stage: *artificial intelligence*. Machine learning algorithms are bringing in a new era in the management of massive amounts of data, and they are enabling us to solve much more complex problems. Within this context, the integration of exoplanet direct imaging with machine learning holds the promise of significantly advancing exoplanet detection.

Through the five parts of this thesis, the reader is invited to embark on a voyage to witness firsthand the birth of a powerful exoplanet imaging algorithm based on machine learning. As this algorithm reveals its potential, it reflects the spirit of philosophers and scientists past, who sought to unlock the mysteries of existence through observation and reason. Building upon their legacy, we advance not only technologically, but also intellectually.

CONTENTS

LIST OF FIGURES

LIST OF TABLES

ACRONYMS

ADI	Angular Differential Imaging
AI	Artificial Intelligence
AO	Adaptive Optics
ANDROMEDA	ANgular Differential OptiMal Exoplanet Detection
AU	Astronomical Unit
AUC	Area Under the Curve
CEVR	Cumulative Explained Variance Ratio
CNN	Convolutional Neural Network
DM	Deformable Mirror
DNN	Deep Neural Networks
EIDC	Exoplanet Imaging Data Challenge
ELT	Extremely Large Telescope
ESO	European Southern Observatory
FDR	False Discovery Rate
FITS	Flexible Image Transport System
FMMF	Forward Model Matched Filter
FN	False Negative
FP	False Positive
FPR	False Positive Rate
FWHM	Full Width High Maximum
GAN	Generative Adversarial Network
GMT	Giant Magellan Telescope
GPI	Gemini Planet Imager
GRU	Gated Recurrent Unit
HCI	High Contrast Imaging
HSR	Half-Sibling Regression
IFS	Integral Field Spectrograph
IRDIS	InfraRed Dual-band Imager and Spectrograph
IWA	Inner Working Angle
LBT	Large Binocular Telescope

LLSG	Local Low-rank plus Sparse plus Gaussian decomposition
LMIRCam	LBTI's L and M Infrared Camera
LOCI	Locally Optimized Combination of Images
LSTM	Long-Short Term Memory
METIS	Mid-infrared ELT Imager and Spectrograph
ML	Machine Learning
MLAR	Multi-level Low-rank Approximation Residuals
MLP	MultiLayer Perceptron
MOA	Microlensing Observations in Astrophysics
NA-SODINN	Noise-Adaptive SODINN
NIRC2	Near InfraRed Camera 2
NMF	Non-Matrix Factorization
OGLE	Optical Gravitational Lensing Experiment
OWA	Outer Working Angle
PACO	PAtch COvariances
PC	Principal Component
PCA	Principal Component Analysis
PSF	Point Spread Function
RDI	Reference-star Differential Imaging
RNN	Recurrent Neural Network
ROC	Receiver Operating Characteristic
RSM	Regime Switching Model
RTC	Real-Time Control system
SDI	Spectral Differential Imaging
SHINE	SpHere INfrared survey for Exoplanets
SODINN	Supervised exOplanet detection via Direct Imaging with DNN
STIM	Standarized Trajectory Intensity mean Map
SVD	Singular Value Descomposition
SVM	Support Vector Machine
S/N	Signal-to-Noise ratio
SPHERE	Spectro Polarimetric High contrast Exoplanet Research
SR	Strehl Ratio
TMT	Thirty Meter Telescope
TN	True Negative
TP	True Positive
TPR	True Positive Rate

TRAP   Temporal Reference Analysis of Planets

VIP   Vortex Image Processing

VLT   Very Large Telescope

*W*FS   WaveFront Sensor

RESEARCH CONTRIBUTIONS

PUBLICATIONS

- <u>C. Cantero</u>, O. Absil, C-H. Dahlqvist and M.Van Droogenbroeck. *NA-SODINN: a deep learning algorithm for exoplanet image detection based on residual noise regimes*. Accepted for publication in A&A.

- V. Christiaens, C. Gomez-Gonzalez, R. Farkas, C.-H. Dahlqvist, E. Naskedin, J. Milli, O. Absil, H. Ngo, <u>C. Cantero</u>, A. Rainot, I. Hammond, M.J. Bonse, F. Cantalloube, A. Vigan, V. Kompella and P. Hancock. *VIP: A Python package for high-contrast imaging* Journal of Open Source Software (JOSS), vol. 8 (2023).

- F. Cantalloube, V. Christiaens, <u>C. Cantero</u>, E. Naskedin, A. Cioppa, O. Absil, M.J. Bonse, P. Delorme, C. Gomez-Gonzalez, S. Juillard, J. Mazoyer, M. Samland, J.-B. Ruffio and M. Van Droogenbroeck. *Exoplanet Imaging Data Challenge, phase II: Characterization of exoplanet signals in high-contrast images*. Proceedings of the SPIE, Volume 12185, id. 1218505 17 pp. (2022).

- F. Cantalloube, C. Gomez-Gonzalez, O. Absil, <u>C. Cantero</u>, R. Bacher, M.J. Bonse, M. Bottom, C.-H. Dahlqvist, C. Desgrange, O. Flasseur, T. Fuhrmann, Th. Henning, R. Jensen-Clem, M. Kenworthy, D. Mawet, D. Mesa, T. Meshkat, D. Mouillet, A. Mueller, E. Nasedkin, B. Pairet, S. Pierard, J.-B. Ruffio, M. Samland, J. Stone and M. Van Droogenbroeck. *Exoplanet Imaging Data Challenge: benchmarking the various image processing methods for exoplanet detection*. Proceedings of the SPIE, Volume 11448, 1027 − 1062 (2020).

TALKS AND POSTERS IN CONFERENCES AND SEMINARS

- Planned poster: *Imaging hidden worlds? Exploring the SpHere INfrared survey for Exoplanets (SHINE) through deep learning*. The 2023 conference on Machine Learning in astronomical surveys. November 27-December 1st IAP, Paris / Flatiron institute, New York.

- Talk: *Using local noise statistics to improve the supervised learning of exoplanets detection*. In spirit of Lyot Conference. University of Leiden, 27 June - 1 July 2022, Leiden (The Netherlands).

- Talk: *Supervised deep learning for exoplanet imaging*. L'Observatoire de Paris: Laboratoire d'Etudes Spatiales et d'Instrumentation en Astrophysique (LESIA) - Laboratory for Space Science and Astrophysical Instrumentation. June 2023, Paris (France).

Part I

INTRODUCTION

EXOPLANET DETECTION

The concept of a *planet* in astronomy has evolved over time. In 2006, the International Astronomical Union (IAU) established criteria for an object to be classified as a planet: *it must orbit a star, have sufficient mass to form a spherical shape, and clear its orbit of other objects*. Although this definition was clear and concise, it was designed for solar system planets, and it thus failed to encompass other planet-like objects, such as brown dwarfs[1] (Schneider et al., 2011), free-floating planets[2] (Sumi et al., 2011), and exoplanets.

Although alternative planet definitions have emerged to incorporate all planet-like objects (e.g., Boss et al., 2005; Margot, 2015), distinguishing between these objects remains unclear due to the limited number of observed cases. Currently, around 5500 exoplanets have been confirmed[3], with an additional 9800 candidates awaiting confirmation. These findings collectively account for about 4100 planetary systems in the vicinity of our star, the Sun. These discoveries have been made possible through complex detection techniques employed by ground- and space-based telescopes.

The aim of this first chapter is to provide a description of all these detection techniques. However, due to its relevance for the presented work, the focus is on exoplanet direct imaging, and therefore a full section is dedicated to providing the reader with all the necessary concepts to understand this revolutionary method.

1.1 INDIRECT DETECTION

Thus far, the detection of exoplanets has mostly relied on the application of indirect detection methods. The underlying concept behind these techniques is to infer the existence of orbiting planets around a star by detecting various indirect effects or phenomena, such as changes in the star's light, or alterations in the motion of the host star.

---

1 Brown dwarfs are sub-stellar objects that lack sufficient mass for nuclear fusion of ordinary hydrogen into helium in their cores. However, they are massive enough to fuse deuterium.

2 Free-floating planets are planetary-mass objects that do not orbit any star or brown dwarf, and therefore, they are not gravitationally bound.

3 NASA exoplanet archive: https://exoplanetarchive.ipac.caltech.edu/
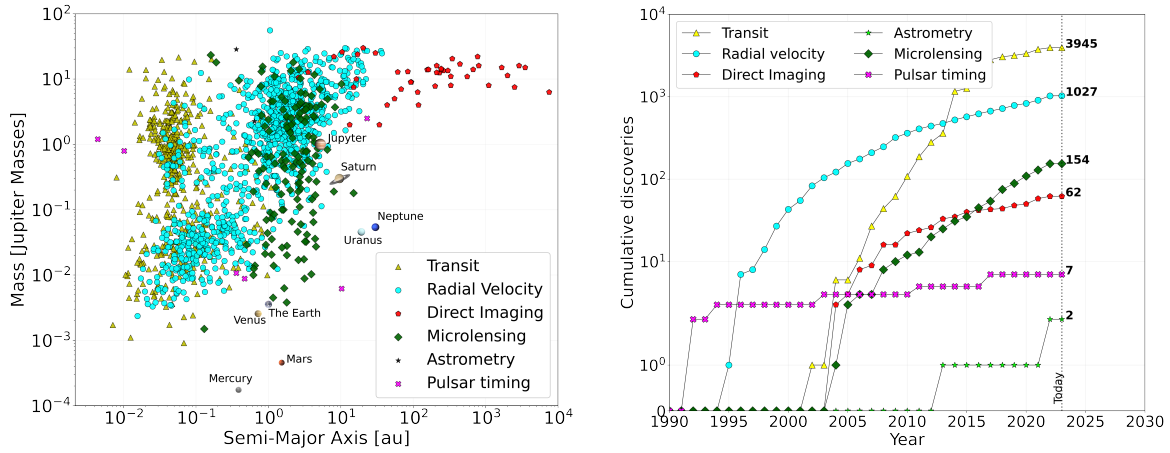
Figure 1.1: Overview of the current exoplanetary census. *Left:* Planetary mass versus semi-major axis space in which confirmed exoplanets and brown dwarfs are displayed according to the detection method. Solar system planets are drawn through their own illustrations. *Right:* Cumulative amount of exoplanet discoveries over time according to the detection method. The vertical dashed black line denotes the present day in this timeline, while the terminal points of each curve represent the total number of discoveries per method. Data extracted from the NASA exoplanet archive.

1.1.1 *Pulsar timing*

The pulsar timing technique stands as the initial breakthrough in detecting exoplanets (Wolszczan & Frail, 1992) as shown in Fig. 1.1-right. Pulsars[4] emit regular radio waves from their magnetic poles as they undergo rotation. By monitoring the arrival time of these pulses on Earth, it becomes possible to trace these electromagnetic beams over time. Consequently, the presence of unseen planets orbiting pulsars results in subtle but systematic changes in the expected timing of pulse arrival on Earth. Nonetheless, the practical applicability of this technique is hindered by several limitations. Pulsars are exceedingly rare when juxtaposed with main-sequence stars, and the intricate process of planetary formation around pulsars requires singular conditions, resulting in a low occurrence rate of planets. Consequently, only a few exoplanets have been detected using this technique over the past two decades (Fig. 1.1).

1.1.2 *Radial velocity*

The discovery of the first exoplanets orbiting a pulsar engaged numerous astronomers in the pursuit of detecting the first planet orbiting a main-

---

4 Pulsars are compact remnant neutron stars that form as a result of supernova explosions.
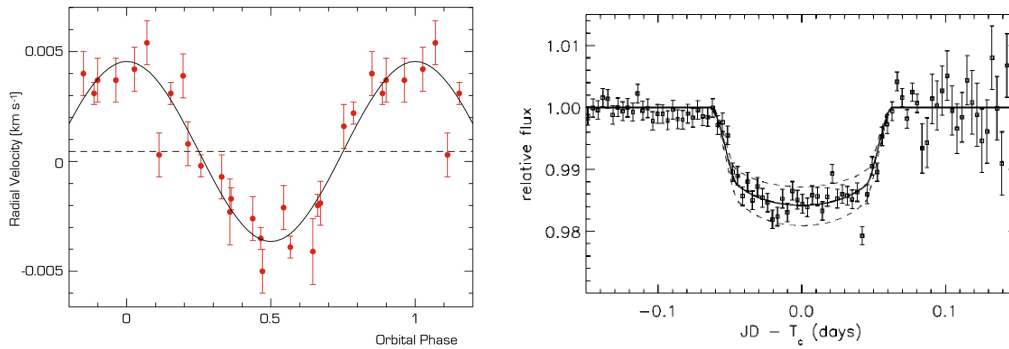
Figure 1.2: Examples of radial velocity and transit detections. *Left:* RV curve of 51 Peg, phased to a period of 4.23 days. The solid line is the fit to the observational data (red dots). Figure from Mayor & Queloz (1995). *Right:* Photometric time series of HD209458 during a transit. The solid line represents the best fit model indicating a maximum reduction of 1.7% of the host star brightness during the transit. Figure from Charbonneau et al. (2000).

sequence star. It was an observation in January 1995 that validated this endeavor. Professor Michael Mayor and his Ph.D. student Didier Queloz announced the groundbreaking detection of an exoplanet in orbit around the nearby G-type star 51 Pegasi (Mayor & Queloz, 1995) employing the radial velocity (RV) method. The fundamental principle underlying the RV method lies in the fact that stars, when orbited by planets, do not remain stationary. Instead, they exhibit subtle oscillations around the center of mass of the star-planet system. Consequently, when the exoplanet is massive enough and/or close enough to its parent star, the center of mass shift becomes, through Doppler spectroscopy[5], sufficiently large to allow a measurable periodic radial motion of the host star (Fig. 1.2-left). This phenomenon clarifies why the RV method has primarily succeeded in identifying exoplanets characterized by relatively short orbital periods and masses surpassing that of Earth (Fig. 1.1-left). The RV method has been able to find a total of 1044 exoplanets to date (Fig. 1.1-right).

1.1.3 *Transit photometry*

After the emergence of the RV method, two different teams were able to reveal for the first time a transiting exoplanet (Charbonneau et al., 2000; Henry et al., 1999). A transit is done when a planet passes in front of their host star (as seen from Earth), so that it causes a slight reduction in the star's

---

5 The motion of the star causes a shift in the wavelengths of its emitted light. When the star moves toward the Earth, its light becomes slightly blueshifted, and when it moves away, the light becomes slightly redshifted.

apparent brightness (Fig. 1.2-right). Consequently, whether the exoplanet is massive/big enough with respect to its parent star, this apparent brightness reduction becomes sufficiently large to be measurable by telescopes. This explains the fact that astronomers have been able to detect transits of super-Earths and giant planets very close to their parent star (Fig. 1.1-left). The transit photometry method has discovered 3945 exoplanets (Fig. 1.1-right), and it is nowadays the most successful detection technique. This is mainly due to the NASA *Kepler/K2* space mission (Borucki et al., 2010), which confirmed 3251 new detections, and the ongoing TESS mission (Ricker et al., 2015) with 396 confirmed detections so far.

1.1.4 *Microlensing*

Although the RV and transit photometry methods have proven to be highly successful, they have only detected companions in the vicinity of the Sun, approximately 1 kpc away from Earth. However, in April 2004, a breakthrough occurred when the OGLE and MOA programs[6] presented the first exoplanet discovery (Fig. 1.1-right) near the center of our galaxy using the microlensing method (Bond et al., 2004). When a distant background star becomes precisely aligned with a foreground star, the gravitational field of the latter causes the light from the background star to bend, resulting in the appearance of two distorted, brightened images. This observable phenomenon is known as gravitational lensing (Fig. 1.3-left). The resulting effect is a sudden dramatic increase in the brightness of the background star, which is commonly known as *magnification* (Fig. 1.3-right). In instances where a planet orbits in close proximity to the foreground star, crossing one of the two light paths emanating from the background star, the planet's gravitational force bends the light stream, momentarily generating a third image of the source star. This phenomenon, when observed from Earth, manifests as a temporary spike in brightness superimposed on the regular magnification pattern (Fig. 1.3-right). The number of exoplanets detected through this strategy is currently up to 150 (Fig. 1.1-right). The microlensing method possesses a particular disadvantage. It does not allow to reproduce observations, given the extremely low probability of follow-up alignment with another background star.

1.1.5 *Astrometry*

Since the first detection through the pulsar timing strategy in 1992, there has been a remarkable advancement in the precision and accuracy of instruments in the telescope. These advancements have spurred the development of

---

6 The Optical Gravitational Lensing Experiment (OGLE) and the Microlensing Observations in Astrophysics (MOA) are long term projects with the main goal of searching for microlensing phenomena and detect dark matter and extra-solar planets.
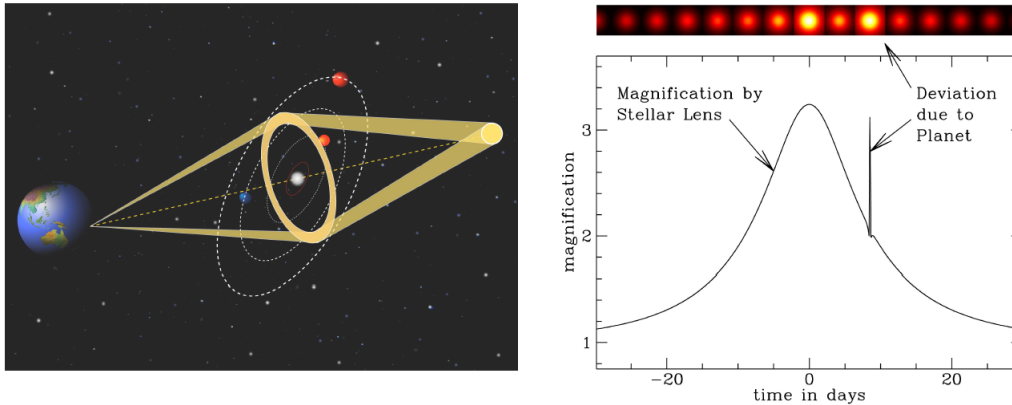
Figure 1.3: The microlensing method. *Left:* Illustration of a microlensing event. *Right:* Light curve magnification example, where a second peak reveals the presence of an orbiting planet. Image from the NASA Exoplanet Science Institute.

more sophisticated detection techniques, such as the astrometry method. Instead of relying on Doppler spectroscopy (RV method) to identify periodic movements of stars, astrometry looks for these movements directly on the celestial sphere. This strategy demands an extraordinary degree of precision for ground-based telescopes, which explains why only two exoplanets (Curiel et al., 2022; Sahlmann et al., 2013) have been discovered through astrometry measurements so far (Fig. 1.1). Nonetheless, equipped with an exceptionally high level of precision, the Gaia space mission is expected to overcome the limitations faced by ground-based telescopes holding immense promise for significantly increasing the number of exoplanet detections via astrometry in the coming years.

1.2 DIRECT DETECTION

Parallel to the use of indirect detection techniques, significant progress has been made in various technologies in the telescopes, such as adaptive optics and coronagraphy. The combined progress in these areas has offered an opportunity to explore strategies for directly imaging exoplanets through infrared observations using 10-m class telescopes. Stars emit considerably less radiation in the infrared band compared to the visible and ultraviolet spectra. Consequently, astronomers can directly capture the thermal emission emanating from orbiting exoplanets, as opposed to attempting to detect their reflected starlight in the visible range.

The first successful instance of detection of an exoplanet thermal emission took place in 2004 (Fig. 1.1-right). A research team captured an image of the giant planet 2M1207 b (Chauvin et al., 2004) orbiting the brown dwarf
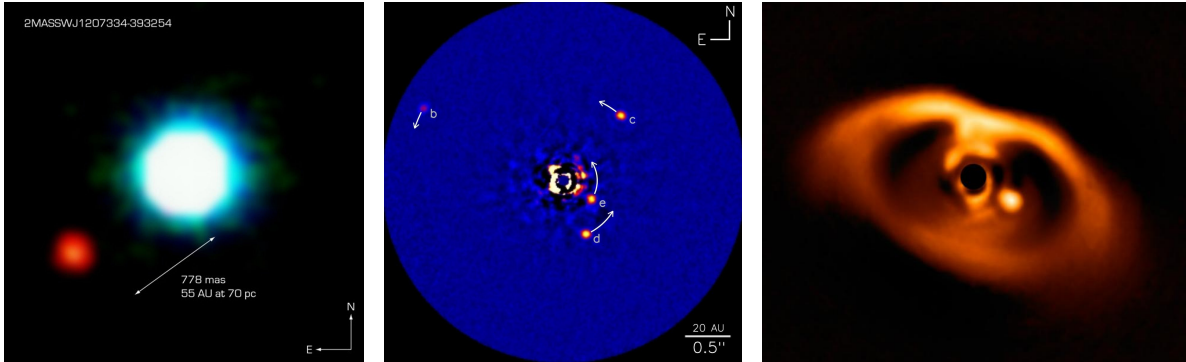
Figure 1.4: Examples of three imaged exoplanets through ground-based telescopes. *Left:* First ever image of an exoplanet (red source), which is orbiting the $2MASSWJ\ 1207334 - 393254$ brown dwarf (blue source). Image from Chauvin et al. (2004). *Middle:* Four giant planets orbiting the HR8799 main-sequence star. Image from NRC-HIA, C. Marois, and Keck Observatory. *Right:* Planet (bright point to the right of the centre of the image) caught in the very act of formation around the T Tauri star PDS70 and its protoplanetary disk. Image from Müller et al. (2018).

$2MASSWJ\ 1207334 - 393254$ (Fig. 1.4-left) using the Very Large Telescope (VLT). Since this remarkable discovery, a total of 66 exoplanets and brown dwarfs have been directly imaged. Some notable examples include the detection of the HR8799 b, c, d, and e giant planets (Fig. 1.4-middle) using the Keck and Gemini-South telescopes (Marois et al., 2008b, 2010), the discovery of Beta Pictoris b using the VLT (Lagrange et al., 2009), the detection of the lowest mass planet yet with direct imaging (51 Eridani b) with the Gemini-South telescope (Macintosh et al., 2015), and the observation of a protoplanet within the PDS70 disk (Keppler et al., 2018a) as shown in Fig. 1.4-right.

1.2.1 *High-contrast imaging*

The direct imaging of exoplanets through ground-based telescopes is a very challenging task. The angular separation between a nearby star and its orbiting exoplanets is extremely small when observed from Earth, typically within the range of a few milli-arcseconds to a few arcseconds. Furthermore, even when operating within the infrared, the very high flux ratio (or contrast) between an exoplanet and its parent star significantly complicates the isolation of the planet's signal from the overwhelming brightness of the star (Fig. 1.5). Typical contrasts range from $10^{-3} - 10^{-4}$ for hot Jupiters and can be as low as 10^{-10} for Earth-like planets in the habitable zone. The Earth's atmosphere further complicates the direct detection. As starlight passes through the atmosphere, turbulent regions cause the light wavefront

Figure 1.5: Analogy of the contrast problem. The lighthouse represents the star and the firefly the orbiting exoplanet. *Left:* Desired scenario for imaging the planet. *Right:* Real scenario where starlight overwhelm planetary signal and avoids its detection.

to distort, subsequently degrading the quality of images obtained when the light reaches telescopes.

In order to deal with the aforementioned challenges, the field of high-contrast imaging (HCI) relies on four fundamental pillars that are used in synergy to directly image exoplanets. The practical application of these four pillars is illustrated through the imaging example of Fig. 1.6:

1. Given a long exposure of a star, which is affected by the Earth's atmosphere (Fig. 1.6-a), the first HCI pillar concerns correcting this image degradation. This is done through **Adaptive Optics (AO)** systems implemented on the telescopes, which improve image quality and angular resolution (Fig. 1.6-b). This pillar is addressed later in Section 1.2.2.

2. After this AO correction, HCI makes use of a **coronagraphic** instrument to block out the starlight and decrease the contrast between the star and its unseen companions. Unfortunately, the starlight is never perfectly removed in practice, and some residuals remain in the coronagraphic image in the form of speckles (Fig. 1.6-c). Speckles can mimic the expected signal of an exoplanet in both shape and contrast. This pillar is explained later in Section 1.2.3 and Section 1.2.4.

3. In order to deal with quasi-static speckles in coronagraphic images, HCI employs specific **observing strategies** in the telescope, enabling the acquisition of data structures for modeling the residual speckle pattern. This pillar is addressed in Section 1.2.5.

4. Complementing observing strategies, HCI finally relies on powerful **image post-processing** techniques that are designed to effectively remove the modelled speckle pattern and reveal hidden companions (Fig. 1.6-d). This pillar is described in Section 1.2.6.
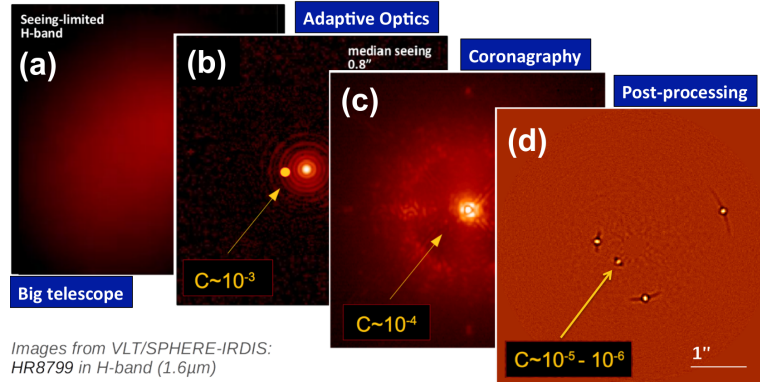
Figure 1.6: Practical example of the use of the four pillars in HCI for the imaging of the four giant planets around the HR8799 star. *(a)* Telescope exposure of HR8799 degraded by the Earth's atmosphere. *(b)* Same exposure after AO-correction. *(c)* Coronagraphic image after the propagation of the AO-corrected image, in which the residual speckle pattern is shown. *(d)* Residual processed frame after applying a post-processing algorithm into a data structure acquired through a given observing strategy, which reveals the four planet signatures. The reached contrast C is decreased on each of these steps.

1.2.2 *Angular resolution and adaptive optics*

A distant star can be considered as point-like source of light. Due to the principles of optics, this point-like source undergoes diffraction when it passes through the circular aperture of the telescope. Consequently, it is spread out creating a pattern known as the *point-spread function* (PSF, Racine, 1996). The PSF is mathematically described by an Airy function, which shows a central peak (or Airy disk) representing the main concentration of light from the star (Fig. 1.7-left). Surrounding this peak, there are a series of concentric rings with diffracted starlight that spread out from the central peak. In astronomy, an important measure of the PSF is the Full Width at Half Maximum (FWHM), which represents the width of the PSF at the intensity level equal to half of its peak intensity (Fig. 1.7-right).

The angular resolution of a telescope refers to its ability to distinguish between two closely spaced objects in the sky, such as two stars, and their corresponding PSFs. Under ideal observing conditions, this resolving power is only limited by optical diffraction effects, and is typically expressed in terms of the smallest angle θ_L that the telescope can resolve between the two star PSFs. This angle is known as the *diffraction limit* and it is given by the Rayleigh criterion:

$$\theta_L = 1.22 \cdot \frac{\lambda}{D}, \tag{1}$$
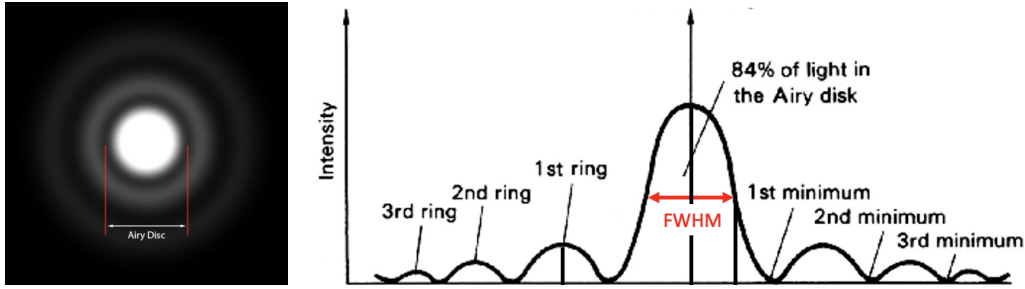
Figure 1.7: *Left:* Point spread function of a circular aperture showing the Airy-disk and the three first Airy rings. Image from Waterman (2019). *Right:* Illustration of the same PSF showing the full width at half maximum (FWHM) measure in red. Image from Majewski lecture notes (University of Virginia).

where λ is the wavelength of light being observed, and D is the diameter of the telescope's aperture.

From Eq. 1, it is directly inferred that the larger the telescope's aperture, the better its resoluving power. However, for a ground-based telescope, this diffraction-limited scenario is never achieved in practice, since its resolution power is also limited by atmospheric turbulence. When light enters the Earth's atmosphere, the different temperature layers and different wind speeds distort the light waves, leading to time and space-varying phase shifts of the wavefronts. As a result, the expected sharp PSF core is instead replaced by a fuzzy blob or halo (Fig. 1.8-left), decreasing the angular resolution limit of the telescope, which is now given by the Fried criterion (commonly known as *seeing*):

$$\theta_{\mathrm{L}} = 0.98 \cdot \frac{\lambda}{r_0},$$ (2)

where r_0 is the so-called Fried parameter, which is a measure of the strength of atmospheric turbulence. More precisely, r_0 quantifies the distance over which the wavefront of incoming light remains relatively undistorted by atmospheric turbulence. Larger values of r_0 indicate a more stable atmosphere, while smaller values indicate stronger turbulence. Therefore, the angular resolution limit of the telescope becomes independent of its aperture D, and it instead depends on atmospheric conditions.

In order to partially correct this wavefront distortion phenomena and improve angular resolution, the concept of adaptive optics was originally proposed by Babcock (1953) and was first applied in astronomy by ESO in 1990 at La Silla Observatory (Rousset et al., 1990). Generally, an AO-system consists of three main components that work in synergy in the telescope: the *wavefront sensor* (WFS, e.g. Shack & Platt, 1971; Ragazzoni & Farinato,
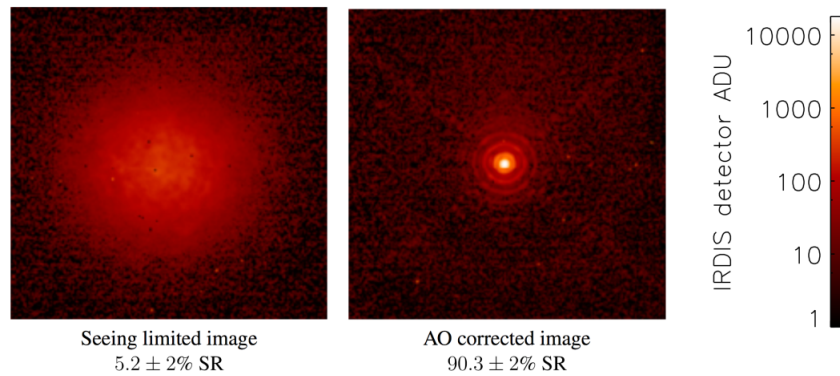
Figure 1.8: Example of an distorted image PSF due to atmosphere turbulence (left) and its AO-correction (right) in H band at VLT/SPHERE. The corresponding SR values are shown at each image case. Images from Sauvage et al. (2016).

1999), the *deformable mirror* (DM), and the *real-time control (RTC) system*. Using a guide star (or a laser guide star), the WFS measures the phase variations of the light wavefront. Then, this information is sent to the RTC, which reconstructs the entire wavefront. Based on this reconstructed wavefront, the RTC computes the correction to be applied to the DM (consisting in path delays or advances) and send it to numerous small actuators placed behind the DM, which locally deform it accordingly. By doing this, the DM cancels out the wavefront errors, flattening the wavefront and therefore sharpening the PSF in real-time. These steps are repeated in a closed loop mode at a high frequency (typically ∼ 1 kHz). Fig. 1.9 illustrates this AO-system loop process.

To quantify the performance of an AO-system, the *Strehl Ratio (SR)* metric is commonly used (Perrin et al., 2003). SR is defined as the ratio of the peak aberrated PSF intensity from a point source compared to the maximum attainable intensity using an ideal optical system limited only by diffraction (no atmosphere turbulence). Consequently, SR provides an indication of how well the telescope is performing after AO correction compared to an ideal diffraction-limited system. SR can be expressed as a value between 0 and 1, where SR = 1 means that the system is diffraction-limited, and SR < 1 that the system has aberrations. The smaller the SR, the more severe these aberrations, and the poorer the image PSF quality (Fig. 1.8). A complete review about AO systems can be found in Milli et al. (2016).
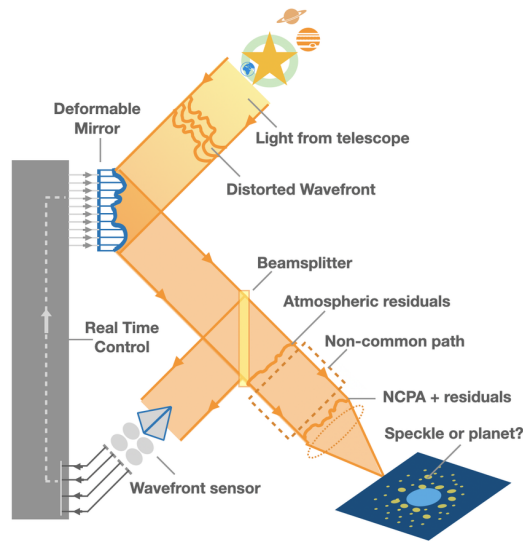
Figure 1.9: Illustration of a simplified adaptive optics system. Image taken from Skaf et al. (2022).

1.2.3 *Contrast and coronagraphy*

The challenges associated with the star-planet contrast persist even after AO correction. HCI deals with the contrast problem (Fig. 1.5) through the use of coronagraphs that are attached to the telescope within the a dedicated HCI instrument. The fundamental principle behind a coronagraph is to block out the glaring starlight, enabling the observation of nearby objects such as orbiting planets. Coronagraphs employ various techniques to mitigate starlight, based on their ability to manipulate the light's amplitude or phase. Additionally, these methods can be applied either in the focal plane or the pupil plane of the telescope, depending on the specific optical configuration used. For example, the first coronagraph configuration, commonly known as the *Lyot coronagraph*, dates back to 1939 (Lyot, 1939) and comprises an opaque disk (the Lyot mask), placed at the focal plane to block the starlight. Additionally, a second annulus-shaped opaque mask (the Lyot stop), is positioned at the pupil plane to further eliminate most of the remaining diffracted starlight (Fig. 1.10). Thus, the Lyot coronagraph acts on the amplitude of starlight at both the focal and pupil planes. In terms of performance, the Lyot coronagraph design has important drawbacks, such as it has not a perfect cancellation of the starlight even when the Lyot mask and the star are aligned,
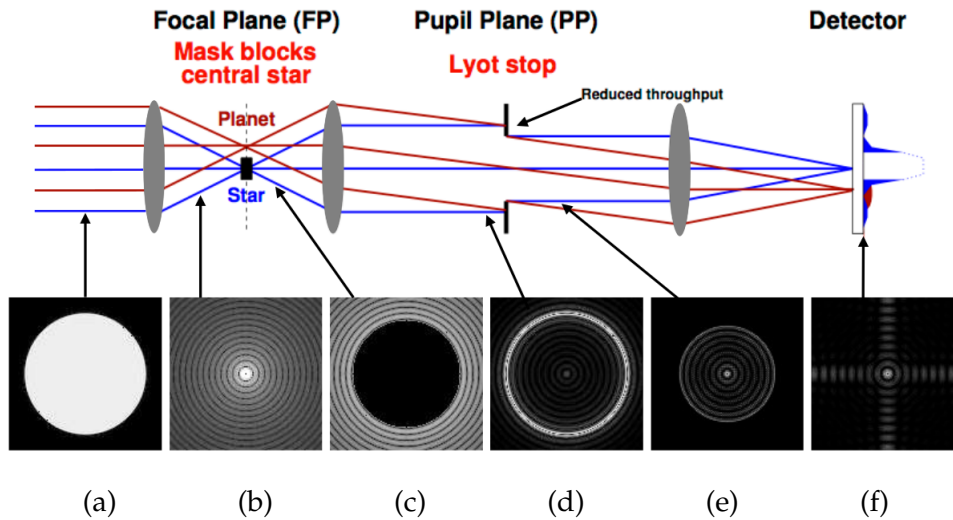
Figure 1.10: Lyot coronagraph optical design. Beams in blue and red represents the star and exoplanet incoming light, respectively. *(a)* Intensity in the entrance pupil; *(b)* Star PSF; *(c)* Star PSF after FP, where the Lyot mask is located and aligned; *(d)* Star PSF before Lyot stop; *(e)* Star PSF after Lyot stop; *(f)* Final coronagraphic image. Image based on a figure by M. Kenworthy.

it has a reduced *throughput*[7] due to the smaller size of the Lyot stop, and it has a large *inner working angle*[8] (IWA).

More advanced coronagraph designs have been proposed and tested on various ground-based telescopes. For instance, the four quadrant phase mask (FQPM, Rouan et al., 2000) and the vortex (Mawet et al., 2005) coronagraphs make use of transparent masks to shift the phase of star light, creating self-destructive interference instead of simply blocking it with an opaque disc as done with the Lyot mask. These designs significantly improve throughput and reduce the IWA. However, they are more sensitive to instrument misalignments (tip-tilt). In addition, the apodized pupil Lyot coronagraph (APLC, Soummer, 2005) is an hybrid coronagraph combining a Lyot coronagraph and a pupil plane apodizer, which helps further reduce the on-axis light intensity. Other designs such as apodized vortex coronagraphs are currently under development and foreseen for current and future ground-based instruments. A detailed review of most of these coronagraphic technologies may be found in Galicher & Mazoyer (2023).

---

7 The throughput refers to the fraction of the companion's light that reaches the detector after passing through the entire coronagraph system.

8 IWA is the smallest angular separation from the star at which the companion throughput reaches 50%.

1.2.4   *Speckle noise*

Despite of AO correction (Section 1.2.2) and the use of the coronagraph (Section 1.2.3), some residual starlight still reaches the detector in the form of *speckles*. Speckles are scattered starlight blobs that resemble the diffraction-limited PSF of the telescope, and can therefore mimic the signature of planets in both shape ($\sim \lambda/D$ scale) and contrast, which greatly affects the detectability of such companions in high contrast images.

According to their origin, speckles can be classified as atmospheric and instrumental speckles. Atmospheric speckles (Males et al., 2021) appear due to atmospheric residual aberrations that have not been totally corrected in the AO system (Fig. 1.9) and they have a short lifetime (few miliseconds). On the other hand, instrumental speckles (Hinkley et al., 2007; Goebel et al., 2016) are produced by instrumental aberrations, commonly known as non-common path aberrations (NCPA), that appear after the beam splitter (Fig. 1.9) and have much longer lifetime (several minutes to hours). Because of this long-lived behaviour, they are commonly referred as *quasi-static speckles*, and are very difficult to remove for image post-processing techniques. Quasi-static speckle represent the main challenge for current algorithms to identify companions in the image field of view.

1.2.5   *Observing strategies*

Different data acquisition techniques in the telescope (or observing strategies) have been proposed to deal with quasi-static speckles in HCI. These are based on *differential imaging*, which relies on a sequence of coronagraphic images of a single target (or multiple targets) to model the speckle noise structure. This model is then used to remove the quasi-static speckle pattern from each image in the sequence, affecting the planetary signal as little as possible during the subtraction process. Astronomers distinguish between different observing strategies according to the manner the speckle noise pattern is modelled.

1.2.5.1   *Angular differential imaging*

The most commonly used observing strategy is *Angular Differential Imaging* (ADI, Marois et al., 2006). An ADI data set consists of a sequence of coronagraphic images acquired in pupil-stabilized mode, where the instrument derotator tracks the telescope pupil instead of the field, in such a way that the instrument and optics in the telescope stay aligned while the image rotates in time due to the Earth rotation. As a result, quasi-static speckles remain mostly fixed in the focal plane while the exoplanet signal rotates around the star as a function of the parallactic angle. By using this angular diversity, a

speckle model may be built from the data and subtracted from the set of ADI images (see later in Section 1.2.6).

ADI has some limitations. One major drawback is the significant amount of observing time required to obtain sufficient angular diversity (usually around one hour) as well as the planetary signal self-subtraction observed at close separations. Moreover, ADI has limitations in terms of sky coverage, as achieving the required total parallactic angle rotation for an acceptable observing time can be challenging.

1.2.5.2 *Spectral differential imaging*

Another observing strategy, which is commonly used to complement ADI, is the *Spectral Differential Imaging* (SDI). Unlike ADI, SDI aims to separate the planetary signal from the speckle field based on their wavelength dependencies. Originally proposed by Racine (1996), SDI originally relied on selecting two wavelengths to insure the presence of the exoplanet in one image but limit its brightness in the other in such a way that speckle noise can be removed while preventing self-cancellation during the subtraction process. A more advanced version of SDI, known as multi-spectral SDI (mSDI), was later introduced by Sparks & Ford (2002). mSDI (nowadays more commonly referred to as SDI) takes advantage of the fact that speckles expand radially in the field of view as the wavelength increases, while planetary signals remain fixed.

1.2.5.3 *Reference-star differential imaging*

To overcome the limitations of ADI at small angular separations, Reference-star Differential Imaging (RDI, Lafreniere et al., 2007; Ruane et al., 2019) was proposed. The principle behind RDI is to model the speckle pattern through collecting images of similar stars in the immediate vicinity of the target star. However, this strategy needs a high stability of the instrument. RDI is therefore preferentially used with space-based telescopes which avoids the time-variable aberrations due to uncorrected atmospheric turbulence.

1.2.6 *Image processing techniques*

As shown in the example of Fig. 1.6, the implementation of image processing techniques represents the last cornerstone to directly image exoplanets. A plethora of such techniques have been developed in the last two decades, and it is nowadays a very active field of research in HCI. The main objective of these techniques is to remove the residual quasi-static speckle pattern observed in coronagraphic images (Section 1.2.4), and identify potential exoplanet candidates. These techniques have been adapted to work with

RAW DATA
(i.e., ADI sequence)

RESIDUAL IMAGE

PRE-PROCESSING
Task: clean data

POST-PROCESSING
Task: detect companions
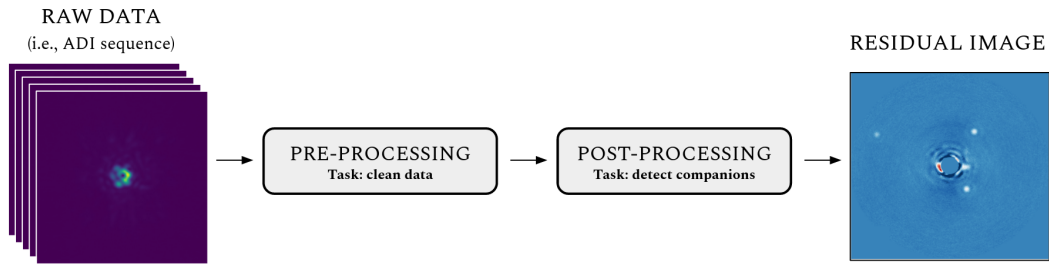
Figure 1.11: General image processing steps from raw data coming from the telescope, i.e., an ADI sequence. The basic idea is to apply pre- and post-processing image techniques to finally generate a residual image, also called processed frame, where the exoplanet detection is performed. See text for more details.

different observing strategies (Section 1.2.5), with ADI (Section 1.2.5.1) being the most commonly used approach.

In general terms, performing image processing entails two consecutive steps: applying image *pre-processing* to clean the raw data of possible errors/artifacts produced along with the acquisition of the images, and after that, using dedicated *post-processing* algorithms to perform the detection task (Fig. 1.11). There are three main corrections performed by pre-processing techniques: (i) *Image calibration*, including dark current subtraction, flat field correction, subtraction of the thermal background radiation of the sky, and bad pixels removal (dead or hot pixels) in images; (ii) *Bad frames removal* (caused by star/coronagraph misalignment, bad observing conditions or AO correction errors) through frame correlation analyses or pixel statistics analysis; (iii) *Image recentering* to solve potential image misalignment of the central star along the image sequence.

Image post-processing algorithms are classified into three main families: speckle subtraction-based techniques (also known as PSF subtraction techniques), inverse problem techniques, and supervised machine learning techniques.

1.2.6.1 *PSF subtraction techniques*

PSF subtraction techniques are the most commonly used post-processing techniques in the HCI community to detect exoplanet signatures. The concept behind these methods is to model the residual speckle noise as good as possible and subtract it from science images to finally detect unseen companions. As illustrated in Fig.1.12, four basic steps are usually followed for the case of ADI: (i) estimation of the speckle pattern, or PSF, by means of a dedicated algorithm; (ii) subtraction of this PSF model from each frame in the sequence; (iii) derotation of residual frames according to the parallactic

angle (Section 1.2.5.1); (iv) combination of derotated frames to generate a residual image, commonly known as *processed frame* (this convention is used from now on). All PSF subtraction techniques follow these four steps. They mostly differ in the manner the PSF is modelled. In the following, the most used PSF subtraction algorithms are described.

MEDIAN SUBTRACTION

The *median subtraction* algorithm (Marois et al., 2006) relies on the median operator to model the PSF through all science images in the ADI sequence (Fig. 1.12-a). The idea behind this approach is that due to its rotation in time, the planetary signal minimally affects the estimation of the median. After performing the subtraction, the residual noise is centered around zero in such a way that, when all the PSF-subtracted images are de-rotated and combined, the residual noise should average out. However, this approach does not perform well in the innermost region, as self-subtraction is strong at these separations and residual speckles remain even after subtraction.

LOCI

The *Locally Optimized Combination of Images* algorithm (LOCI, Lafreniere et al., 2007) aims to model the PSF as a linear combination of coronagraphic images taken from the ADI sequence (Fig. 1.12-b). These images are selected based on a field rotation criterion and their coefficients for the linear combination are computed through a least square minimization of the residuals after subtraction of the speckle field. In order to minimize the impact of a potential planetary signal when estimating the coefficients, LOCI processes independently sub-regions of the field of view. A region larger than the one for which the reference PSF is computed, is used for the least square minimization. Improved versions of LOCI have been proposed in the literature in the last decade (e.g., Pueyo et al., 2012; Marois et al., 2014; Wahhaj et al., 2015).

PCA

The *Principal Component Analysis* algorithm (PCA, Soummer et al., 2012; Amara & Quanz, 2012) aims to model the PSF from each frame in the ADI sequence by projecting it onto a lower-dimensional orthogonal space (Fig. 1.12-c). This projected space is constructed by means of the so-called Principal Components (PCs), i.e., linear combinations of the original space (the frame) which are computed using eigen decomposition or singular value decomposition (SVD). PCA orders PCs according to the variance they capture from the original space, such that first PC captures the maximum variance in the image, the second PC captures the second highest variance, and so on. Amara & Quanz (2012) show that PCA outperforms LOCI at detecting
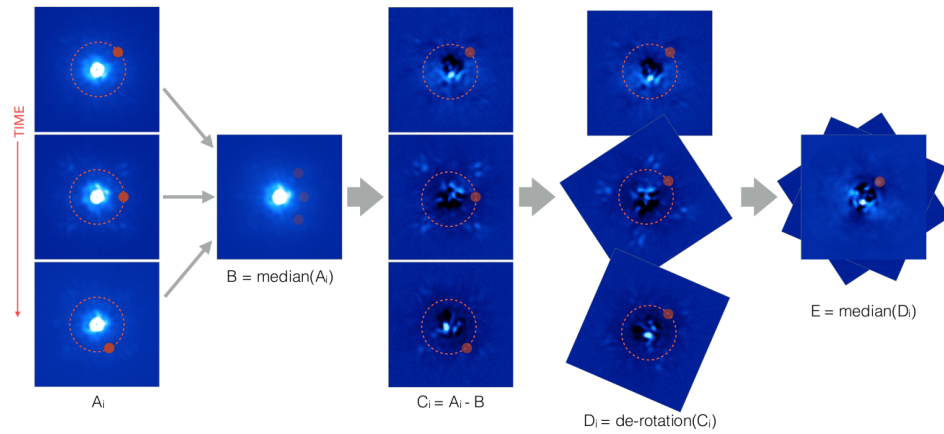
(a) Median subtraction
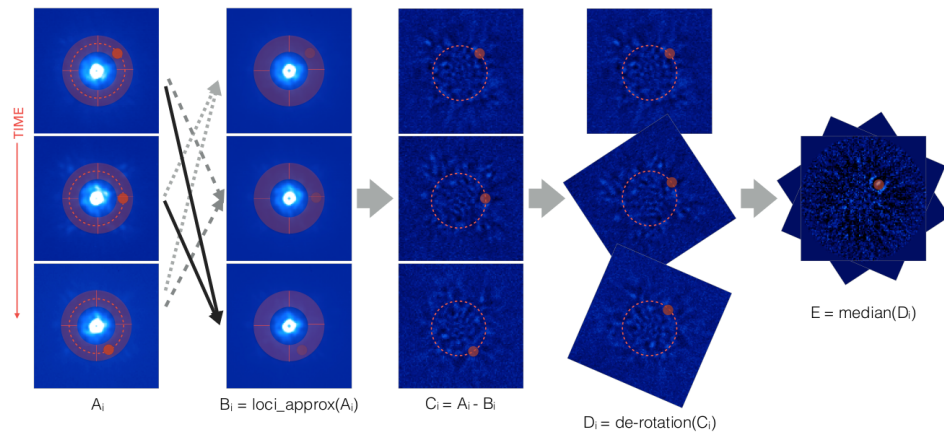
(b) LOCI
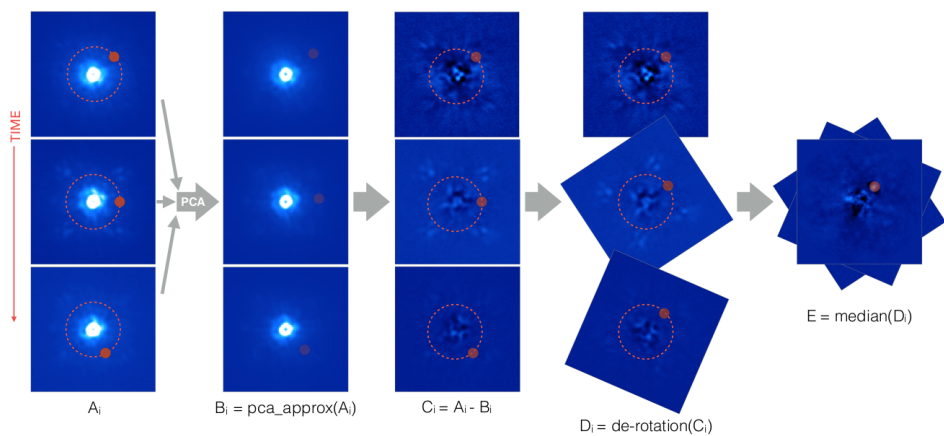
(c) PCA

Figure 1.12: Illustration of median subtraction, LOCI and PCA algorithms in an ADI sequence (A with i frames) showing the four steps in PSF subtraction techniques: PSF modelling (B_i), its subtraction (C_i), the de-rotation of residuals (D_i), and their combination (E) generating the processed frame. Red dots over frames represent the planet position. Images taken from Gómez González (September 2017).

companions at close separations from the star. Absil et al. (2013) improves the original version of PCA, often referred as full-frame PCA, by adapting it to work in annuli, processing the speckle noise in a more local manner and improving detectability in front of its predecessor.

LLSG

The *Local Low-rank plus Sparse plus Gaussian-noise decomposition* algorithm (LLSG, Gómez González et al., 2016) makes use of the *Go Decomposition robust PCA algorithm* (Zhou & Tao, 2011) to locally decompose the ADI sequence into three sub-spaces: the low-rank, sparse, and Gaussian spaces. This local three-term decomposition separates the starlight and the associated speckle noise from the planetary signal, which mostly remains in the sparse term. The LLSG algorithm improves the detectability of faint planets compared to full-frame PCA, but it is sensitive to outliers that can appear in the sparse term along with planetary signals.

NMF

The *Non-negative Matrix Factorization* algorithm (NMF, Lee & Seung, 1999) aims to find a k-dimensional approximation of the ADI sequence in terms of the product of two non-negative components through the minimization of their Frobenius norm. Ren et al. (2018) applies NMF for the case of circumstellar disk directly imaging.

S/N & STIM MAPS

The aforementioned PSF subtraction algorithms transform the raw data (i.e., ADI sequence) into a processed frame where residual speckle noise is mostly removed and the star-planet contrast is improved. The identification of planets within these processed frames entails the visual recognition of pixel patches exhibiting similar characteristics to the instrument's PSF. However, the effectiveness of human perception in this task can be constrained by inherent biases.

To address this limitation, a widely adopted solution involves incorporating the Signal-to-Noise ratio (S/N) metric to assist in the detection process. Building upon the approach outlined in Mawet et al. (2014), the S/N for each pixel in the processed frame can be calculated, enabling the transformation of the processed frame into a *S/N map*. As of today, this methodology stands as the prevailing standard for observational HCI campaigns.

The S/N map is based on the assumption that the residual noise in the processed frame is Gaussian. However, it is known that ADI processing does not completely remove speckle noise, especially at the innermost region, and therefore, assuming Gaussian noise in the processed frame leads to high

false positives rates (Marois et al., 2008a). Pairet et al. (2019) introduces a more advanced detection map called *Standarized Trajectory Intensity mean Map* (STIM), which computes a trajectory intensity metric for each pixel along time domain in the ADI residual maps, avoiding any Gaussian assumption.

RSM

The *Regime-Switching Model* algorithm (RSM, Dahlqvist et al., 2020), originally developed for econometrics, employs Markov-switching regressions to identify significant shifts in the behavior of time series data. It aims to describe different states that a time series system can exhibit. In the context of HCI, the RSM is applied by combining ADI residual cubes produced by different post-processing techniques, such as annular PCA, LLSG, NMF, and LOCI, among others, to construct the time-series. The RSM algorithm models two distinct states: one representing speckle noise in the data and the other incorporating both speckle noise and potential planetary signals. This model assigns probabilities to each element of the time series, indicating which regime it belongs to, and uses this information to construct a detection map. RSM is time-consuming and parameter selection complex. To address this issue, Dahlqvist et al. (2021a) proposes an unsupervised optimization framework based on a clustering approach (see Section. 2.1) to determine optimal parameters.

1.2.6.2 *Inverse problem techniques*

Another family of image post-processing techniques are based on inverse problem approaches. Unlike PSF subtraction, these algorithms directly model the expected planetary signal and track it in the image cube raw data based on the knowledge of the speckle noise statistics, the expected planetary movement (depending on the observing strategy), and the impact of the speckle field modelling. By construction, these methods estimate the contrast of the potential planetary signal, at any position in the field of view, via a maximum likelihood estimation. In the following, the main inverse problem approaches in HCI are described.

ANDROMEDA

The *ANgular DiffeRential OptiMal Exoplanet Detection Algorithm* algorithm (ANDROMEDA, Cantalloube et al., 2015) performs pairwise subtraction of adjacent frames in the ADI sequence to reduce speckle noise, making the assumption that the speckle noise in adjacent images is highly correlated. Through this pairwise subtraction, ANDROMEDA achieves the creation of a distinctive signature or the planetary signal (Cantalloube et al., 2015) which can be modelled. This signature becomes the cornerstone of ANDROMEDA's

methodology, facilitating the algorithm's ability to perform estimations of planetary flux. Such estimations are accomplished for every position within the field of view via maximum likelihood approach.

FMMF

The *Forward Model Matched Filter* algorithm (FMMF, Pueyo, 2016; Ruffio et al., 2017) employs the Karhunen-Loève transformation to calculate a forward-modeled planetary template for the KLIP PSF-subtraction methodology (Soummer et al., 2012). This forward-modeled approach effectively encompasses the perturbations induced in the PSF due to the process of subtracting the speckle field model (accounting for both self-subtraction and over-subtraction). To compute the flux at any given position within the field of view, FMMF incorporates a Gaussian maximum likelihood strategy, similar to the ANDROMEDA technique.

PACO

The *PAtch COvariances* algorithm (PACO, Flasseur et al., 2018) considers each pixel within the field of view and, for every frame in the ADI sequence, analyzes patches centered on the selected pixel across all other science images. It then relies on a maximum likelihood estimator based on a multi-variate Gaussian model to compute the estimated flux using the off-axis PSF as a planetary template. The existence of a companion is inferred at a predefined level through a generalized likelihood ratio test. Therefore, unlike other inverse problem approaches, PACO does not perform any subtraction prior to tracking the planetary signal. A more advanced version, referred as PACO ASDI, is proposed in Flasseur et al. (2020), where PACO is adapted to also capture the spectral and temporal fluctuations of background structures. Flasseur et al. (2021) proposed REXPACO, an extension of the original PACO to work with extended features, i.e. circumstellar disks in ADI sequences. More recently, Flasseur et al. (2023) proposes deep PACO, a combination of the original PACO with supervised deep learning to improve detection performance.

TRAP

Unlike other methods that model the planetary signal for each frame in the ADI sequence, the *Temporal Reference Analysis of Planets* (TRAP, Samland et al., 2021) estimates both the starlight residuals and the planetary signal along the temporal axis. The former is modelled by considering pixels that should share similar noise statistical properties but do not include the planetary signal. The latter is fitted alongside the obtained temporal model describing

the speckle noise to best fit the temporal evolution of the pixel intensity and determine the presence or absence of planetary signal.

1.2.6.3 *Supervised Machine Learning techniques*

More recently, the field of supervised machine learning has been introduced in HCI, especially for image post-processing. As explained later in Section 2.2, supervised learning aims to build a model directly from data, enabling the automatic extraction of patterns and relationships, which are then used for achieving accurate predictions on new data.

SODIRF & SODINN

The *Supervised exOplanet detection via Direct Imaging with a Random Forest* (SODIRF) and *Neural Networks* (SODINN) models (Gómez González et al., 2018) employ a random forest algorithm (Breiman, 2001) and a convolutional neural network, respectively. These are binary classifier models that learn to distinguish between two classes of square patch sequences, respectively with and without planetary signal. Based on this learning, they are able to classify new square patch sequences and generate a detection map where each pixel value refers to the model *confidence* to contain exoplanetary signal. SODINN is further explained in Chapter 8.

HSR

The *Half-Sibling Regression* method (HSR, Gebhard et al., 2022) aims to estimate the systematic noise in a pixel in the ADI sequence by regressing the time series of this pixel onto a set of causally independent, signal-free predictor pixels that are situated in specific areas that should ensure some mutual information. A modified Half-sibling regression (Schölkopf et al., 2016) is then used to learn a supervised model of the pixel speckle noise, based on the information contained in these areas, and predict the systematic noise associated to the selected pixel. It also incorporates observing conditions such as wind speed or air temperature as additional predictors.

GAN + CNN

Yip et al. (2020) train a Generative Adversarial Network (GAN) on real data from the *Near Infrared Camera and Multi-Object Spectrometer* (NICMOS) on the Hubble Space Telescope (HST) to obtain a generative model of the speckle noise pattern. This generative model can produce HST images without planets. It then uses this generative model to obtain a suitable dataset for training a convolutional neural network classifier to detect and locate planets across a wide range of SNRs on HST data.

2

MACHINE LEARNING

Artificial intelligence (AI) is completely changing the way humans engage with technology and make decisions in the modern society. At the heart of AI lies Machine Learning (ML), a set of computer science algorithms that are able to learn and model complex patterns directly from data. This radically differs from the classical programming approach of static program instructions and rules, in which machines follow predefined steps without the capacity to adapt to changing situations. ML systems, on the other hand, are dynamic and data-driven, constantly evolving and refining their understanding of the problem at hand as they encounter more information. This capacity to learn and adapt is what sets ML apart and makes it a cornerstone of AI's transformative potential.

A powerful synergy between astrophysics and machine learning has emerged over the past decade. With the advent of large astronomy data surveys, our access to an exceptionally rich repository of astronomical information has widened significantly. These surveys have enabled us to explore further into the universe, discovering new astrophysical phenomena, further understanding its origin, and modelling the evolution of stars and planets. In such a scenario, ML is providing an automated process of data analysis, uncovering hidden patterns, and enabling predictions with unprecedented accuracy. As this synergy evolves, it holds great promise for pushing the boundaries of our understanding of the universe.

This second chapter aims to provide a general view of ML, exploring the fundamentals of this technology. Our focus is, however, on the sub-field of deep learning, where neural networks and their optimisation processes are introduced. The chapter concludes by illustrating the link between machine learning and astronomy through a selection of published applications, with a particular emphasis on exoplanet detection.

(a) *Centroid-based*   (b) *Density-based*   (c) *Distribution-based*   (d) *Hierarchically-based*
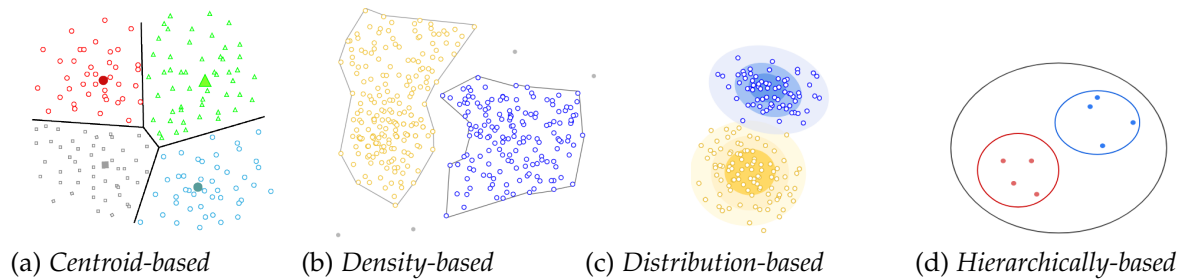
Figure 2.1: Illustration of the four types of clustering methods. Images from *Google for developers*.

2.1 UNSUPERVISED LEARNING

Unsupervised learning is a category of ML techniques used to analyze and extract patterns from unlabeled data, where data points are not associated with any specific categories, classes, or target labels and there is no predefined information about what they represent. There exist two general types of unsupervised learning algorithms according to their task: clustering and dimensionality reduction algorithms.

A clustering algorithm allows to organize a dataset into meaningful subgroups (clusters) based on some similarity metric. Different clustering models differ in the particular definition of a cluster. *Centroid-based clustering* relies on grouping similar data points based on their proximity to a central point known as centroid (Fig. 2.1-a). *Density-based clustering* identifies clusters as regions of high data point density, effectively handling outliers and irregular shapes (Fig. 2.1-b). *Distribution-based clustering* assume data arises from various probability distributions, estimating the underlying data distribution to assign points to clusters based on likelihood (Fig. 2.1-c). *Hierarchical clustering* construct cluster hierarchies, which merge individual data points into clusters based on linkage criteria, facilitating hierarchical organization of data into clusters of varying granularity levels (Fig. 2.1-d). We refer to Xu & Tian (2015) for an extended review of clustering methods.

Dimensionality reduction algorithms seek to project input data onto a lower-dimensional subspace while preserving most of the relevant information. This approach is commonly used for feature pre-processing because it reduces computational time and storage demands while facilitating improved visualization. PCA is the most prevalent technique. As explained in Section 1.2.6, it linearly decomposes a multivariate dataset into a sequence of orthogonal components that explain the maximum amount of variance. Consequently, it may not effectively capture non-linear patterns inherent in the data. However, techniques like t-SNE (Van der Maaten & Hinton, 2008) and UMAP (McInnes et al., 2018) are particularly well-suited for handling non-linear structures.

2.2 SUPERVISED LEARNING

Supervised learning aims to build a model from labeled data. The term *supervised* refers to the need for a ground truth or set of examples where the desired output signals (targets or labels) are already known. For instance, an image of a cat paired with the label *cat* serves as a clear example of this concept. The model learns the mapping function from input data features (i.e., the cat image) to targets (i.e., its label) by observing many examples of inputs and targets. This process is commonly referred as *training*.

Supervised tasks can be broadly categorized into two families: classification, where the labels are categories (as in the cat example), and regression, where the labels represent real numeric values (e.g., the cat's weight). Among the most important families of supervised machine learning algorithms that work in these categories of problems, we count the linear methods (Hastie et al., 2009), support vector machines (SVM, Boser et al., 1992), nearest neighbor methods, and tree-based methods (Breiman, 2001). However, regardless both the label and the algorithm nature, the ultimate goal of any supervised training process is to achieve optimal *generalization* capabilities. Generalization refers to the model's ability to go beyond simple memorization of the data set and, instead, capture the fundamental relationships inherent in the data, allowing accurate model predictions on data that it has never encountered during the training.

The prediction error of a supervised model can be decomposed into three components: an *irreducible* error, a *bias*, and a *variance* (Yu et al., 2006). The irreducible error represents the inherent uncertainty in the data set, setting the lower limit on a model's predictive power due to factors beyond its control. Bias, on the other hand, refers to the error introduced by approximating a real-world problem, which may be complex, by a simplified model that makes strong assumptions. At last, variance accounts for errors introduced by the model's sensitivity to small fluctuations or noise in the data set. The trade-off between bias and variance presents a fundamental challenge during the training process. In the early stages of training, when the model's complexity is low, it struggles to capture the underlying data relationships, resulting in a high bias and low variance scenario, which is commonly known as *underfitting* (Fig. 2.2-left). However, as the training progresses and the model becomes more complex, it fits its parameters better to the data set. There comes a point where the model starts *overfitting* the data, effectively modeling random noise as well, leading to lower bias but higher variance (Fig. 2.2-left). Finding the right balance between bias (underfitting) and variance (overfitting) is crucial to achieve optimal predictive performance and generalization.

In order to control this bias-variance trade-off and assess the generalization error during the model training, the *hold-out* method is usually employed. It consists on randomly dividing the data set into three subsets: the training,
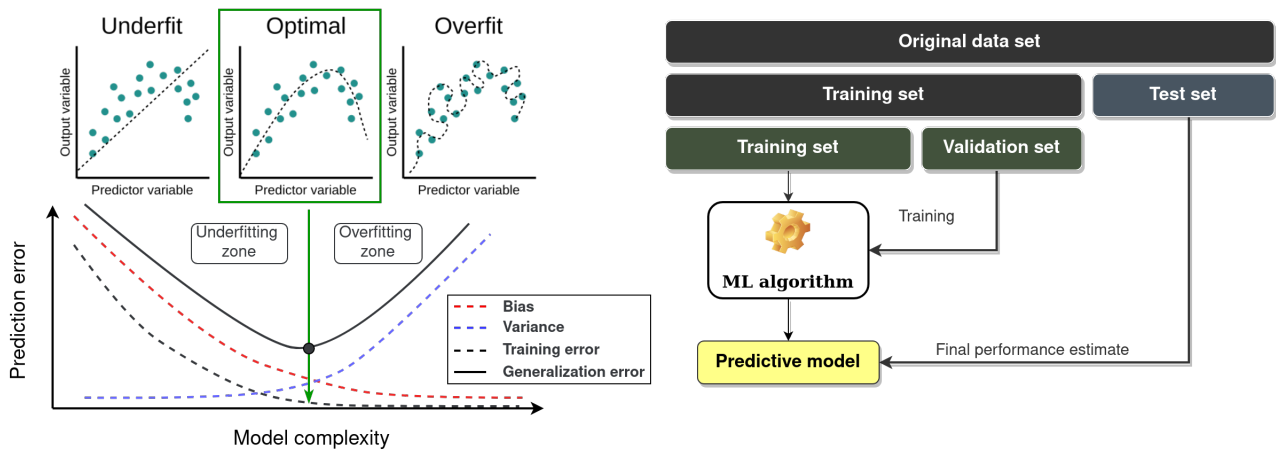
Figure 2.2: Supervised learning optimization strategy. *Left panel*: Representation of the bias-variance trade-off showing the typical U-shaped curve behavior of the generalization error together with the three possible scenarios (underfitting, optimal and overfitting models). *Right panel*: Typical hold-out partition method used to train a supervised ML algorithm and asses its generalization error.

the validation and the test sets (Fig. 2.2-right). The training set is exclusively used to train the model, allowing it to learn inherent relationships in the data. The validation set is used to assess the model's performance during training and make decisions about model hyperparameters and architecture. It is essential for tuning the model to ensure it generalizes well to unseen data. Finally, the test set is used to evaluate the final model's performance after training and hyperparameter tuning. Later, in Section 2.3.1, a more illustrative example of this supervised training process is provided through neural networks. More advanced partition strategies exists, such as the *k-fold cross-validation* (Hastie et al., 2009), which involves iteratively splitting the data into multiple train-validation sets, providing a more robust estimation of model performance and helping to reduce the risk of overfitting.

2.3 DEEP LEARNING

Deep learning is a sub-field of machine learning. The term *deep* refers to the use of successive layers of representations from data that are learned through *neural networks* models. These are inspired by the brain's use of layers of neurons working together, although there is no evidence that the brain implements anything like the learning mechanisms used in modern deep learning models.
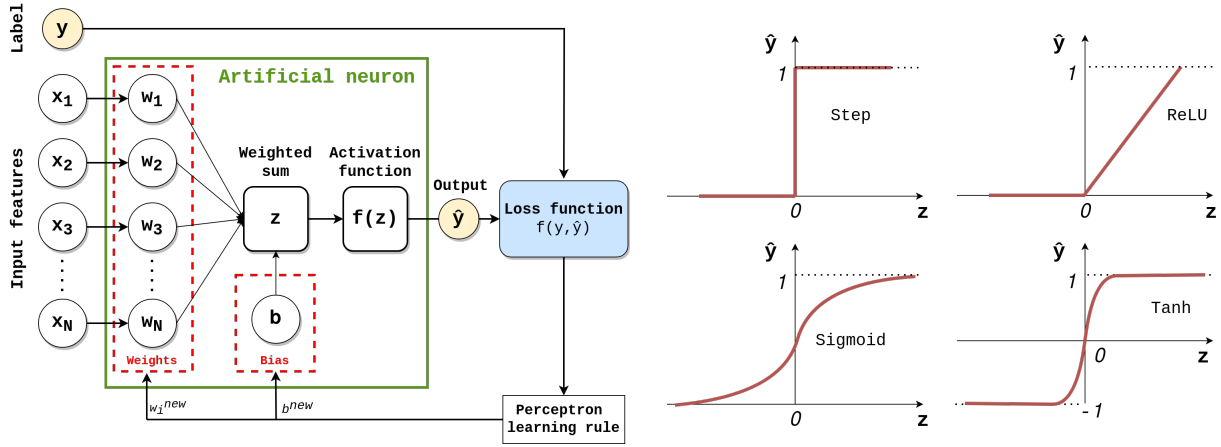
Figure 2.3: Basics of artificial neural networks. *Left panel:* Diagram of the *perceptron* model (green box) with N inputs features, and its optimization process through the *perceptron learning rule*. See text for more details. *Right panel:* The step activation function used in the perceptron model together with three of the most common non-linear activation function used in neural networks.

2.3.1 *The artificial neuron*

Understanding artificial neural networks requires revisiting the most basic neuron unit, the so-called *perceptron* (Rosenblatt, 1958). As depicted in Fig. 2.3-left, this computational model receives multiple inputs x_i (e.g. features in the training data) and multiplies a continuous-valued weight w_i to each of them. These weighted inputs are summed up, along with a random bias term b as follows:

$$z = \sum_i (x_i \cdot w_i) + b. \tag{3}$$

The final step involves passing this weighted sum z through an *activation function*, which essentially decides the final output $\hat{y}$ of the neuron. In Rosenblatt's perceptron, the activation function is a simple step function (Fig. 2.3-right): if z exceeds a specific threshold, $\hat{y} = 1$, otherwise, $\hat{y} = 0$.

Originally designed for supervised learning, this neuron model is tailored for binary classification tasks. When provided with a labeled dataset containing numerous examples from two classes, the training of this artificial neuron model, as described in Section 2.2, refers to the process of learning a mapping function between classes and their labels. This is achieved through the fine-tuning of the model's weights w_i and bias b (Eq. 3) by conducting numerous forward and backward passes through the neuron using the training set (Fig. 2.2-right): A forward pass entails feeding a mini-batch of training

samples into the neuron and calculating the error (or loss) between the true label y and the predicted label $\hat{y}$ (Fig. 2.3). Then, if $y \neq \hat{y}$, the weights w_i and bias b are updated during a backward pass, which involves computing new values w_i^{new} and b^{new} using the *perceptron's learning rule*:

$$w_i^{new} = w_i + \alpha \cdot (y - \hat{y}) \cdot x_i, \tag{4}$$

$$b^{new} = b + \alpha \cdot (y - \hat{y}), \tag{5}$$

where the term $\alpha \cdot (y - \hat{y})$ is the error (or loss) function and α is the so-called *learning rate*, an hyperparameter controlling the step size of parameter updates which plays a pivotal role when optimizing neural networks (described later).

This forward-backward process typically involves multiple passes through the entire training set, also known as *epoch*. An epoch is completed when the perceptron has seen and updated its parameters using all the training samples once. After each epoch, the whole validation set is fed into the neuron and the validation error is computed to assess how well the perceptron, with the adjusted parameters from that epoch, is generalizing to new data. The process of fine-tuning parameters and continuously evaluating validation performance throughout epochs is tracked by monitoring both training and validation errors. Typically, the process is stopped when a predefined criterion is met, such as when the validation error converges, no longer improves, or exhibits signs of overfitting (where the validation error begins to rise while the training error remains relatively constant, Fig. 2.2-left).

This artificial neuron model, as described, relies on a single layer of weights, and this simplicity imposes a significant constraint on its ability to handle more complex data. While it effectively captures linear relationships (Eq. 3), the majority of data sets are composed of intricate structures and non-linear correlations. This is where neural networks come into play.

2.3.2 *Neural networks*

Artificial neural networks (e.g., Abiodun et al., 2019) can be thought as a composition of multiple layers of interconnected perceptrons (Fig. 2.4), which is commonly known as Multilayer Perceptron (MLP). Within this structure, each perceptron receives an input value from every neuron in the preceding layer. Each of these inputs is then associated with specific weight and bias parameters through Eq. 3, and the output value $\hat{y}$ of the perceptron is then passed to each perceptron in the next layer. Through this concatenation, the MLP is able to transform the input data into increasingly complex representations. Neural networks are often referred to *deep neural networks* (DNNs) when they consist of numerous layers, also referred to as hidden layers (Fig. 2.4). Finally, the output layer consists on one or
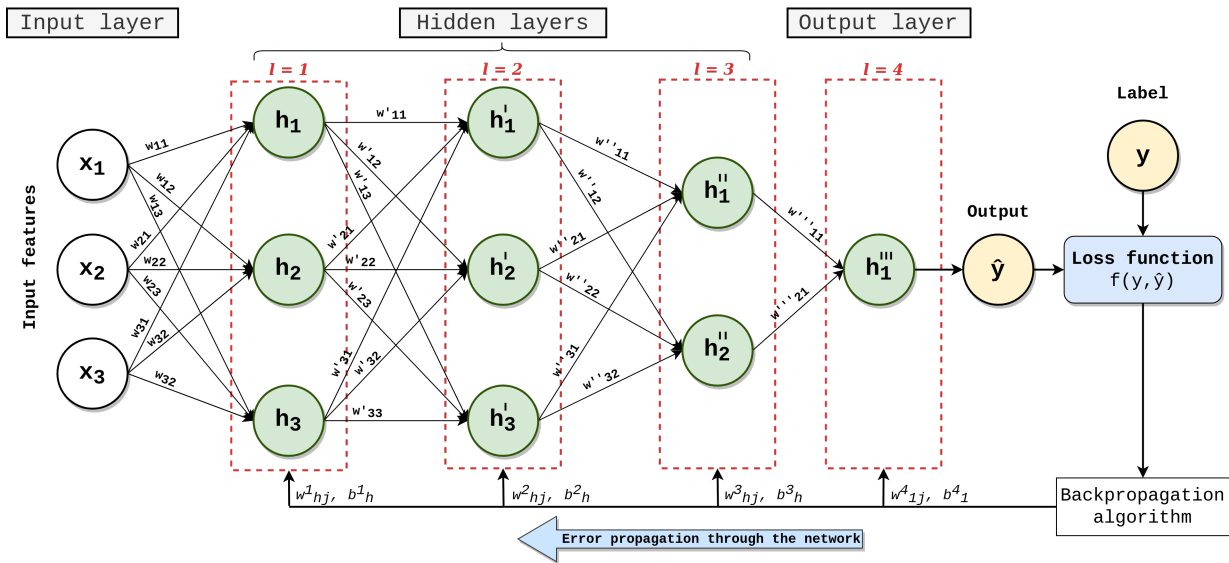
Figure 2.4: Illustration of a Multilayer Perceptron. The network comprises three input features x_i and four layers (l) of perceptrons (green circles denoted by h): three hidden layers ($2-3$ neurons each), and one output layer (single neuron). We use the index notation i (origin) and j (target) for weight connections, being w_{ij}, w'_{ij}, w''_{ij} for hidden layers, and w'''_{ij} for the output layer. The illustration also depicts a backward pass through the backpropagation algorithm.

more perceptrons depending on the specific task at hand. Its purpose is to generate the final prediction or decision based on the transformed information processed through the hidden layers.

While the original perceptron model relies on the simple step activation function to generate the neuron's output (Section 2.3.1), neural networks employ more advanced activation functions enabling the capture of non-linear data patterns. Fig. 2.3-right shows three of the most common non-linear activation functions, the sigmoid (smooth, differentiable with a range of 0 to 1), ReLU (efficient, setting negative values to 0, with a range from 0 to infinity), and hyperbolic tangent (similar to sigmoid but with a range of -1 to 1, helping center data around zero). We refer to Dubey et al. (2022) for more information about linear and non-linear activation functions in deep learning.

Thus, neural networks can be seen as a composition of simple linear data transformations (matrix multiplications and summations), specified by the layer's weights, and non-linearities introduced by the activation functions.

2.3.2.1 *Optimization of neural networks*

As described, the optimization of a single perceptron entails fine-tuning the weights and the bias through an iterative forward-backward process of batches of training samples. The aim of this process is to minimize the loss function associated with the perceptron's learning rule (Section 2.3.1). However, when dealing with neural networks, the adjustment of weights and biases demands a more intricate procedure involving the propagation of errors across the network's layered architecture. This propagation is typically achieved by means of the so-called *backpropagation algorithm* (Rumelhart et al., 1986).

Backpropagation relies on gradient descent and the chain rule to compute and propagate errors through the network, updating weights and biases for each neuron at each layer. Gradient descent, at its core, aims to minimize a function $f(x)$ by iteratively updating its input x in small steps in the opposite direction of its derivative $\frac{df}{dx}$. When dealing with multidimensional functions, the concept of derivatives is extended to partial derivatives $\frac{\partial f}{\partial x_i}$, which measure how $f(x)$ changes as only the variable x_i increases at point x. Note that in a neural network with l layers, h neurons in each layer, and j connections in each neuron (e.g., Fig. 2.4), the loss function is a complex multidimensional function defined as $L = L(\hat{y}_h^l(z_h^l(w_{hj}^l, b_h^l)))$. Computing errors associated to weights w_{hj}^l and biases b_h^l in a backward pass thus implies the computation of the gradient of the loss function with respect to each of these parameters. This computation is carried out using the chain rule,

$$\frac{\partial L}{\partial w_{hj}^l} = \frac{\partial L}{\partial \hat{y}_h^l} \cdot \frac{\partial \hat{y}_h^l}{\partial z_h^l} \cdot \frac{\partial z_h^l}{\partial w_{hj}^l}, \tag{6}$$

$$\frac{\partial L}{\partial b_h^l} = \frac{\partial L}{\partial \hat{y}_h^l} \cdot \frac{\partial \hat{y}_h^l}{\partial z_h^l} \cdot \frac{\partial z_h^l}{\partial b_h^l}, \tag{7}$$

where Eq. 6 and Eq. 7 account for the gradient of the loss with respect to weights and bias, respectively. These gradients are then used for updating the neuron's parameters as follows:

$$w_{hj}^{l(new)} = w_{hj}^l - \alpha \cdot \frac{\partial L}{\partial w_{hj}^l}, \tag{8}$$

$$b_h^{l(new)} = b_h^l - \alpha \cdot \frac{\partial L}{\partial b_h^l}, \tag{9}$$

where α is the learning rate. Choosing an appropriate learning rate is crucial to minimize the loss function. If α it is too small, the process would take

many iterations (and it could get stuck in a local minimum), whereas, if the step is too large, it would never converge. A way to avoid getting trapped in local minima is to use *momentum* (Sutskever et al., 2013), which draws inspiration from physics, and updates the weights based not only on the current gradient value but also based on the previous weight updates. Other methods have been proposed to automatically tune the learning rates, such as Adagrad (Duchi et al., 2011) and Adam (Kingma & Ba, 2015). For an overview of gradient descent optimization algorithms, see Ruder (2016).

One of the most important aspects when optimizing neural networks is *regularization*. As described in Section 2.2, overfitting is a challenge for the generalization capacity of supervised learning algorithms. Regularization techniques play a pivotal role in addressing this issue by constraining the network's capacity for memorization. Common regularization techniques are *dropout* (Srivastava et al., 2014), *batch normalization* (Ioffe & Szegedy, 2015), data *augmentation* techniques, and *early stopping*. In general terms, dropout consists of randomly "dropping out" (deactivating) a fraction of neurons during the training to introduce randomness into the network. Designed for solving other issues like the vanishing problem (explained later), batch normalization is also a slight form of regularization, which normalizes the activations of each layer in a mini-batch. Data augmentation is the process of creating synthetic training data through different data transformations to make a model generalize better. Early stopping involves monitoring the model's performance on a validation dataset during training. Training is stopped when the performance on the validation set starts to degrade, indicating overfitting. The model is saved at this point. We refer to Goodfellow et al. (2016) for more information about other regularization techniques.

2.3.3 *Types of neural networks*

The MLP (Fig. 2.4) establishes an initial basis to understand neural networks and its optimization process. However, over the last few decades, deep learning has experienced rapid transformation by developing more complex network architectures capable of capturing stronger relationships within diverse types of data, such as images and time-series information. These advances have surpassed the capabilities of MLPs, empowering the field of deep learning and broadening its applications across a wide spectrum of domains. In the following, two of the most used architectures are explained.

2.3.3.1 *Convolutional neural networks*

Convolutional Neural Networks (CNNs, Krizhevsky et al., 2012) are a type of deep learning model well-suited for processing grid-like data, such as
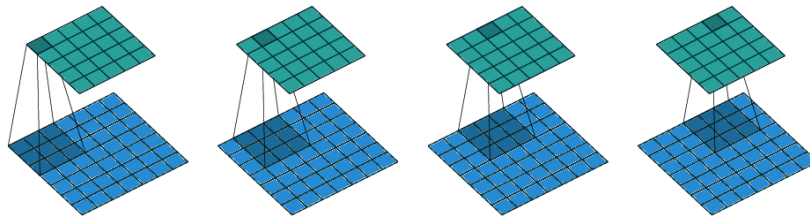
Figure 2.5: Convolution of a 3×3 kernel (dark blue grid) over a 6×6 input image (blue grid) using unit strides. Images from left to right illustrates the kernel movement along the input image, which generates and output image, commonly known as feature map. Figure from Dumoulin & Visin (2016).

images or 3D structures (videos). In essence, a CNN is composed by three consecutive layers. First, the *convolutional layer* involves applying a set of 2D or 3D learnable filters (also known as *kernels*) to small, overlapping regions of a 2D image (Fig. 2.5) or 3D cube, respectively. By sliding these filters across the entire input (Fig. 2.5), the convolutional layer generates feature maps that capture spatial correlations, such as edges, textures, and shapes, at different spatial locations. Second, after the convolution operation, an activation function (usually a ReLU function, Fig. 2.3-right) is applied element-wise to the feature maps helping the network capture non-linear relationships. Finally, a pooling layer is used for downsampling the spatial dimensions of the feature maps while retaining essential information. A common pooling operation is max-pooling, where the maximum value within a small window is retained, and the rest is discarded.

2.3.3.2 *Recurrent neural networks*

Recurrent Neural Networks (RNNs, Rumelhart et al., 1986) are a type of neural network architecture designed for processing one-dimensional sequential data. RNNs have connections that loop back on themselves, allowing them to maintain a form of memory (or state) that captures information about previous time steps in the data sequence. However, despite their effectiveness in modeling time-series correlations, traditional RNNs suffer from the *vanishing* gradient problem[1] during training. More advanced RNN variants, such as *Long-Short-Term Memory* (LSTM, Hochreiter & Schmidhuber, 1997), were developed to solve this problem. The major innovation of LSTM is its memory cell, which essentially acts as an accumulator of the state information. The cell is accessed, written and cleared by several controlling gates. An alternative is to use *Bi-directional RNNs* (Schuster & Paliwal, 1997). They consist of two separate RNNs, one processing the sequence from left to right

---

1 The vanishing problem happens when gradients become very small during backpropagation over many time steps, hindering long-range dependency learning.

(forward RNN) and the other processing it from right to left (backward RNN). This strategy helps the model to understand the context surrounding each element in the sequence, and leads to better performance. More recently proposed, *Gated Recurrent Unit* (GRU, Cho et al., 2014) RNNs are similar to LSTMs but have a simplified architecture with fewer gates, making them computationally more efficient while still addressing the vanishing gradient problem to some extent.

2.4 MACHINE LEARNING FOR EXOPLANET DETECTION

Machine and deep learning techniques have instigated a profound transformation within the field of astronomy. These cutting-edge methodologies have found diverse applications in astronomical research, including but not limited to galaxy morphology prediction (Dieleman et al., 2015; Vavilova, I. B. et al., 2021), astronomical image reconstruction (Flamary, 2017; Schmidt, K. et al., 2022), photometric redshift prediction (Hoyle, 2016; Brescia et al., 2021), and star-galaxy classification (Kim & Brunner, 2016; Baqui, P. O. et al., 2021), among others.

In the realm of exoplanet detection, machine and deep learning techniques have made significant impacts on both indirect (see Section 1.1) and direct (see Section 1.2) methods. For instance, within the domain of transit photometry, machine learning has played a pivotal role in augmenting detection capabilities. Space-based missions like *Kepler* and the TESS provide large data sets that require efficient and systematic analysis. The application of deep learning techniques has enabled the automatic detection of exoplanetary transits with unprecedented accuracy (Ansdell et al., 2018; Valizadegan et al., 2022; Malik et al., 2021). In the context of the radial velocity method, where instrumental precision continually improves but stellar activity remains a significant obstacle to achieving reliable measurements, deep learning has proven its ability to model and mitigate this stellar activity, thereby enhancing the accuracy of Doppler measurements (Perger, M. et al., 2023; de Beurs et al., 2022; Nieto, L. A. & Díaz, R. F., 2023). Even the microlensing method has not been immune to the influence of machine learning, benefiting from its data-driven insights (Zhang et al., 2022). In the case of direct imaging, both unsupervised and supervised machine learning techniques have been harnessed for various purposes, including the improvement of focal-plane wavefront sensing (Quesnel, M. et al., 2022) and the enhancement of detection in image post-processing (Fergus et al., 2014; Gómez González et al., 2018; Yip et al., 2020; Gebhard et al., 2022).

3

SCOPE AND OUTLINE OF THIS DISSERTATION

In this introductory Part I, the groundwork for this thesis has been established through two chapters. On one hand, in Chapter 1, we have explored exoplanet detection methods, tracing the history of indirect techniques and their associated limitations. Our primary focus, however, has been on the field of HCI, which tackles the challenges of directly imaging exoplanets. Within HCI, we have covered its four pillar strategies: adaptive optics systems, coronagraphy, observing strategies, and image post-processing. The synergy of these techniques has so far pushed contrast levels to below 10^{-6}, enabling the direct imaging of giant exoplanets. Nevertheless, the emergence of $20-40m$ class ground-based telescopes such as the Extreme Large Telescope (ELT[1]), the Thirty Meter Telescope (TMT[2]), and the Giant Magellan Telescope (GMT[3]), as well as space-based observatories such as the operational James Webb Space Telescope (JWST) and the upcoming Roman space telescope, hold promise to achieve even better contrasts, opening up new opportunities to directly image medium to small-sized exoplanets for the first time. Pursuing these ambitions requires the improvement of image post-processing algorithms, and machine learning-based techniques have proven to be very powerful with respect to more classical approaches. In Chapter 2, we have introduced the field of machine learning, with a special focus on deep learning. Through the fundamentals of neural networks and their optimization processes, we have explored new methodologies to solve intricate problems, such as sample classification, directly from labeled data. Due to its high impact in astronomy, we have finally reviewed its increasing role in exoplanet detection.

Within this context, my journey as a Ph.D. candidate started by becoming a new team member of the *Exoplanet Imaging Data Challenge* (EIDC Cantalloube et al., 2020, 2022), a community-wide data challenge for HCI post-processing techniques. The Part II of this thesis is devoted to explaining my contribution to the EIDC development, as well as results and main conclusions we have derived from all submission analysis.

---

1 ELT webpage: https://elt.eso.org/
2 TMT webpage: https://www.tmt.org/
3 GMT webpage: https://giantmagellan.org/

The core of this thesis has significantly been shaped by the EIDC's success. One of the EIDC conclusions has been the identification of a notable issue with the SODINN deep learning algorithm, which has frequently produced false detections in the final detection maps. Furthermore, we have also observed that the best EIDC results have been achieved by those algorithms that process image noise at a local level, allowing them to capture stronger physical-based dependencies within the HCI data. In light of these findings, my principal aim during my PhD thesis has been to enhance the performance of SODINN by developing novel strategies to capture better the physics of image noise. Our approach has focused on studying the spatial behavior of residual noise within the ADI-PCA processed frame, where despite the ADI processing, speckle noise still dominates at small angular separations, leading to different noise regimes across the image field of view. The Part III of the thesis is devoted to describing all statistical strategies we have proposed to detect these noise regimes, as well as derived conclusions regarding the nature of residual noise.

The Part IV of this thesis stands as the culmination of my research, introducing the novel NA-SODINN algorithm (Cantero et al., 2023), an adapted version of SODINN tailored to the noise regimes approach. We first explain the adaptation process of the neural network, designed to learn from image noise regimes, and the consequential implications for training. We then subject our novel NA-SODINN to rigorous evaluation, comparing it against its predecessor and other standard post-processing techniques across various ADI data sets from different HCI instruments. NA-SODINN is also entered into the first phase of the EIDC, allowing for a direct comparison with state-of-the-art detection techniques. Ultimately, to further test its potential, we employ NA-SODINN in the analysis of the SHINE HCI survey (Desidera et al., 2021), aiming to apply NA-SODINN to real HCI data and possibly uncover previously undetected exoplanetary candidates.

The concluding Part V of this dissertation is dedicated to deriving valuable insights from our research journey, particularly in the realms of exoplanet direct imaging and image noise analysis. Furthermore, we provide a glimpse into the promising future prospects of NA-SODINN, demonstrating its potential to drive substantial advancements in the field of HCI.

Part II

EXOPLANET IMAGING DATA CHALLENGE

INTRODUCTION

Over the past two decades, the field of HCI post-processing (Section 1.2.6) has been very active in developing and publishing numerous algorithms to detect and characterize exoplanets. However, one inherent difficulty has emerged in this progress: each of these algorithms has been tested on different data sets, under varying observing conditions, and using different metrics. This disparity has caused confusion in the HCI community when trying to determine the best-suited method for a given task.

To address these limitations, the *Exoplanet Imaging Data Challenge* (EIDC[4]) was conceived with a specific objective in mind: to homogenize the evaluation of current HCI post-processing methods across various scientific cases and serve as a reference for future algorithm developments. Initially conceived by Dr. Carlos Alberto Gómez González and a small initial team, the EIDC has evolved into a collaborative effort among multiple international institutions under the leadership of Dr. Faustine Cantalloube. Today, it stands as an open-source community initiative, inviting participation from anyone interested in contributing.

This second part of the thesis is devoted to introducing the EIDC through three chapters. Chapter 4 describes and discusses results from the inaugural phase of the EIDC (Cantalloube et al., 2020) which was dedicated to the task of exoplanet detection. Similarly, Chapter 5 explains the second EIDC phase (Cantalloube et al., 2022) dedicated to exoplanet characterization. My contribution as a team member of the EIDC is highlighted for both phases.

---

4 EIDC official webpage: https://exoplanet-imaging-challenge.github.io/

4

PHASE-1: EXOPLANET DETECTION

The first phase of the EIDC (Cantalloube et al., 2020), launched on September, 2019, with a deadline of October, 2020, was entirely dedicated to assessing the capability of image post-processing algorithms to detect exoplanets (point-like sources). The ensemble of data sets is hosted on a *Zenodo* open-access repository[1]. Participants were invited to submit their results via the *CodaLab* competition platform[2], which computes various detection metrics and calculates a score publicly displayed on a leader-board.

The data challenge was communicated through various media, including mailing lists, social networks, instrument consortia, and advertisements during conferences. The outcome of this phase was discussed during a dedicated workshop called *Post-processing for high-contrast imaging of exoplanets and circumstellar disks*, which took place at the end of January 2020 at the Max Planck Society Harnack-Haus in Berlin, Germany. During this workshop, the EIDC team discussed the feedback from participants and the relevance of the metrics used in the data challenge.

This first phase of the EIDC consisted of two subchallenges to be completed by each participant. The first subchallenge was devoted to assessing the task of exoplanet detection in ADI sequences. The second subchallenge was designed to evaluate the task of detection in combined ADI+mSDI sequences. This chapter includes different sections to explain each subchallenge. To conclude, there is a final section where my contribution is explicitly described.

4.1 SUBCHALLENGE-1: ADI

As explained in Section 1.2.5.1, the most common observing strategy when attempting to directly image exoplanets with ground-based telescopes is the so-called angular differential imaging (ADI, Marois et al., 2006). Therefore, the first subchallenge of the EIDC was designed to evaluate the capability of post-processing algorithms to detect injected fake companions in different ADI sequences.

---

1 EIDC phase-1 data repository: https://zenodo.org/record/3361544
2 EIDC phase-1 competition platform: https://competitions.codalab.org/competitions/20693

4.1.1 *Data sets*

The ADI sequences were carefully chosen, considering that the performance of an image post-processing algorithm can vary significantly depending on the characteristics of the data itself, such as the distribution of speckle noise along the sequence and the observing conditions (e.g., air mass, seeing, etc.). To minimize these effects in the final comparison of algorithms, we used data from various high-contrast instruments installed on ground-based telescopes. This selection process aimed to encompass a broad range of data diversity to ensure that no single algorithm would gain an unfair advantage. Additionally, even within a single instrument, we thoughtfully chose multiple data sets captured under various observing conditions, further enhancing this diversity.

As a result, we provided temporal ADI sequences from HCI instruments installed on three different ground-based telescopes: VLT/SPHERE-IRDIS (Beuzit et al., 2019), Keck/NIRC2 (Serabyn et al., 2017), and LBT/LMIRCam (Skrutskie et al., 2010). For each instrument, three representative data sets were provided, making a total of nine ADI sequences. The VLT/SPHERE instrument is a second-generation instrument equipped with extreme adaptive optics (Fusco et al., 2006) and an apodized Lyot coronagraph (APLC, Soummer, 2005), feeding light into three subsystems, including the IRDIS dual-band imager (Vigan et al., 2010), working from the Y-band (1.02 μm) to the K-band (2.25 μm). The Keck/NIRC2 instrument is equipped with an adaptive optics system (Wizinowich et al., 2000) and an Annular Groove Phase Mask (AGPM) vector vortex coronagraph (Mawet et al., 2009), optimized for observations in the Lp-band (3.78 μm). The LBT/LMIRCam instrument is equipped with an extreme adaptive optics system (Esposito et al., 2010) and the data for the EIDC are taken without coronagraph, in the Lp-band (3.78 μm).

Each of these nine ADI data sets comprised four files (in *.fits* format): (i) the *ADI sequence* (3-D image cube, illustrated in Fig. 4.1), (ii) the *parallactic angle* variation corrected from true North, corresponding to each frame in the cube, (iii) the *pixel scale* of the detector, and (iv) a non-coronagraphic (and non-saturated) *instrument PSF* taken either before or after the observing sequence, used to calibrate the detection in terms of contrast and which can be used as a model for a planetary signal.

The provided images were pre-processed to remove bad pixels, subtract dark current and background, flat fielding, and normalize the flux for the PSF. We assumed that the users would not perform further frame selection and that all the images were to be exploited. The VLT/SPHERE-IRDIS data were pre-reduced with the SPHERE Data Center (Delorme et al., 2017) using the SPHERE Data Reduction and Handling pipeline (Pavlov et al., 2008). The Keck/NIRC2 data were pre-reduced by the dedicated pre-processing

pipeline for AGPM images (Xuan et al., 2018). The LBT/LMIRCam data were pre-reduced by the pipeline developed for the LEECH exoplanet survey (Stone et al., 2018). The properties of the nine ADI sequences are summarized in Table 1.

ID	Telescope/Instr.	FWHM [px]	N_t	N_{img} [px×px]	λ_{obs} [μm]	Δ_{rot} [°]	Inj.
sph1	VLT/SPHERE	4	252	160×160	1.625 ± 0.29	40.3	1
sph2	VLT/SPHERE	4	80	160×160	1.593 ± 0.052	31.5	0
sph3	VLT/SPHERE	4	228	160×160	1.593 ± 0.052	80.5	5
nrc1	Keck/NIRC2	9	29	321×321	3.776 ± 0.70	53.0	3
nrc2	Keck/NIRC2	9	40	321×321	3.776 ± 0.70	37.3	4
nrc3	Keck/NIRC2	9	50	321×321	3.776 ± 0.70	166.9	0
lmr1	LBT/LMIRCAM	5	4838	200×200	3.780 ± 0.10	153.4	2
lmr2	LBT/LMIRCAM	4	3219	200×200	3.780 ± 0.10	60.6	2
lmr3	LBT/LMIRCAM	4	4620	200×200	3.780 ± 0.10	91.0	3

Table 1: Features of the nine ADI sequences from the EIDC subchallenge-1. N_t is the number of frames, N_{img} the frame size, λ_{obs} is the wavelength, and Δ_{rot} is the field rotation. The column on the right shows the number of fake companions injected in each ADI sequence.

4.1.1.1 *Injection procedure*

In each ADI sequence listed in Table 1, a different number of fake companions, ranging from none to five, were injected using the *Vortex Imaging Processing* (VIP, Gómez González et al., 2017; Christiaens et al., 2023) open source package[3]. To avoid interfering with potential real planetary signals or extended sources (e.g., circumstellar disks) in the ADI sequences, the point sources were injected using the opposite parallactic angles. This is a common practice in HCI in which it is assumed that the temporal statistical behavior of the starlight speckles is kept, while smearing out the potential circumstellar signals.

In HCI, the injection of an exoplanet involves first modeling the non-coronagraphic PSF, and pasting it into each image in the ADI sequence according to the parallactic angles. This injection process is further detailed in a dedicated Appendix C. The coordinates of each injection were randomly selected within angular separations between the IWA of the coronagraph and the edge of the AO correction zone making sure that the injected signals will

---

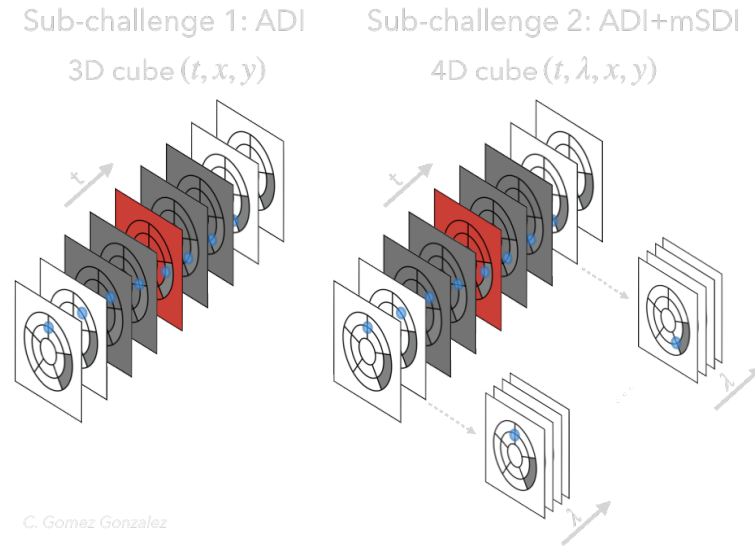3 VIP: https://vip.readthedocs.io/en/v1.4.0/

Figure 4.1: Dimensionality of the image cubes used in the EIDC: the left panel shows a single ADI data cube and the right panel shows an ADI + mSDI data cube. Blue spots in each frame represents the position of the exoplanet. Figure taken from EIDC webpage.

not overlap. The flux (or contrast) of each injection was selected in a range of $\pm 3\sigma$ from the 5σ contrast curve provided when running the chosen baseline algorithm, which is an annular PCA (Amara & Quanz, 2012; Soummer et al., 2012), also using the VIP package implementation.

4.1.2 *Evaluation procedure*

Participants were requested to provide three types of files (all in *.fits* format) for each ADI data set: a detection map (the output of the algorithm), a detection threshold applicable to all data sets, and the FWHM of the expected planetary signal within the detection map.

To assess the performance of each participant's submission, we approached the analysis as a classification problem. Specifically, we examined each submitted detection map in terms of identifying *detections* and *non-detections*. A detection was defined as any signal above the detection threshold in the detection map. Thereby, a true positive (TP) was defined as a detection within a circular aperture of FWHM diameter (we considered the instrumental PSF FWHM instead of the submitted FWHM) centered on the position of an injected companion. Conversely, a false positive (FP) was defined as a detection at any other location within the map's field of view. A false negative (FN) encompassed instances where no detection occurred at the positions of

injected companions, while a true negative (TN) accounted for the absence of detections at all other locations, considering the FWHM aperture grid applied to the image. For the non-detections, we computed the number of possible detections in the image and subtracted the number of detections. Therefore, following with this criterion, we counted the number of TPs, FPs, TNs and FNs at the detection threshold for each submitted detection map provided by the participants. We then repeated this procedure for a range of thresholds. In addition, each image post-processing algorithm has its own inner and outer working angles. To allow a fair comparison, we applied to all the detection maps received for a given data set, a unique binary mask to select the smallest IWA and largest OWA submitted for this data set.

Based on these detection considerations, we computed the following metrics for each submitted detection map at different detection thresholds (ranging from 0 to twice the submitted threshold):

- The True Positive Rate (TPR):

$$TPR = \frac{TP}{TP + FN} \tag{10}$$

- The False Positive Rate (FPR):

$$FPR = \frac{FP}{FP + TN} \tag{11}$$

- The False Discovery Rate (FDR):

$$FDR = \frac{FP}{FP + TP} \tag{12}$$

- The F1-score:

$$F1 = \frac{2 \cdot TP}{2 \cdot TP + FP + FN} \tag{13}$$

The TPR measures the proportion of injections correctly identified by a submitted algorithm. If the number of injection is non-null, the TPR as a function of the threshold is a decreasing step function. An ideal algorithm should provide a TPR of 1 whatever the threshold (up to the maximum value of the detection map). On the contrary, the FPR characterizes the residual noise in the detection map. It decreases monotonically as a function of the threshold. An ideal algorithm should provide a FPR of 0 whatever the threshold. The FDR gives information about the detections, regardless of the true negatives, which is more important for our science case as we want to detect planetary signals (and we are not interested in knowing how we cannot detect them). It is a decreasing step function with the threshold. An ideal algorithm should also provide an FDR of 0 whatever the threshold. The

F1-score combines information from both TPR and FPR into a single metric, and it provides a balanced measure of an algorithm's performance. It is also a metric that does not include TN, avoiding the need and artificial count of TNs.

To rank the performance of submissions, we relied on the area under the curve (AUC) for both TPR (denoted as AUC_{TPR}) and FDR (denoted as AUC_{FDR}), as well as the F1-score, as indicators of merit. The area under the curve regarding the FPR metric is used later in Chapter 10. For the sake of clarity, both the AUC_{TPR} and the F1-score range between 0 (indicating poor performance) and 1 (indicating exceptional performance). However, the AUC_{FDR} ranges between 0 (indicating exceptional performance) and 1 (indicating poor performance). Note that if no synthetic planetary signals were injected into the data set (e.g., *sph2* and *nrc3* sequences in Table 1), these three scores would be undefined. These scores were computed for each data set separately, on average for each instrument, and finally on average for all the data sets.

4.1.3 *Submissions and results*

For this first ADI subchallenge, 22 valid submissions were received: 11 for speckle subtraction techniques, 5 for inverse problem techniques, 5 for supervised machine learning techniques, as well as a reference-less submission, which is denoted as *unknown* hereafter. Table 2 summarizes these submissions. A more detailed description of algorithms can be found in Section 1.2.6 or in Cantalloube et al. (2020). The metrics AUC_{TPR}, AUC_{FDR} and F1-score proposed in Section 4.1.2 are gathered in Tables 3 and 4 for the 11 speckle subtraction techniques, in Table 5 for the unkwnown submission, in Table 6 for the 5 inverse problem approaches, and in Table 7 for the 5 supervised machine learning techniques. The final ranking leader-board of all these detection algorithms is shown in Fig. 4.2. Additionally, the 22 submitted detection maps obtained for the nine ADI sequences of this subchallenge can be found in Appendix A.

Algorithm	Family	Reference	Subchallenge-1	Subchallenge-2	Code source
cADI$_{\text{Specal}}$	Speckle sub.	Galicher, R. et al. (2018)	✓		SpeCal
LOCI	Speckle sub.	Lafreniere et al. (2007)	✓		VIP
TLOCI$_{\text{Specal}}$	Speckle sub.	Marois et al. (2014)	✓		SpeCal
PCA$_{\text{Specal}}$	Speckle sub.	Amara & Quanz (2012)	✓		SpeCal
PCA$_{\text{MPIA}}$	Speckle sub.	Launhardt, R. et al. (2020)	✓		SpeCal
PCA$_{\text{Padova}}$	Speckle sub.	Chauvin et al. (2017)	✓	✓	SpeCal
Unknown	?	?	✓		?
STIM$_{\text{fullframe}}$	Speckle sub.	Pairet et al. (2019)	✓		VIP
STIM$_{\text{annuli}}$	Speckle sub.	Pairet et al. (2019)	✓		VIP
STIM$_{\text{hpf}}$	Speckle sub.	Pairet et al. (2019)	✓	✓	VIP
SLIMask	Speckle sub.	Pairet et al. (2019)	✓		VIP
RSM	Speckle sub.	Dahlqvist et al. (2020)	✓		VIP
ANDROMEDA	Inverse	Cantalloube et al. (2015)	✓	✓*	SpeCal, VIP
FMMF	Inverse	Ruffio et al. (2017)	✓	✓	pyKLIP, VIP
PACO	Inverse	Flasseur et al. (2018)	✓	✓	Github
pyPACO	Inverse	Flasseur et al. (2018)	✓		VIP
TRAP	Inverse	Samland et al. (2021)	✓		Github
SODIRF$_{\text{original}}$	ML	Gómez González et al. (2018)	✓		Github
SODIRF$_{\text{adapted}}$	ML		✓		
SODINN$_{\text{LSTM}}$	ML	Gómez González et al. (2018)	✓		Github
SODINN$_{\text{BiLSTM}}$	ML		✓		
SODINN$_{\text{3D}}$	ML	Gómez González et al. (2018)	✓		Github

Table 2: Submitted algorithms in the EIDC phase-1. (✓*) Two ANDROMEDA versions were submitted for the subchallenge-2: ANDROMEDA$_{\text{ADI}}$ and ANDROMEDA$_{\text{ASDI}}$. SODIRF$_{\text{adapted}}$ and SODINN$_{\text{BiLSTM}}$ are modified versions regarding the model training.

Algorithm	VLT/SPHERE-IRDIS				Keck/NIRC2				LBT/LMIRCam				All
	sph1	sph2	sph3	Mean	nrc1	nrc2	nrc3	Mean	lmr1	lmr2	lmr3	Mean	
Baseline	1.00	*u*	0.75	0.88	0.00	0.00	*u*	0.00	0.67	0.50	0.00	0.39	0.42
	0.52	*u*	0.54	0.53	0.35	0.24	*u*	0.29	0.50	0.49	0.17	0.38	0.40
	0.42	*u*	0.21	0.32	0.29	0.54	*u*	0.41	0.32	0.49	0.31	0.37	0.37
cADI$_{SpeCal}$	0.00	*u*	0.03	0.02	0.00	0.00	*u*	0.00	0.00	0.00	0.00	0.00	0.01
	0.00	*u*	0.80	0.40	0.01	0.01	*u*	0.01	0.00	0.00	0.01	0.01	0.14
	1.00	*u*	0.98	0.99	0.01	0.01	*u*	0.01	0.01	0.01	0.01	0.01	0.34
LOCI	1.00	*u*	0.67	0.83	0.86	0.50	*u*	0.68	0.67	0.50	0.80	0.66	0.72
	0.74	*u*	0.75	0.75	0.48	0.30	*u*	0.39	0.65	0.55	0.60	0.60	0.58
	0.42	*u*	0.35	0.39	0.36	0.43	*u*	0.40	0.39	0.43	0.36	0.39	0.39
TLOCI$_{SpeCal}$	0.00	*u*	0.75	0.38	0.00	0.00	*u*	0.00	0.00	0.00	0.00	0.00	0.12
	0.39	*u*	0.49	0.44	0.21	0.08	*u*	0.15	0.00	0.25	0.00	0.08	0.22
	0.27	*u*	0.20	0.23	0.37	0.39	*u*	0.38	0.82	0.98	0.79	0.86	0.49
PCA$_{SpeCal}$	0.00	*u*	0.20	0.10	0.00	0.00	*u*	0.00	0.00	0.00	0.00	0.00	0.03
	0.00	*u*	1.00	0.50	0.01	0.01	*u*	0.01	0.00	0.00	0.01	0.00	0.17
	1.00	*u*	0.81	0.90	0.01	0.01	*u*	0.01	0.01	0.01	0.01	0.01	0.31
PCA$_{MPIA}$	1.00	*u*	0.75	0.88	0.67	0.00	*u*	0.33	0.67	0.80	0.50	0.66	0.62
	0.68	*u*	0.65	0.67	0.41	0.22	*u*	0.31	0.50	0.71	0.45	0.55	0.51
	0.31	*u*	0.29	0.30	0.32	0.37	*u*	0.34	0.33	0.42	0.32	0.36	0.33
PCA$_{Padova}$	0.50	*u*	0.83	0.67	0.00	0.00	*u*	0.00	0.40	0.50	0.22	0.37	0.35
	0.66	*u*	0.84	0.75	0.16	0.17	*u*	0.17	0.66	0.53	0.54	0.58	0.50
	0.48	*u*	0.43	0.46	0.22	0.25	*u*	0.23	0.64	0.50	0.56	0.57	0.42

Table 3: Results from the subchallenge-1 (ADI) for classic **speckle subtraction techniques**. The table shows, for each algorithm and data set, the F1-score (in black) computed at the submitted threshold, the AUC_{TPR} (in green) and the AUC_{FDR} (in red). When there are no injected planetary signals, the scores cannot be computed and are therefore undefined (indicated with *u*). The last column is the mean of the scores for the seven data sets that include injected planetary signal(s). The *baseline* algorithm is annular PCA with standard hyperparameters. Table from Cantalloube et al. (2020).

Algorithm	VLT/SPHERE-IRDIS				Keck/NIRC2				LBT/LMIRCam				All
	sph1	sph2	sph3	Mean	nrc1	nrc2	nrc3	Mean	lmr1	lmr2	lmr3	Mean	
STIM$_{fullframe}$	1.00	u	1.00	1.00	0.00	0.50	u	0.25	0.00	0.67	0.50	0.39	0.55
	0.79	u	0.88	0.84	0.36	0.19	u	0.28	0.23	0.48	0.62	0.44	0.52
	0.40	u	0.36	0.38	0.44	0.39	u	0.41	0.45	0.42	0.40	0.42	0.41
STIM$_{annuli}$	0.67	u	1.00	0.83	0.00	0.00	u	0.00	0.67	0.67	0.67	0.67	0.50
	0.84	u	0.81	0.83	0.21	0.22	u	0.21	0.26	0.68	0.67	0.54	0.53
	0.49	u	0.36	0.43	0.52	0.38	u	0.45	0.37	0.42	0.43	0.40	0.43
STIM$_{hpf}$	0.67	u	1.00	0.83	0.00	0.50	u	0.25	0.00	0.00	0.50	0.17	0.42
	0.81	u	0.85	0.83	0.23	0.21	u	0.22	0.33	0.35	0.43	0.37	0.47
	0.48	u	0.35	0.42	0.49	0.41	u	0.45	0.39	0.50	0.30	0.40	0.42
SLIMask	1.00	u	1.00	1.00	0.67	0.50	u	0.58	0.67	0.80	1.00	0.82	0.80
	0.88	u	0.89	0.89	0.39	0.27	u	0.33	0.67	0.64	0.71	0.67	0.63
	0.37	u	0.07	0.22	0.34	0.40	u	0.37	0.36	0.36	0.31	0.34	0.31
RSM	1.00	u	1.00	1.00	0.86	0.50	u	0.68	0.67	1.00	1.00	0.89	0.86
	0.84	u	0.88	0.86	0.55	0.21	u	0.38	0.45	0.62	0.73	0.60	0.61
	0.09	u	0.04	0.06	0.06	0.02	u	0.04	0.14	0.29	0.08	0.17	0.09

Table 4: Same as Table 3 for **advanced** speckle subtraction techniques. Table from Cantalloube et al. (2020).

Algorithm	VLT/SPHERE-IRDIS				Keck/NIRC2				LBT/LMIRCam				All
	sph1	sph2	sph3	Mean	nrc1	nrc2	nrc3	Mean	lmr1	lmr2	lmr3	Mean	
	0.00	*u*	0.33	0.17	0.00	0.00	*u*	0.00	0.00	0.00	0.00	0.00	0.06
Unknown	0.00	*u*	0.38	0.19	0.15	0.14	*u*	0.15	0.00	0.12	0.07	0.06	0.13
	1.00	*u*	0.37	0.69	0.60	0.37	*u*	0.48	0.39	0.38	0.43	0.40	0.52

Table 5: Same as Table 3 for the **Unknown** submission. Table from Cantalloube et al. (2020).

Algorithm	VLT/SPHERE-IRDIS				Keck/NIRC2				LBT/LMIRCam				All
	sph1	sph2	sph3	Mean	nrc1	nrc2	nrc3	Mean	lmr1	lmr2	lmr3	Mean	
ANDROMEDA	1.00	u	1.00	1.00	0.00	0.50	u	0.25	0.00	1.00	0.00	0.33	0.53
	0.53	u	0.82	0.68	0.30	0.40	u	0.35	0.18	0.63	0.21	0.34	0.46
	0.38	u	0.35	0.36	0.36	0.39	u	0.38	0.38	0.39	0.38	0.38	0.37
FMMF	0.67	u	1.00	0.83	0.67	0.50	u	0.58	0.67	0.80	1.00	0.82	0.75
	1.00	u	0.87	0.93	0.51	0.27	u	0.39	0.65	0.80	0.85	0.77	0.70
	0.43	u	0.33	0.38	0.39	0.39	u	0.39	0.43	0.43	0.33	0.40	0.39
PACO	1.00	u	1.00	1.00	0.60	0.40	u	0.50	0.67	0.57	0.06	0.43	0.64
	1.00	u	0.93	0.97	0.44	0.34	u	0.39	0.29	0.58	0.51	0.46	0.61
	0.39	u	0.32	0.36	0.43	0.48	u	0.45	0.30	0.51	0.90	0.57	0.46
pyPACO	0.08	u	0.83	0.46	0.00	0.00	u	0.00	0.07	0.09	0.12	0.09	0.18
	1.00	u	0.94	0.97	0.23	0.10	u	0.16	0.78	1.00	1.00	0.93	0.69
	0.70	u	0.50	0.60	0.40	0.69	u	0.55	0.91	0.75	0.68	0.78	0.64
TRAP	1.00	u	1.00	1.00	0.00	0.50	u	0.25	0.67	0.80	0.80	0.76	0.67
	0.68	u	0.91	0.80	0.33	0.33	u	0.33	0.50	0.70	0.61	0.60	0.58
	0.37	u	0.36	0.36	0.32	0.35	u	0.33	0.32	0.45	0.33	0.37	0.35

Table 6: Same as Table 3 for **inverse problem techniques**. Table taken from Cantalloube et al. (2020).

Algorithm	VLT/SPHERE-IRDIS				Keck/NIRC2				LBT/LMIRCam				All
	sph1	sph2	sph3	Mean	nrc1	nrc2	nrc3	Mean	lmr1	lmr2	lmr3	Mean	
SODIRF$_{original}$	0.40	u	0.59	0.49	0.22	0.00	u	0.11	0.18	0.33	0.86	0.46	0.35
	0.70	u	0.64	0.67	0.36	0.10	u	0.23	0.28	0.58	0.52	0.46	0.45
	0.55	u	0.48	0.52	0.66	0.62	u	0.64	0.52	0.53	0.47	0.50	0.55
SODIRF$_{adapted}$	0.33	u	0.91	0.62	0.22	0.00	u	0.11	0.33	0.80	0.86	0.66	0.47
	0.71	u	0.55	0.63	0.42	0.22	u	0.32	0.30	0.57	0.54	0.47	0.48
	0.56	u	0.41	0.48	0.64	0.62	u	0.63	0.51	0.44	0.45	0.47	0.53
SODINN$_{LSTM}$	0.67	u	0.83	0.75	0.33	0.00	u	0.17	0.33	0.57	0.55	0.48	0.47
	0.50	u	0.50	0.50	0.19	0.16	u	0.17	0.50	0.50	0.50	0.50	0.39
	0.47	u	0.43	0.45	0.43	0.34	u	0.38	0.47	0.47	0.48	0.48	0.44
SODINN$_{BiLSTM}$	0.40	u	0.71	0.56	0.00	0.50	u	0.25	0.11	0.33	0.20	0.21	0.34
	0.50	u	0.50	0.50	0.08	0.17	u	0.13	0.50	0.50	0.50	0.50	0.38
	0.48	u	0.45	0.47	0.45	0.22	u	0.34	0.49	0.49	0.49	0.49	0.43
SODINN$_{3D}$	0.29	u	0.83	0.56	0.25	0.29	u	0.27	0.50	1.00	0.86	0.79	0.54
	0.84	u	0.50	0.67	0.29	0.35	u	0.32	0.47	0.50	0.50	0.49	0.50
	0.65	u	0.40	0.53	0.70	0.68	u	0.69	0.48	0.46	0.48	0.47	0.56

Table 7: Same as Table 3 for **supervised machine learning techniques**. Table from Cantalloube et al. (2020).
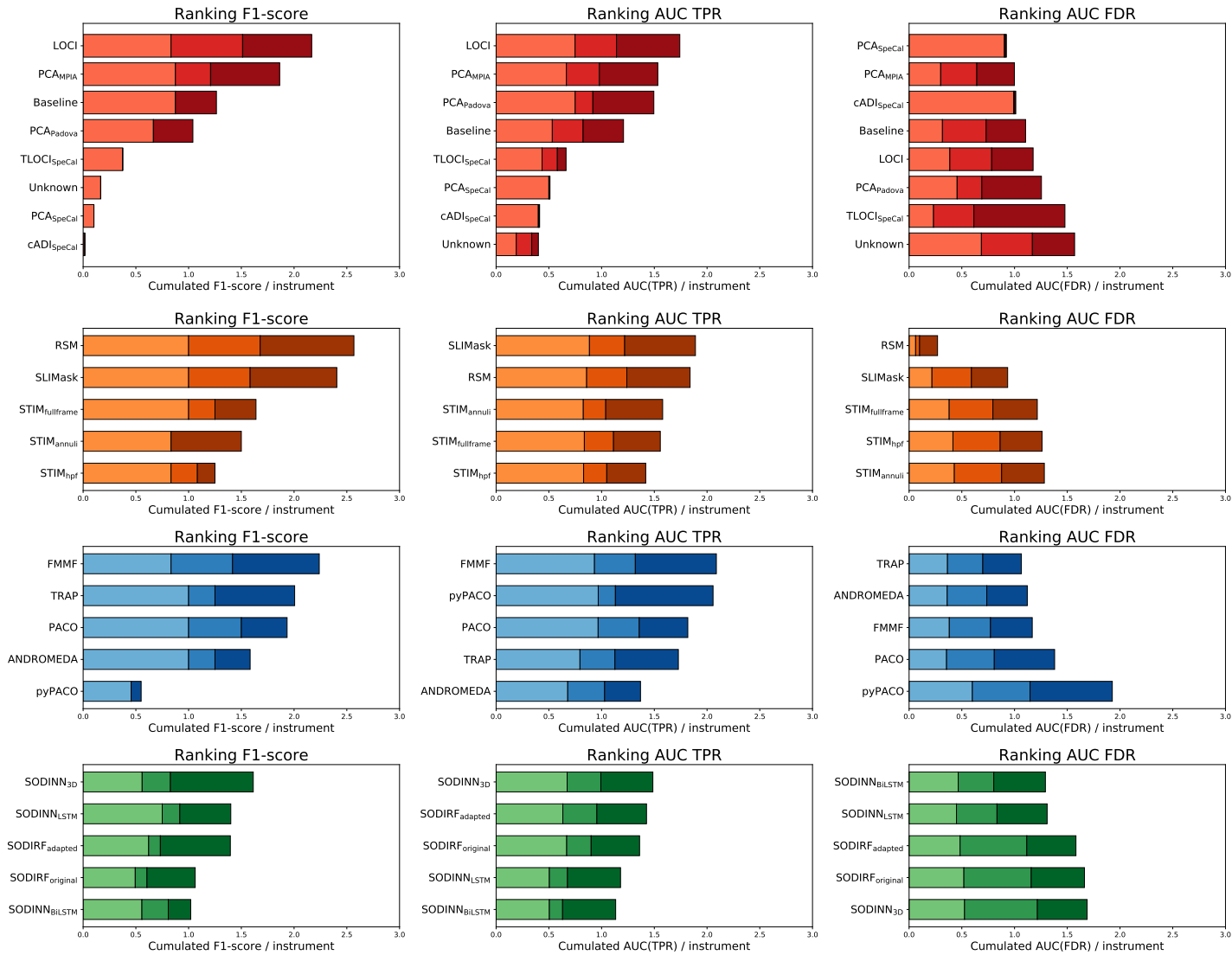
Figure 4.2: ADI subchallenge leader-board according to the F1-score (left column), AUC_{TPR} (middle column), and AUC_{FDR} (right column). The light, medium and dark colors correspond to the three SPHERE, NIRC2, and LMIRCam data sets respectively. Figure from Cantalloube et al. (2020).

4.1.4 *Discussion*

Valuable insights can be gathered from the results (Section 4.1.3) of this initial ADI subchallenge:

- **Consistency in rankings:** Results are consistent regarding the considered metrics. Specifically, a high F1-score consistently corresponds to a high AUC_{TPR} and a low AUC_{FDR} for a given method (Fig. 4.2). However, it is worth mentioning that in some cases, the AUC_{FDR} may deviate significantly from other scores. For example, certain algorithms might excel in minimizing false alarms (high AUC_{FDR}) but perform less effectively in detecting faint signals (low AUC_{TPR}). Depending on the science case, the choice of the most relevant metric becomes crucial in selecting the optimal method.

- **Poor performance of classical techniques:** As expected, classical speckle subtraction techniques (depicted in red in Fig. 4.2) demonstrate relatively poorer performance compared to more advanced approaches.

- **Challenges with supervised ML:** The exception goes to the supervised machine learning techniques (in green in Fig. 4.2) for which we observe numerous false positives. It is worth noting that applying supervised machine learning to HCI is relatively new, and ongoing efforts are aimed at enhancing their performance. Another source of bias in the current ranking of these techniques arises from the nature of the detection maps they produce. These maps are binary classifiers normalized to one, causing the true positive rate (TPR) to abruptly drop to zero for thresholds greater than the submitted threshold. Consequently, computing AUC_{TPR} over a range of thresholds from 0 to twice the submitted threshold may not be an appropriate evaluation, potentially disadvantaging these methods.

- **Instrument and data dependency:** Fig. 4.2 also highlights that the performance of algorithms is clearly dependent on the type of instrument used. Coronagraphic images (represented by light and medium colors) exhibit different characteristics in terms of stellar light residuals compared to non-coronagraphic images (depicted by dark colors). Additionally, wavelength and exposure time (number of frames) play a role, especially for algorithms that operate along the temporal axis.

- **High performance of recent algorithms:** The most recent algorithms, RSM and SLIMask for speckle subtraction techniques, and FMMF, PACO, and TRAP for inverse problem approaches, exhibit excellent performance across all three evaluation metrics employed in this study.

4.2 SUBCHALLENGE-2: ADI + MSDI

The second generation of instruments dedicated to exoplanet imaging, such as VLT/SPHERE and Gemini-S/GPI, are equipped with integral field units (IFUs) that have a relatively low spectral resolving power. These IFUs produce images simultaneously at different wavelengths, which enables the combination of ADI sequences with mSDI sequences (Section 1.2.5.2) in such a way that for each parallactic angle, frames at different wavelengths are captured (Fig. 4.1-right). Thus, the second subchallenge aimed to assess the performance of current image post-processing techniques when applied to these 4-D ADI+mSDI sequences.

4.2.1 *Data sets*

For this subchallenge, five ADI+mSDI sequences were provided from two different instruments: VLT/SPHERE-IFS (Beuzit et al., 2019), and Gemini-S/GPI (Macintosh et al., 2008), thus making a total of ten data sets. The VLT/SPHERE-IFS has two wavelength ranges, either covering the YJH bands (0.95 to 1.64 μm) or the YJ bands (0.95 to 1.33 μm). Gemini-S/GPI is similarly equipped with an extreme AO system and an APLC, and works from the J-band (0.95 μm) to the K-band (2.12 μm). In these ADI+mSDI data sets, a total of 23 planetary signals were injected following the same specifications as in Section 4.1.1.1.

Each of the ten data sets consisted of five *.fits* files. These files included the same four as those used for the ADI subchallenge data sets (Section 4.1.1), along with an additional vector that contains wavelength information corresponding to each spectral channel of the IFU. The pre-processing of image sequences was conducted using the SPHERE Data Center (Delorme et al., 2017) for the VLT/SPHERE-IFS data, employing the SPHERE Data Reduction and Handling pipeline (Pavlov et al., 2008). On the other hand, the Gemini-S/GPI data was pre-processed using the GPI Data Cruncher (Maire et al., 2010; Perrin et al., 2016) and the GPI reduction pipeline (Wang et al., 2018). A summary of the properties of these ten data sets can be found in Table 8.

4.2.2 *Evaluation procedure*

The evaluation of submissions for this second subchallenge was based on the same metrics (AUC_{TPR}, AUC_{FDR} and F1) as proposed for the ADI subchallenge (Section 4.1.2).

ID	Telescope/Instr.	λ_{range} [μm]	N_t	N_{img} [px×px]	N_λ	Δ_{rot} []	Inj.
ifs1	VLT/SPHERE-IFS	$0.957 - 1.329$	128	200×200	39	25.6	2
ifs2	VLT/SPHERE-IFS	$0.957 - 1.636$	112	200×200	39	131.9	4
ifs3	VLT/SPHERE-IFS	$0.957 - 1.636$	109	200×200	39	43.5	2
ifs4	VLT/SPHERE-IFS	$0.957 - 1.636$	112	200×200	39	46.2	4
ifs5	VLT/SPHERE-IFS	$0.957 - 1.329$	80	200×200	39	31.8	0
gpi1	Gemini-S/GPI	$1.495 - 1.797$	35	161×161	37	54.7	1
gpi2	Gemini-S/GPI	$1.495 - 1.797$	41	161×161	37	22.5	3
gpi3	Gemini-S/GPI	$1.495 - 1.797$	38	161×161	37	12.6	0
gpi4	Gemini-S/GPI	$1.495 - 1.797$	37	161×161	37	13.8	3
gpi5	Gemini-S/GPI	$1.495 - 1.797$	44	161×161	37	24.4	4

Table 8: Features of the ten ADI+mSDI sequences from the EIDC subchallenge-2. N_t is the number of frames, N_{img} the frame size, λ_{range} is the range of observation wavelength, N_λ is the number of channels along the spectral axis, and Δ_{rot} is the field rotation. The column on the right shows the number of fake companions injected in each ADI+mSDI sequence.

4.2.3 *Submissions and results*

A total of 6 valid submissions were received for this subchallenge: 2 for speckle subtraction techniques, and 4 for inverse problem techniques (see Table 2). Their evaluation scores (AUC_{TPR}, AUC_{FDR} and F1) proposed in Section 4.1.2 are gathered in Table 9. The final ranking leader-board is shown in Fig. 4.3. Additionally, the 6 submitted detection maps obtained for the 10 data sets of this subchallenge can be found in Appendix B.

Algorithm	VLT/SPHERE-IFS						Gemini-S/GPI						All
	ifs1	ifs2	ifs3	ifs4	ifs5	Mean	gpi1	gpi2	gpi3	gpi4	gpi5	Mean	
Baseline	0.80	0.75	0.40	0.00	u	0.49	0.00	0.00	u	0.00	0.67	0.17	0.33
	0.78	0.77	0.63	0.21	u	0.60	0.34	0.24	u	0.19	0.60	0.34	0.47
	0.57	0.36	0.71	0.98	u	0.65	0.46	0.39	u	0.46	0.30	0.40	0.53
PCA$_{\text{Padova,ASDI}}$	0.50	0.25	0.18	0.17	u	0.27	0.00	0.15	u	0.22	0.57	0.24	0.26
	0.94	0.87	0.73	0.50	u	0.76	0.46	0.44	u	0.41	0.99	0.57	0.67
	0.59	0.78	0.83	0.58	u	0.69	0.60	0.97	u	0.61	0.54	0.68	0.69
STIM$_{\text{ADI}}$	1.00	0.86	0.67	0.40	u	0.73	0.00	0.00	u	0.00	0.86	0.21	0.47
	0.86	0.80	0.65	0.42	u	0.68	0.39	0.29	u	0.24	0.82	0.44	0.56
	0.32	0.30	0.29	0.29	u	0.30	0.36	0.38	u	0.30	0.39	0.36	0.33
ANDROMEDA$_{\text{ADI}}$	0.80	1.00	0.67	0.40	u	0.72	1.00	0.00	u	0.29	0.86	0.54	0.63
	0.75	0.81	0.66	0.44	u	0.66	0.73	0.26	u	0.38	0.76	0.53	0.60
	0.46	0.36	0.39	0.41	u	0.41	0.38	0.44	u	0.55	0.36	0.43	0.42
ANDROMEDA$_{\text{ASDI}}$	1.00	1.00	0.50	0.33	u	0.71	1.00	0.00	u	0.29	1.00	0.57	0.64
	0.81	0.76	0.65	0.53	u	0.69	0.51	0.35	u	0.34	0.89	0.52	0.60
	0.44	0.32	0.44	0.44	u	0.41	0.37	0.53	u	0.58	0.40	0.47	0.44
FMMF$_{\text{ASDI}}$	1.00	1.00	0.80	1.00	u	0.95	0.00	0.80	u	0.00	1.00	0.45	0.70
	1.00	0.97	1.00	0.98	u	0.99	0.37	0.55	u	0.33	1.00	0.56	0.77
	0.39	0.34	0.40	0.33	u	0.36	0.43	0.38	u	0.39	0.33	0.38	0.37
PACO$_{\text{ASDI}}$	1.00	0.86	0.67	0.86	u	0.85	x	x	u	x	1.00	x	x
	1.00	0.86	0.57	0.78	u	0.81	x	x	u	x	0.98	x	x
	0.34	0.37	0.38	0.33	u	0.36	x	x	u	x	0.36	x	x

Table 9: Same as Table 3 for **subchallenge-2 (ADI+mSDI)**, encompassing both speckle subtraction and inverse problem algorithms. The x symbol means that the detection map was not submitted. The corresponding algorithm, PACO$_{\text{ASDI}}$, will not be taken into account in the ranking. Table from Cantalloube et al. (2020).
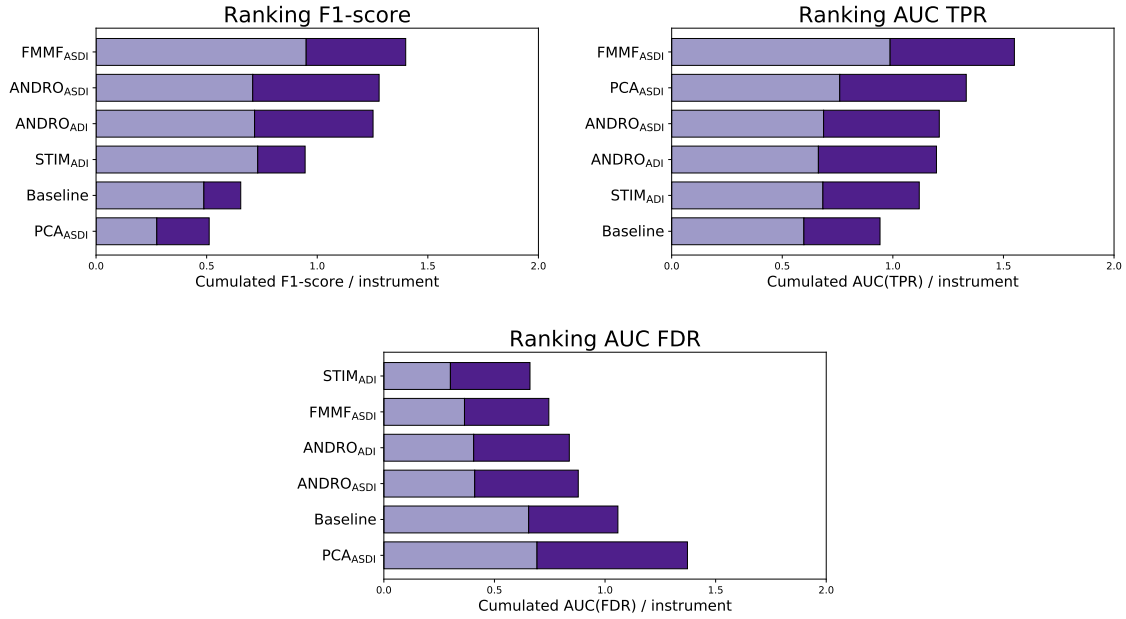
Figure 4.3: EIDC ranking of submitted algorithms for the subchallenge-2 (ADI+mSDI) according to the F1-score (top left), AUC_{TPR} (top right), and AUC_{FDR} (bottom). The light and dark colors correspond to the five VLT/SPHERE-IFS and five Gemini-S/GPI data sets respectively. Figure taken from Cantalloube et al. (2020).

4.2.4 Discussion

Different insights can be gathered from the results (Section 4.2.3) of this ADI+mSDI subchallenge:

- **Effective exploitation of spectral information:** It is clear from Fig. 4.3 that exploiting the spectral information enhances the ability to detect faint planetary signals. For example, when comparing the detection maps of $STIM_{ADI}$ and PCA_{Padova} to PCA_{ASDI}, or $ANDROMEDA_{ADI}$ to $ANDROMEDA_{ASDI}$ in Fig. B.10, we observe a clear disadvantage in detecting the faintest companions.

- **Impact of spectral templates:** The spectral template used as a prior for the planetary signal in some methods plays an important role. For instance, in Fig B.4, $PACO_{ASDI}$ uses a uniform spectral template prior and does not detect one of the four planetary signal. However, by using a non-flat spectrum as a prior, the signal of the fourth planet is above the submitted threshold.

- **Inconsistent performance:** As a general rule, based on the image galleries in Appendix B, the more advanced/recent techniques perform

better at detecting planetary signals but the results are not homogeneous. This shows once again that applying various algorithms based on different concept is the most appropriate way of validating or invalidating a candidate based on a single data set.

- **Unique value of inverse problem approaches:** Again, inverse problem approaches stand out as the only methods that directly yield information about the contrast of the planetary signal candidates. This capability enables to further disentangle the candidate from any remaining stellar residuals by comparing the extracted spectrum of the candidate with that of a residual speckle.

4.3 MY CONTRIBUTION

During the first phase of the EIDC, I played a dual role as both a team member and an active participant. My contributions included providing support during group meetings to facilitate decision-making processes, submitting supervised machine learning algorithms, and conducting a thorough evaluation of all the data challenge submissions.

With respect to the challenge submissions, owing to my line of research, I was exploring and implementing supervised machine learning algorithms. Specifically, my focus was on the development and deployment of SODIRF and SODINN (Gómez González et al., 2018), two binary classifiers that uses a random forest and CNNs, respectively. For the case of SODINN, I implemented the two versions – one using convolutional 3D layers ($SODINN_{3D}$) and the other employing Convolutional-LSTM layers ($SODINN_{LSTM}$). Initially, I applied the original versions of these algorithms to the EIDC dataset. As I delved deeper into their functionalities, I recognized opportunities for enhancing their architectures and refining training methodologies. In the case of SODIRF, I introduced a *Grid Search Cross-Validation* during the training. This strategy, unlike the common hold-out method, systematically explores a predefined set of hyperparameters by evaluating each combination through k-fold cross-validation (see Section 2.2). This adaptation was referred to as $SODIRF_{adapted}$ (Table 2) and resulted in a better performance than the $SODIRF_{original}$ (Fig 4.2). For the case of SODINN, I modified its network through introducing GRU and Bidirectional layers (see Section 2.3.3.2). This was motivated by the fact that these layers better capture temporal information in time-series data, such as the patch sequences used in SODINN. My experiments with the GRU version did not yield substantial improvements, and that is the reason why I finally opted not to submit it. However, my tests with the Bidirectional version proved to be insightful, leading me to submit this iteration, denoted as $SODINN_{BiLSTM}$, to the EIDC. Given the time constraints imposed by the challenge deadline, I was unable to conduct

more complex testing on these algorithms. Nevertheless, this experience was valuable as it marked my initial contact into these advanced techniques.

Once the EIDC challenge concluded, my role, as a team member, was to evaluate all of submitted detection maps according to the criteria explained in Section 4.1.2. I carefully reviewed each submission file to ensure compliance with the prescribed format and EIDC guidelines. To streamline the evaluation process and maintain consistency, I then developed a specialized code. This code automatically extracted proposed metrics from the detection maps provided by each algorithm submission. With the extracted metrics in hand, I finally conducted a comprehensive analysis of all the results. This involved examining performance metrics and looking for patterns and trends within the submissions to gain insights into the strengths and weaknesses of different approaches. It is important to mention that this evaluation process was conducted by another team member in parallel. This was crucial in providing an objective and unbiased interpretation of the results. It helped ensure that our assessments were robust and reliable, ultimately contributing to fair judgment and selection of the most effective algorithms.

PHASE-II: CHARACTERIZATION OF EXOPLANETS

Following the successful completion of the first phase of the EIDC (Chapter 4), the endeavour of the EIDC team was to expand its scope with a second phase dedicated to exoplanet characterization. When an exoplanet is detected within high-contrast images, it needs to be characterized. This involves estimating its relative projected position and brightness with respect to the target star, across one or more wavelengths. This characterisation step is essential to confirm that the detected signal is gravitationally bound to the star and is of a (sub)stellar nature, making it a firm companion detection. Additionally, characterizing the detected object is essential for extracting information about its orbital and atmospheric properties.

This second phase of the EIDC (Cantalloube et al., 2022) was launched on April, 2022, and it is still open for submissions. The goal is to assess the characterization capabilities of various HCI post-processing techniques. To achieve this, each participant is tasked with two specific subchallenges, diverging from the previous phase where subchallenges were related to the observing strategy. In EIDC phase-2, participants must accurately recover the position (subchallenge-1) of each injected object in the dataset and precisely recover their spectral information (subchallenge-2). The ensemble of data sets for this phase are again hosted on *Zenodo*[1]. The participants are invited to submit their results via the *EvalAI*[2] competition platform.

Because the competition is still ongoing, official results are yet to be published. Nevertheless, this short chapter aims to provide a general description of the challenge, including a submission example, as well as to highlight my ongoing contribution to it.

5.1 DATA SETS

This challenge is composed by eight ADI+mSDI cubes (Table 10) from where participant's algorithm have to characterize injected companions. These data sets are taken with the integral field units (IFU), installed at the Gemini-South

---

1 EIDC phase-2 data repository: https://zenodo.org/record/6902628
2 EIDC phase-2 competition platform: https://eval.ai/web/challenges/challenge-page/1717/

telescope GPI (Macintosh et al., 2008), and SPHERE-IFS (Beuzit et al., 2019), installed at the Very Large Telescope (VLT). The various data sets are taken under different observing conditions, ranging from very good observing conditions on a bright target star to very bad observing conditions on a faint target star (Table 10).

ID	Target	λ_{range} [μm]	N_t	N_{img} [px×px]	N_λ	Δ_{rot} [°]	Obs. conditions
gpi1	B	1.495 - 1.797	37	169×169	37	14.4	Very good
gpi2	B	1.495 - 1.797	36	169×169	37	156.6	Medium (WDH)
gpi3	B	1.495 - 1.797	38	169×169	37	13.3	Medium
gpi4	F	1.495 - 1.797	37	169×169	37	14.2	Poor (LWE)
sph1	B	0.957 - 1.329	144	189×189	39	26.8	Very good
sph2	B	0.957 - 1.329	80	189×189	39	14.4	Poor (WDH)
sph3	F	0.957 - 1.329	64	189×189	39	25.8	Very good
sph4	B	0.957 - 1.329	90	189×189	39	144.8	Poor (WDH)

Table 10: Features of the eight data sets provided for the EIDC phase-2. N_t is the number of frames, N_{img} the frame size, λ_{range} is the range of observation wavelength, N_λ is the number of channels along the spectral axis, and Δ_{rot} is the field rotation. The target star is labeled as *bright (B)* for magnitude in the J-band below 7 and as *faint (F)* above. The last column qualitatively indicates the observing conditions: *LWE* stands for low-wind effect and *WDH* stands for wind-driven halo.

Each data set is composed of different files (in *.fits* format): (i) the ADI+mSDI sequence (4-D image cubes, see right of Fig. 4.1), (ii) vectors of parallactic angles and airmass variation, the multispectral PSF (non-coronagraphic) of the target, (iii) the vector of the central wavelength of each IFU channel, and (iv) a first guess position of the injected signals.

The pre-processing of the raw images (i.e. dark subtraction, flat fielding, bad pixel correction, re-centering, cropping, flux normalization and frame selection) was performed by the GPI and SPHERE consortia via the custom-tools they developed: the GPI data cruncher (Perrin et al., 2016), and the SPHERE data center (Delorme et al., 2017), respectively. Before injecting synthetic planetary signals, we homogenized the data (centering, cropping and setting of a parallactic angles direction convention).

5.1.1 *Injection procedure*

In each ADI+mSDI cube, two to three synthetic planetary signals are injected at various locations of the field of view. Each companion is injected with subpixel precision through Fourier-transform methods to avoid interpolation errors (Larkin et al., 1997). As in EIDC phase-1, the synthetic planetary signals were injected using the opposite parallactic angle variation in order to avoid any real astrophysical signal to interfere. Additionally, because the final goal of planetary spectrum retrieval is to estimate the atmospheric physical parameters of the planet, the companions have been injected following emission spectra simulated with the radiative transfer tool `petitRADTRANS` (Mollière et al., 2019) that is available in open source[3]. For these injected spectra (unknown to the participants), we chose realistic physical parameters (L- or T-dwarf typical spectra) and sometimes added the contribution of circumplanetary material emission by adding a black-body contribution using the *SPEctral Characterization of directly ImAged Low-mass companions* (`SPECIAL`, Christiaens, 2022) open-source package[4], and sometimes a bit of noise. To choose the signal-to-noise of the injected planetary signals, we ran an annular PCA, as implemented in `VIP` (Gómez González et al., 2017; Christiaens et al., 2023), and extracted the average contrast over all wavelengths that we defined for the injection. We refer to Cantalloube et al. (2022) for a detailed description of this injection procedure, the spectra simulation, and their potential limitations.

5.2 EVALUATION PROCEDURE

For every planetary injection, participants are tasked with two subchallenges: accurately estimating the planet astrometry (distance to the star in pixels, using Cartesian coordinates) and its spectrum (contrast to the star, estimated at each wavelength λ).

Based on the submitted astrometry, EvalAI calculates the L2-norm (Euclidean distance) between the estimated position $\hat{p}_i$ and the ground truth position p_i^{GT} for each injection i, and then aggregate these distances across all injections. The resulting astrometry metric, denoted as D_{XY}, represents the mean distance for all N_{inj} injections, where the closer to 0 the better:

$$
\begin{aligned}
D_{XY} &= \frac{1}{N_{inj}} \cdot \sum_i |\hat{p}_i - p_i^{GT}|_2 \\
&= \frac{1}{N_{inj}} \cdot \sum_i \sqrt{(\hat{x}_i - x_i^{GT})^2 + (\hat{y}_i - y_i^{GT})^2}.
\end{aligned}
\tag{14}
$$

---

3 `petitRADTRANS`: https://petitradtrans.readthedocs.io/en/latest/
4 `SPECIAL`: https://special.readthedocs.io/en/latest/

For the spectral retrieval, EvalAI computes the L1-norm-based distance, calculated independently for each spectral channel (λ). It quantifies the absolute difference between the estimated value $\hat{c}_\lambda$ and the corresponding ground truth value c_λ^{GT}. This difference is normalized by the ground-truth contrast for each channel, ensuring equal weight for relative differences across all spectral channels. The final metric D_C is the mean of these normalized distances across all N_{inj} injections and N_λ spectral channels of the IFU, where again, the closer to 0 the better:

$$D_C = \frac{1}{N_{inj}} \cdot \frac{1}{N_\lambda} \cdot \sum_i \sum_\lambda \frac{|\hat{c}_{\lambda,i} - c_{\lambda,i}^{GT}|_1}{c_{\lambda,i}^{GT}}. \tag{15}$$

It is worth mentioning that both the D_{XY} and D_C metrics do not take into account the uncertainties on the estimations $\hat{c}_\lambda$ and $\hat{c}_\lambda$. The decision to omit uncertainties was driven by the fact that some algorithms, particularly those based on supervised machine learning, do not provide uncertainty estimates.

5.3 SUBMISSION EXAMPLE

The EIDC team used two image post-processing algorithms to exemplify a submission for this second phase of the EIDC. These are the PCA-NEGFC (Marois et al., 2010) and ANDROMEDA (Cantalloube et al., 2015), two techniques widely used in the community to characterize companions.

5.3.1 *Test data set*

In this submission example, we make use of an ADI+mSDI data set obtained from the SPHERE-IFS instrument. Hereafter, this data set is referred to as *sph-test*. It is also provided to the participants to estimate hyper-parameters of algorithms when necessary and perform various tests before their final submission on the EvalAI platform. The observations were conducted under average conditions, with a mean seeing of 0.99 ± 0.22 arcsec and a mean coherence time of 5.8 ± 1.3 ms. The target star has a magnitude of $H_{mag} = 6.22$ and $V_{mag} \simeq 9.4$, resulting in a Strehl ratio of $68 \pm 10\%$ in the H-band. It is a bright target star observed for about one hour, with an exposure time of 64 s, giving 65 images with a field rotation of 22.2°. The airmass variation during the observing time is shown in Fig. 5.1 (bottom-left panel). The stellar flux extracted from Gaussian fits to the non-coronagraphic multispectral images is shown in Fig. 5.1 (bottom-central panel). The model stellar spectral energy distribution (SED) used for calculation of the atmospheric and instrumental transmission is a K7V spectral type, with an effective temperature $T_{eff} = 4000$ K and a surface gravity $\log(g) = 4.5$ cm/m^2, whose shape is shown in Fig. 5.1 (bottom-right panel).

Two fake companions are injected in the *sph-test* sequence. The first, referred to as planet *b*, is injected close to the star at a separation of 155.3 mas. The second, referred to as planet *c*, is injected outside of the AO correction zone, at a separation of 615.9 mas. Fig. 5.1 (top-left panel) shows the ADI median subtraction processed frame at the shortest wavelength (0.957 μm) along with the location of the two injected planets. The model planet spectra considered for the two injections are shown in Fig. 5.1 (top-central panel). These correspond to a 1800 K black body (orange line) and the best-fit model to planet HR8799e (red line), for *b* and *c* respectively. These spectra are also shown in Fig. 5.1 after convolution and resampling considering the SPHERE-IFS spectral resolving power and wavelength sampling (top-right panel). The actual spectra injected in the data cube further consider atmospheric+instrumental transmission, and the effect of airmass. The mean contrast over all the spectral channels chosen for the injections is set to 1.8×10^{-4} and 2.0×10^{-4} for planets *b* and *c*, respectively. After a simple full frame ASDI PCA processing, using 10 principal components to build the model PSF that is subtracted, it corresponds to S/N values of 5σ and 25σ in the post-processed image, respectively.
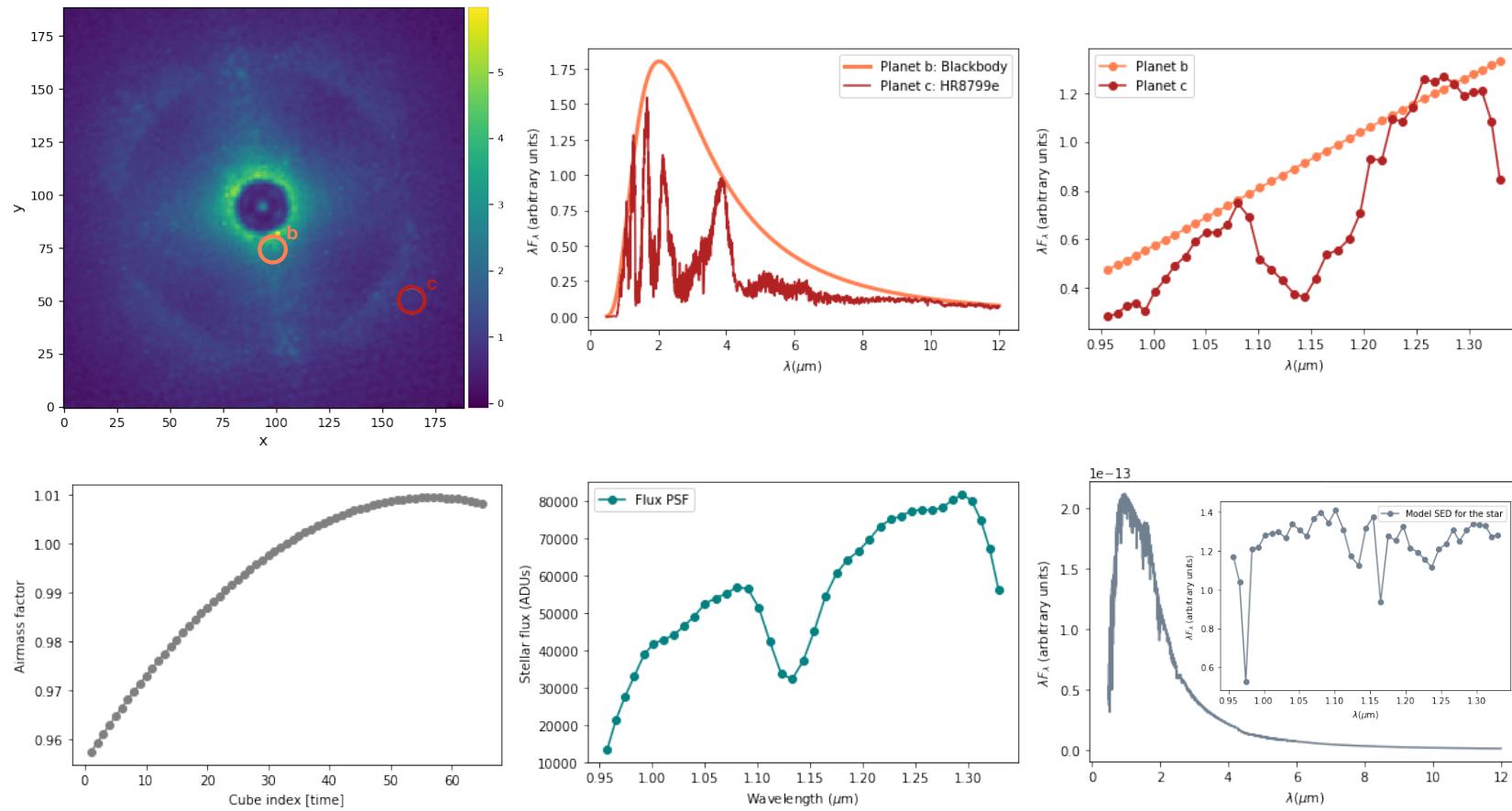
Figure 5.1: Properties of the *sph-test* data set. *Top:* Median-subtraction processed frame at the shortest wavelength highlighting the two injections *b* and *c* with colored circles (left) and their injected spectra of the two planetary signals (middle), sampled at the SPHERE-IFS spectral resolving power (right). *Bottom:* Airmass factor used for the whole observing sequence (left), extracted spectrum of the non-coronagraphic PSF (middle), and stellar SED model used for the target star (right), sampled at the SPHERE-IFS spectral resolving power. Plots taken from Cantalloube et al. (2022).

Algorithm	Astrometry			Spectro-photometry		
	Planet b	Planet c	Mean	Planet b	Planet c	Mean
PCA-NEGFC	0.37	0.03	0.20	16.98	1.03	9.00
ANDROMEDA	1.95	0.06	1.01	35.67	2.29	18.99

Table 11: Distance metrics D_{XY} (astrometry) and D_C (spectro-photometry) of Section 5.2 computed from the PCA-NEGFC and ANDROMEDA algorithm submissions for the two injections b and c on the sph − test data set. The closer to 0 the better.

5.3.2 *Results*

The final detection maps from the two considered algorithms are shown in the left column of Fig. 5.2, and their astrometry distance metrics (Eq. 14) are shown in Table 11. To complement, Fig. 5.3 (top panels) illustrates the subpixel precision of both methods at estimating the position of planets b and c.

The detection limits for both methods as 5σ contrast curves are shown in the right column of Fig. 5.2, and their contrast distance metrics (Eq. 15) are shown in Table 11. Moreover, Fig. 5.3 (middle and bottom panels) illustrates the precision of both methods at estimating the contrast of planets b and c at each wavelength channel.

5.3.3 *Discussion*

Table 11 shows that distance metrics are always better (closer to 0) for planet c than for planet b, regardless of the subchallenge or the algorithm used. This can be explained in terms of image noise: planet b lies very near the star (Fig. 5.1 top-left), in an area where residual speckles dominate, conditions for which HCI algorithms struggle. On the contrary, planet c is easier to detect/characterize because it is brighter, distant from the star, and less impacted by residual starlight.

Valuable conclusions can be gathered regarding the astrometry task:

- **Planet b:** PCA-NEGFC obtained better results than ANDROMEDA. In addition to being located at small angular separations, planet b lies on a bright speckle, with a S/N spot that is quite elongated radially for the case of ANDROMEDA (Fig.5.2, bottom-left). This biases its estimation towards a closer separation. The PCA-NEGFC technique appears to be less affected by this effect.
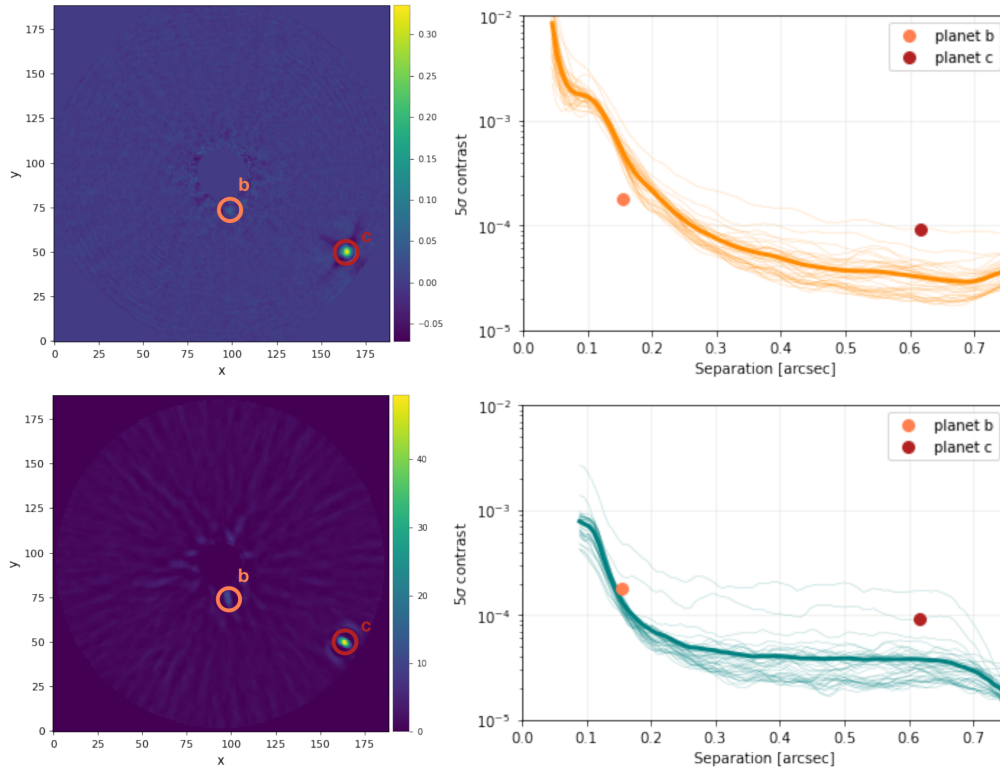
Figure 5.2: PCA (row on top) and ANDROMEDA (row on bottom) results from the
$sph-test$ sequence. The left column show the detection maps, a residual
map obtained using 10 principal components (for PCA) and a S/N map
(for ANDROMEDA). The right column the corresponding detection limit
as 5σ contrast curves, where the 39 thin lines are the contrast curve for
each channel of the spectro-imager. The thick line is the mean of all the
thin lines. The two dots show the radial position and mean contrast of
the two injected planetary signals. Plots taken from Cantalloube et al.
(2022).

- **Planet c:** Both methods provide estimations within ∼ 0.05 pixel from
  the ground truth, although it is worth mentioning that the associated
  uncertainties appear slightly underestimated in both cases.

Regarding the spectro-photometry task:

- **Planet b:** ANDROMEDA provides the correct trend but seems to be
  always slightly higher than the ground truth, in particular in the redder
  spectral channels (i.e. the residuals are flat with wavelength). This
  can again be explained by the presence of the bright speckle that lies
  below the injection and that crosses the injection location at larger
  wavelength. On the contrary, PCA-NEGFC slightly overestimates the
  bluer spectral channels, while extracting very accurate values at longer

wavelengths (i.e. the residuals are decreasing with wavelength). PCA-NEGFC provides a rather flat spectrum. This can be understood by the residual minimization procedure performed by NEGFC that is more aggressive towards residual speckles. However, we can see that even though both methods give results within 5σ from the ground truth, this is still sub-optimal as many points are not within 3σ (for both methods), demonstrating that there is still room for improvement.

- **Planet c:** PCA-NEGFC provides an almost perfect estimate of the spectrum. ANDROMEDA provides slightly worst results at bluer wavelengths. This is probably because the starlight residuals distribution is more intense and shaped in this part of the spectrum and ANDROMEDA heavily relies on the assumption that the subtraction residuals are Gaussian and white, which we now know is not a perfect assumption (this Gaussianity problem is further explained in Part III of the thesis). Both methods have larger uncertainties at short wavelength due to the inherent shape of the spectrum.

5.4 MY CONTRIBUTION

For this second phase of the EIDC, my contributions included providing support during group meetings to facilitate decision-making processes, as well as developing the challenge's evaluation back-end code (Section 5.2) for the EvalAI platform. Furthermore, as in the first phase of the EIDC, it is expected that I will share joint responsibility with another member of the team for conducting the evaluation analysis once the challenge is completed.
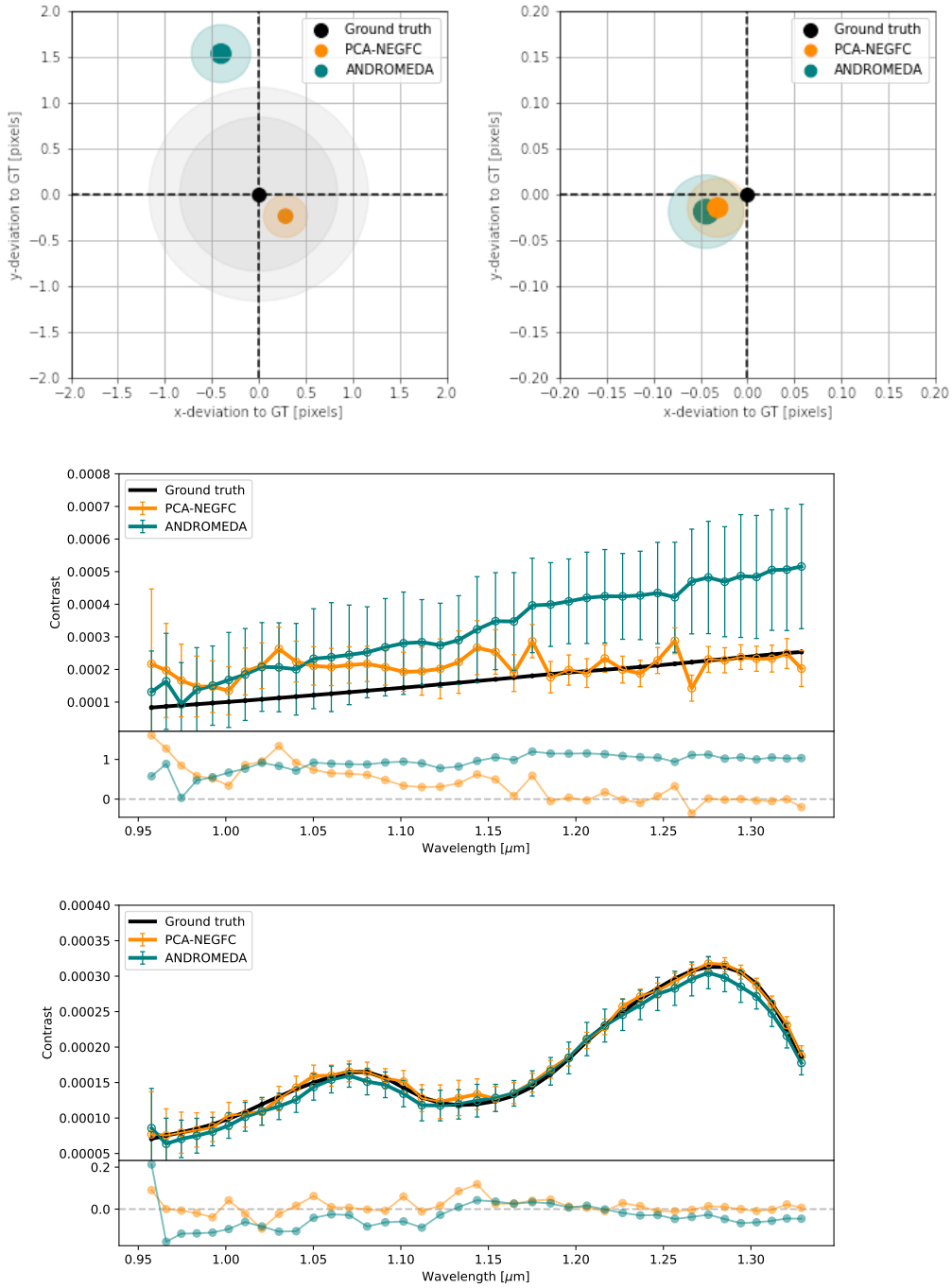
Figure 5.3: Estimations of PCA (in orange) and ANDROMEDA (in blue) compared to the ground truth (in black) for the **astrometry** task (top) for planet b (top-left) and c (top-right), and the **spectro-photometry** task for planet b (middle) and planet c (bottom). For the astrometry plots, the size of the symbols corresponds to the 1σ uncertainty and the shaded area to the 3σ uncertainty. The two centered grey shaded areas represent the size of a half resolution element (0.5 λ/D) for the shortest and largest wavelengths of the spectro-imager. For the spectro-photometry plots, the error bars displayed correspond to the 3σ uncertainties on the photometry estimation. Plots taken from Cantalloube et al. (2022).

CONCLUSIONS

In this part II of the thesis, the first phase (exoplanet detection, Cantalloube et al., 2020) and the second phase (exoplanet characterization, Cantalloube et al., 2022) of the *Exoplanet Imaging Data Challenge*[5](EIDC) were presented, as well as my contribution to them. A clear message emerges from the whole set of conclusions extracted from the EIDC: The most recent HCI post-processing algorithms outperform more traditional techniques commonly employed in direct imaging campaigns. This enhanced performance can be directly attributed to the substantial advancements in our understanding of the underlying physics governing high-contrast images and observing strategies, particularly concerning the temporal and spatial characteristics of image noise (speckle noise) within HCI data, such as ADI sequences. This, in turn, paves the way for the development of novel strategies that, when integrated into post-processing algorithms, enable the capture of stronger image pixel correlations. Consequently, this leads to a notable improvement in the ability to differentiate residual speckles from planetary signatures.

Plans for future EIDC phases involve expanding the challenge's horizons to other imaging tasks and HCI instruments. In the third phase, the focus should shift towards circumstellar disk imaging. Recent advancements, including methods such as MAYONNAISE (Pairet et al., 2021), REXPACO (Flasseur et al., 2021) and MUSTARD (Juillard et al., 2023), alongside adaptations of classical techniques like iterative PCA (Pairet et al., 2018) and NMF (Ren et al., 2018), will be used. This phase aims not only to detect circumstellar signals but also to accurately reconstruct their total intensity distribution. In a potential fourth phase, the focus could shift to High-Resolution Spectroscopy (HRS) with instruments like VLT/ERIS (Davies et al., 2023), VLT/MUSE (Bacon et al., 2010), VLT/CRIRES+ (Follert et al., 2014), and Keck/NIRSPEC (McLean et al., 1998). This phase will specifically focus on techniques based on molecular mapping, which are currently in active development (Rameau et al., 2021). Additionally, this phase could involve simulating high-contrast images from the coming ELT to assess the adaptability of post-processing techniques and prepare the image processing toolkit for the forthcoming first light (Houllé et al., 2021).

---

5 EIDC webpage: https://exoplanet-imaging-challenge.github.io/

Part III

NOISE REGIMES IN PROCESSED ADI IMAGES

INTRODUCTION

The research conducted in the EIDC (Part II) has exposed the limitations of recent image post-processing techniques based on supervised machine learning, such as SODINN. While this method has showcased its potential in enhancing traditional PSF subtraction approaches (Gómez González et al., 2018), it has also revealed a significant susceptibility to various factors, including data characteristics and observing conditions. These factors can significantly impact its effectiveness in detecting exoplanets, leading to a notable occurrence of false positives. In contrast, more recent inverse problem techniques (Section 1.2.6.2), such as FMMF (Pueyo, 2016; Ruffio et al., 2017), PACO (Flasseur et al., 2018) and TRAP (Samland et al., 2021), as well as advanced PSF subtraction methods (Section 1.2.6.1) like RSM (Dahlqvist et al., 2020) and its subsequent refinements (Dahlqvist et al., 2021a,b), have demonstrated higher detection performance. As discussed in Part II, this improvement can be directly attributed to the fact that, along the last two decades, we have accumulated a better understanding of high-contrast imaging data, including the temporal and spatial behaviours of speckle noise. As a result, these insights have been smartly integrated into novel post-processing techniques.

In this context, a trend has emerged when designing novel post-processing techniques: exploiting the local characteristics of image noise yields significant advantages in exoplanet detection. The term *local* is often used in image processing to describe a process applicable to a smaller portion of the image, such as the neighborhood of a pixel, in which pixel values exhibit a certain amount of correlation. In HCI, defining image locality implies a good understanding of the physical information captured in the image. A common way to define this locality is linked to the noise distribution along the field of view. For example, after some pre-processing steps (including background subtraction), a high-contrast image is composed of three components: (i) residual starlight under the form of speckles; (ii) the signal of possible companions; and (iii) the statistical noise associated with all light sources within the field of view, generally dominated by background noise in infrared observations. In these raw images, exoplanets are hidden because starlight speckles and/or background residuals dominate at all angular separations, and act as a noise source for the detection task. Here, the locality of the noise is driven by the distance to the host star (Marois et al., 2008a), which already gives an indication on how local noise will be defined in a processed image. Consequently, a large fraction of post-processing algorithms currently

work and process noise on concentric annuli around the star. For example, the annular-PCA algorithm (Absil et al., 2013; Gómez González et al., 2016) performs PSF subtraction with PCA on concentric annuli. Nevertheless, more sophisticated local approaches have recently been proposed in the literature. For instance, both the TRAP algorithm (Samland et al., 2021) and the HSR algorithm (Gebhard et al., 2022) take into account the symmetrical behavior of speckles around the star when defining pixel predictors for the model.

In light of these recent advancements on capturing improved image correlations from a local perspective, our main goal for this third part of the thesis is to explore and develop a novel local noise approach tailored to enhance the performance of image post-processing techniques, especially for SODINN. The presented approach relies on the existence of two noise regimes in the ADI processed frame: a speckle-dominated residual noise regime close to the star, and a background-dominated noise regime further away. The presence of these two different regimes along the field of view is usually assumed for HCI studies, however, to the best of our knowledge, their identification has never been thoroughly addressed. Thereby, our goal is to spatially define these regimes in the processed frame through the study of their statistical properties.

This third part of the thesis explains part of our recent publication Cantero et al. (2023) and consists of three chapters. Chapter 6 is dedicated to revisit image noise statistics from different HCI stages, from raw data such as AO-corrected and coronagraphic images, to processed frames after ADI processing. Chapter 7 is then devoted to present different statistical methods to identify noise regimes in the ADI processed frame, list their limitations from an statistical point of view, and discuss their applicability for the task of exoplanet detection.

SPECKLE NOISE STATISTICS

The statistical behavior of starlight speckles emerged as a central focus of attention in early publications in the field of direct imaging. This emphasis was due, in part, to the importance of understanding the limitations introduced by noise when detecting companions in images.

6.1 SPECKLE NOISE IN RAW DATA

In order to model the intensity distribution of speckle noise in both corrected and non-corrected AO images from ground-based telescopes, a series of pioneering investigations in HCI proposed to adapt laser speckle theory (Goodman, 1975). For example, Aimé & Soummer (2004) proposed that the mean intensity I of a long-exposure AO-corrected image can be described as the sum of two independent intensity sources: the deterministic diffraction pattern I_c (perfect PSF) and a halo produced by random speckles I_s. This standpoint led to the derivation of the probability density function (PDF) of the speckle intensity for a given location in the image plane, resulting in a modified Rician (MR) probability distribution:

$$p_{MR}(I) = \frac{1}{I_s} \exp\left(-\frac{I + I_c}{I_s}\right) I_0 \left(\frac{2\sqrt{I I_c}}{I_s}\right),$$ (16)

where I_0 denotes the zeroth-order modified Bessel function of the first kind, and the expectation and variance of I are given by:

$$\mathbb{E}I = I_s + I_c,$$ (17)

$$\sigma_I^2 = I_s^2 + 2 I_s I_c.$$ (18)

These equations describe the statistics of image plane intensity in an idealized absence of other noise sources, such as photon and detector noise. In high flux regimes, these additional noise sources are negligible in front of speckle noise. However, in low flux regimes, these must be taken into account (Aimé & Soummer, 2004).

Later, through using the Lick Observatory AO system, Fitzgerald & Graham (2006) showed for various locations in the image plane that the Rician model (Eq. 16) is consistent with the observed data. Similarly, Soummer et al. (2007) also tested the Rician model, this time with thousands of AO-corrected simulated images corresponding to an ExAO system on a 8-m telescope. They concluded that the Rician statistics were compatible with their simulated data. Soummer et al. (2007) also addressed the problem of long-lived quasi-static speckles in coronagraphic images. They proposed a generalization of the Rician model to include the description of static, quasi-static and fast residual atmospheric speckles. They concluded that the Rician model in coronagraphic images is only valid outside of the focal plane mask occulting area.

Beyond the validity of the Rician statistics in AO-corrected and coronagraphic images, another important aspect of quasi-static speckles is the different timescales at which they form and evolve. Through using a long series of AO-corrected and coronagraphic H-band images from the AEOS telescope, Hinkley et al. (2007) found two different lifetime regimes of quasi-static speckles: a short timescale regime τ_1 corresponding to lifetimes of a few seconds ($1 - 10$ s), and a longer timescale regime τ_2 corresponding to lifetimes of a few hundred seconds (~ 400 s). When adapting the Rician model to quasi-static speckles, Soummer et al. (2007) also included these two lifetime regimes arguing that the effect can be modeled by changing I_s to $I_{s1} + I_{s2}$ in Eq. 16, where I_{s1} and I_{s2} are the random speckle noise instensity of timescales τ_1 and τ_2.

Most of these studies focused on the temporal aspects of speckle noise by demonstrating that time intensity variations of speckles follow an MR distribution. However, to assess the significance of a point source detection (exoplanet), studying the speckle noise spatial distribution is necessary. Using numerical simulations for coronagraphic and non-coronagraphic data, Marois et al. (2008a) demonstrated that this temporal intensity distribution also represents the speckle spatial intensity distribution, and therefore, quasi-static speckle noise inside annuli centered on the PSF core follows the MR PDF.

6.2 SPECKLE NOISE IN ADI PROCESSED FRAMES

To deal with this complex spatio-temporal speckle noise distribution and detect companions in the images, the majority of post-processing algorithms rely on modelling the speckle noise pattern and subtracting it from ADI high contrast images. As illustrated in Fig. 1.12, performing speckle (or PSF) subtraction on each high-contrast image in an ADI sequence generates a sequence of residual images where speckle noise is significantly reduced, and partly whitened (Mawet et al., 2014). After de-rotating these residual images

based on their parallactic angle, and combining them into a final frame, the remaining speckles are further attenuated and whitened. This final frame is commonly referred to as *processed frame* (or *post-processed frame*).

Because of the different post-processing steps and the whitening operator that removes correlation effects, the S/N map technique (Mawet et al., 2014), the industry standard for observing campaigns, makes use of the central limit theorem[1] (CLT) to state that residual noise in processed frames follows a Gaussian distribution. This assertion is based on the premise that when a large number of random (uncorrelated) speckles are temporally co-added at a specific location in the image, the sample means will be normally distributed. Within the scenario where speckle noise is only due to atmospheric turbulence, this Gaussian assumption can be accepted since atmospheric speckles have a very short correlation time, and therefore, they can be considered as independent and identically distributed. However, in the realm of quasi-static instrumental speckles, the spatio-temporal autocorrelation of the image PSF is disturbed, and the Gaussian assumption is not valid. Indeed, it is known that this Gaussian assumption leads to high false positive detection rates (Marois et al., 2008a; Mawet et al., 2014) since residual speckle noise in processed frames still dominates at small angular separations.

More recent studies explored the behaviour of residual noise in ADI processed frames. Pairet et al. (2019) found experimentally that the tail decay of residual noise close to the star in PCA-processed frames is better explained by a Laplacian distribution than a Gaussian distribution. Later, Dahlqvist et al. (2020) reached the same conclusion. These experimental results suggest the presence of two residual noise spatial regimes in the ADI processed frame: a non-Gaussian noise regime close to the star, dominated by residual speckle noise, which was not fully removed by the ADI processing, and a Gaussian regime located further away, in which speckles were properly removed and therefore, other noise sources such as photon noise starts to dominate instead. Hereafter, these noise regimes in the ADI processed frame are respectively referred to as *speckle regime* and *background regime*.

---

[1] In probability theory, the CLT states that for independent and identically distributed random variables, the sampling distribution of the standardized sample mean tends towards the standard normal distribution.

7

IDENTIFICATION OF NOISE REGIMES

In HCI, it is common practice to assume the presence of speckle and background noise regimes (Section 6.2) when dealing with ADI processed frames. However, the potential consequences of this spatial stratification, including its impact on detecting point-like sources, have not been thoroughly investigated. In order to understand how this remaining noise structure affects detection algorithms, the first task is to develop a method capable of detecting both noise regimes within the image. In this chapter, this problem is addressed through looking for the best estimate of the radial distance from the star where residual speckle noise starts to become negligible compared to background noise (top-left of Fig. 7.1). To do so, our strategy is to study the evolution of noise statistics as a function of angular separation with the aim to detect anomalies along the transition of both regimes.

For illustrative purposes, we make use, in this section, of two ADI sequences chosen from the set of nine ADI sequences used in the first phase of the EIDC (Cantalloube et al., 2020). Our two sequences, referred to as *sph2* and *nrc3* (see Table 2), were respectively obtained with the VLT/SPHERE instrument (Beuzit et al., 2019) and the Keck/NIRC2 instrument (Serabyn et al., 2017). They have the advantage of not containing any confirmed or injected companions, which makes them appropriate for algorithm development and tests that rely on the injection of exoplanet signatures in the image.

7.1 PAVING THE IMAGE FIELD OF VIEW

First of all, in order to study the noise statistics as a function of the angular separation, the ADI processed frame is paved with concentric annuli of λ/D width (top-left of Fig. 7.1). Each annulus contains pixels that are expected to be drawn from the same parent population (Marois et al., 2008a), although, it is acknowledged that this working hypothesis is not completely fulfilled when diffraction patterns associated with the spiders of the telescope or to the wind-driven halo (see Cantalloube et al., 2019) are present in the image field of view. Note that, in the presence of residual speckles, pixels that contain information from the same speckle are all spatially correlated. When
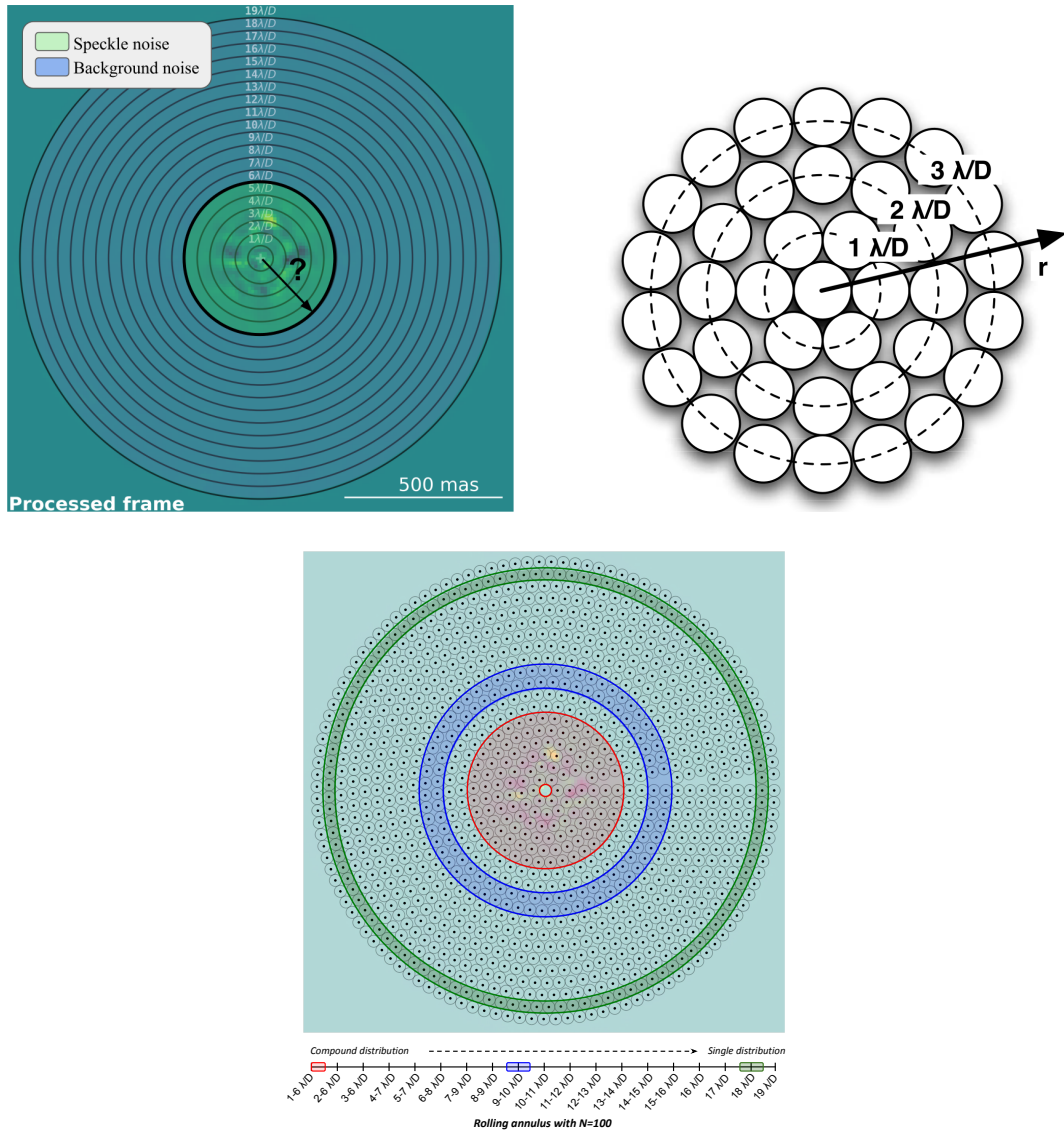
Figure 7.1: The pavement of the processed frame. *Top-left*: Processed frame over which both speckle and background residual noise regimes are high-lighted in green and blue, respectively. The black circle refers to the unknown radial distance where both regimes split. Other concentric circles represent all λ/D-width annuli along the image. *Top-right*: Illustration of the three first annuli ($1 - 3\ \lambda/D$) of the top-left image paved with non-overlapping circular apertures of λ/D diameter. The number of circular apertures for each annulus is given by $N_{aper} = 2\pi r$, where r is the radius in λ/D units. Image taken from Mawet et al. (2014). *Bottom*: Rolling annulus with $N = 100$ over the top-left processed frame. Examples of the first rolling annulus (in red), the ninth rolling rolling annulus (in blue) and the eighteenth rolling annulus (in green) are displayed over the central pixel pavement in the image. Below, the complete set of rolling annuli is shown in a straight line that represents the distance from the star.

background noise dominates over residual speckle noise, it can be instead assumed that all pixels in an annulus are independent, since photon noise occurs on a pixel-wise basis. However, this assumption of independence can be non-optimal when bad pixels are interpolated since it can still leave spatially correlated footprints.

In HCI, a common procedure to guarantee the independence of pixel samples when performing statistical analysis is to work by integrating pixel intensities on non-overlapping circular apertures of λ/D diameter within the annulus (Mawet et al., 2014), as shown in the top-right image of Fig. 7.1. This procedure is based on the characteristic spatial scale of residual speckles ($\sim \lambda/D$ size). However, Bonse et al. (2023) have recently showed that, in the presence of speckle noise, this independence assumption on non-overlapping apertures is incorrect. Instead, they propose to (i) only consider the central pixel value in each circular aperture, to produce a more statistically independent set of pixels, and (ii) possibly repeat the experiment with various spatial arrangements of the non-overlapping apertures to reduce statistical noise in the measured quantities. We follow this recommendation and therefore, for the rest of this study, we define our annulus samples on the processed frame by only taking the central pixel value for each non-overlapping circular aperture. This approach also minimizes the possible effect of bad pixel interpolation.

7.1.1 *The rolling annulus*

One limitation in using non-overlapping apertures instead of pixels for paving the processed frame is the small sample statistics problem, especially at small angular distances (Mawet et al., 2014). Small samples make statistical analysis not significant so that derived conclusions are not strong enough from a statistical point of view. In order to avoid this issue, we propose to use the concept of a rolling annulus that always contains a minimum number of independent pixels N. These N pixels are the central pixels of apertures that pave the field of view and are included in the rolling annulus. It can be understood as an annular window around the star for which the inner boundary moves in $1 \lambda/D$ steps, while the outer boundary is set to achieve the criterion on the minimum number of independent pixels. The movement of the rolling annulus along the field of view is non-continuous; it always moves over the grid of non-overlapping apertures that paves the image. An example of this process with $N = 100$ pixels is shown in the bottom image of Fig. 7.1, where the first rolling annulus that achieves the condition, composed of all central pixels of the non-overlapping apertures between $1 - 6 \lambda/D$, is displayed in red color in the processed frame. Then, the rolling annulus moves away from the star, changing its boundaries as illustrated with the black line at the bottom of Fig. 7.1. For example, the ninth rolling annulus (in

blue) with N = 100 is located between $9 - 10 \, \lambda/D$, and the eighteenth rolling annulus (in green) is at $18 \, \lambda/D$ distance, achieving the N = 100 condition without the need to expand the outer boundary to another annulus. From now on, when using rolling annuli, we select N = 100 minimum samples, considered to be the minimum number of samples required to reach a reliable statistical power and significance for our statistical analysis. The statistical consequences of using a rolling annulus for paving the processed frame field of view are further discussed later in Section 7.4.

7.2 MOMENTS EVOLUTION ANALYSIS

Once the processed frame is paved using a rolling annulus with N = 100 (Section 7.1.1), we are well-positioned to study the evolution of different statistical moments as a function of the angular separation to the star. Three statistical moments are considered to provide valuable information about image noise: the *variance* (amount of energy/power), the *skewness* (distribution symmetry), and the *excess kurtosis* (distribution tails). Figure 7.2 shows this evolution for the case of the *sph2* (top row) and *nrc3* (bottom row) data sets, on which annular-PCA is employed to produce the processed frames. It is observed that the variance (green curves) decreases as the rolling annulus moves away from the star. This trend is common to both data sets and is what we would expect in physical terms as the intensity of residual speckles decreases rapidly with angular separation, especially at short distance. We also see that this behaviour is damped when using a larger number of principal components (PCs), which leads to a more effective speckle subtraction. Regarding the skewness analysis (red curves), the convention of Bulmer (1979) is adopted, which states that a distribution is symmetrical when its skewness ranges from -0.5 to 0.5. For both data sets, we clearly observe a loss of symmetry at small angular separations. The presence of speckles can provoke this distribution asymmetry due to their higher intensity values in comparison with the background. Looking now at the excess kurtosis (blue curves) in Fig. 7.2, we observe a strong leptokurtic[1] trend for the entire set of PCs at small angular separations, and for both data sets. This perfectly matches with the fact that a Laplacian distribution fits better the tail decay of residual noise (Pairet et al., 2019), since it is, by definition, leptokurtic. At larger angular separations instead, we observe differences between both data sets. In the *sph2* processed frames, we detect one mesokurtic regime approximately between $6 - 13 \, \lambda/D$ followed by a weaker leptokurtic regime approximately between $14 - 17 \, \lambda/D$. For *nrc3*, we only observe one mesokurtic regime at large distance from the star, beyond about the $3 - 6 \, \lambda/D$ rolling annulus (Fig. 7.2).

---

1 In statistics, a leptokurtic distribution has a kurtosis greater than the kurtosis of a normal distribution (mesokurtic), and it is associated in HCI to increase the false alarm probability.
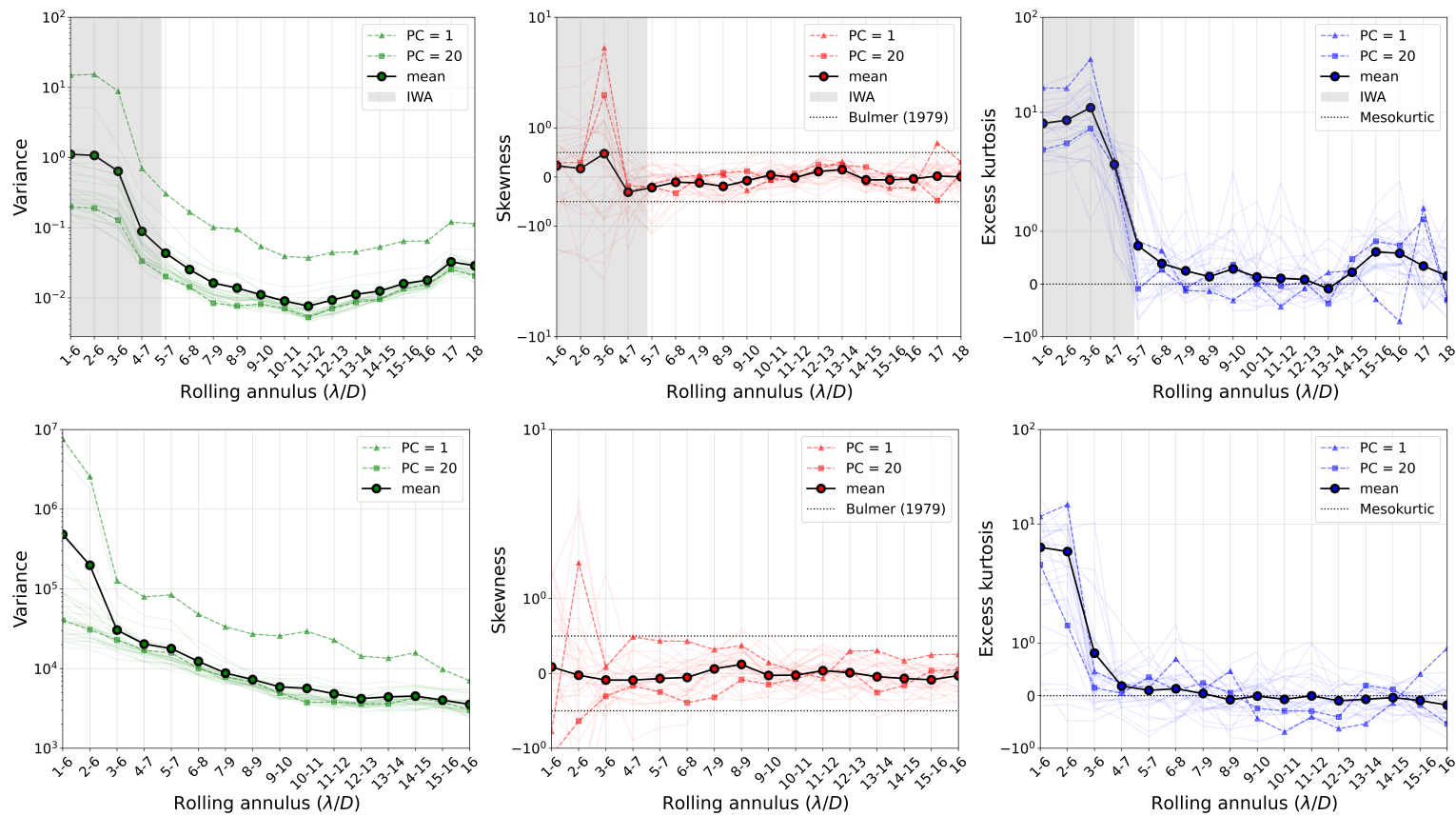
Figure 7.2: Statistical moments evolution based on a rolling annulus which paves the full annular-PCA processed frame. The top and bottom rows refer, respectively, to *sph2* and *nrc3* ADI sequences. Colour curves on each subplot refers to a different number of principal components used to produce the annular PCA processed frame, ranging from 1 to 30. The bold curve on top of each subplot indicates the average of the thirty PCs, and PC=1 and PC=20 are illustrated with specific symbols. In the case of *sph2*, gray areas highlight the IWA.

Another way to explore the spatial distribution of noise is to use hypothesis testing. Assuming that residual speckle noise is non-Gaussian by nature, while background noise is Gaussian (see Sect. 6.2), we can assess the probability of the null hypothesis H_0 that data is normally distributed, i.e., explained solely by background noise. We rely on a combination of a series of normality tests, making use of four of the most powerful tests:

- The Shapiro-Wilk test (*sw*, Shapiro & Wilk, 1965).

- The Anderson-Darling test (*ad*, Anderson & Darling, 1952).

- The D'Agostino-K2 test (*ak*, D'Agostino & Pearson, 1973).

- The Lilliefors test (*li*, Lilliefors, 1967).

This choice is motivated by the fact that they have been well-tested in many studies, including Monte-Carlo simulations (Yap & Sim, 2011; Marmolejo-Ramos & González-Burgos, 2013; Ahmad & Khan, 2015; Patrício et al., 2017; Wijekularathna et al., 2019; Uhm & Yi, 2021). It is worthwhile to remark that the goal is not to benchmark the robustness of all these tests. Our purpose, instead, is to collect a larger amount of statistical evidence for a same hypothesis, which can then be combined to increase the statistical power when making a decision regarding the null hypothesis. Moreover, regarding the statistical requirements, the only constraints to be verified before using these tests are the independence and sufficient size of the sample. In terms of sample size, Jensen-Clem et al. (2017) shows that normality tests can exhibit lower statistical power with sample sizes under 100 observations. Here, the independence and the size constraints are met by the proposed approach to pave the field of view, using the central pixels of non-overlapping apertures within rolling annuli of $N = 100$. Additionally, we follow for this analysis the recommendation of Bonse et al. (2023) to perform our statistical tests with various spatial arrangements for the non-overlapping apertures. We leverage the fact that different aperture arrangements within a same annulus contain valuable noise diversity that can directly benefit the analysis when making a decision about the null hypothesis.

Our analysis is thus composed as follows. Given a processed frame, we test the null hypothesis H_0 in a specific rolling annulus through the following consecutive steps:

1. Randomly select a normality test t from $\mathcal{T} = \{sw, ad, ak, li\}$.

2. Randomly select an angular displacement θ of circular apertures for each single annulus within the rolling annulus. Assuming N_{ann} single

annuli, then, $\Theta = \{\theta_i\}_{i=\{1,\ldots,N_{ann}\}}$, where Θ thus represents a random aperture arrangement.

3. Define the sample of central pixels $X(\Theta)$.

4. Using the selected statistical test t, compute the p-value associated with the null hypothesis for the sample $X(\Theta)$, denoted as $p(t, \Theta)$.

5. Repeat steps $1 - 4$ m times. Because these m p-values computed in step 4 are not statistically independent, we use the harmonic mean as proposed by Vovk & Wang (2020) to combine them into a global p-value noted $\bar{p}$.

6. Compare $\bar{p}$ with a predefined significance threshold α, and reject H_0 if $\bar{p} < \alpha$.

By repeating steps $1 - 6$ for each rolling annulus in the processed frame and for various numbers of principal components in our annular-PCA post-processing algorithm, we can build what we call as a *PCA p-value map*, or *PCA-pmap* for short. Figures 7.3 and 7.4 show examples of PCA-pmaps for the *sph2* and *nrc3* data sets, respectively. For both, we only considered the first 29 principal components to produce the annular-PCA space (y-axis in figures). Each cell in a PCA-pmap shows, through the number in white and its background color, the combined p-value $\bar{p}$ computed in step 5 with $m = 300$. P-values below the pre-defined threshold α (step 6) are marked with yellow stars on the figures. In order to minimize the Type I error (false rejection of the null hypothesis), we selected a conservative threshold value $\alpha = 0.05$ in Figures 7.3 and 7.4. Afterwards, we calculate the ratio of yellow star markers, or H_0 rejection rate, along the PCA domain for each rolling annulus in PCA-pmaps. As selection criterion, we classify rolling annuli as speckle-dominated (or non-Gaussian) when they contain more than 50% of stars. Fig. 7.5 shows this selection criterion for both data sets by plotting the H_0 rejection rate per rolling annulus. In the case of *sph2* (Fig. 7.5-left), we clearly observe the presence of four noise regimes beyond the inner working angle: a first regime dominated by non-Gaussian noise due to residual speckles approximately between $5 - 7$ λ/D angular separation, a second regime where noise is more consistent with Gaussian statistics, probably dominated by background noise between $8 - 14$ λ/D, a third regime with non-Gaussian noise between $15 - 16$ λ/D, where speckles are dominating again as we approach the limit of the well-corrected area produced by the SPHERE adaptive optics (Cantalloube et al., 2019), and finally, a fourth regime with Gaussian noise again between $17 - 19\lambda/D$. This speckle-dominated regime at $15 - 16$ λ/D would also explain the slightly leptokurtic behavior observed at those separations in Fig. 7.2 for *sph2*. However, for the *nrc3* data set (Fig. 7.4), we only observe two noise regimes, with speckle noise dominating approximately between

$1 - 3 \lambda/D$ distance, and background noise dominating beyond $3 \lambda/D$ (Fig. 7.5-right). Fig. 7.6 shows a representation of all detected noise regimes for the *sph2* and *nrc3* data sets. The white dotted line and circles overplotted on the PCA-pmaps of Figures 7.3 and 7.4 will be explained later in Part IV.

7.3.1   *Field of view splitting strategy*

At this point, we can see that, for both *sph2* and *nrc3*, similar estimations of the noise regimes are reached using the two proposed methods: the study of statistical moments and the PCA-pmaps. Figure 7.2 provides a first insight into the spatial structure of residual noise and, thereby, brings us closer to estimating the radius split (top-left of Fig. 7.1) in the processed frame. Indeed, the significant increase of the variance together with the leptokurtic behavior and the positively skewed trend at small angular separations, suggest that this regime is still dominated by residual starlight speckles. On the other hand, PCA-pmaps contain more statistical diversity through the combination of p-values with which very similar regime estimations are reached. Thus, both analyses are complementary from a statistical perspective. Yet, from now on, we elect to use PCA-pmaps to define the noise regime as a baseline, since they can also be used for other purposes.

7.4   INTERPRETATION

The tests developed in this section are designed to identify noise regimes based on their statistical behaviour in a rolling annulus. For example, we have observed that rolling annuli at small angular separations in both *sph2* and *nrc3* data sets are described by non-Gaussian statistics, and therefore, dominated by residual speckles. However, note that these results do not necessarily mean that residual speckle noise is non-Gaussian in the innermost, individual annuli. Instead, *compound distributions* could be at the origin of this non-Gaussian noise behavior.

Compound distributions refer to the sampling of random variables that are not independent and identically distributed. When we sample pixels by expanding the annulus across the image to meet the condition $N = 100$ (see Section 7.1.1), we essentially create samples that encompass pixels from different individual annuli, which by nature, are drawn from different parent populations (Marois et al., 2008a). These samples can be considered as compound distributions. For large angular separations (e.g., the green annulus in the bottom image of Fig. 7.1), we generally observe that the variance is approximately the same for all central pixels. Because they can be considered as independent random variables, we can apply the central limit theorem to state that these samples follow a Gaussian distribution, as
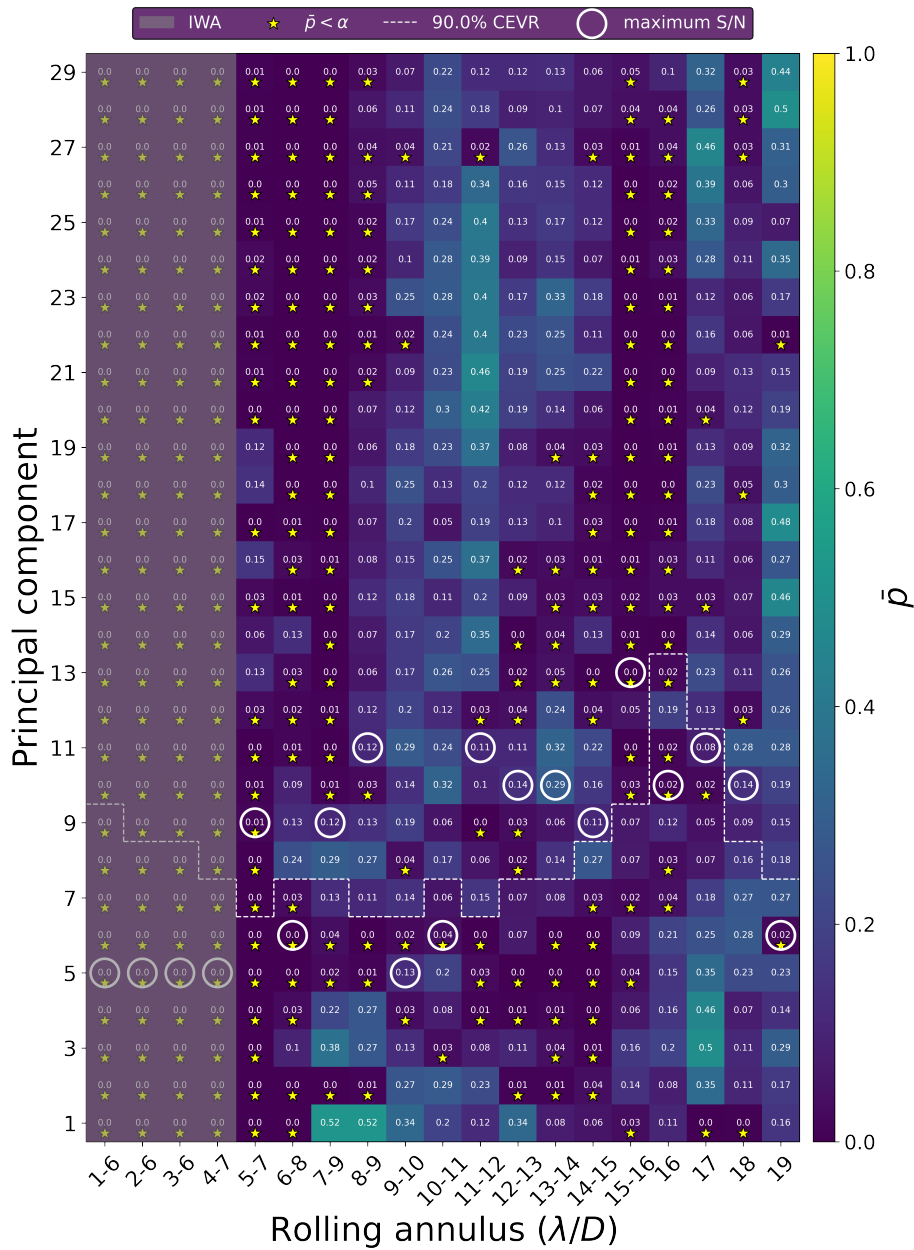
Figure 7.3: PCA-pmap derived from the *sph2* ADI sequence. Each cell shows the combined p-value p̄ both as a color code and as values, for a given distance to the star through the rolling annulus (x axis) and the number of principal components used in the PCA-based PSF subtraction (y axis). Yellow star markers indicate when the null hypothesis H_0 (Gaussian noise) is rejected. The white dashed line shows the 90% CEVR in each rolling annulus. White circles in bold highlight the principal component that maximizes the S/N of fake companion recoveries. The gray area refers to the inner working angle.
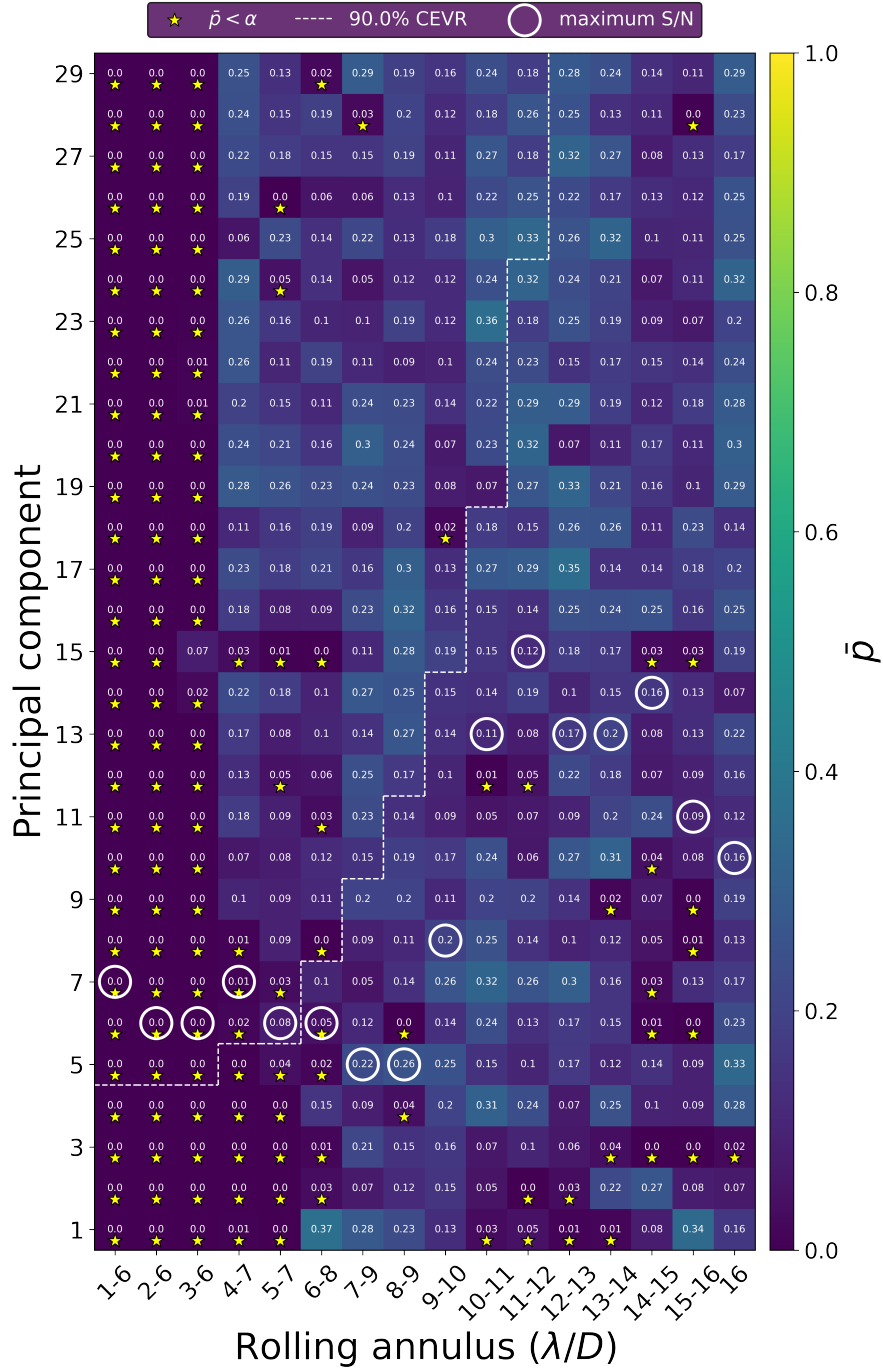
Figure 7.4: Same as Fig. 7.3, for the *nrc3* ADI sequence.
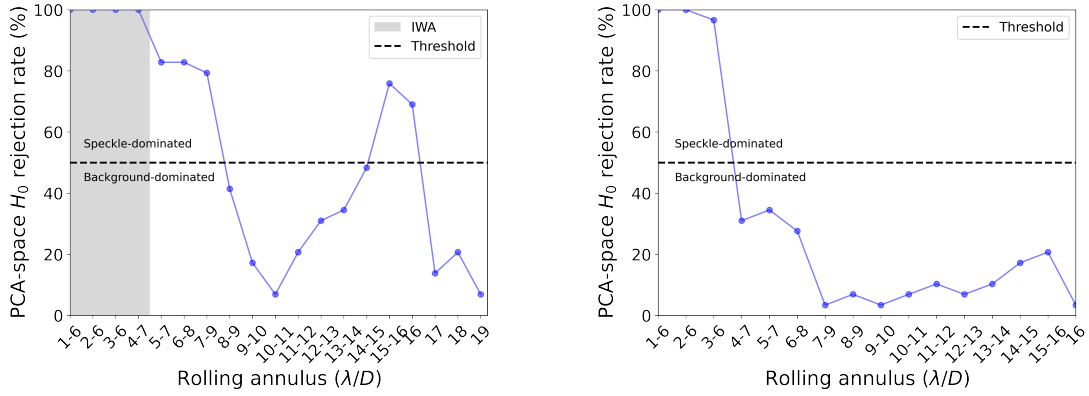
Figure 7.5: H_0 rejection rate (y axis) for each rolling annulus (x axis) for the *sph2* (left) and *nrc3* (right) data sets computed from their PCA-pmaps of Figures 7.3 and 7.4, respectively. The rejection rate is computed as the percentage of yellow star markers for each annulus in PCA-pmaps. The dashed black line highlights the selection criterion for determining the dominant noise at each rolling annulus.
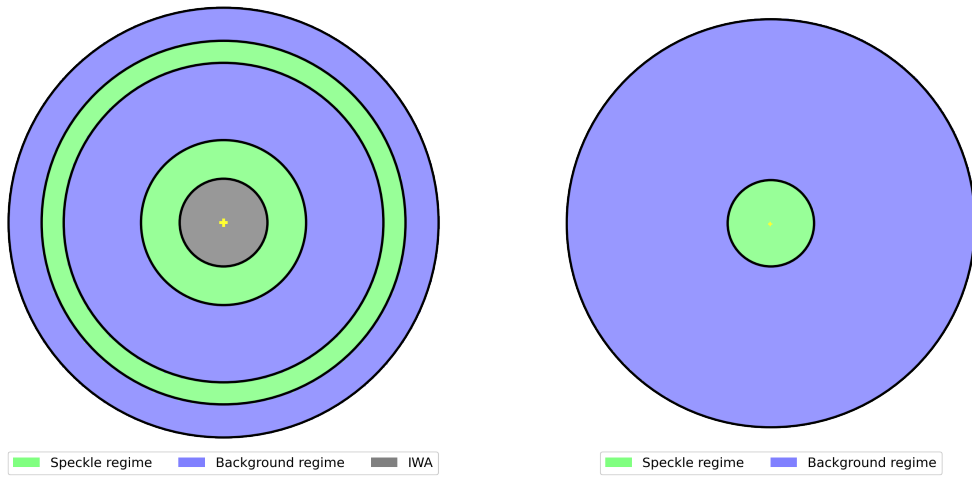
Figure 7.6: Final representation of estimated noise regimes along the ADI-PCA processed frames of *sph2* (left) and *nrc3* (right) data sets. These illustrations are drawn according to the selection criterion for rejecting H_0 presented in Fig. 7.5.

expected for background noise. However, for small angular separations (e.g., red annulus in bottom of Fig. 7.1) where residual speckle noise dominates over background noise, the samples are taken from distributions that might be Gaussian, but with different variances. If they are Gaussian and their variance follows an exponential distribution, then according to Gneiting (1997), the compound distribution follows a Laplacian, as observed by Pairet et al. (2019). Likewise, the compound distribution problem could also explain why we observe a non-Gaussian behavior in the outermost annuli of the *sph2* processed frame. At those separations, our rolling annuli contain samples drawn at exactly the same radial distance, which would lean us to assume that the variances of the underlying distributions are all identical. However, due to different physical reasons, such as the possible presence of a wind-driven halo or of telescope spiders, there is no guarantee for a perfect circular symmetry inside this speckle-dominated annulus. This explanation, which is not a proof, would reconcile the belief that residual speckle noise should be locally Gaussian. Because of the small sample size, there is, however, no proper way to test this interpretation on individual annuli in the innermost regions.

CONCLUSIONS

In this part III of the thesis, we presented the PCA-pmap, a statistical technique that relies on several normality tests and different pixel arrangements to identify both speckle- and background-dominated noise regimes over the ADI-PCA processed frame. The noise analysis conducted with PCA-pmap using two ADI sequences from different HCI instruments suggests that there can be more than two noise regimes over the processed frame depending on the structure of the data. Despite the fact that this is not enough to extract a general conclusion for all HCI instruments, it suggests that noise regions should be defined on a case-by-case basis. Furthermore, this stratification strategy led to interpret the non-Gaussian behavior detected in the speckle-dominated regime through compound distributions. However, this interpretation requires further research for validation. Thus, our main conclusion is that the shape of a local distribution in the processed frame (in this case using PCA as PSF subtraction technique) is influenced by three factors: (i) physics (origin of noise, instrumentation), (ii) post-processing (whitening capability of PCA), and (iii) statistical sampling (compound distribution). For all these reasons, we believe that splitting the processed frame field of view in different noise regimes is duly motivated, and, in Part IV, we will explain how we have implemented this stratified strategy in a new algorithm to improve the detection performance of SODINN.

This study presented in Part III has certain limitations that could become focal points for future research. The noise analysis conducted with both moments analysis and PCA-pmap relies on a rolling annulus to pave the image, which moves away from the star in $1 \lambda/D$ steps instead of pixel-based steps. This approach results in a more discrete than continuous behaviour. The discretization of samples in the field of view leads to less precise estimates of the radial distance from the star where the transition between speckle- and background-dominated regimes occurs. Possible enhancements could involve achieving a continuous behavior concerning angular separation. Another potential area of research involves employing neural networks to improve the identification of regimes compared to normality tests. Simić (2021) proposed addressing the normality testing problem as a binary classification task by constructing a supervised model capable of classifying a distribution as either normal or non-normal by inspecting a small sample drawn from it. This approach, adapted to HCI, could aid in avoiding the use of a rolling annulus and providing a better identification of noise regimes.

Part IV

THE NA-SODINN DEEP LEARNING ALGORITHM

INTRODUCTION

In Part III, our focus has been on exploring and understanding the spatial structure of residual noise in ADI processed frames. This study has led to the development of statistical methods that facilitate the identification of regimes dominated by speckle and background noise. Now, our aim is to employ this local noise approach to enhance the performance of HCI post-processing algorithms, particularly with regard to deep learning. Neural networks are well-suited for capturing a pattern hidden in images, even with a high level of noise, and make complex decisions.

To maximize the value of working within noise regimes and illustrate its benefits for the detection task, we propose to revisit SODINN, the pioneering supervised deep learning algorithm for exoplanet imaging (Gómez González et al., 2018). Chapter 8 is dedicated to providing a comprehensive explanation of the SODINN detection algorithm. As a supervised technique, we begin by describing the methods used to generate a labeled dataset and clarify the types of correlations that SODINN aims to capture. Subsequently, we delve into the training architecture and the learning process. Finally, we detail the inference process through which SODINN detects point-like sources. Chapter 9 is devoted to explaining the adaptation of SODINN to function within our noise regime approach, highlighting its main advantages and drawbacks. This adaptation results in a novel detection algorithm that we refer to as NA-SODINN. In Chapter 10, we focus on evaluating the detection performance of the new NA-SODINN in comparison to its predecessor and to more conventional post-processing techniques. Furthermore, NA-SODINN undergoes assessment in the initial phase of the EIDC to benchmark it against the most powerful HCI algorithms. Chapter 11 centers on the utilization of NA-SODINN with real data, particularly within the SPHERE exoplanet survey. We present preliminary results of NA-SODINN, including detection maps and potential exoplanet candidates that have been identified.

<div align="right">

8

</div>

THE SODINN ALGORITHM

SODINN stands for *Supervised exOplanet detection via Direct Imaging with deep Neural Network*. It is a binary classifier that uses a convolutional neural network (CNN) to distinguish between two classes of square image sequences based on ADI processed frames: sequences that contain an exoplanet signature (c_+, the positive class), and sequences that contain only residual noise (c_-, the negative class). Figure 8.1 (bottom) shows an example sequence for each class, where the individual images are produced with various number of principal components. The first image in the sequence corresponds to the first principal component, while the last corresponds to a number of principal components with which a maximum of 90% cumulative explained variance ratio (CEVR) is captured. Gómez González et al. (2018) refer to these patch sequences as Multi-level Low-rank Approximation Residual (MLAR) samples.

8.1 GENERATION OF THE TRAINING SET

The first step in SODINN is to build a training data set composed of thousands of different c_+ and c_- MLAR sequences. A c_+ sequence is formed through three consecutive steps that are summarized in Fig. 8.1. (i) First, a PSF-like source is injected at a random pixel within a given annulus of the ADI sequence. The flux of this injection is the result of multiplying the normalized off-axis PSF by a scale factor randomly chosen from a pre-estimated flux range that corresponds to a pre-defined range of S/N in the processed frame. The estimation of injection flux ranges is further explained in Appendix C. (ii) Singular value decomposition (SVD, Halko et al., 2011) is then used on this synthetic ADI sequence to perform PSF subtraction for different number of singular vectors (or principal components), thereby producing a series of processed frames. (iii) Finally, square patches are cropped around the injection coordinates for each processed frame. This forms a series of c_+ MLAR sequences, where each sequence contains the injected companion signature for different numbers of principal components. The patch size is usually defined between $1.5 - 2$ times the FWHM of the PSF.
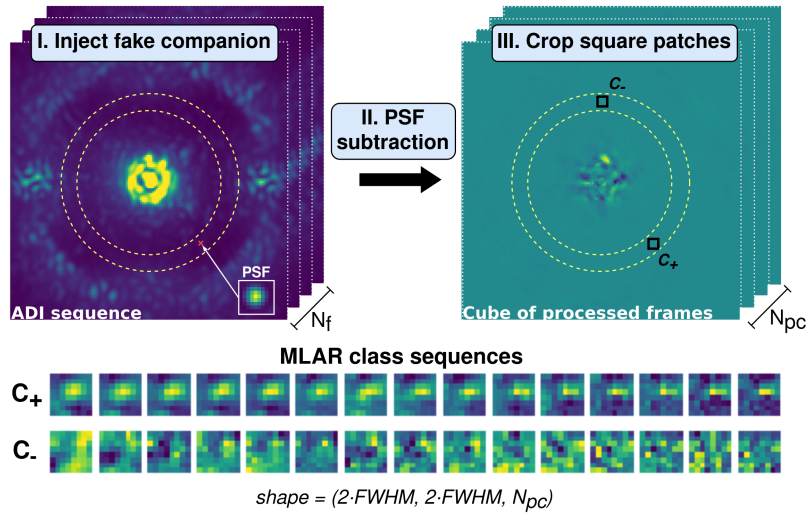
Figure 8.1: SODINN generation stage. *Top*: steps for generating MLAR samples. N_f is the number of frames in the ADI sequence and N_{pc} is the number of principal components in the cube of processed frames and therefore in the final MLAR sequence. *Bottom*: example of an MLAR sequence of each class.

Likewise, we construct a c_- sequence by extracting MLAR sequences for pixels where no fake companion injection is performed. The number and order of singular vectors is the same as those used for the c_+ sequences. For the case of c_- sequences, SODINN must deal with the fact that, using only one ADI sequence, we obtain a single realization of the residual noise, so that the number of c_- sequences we can grab per annulus is not enough to train the neural network without producing over-fitting. SODINN solves this problem by increasing the number of c_- sequences in a given annulus through a dedicated data augmentation strategy that is based on four consecutive steps: (i) Build a first subset randomly grabbing c_- sequences centered on up to ten percent of the total number of pixels; (ii) Build a second subset by grabbing all the available pixels in the annulus and flip the sign of the parallactic angle when de-rotating the residual images, a common practise in HCI to remove possible planetary sources while preserving noise properties; (iii) Randomly pick groups of three c_- sequences from the two subsets and average them to produce new sequences; (iv) Finally, perform random rotations and small shifts of the c_- sequences obtained in the previous three steps to create even more diversity. The same rotation angle and shift is applied to all the slices of a given MLAR sample. Note that this augmentation process ensures that we mostly use augmented c_- sequences for the training.

This procedure of generating c_+ and c_- sequences is repeated thousands of times for each annulus in the field of view. Once the entire field of view

is covered, MLAR sequences of a same class from all annuli are aggregated, and the balanced training set (same amount of c_+ and c_- samples) is built.

8.2 TRAINING OF THE NETWORK

The training set is then used to train the SODINN neural network. This produces a detection model that is specific for the ADI sequence from which MLAR sequences were generated. The SODINN network architecture is composed of two concatenated convolutional blocks. The first block contains a convolutional-LSTM (Shi et al., 2015) layer with 40 filters and an hyperbolic tangent activation function, and kernel and stride size of $(1,1)$, followed by a spatial 3D dropout (Srivastava et al., 2014) and a MaxPooling-3D (Boureau et al., 2010). The second block contains the same except for it has now 80 filters, and kernel and stride size of $(2,2)$. These first two blocks extract the feature maps capturing all spatio-temporal correlations between pixels of MLAR sequences. After that, they are flattened and sent to a fully connected dense layer of 128 hidden units. Then, a rectifier linear unit (ReLU, Nair & Hinton, 2010) is applied to the output of this layer followed by a dropout regularization layer. Finally, the output layer of the network consists of a sigmoid unit, which provide a normalized value between 0 and 1. This value is usually referred as a probability. However, it is known in computer vision that the output of a deep learning architecture normalized between 0 and 1 with classical activation functions (e.g. the sigmoid function) tends to be more binary, and therefore, it cannot be interpreted as a real probability. For this reason, from now on, we refer to this output score as the model *confidence*. The network weights are initialized randomly using a Xavier uniform initializer, and are learned by back-propagation with a binary cross-entropy lost function:

$$L(y_n, \hat{y}_n) = -\sum_n (y_n \ln(\hat{y}_n) + (1 - y_n) \ln(1 - \hat{y}_n)), \tag{19}$$

where y_n is the true label of the nth MLAR sample and $\hat{y}_n$ is the predicted confidence that this n^{th} MLAR sample belongs to the c_+ class. SODINN uses an Adam optimizer with a step size of 0.003, and mini-batches of 64 training samples. An early stopping condition monitors the validation loss. The number of epochs is usually set to 15, with which SODINN generally reaches $\sim 99.9\%$ validation accuracy (Gómez González et al., 2018).

8.3 INFERENCE

Once the detection model is trained and validated, it is finally used to find real exoplanets in the same ADI sequence. Because the input of the model is

an MLAR structure, we first map the entire field of view by creating MLAR samples (with no injection) centered on each pixel. Note that these MLAR samples have never been processed during the training, since the c_- class MLAR samples in the training set are built by augmentation (Sect. 8.1). The goal of the trained model is to assign a confidence value between 0 (no confidence) and 1 (maximum confidence) for each of these new MLAR sequences to belong to the c_+ class. Computing a confidence score for each individual pixel leads to a confidence map, from which exoplanet detection can be performed by choosing a confidence threshold.

THE NA-SODINN ALGORITHM

In SODINN, the training set is built by aggregating all MLAR sequences from a same class, generated on every annulus in the field of view. In the presence of different noise regimes, this way to proceed can complicate the training of the model, as the statistics of an MLAR sequence generated in the speckle-dominated regime differ from a sequence of the same class generated in the background-dominated regime. In order to deal with this, we propose to train an independent SODINN detection model per noise regime instead of a unique model for the full frame field of view. Thereby, each detection model is only trained with those MLAR sequences that contain statistical properties from the same (or similar) probabilistic distribution function. Therefore, our region of interest in the field of view is now smaller. This means that the number of pixels available to generate MLAR sequences is reduced and therefore, that we are losing noise diversity in comparison with a model that is trained in the full frame. However, this diversity loss comes with the benefit of better capturing the statistics of noise within a same noise regime, which improves the training.

9.1 ADDING S/N CURVES TO THE NETWORK

In order to compensate for the noise diversity loss associated with the training on individual noise regimes, we attempt to reinforce the training by means of new handcrafted features. An interesting discriminator between the c_+ and c_- classes, which is also physically motivated, comes from their behavior in terms of signal-to-noise ratio (S/N). The most accepted and used S/N definition in the HCI literature is from Mawet et al. (2014). It states that, given a 1 λ/D wide annulus in a processed frame at distance r (in λ/D units) from the star, paved with $N = 2\pi r$ non-overlapping circular apertures (see top-right image of Fig. 7.1), the S/N for one of these apertures is defined as

$$S/N = \frac{\bar{x}_t - \bar{x}_{N-1}}{\sigma_{N-1} \sqrt{1 + \frac{1}{N-1}}} ,$$

(20)
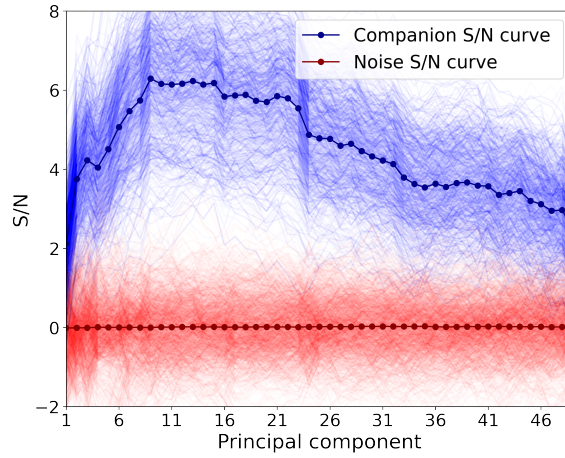
Figure 9.1: S/N curves generated from the *sph2* cube of processed frames at a 8 λ/D distance from the star. Curves in blue contain the exoplanet signature and curves in red just residual noise. The flux of injections is randomly selected from a range that is between one and three times the level of noise. Dotted curves over populations show the mean of each class. Later, in Section 9.2, the principal component where the maximum S/N is reached for an injection (blue curves) is referred to as k_{opt}. In this case, $k_{opt} \simeq 10$.

where $\bar{x}_t$ is the aperture flux photometry in the considered test aperture, $\bar{x}_{N-1}$ the average intensity over the remaining $N-1$ apertures in the annulus, and σ_{N-1} their standard deviation. In order to maximize the S/N, image processing detection algorithms need to be tuned through finding the optimal configuration of their parameters (see e.g., Dahlqvist et al., 2021b). Here, rather than optimizing the algorithm parameters, we use the fact that we can leverage the behavior of the S/N versus some of the algorithm parameters in our deep learning approach. This is especially the case for the number of principal components used in the PSF subtraction. We define an S/N curve as the evolution of the S/N computed for a given circular aperture as a function of the number of principal components (Gómez González et al., 2017). Fig. 9.1 shows an example of 1000 S/N curves generated from the *sph2* ADI sequence. We clearly see in Fig. 9.1 that, in the presence of an exoplanet signature (blue curves), the S/N curve first increases and then decreases, which leads to the appearance of a peak at a given number of principal components. This behavior, capturing the competition between noise subtraction and signal self-subtraction, was already documented elsewhere (e.g., Gómez González et al., 2017). The peak in the S/N curve indicates the number of principal components for which the contrast between the companion and the residual noise in the annulus is maximum. Hereafter, we denote as k_{opt} the principal component at which this S/N peak is located.

For a given 1-FWHM circular aperture, the MLAR sequence (no matter the class) and the S/N curve are linked from a physical point of view. Actually, the evolution of the S/N as a function of the number of principal components can be readily extracted from intermediate products used in the production of the training data set. Therefore, the information conveyed through the S/N curve is already partly contained in the MLAR patches. But while the MLAR sequence contains localized information on the signal and noise behavior, the S/N curve conveys an annulus-wise information, obtained through aperture photometry. Indeed, each aperture S/N estimation depends on the noise in the rest of the annulus (Eq. 20), so that it also contains information that connects with other circular apertures at the same angular separation from the star. This dependency is not captured in MLAR sequences. S/N curves make this rich summary statistics directly available to the neural network to improve the neural network training. One complication in using S/N curves in the training relates to data augmentation, which is mandatory to build up a sufficiently large training data set for SODINN. Because these augmentation operations modify the intensity and distribution of pixels in the MLAR sequence, there is no direct way to compute the associated S/N curve of an augmented MLAR sequence through Eq. 20. To deal with this, we make simplifying assumptions for each augmentation operation in SODINN: (i) image rotations do not affect the S/N curve as the same pixels are kept in the final sequence, (ii) averaging two sequences can be approximated as averaging their S/N curves, and (iii) image shifts do not affect the S/N curve as long as the shift is sufficiently small.

By adding the noise regimes approach and the S/N curves to SODINN, we are building a new detection algorithm. We refer to this novel framework, depicted in Fig. 9.2, as *Noise-Adaptive SODINN*, or NA-SODINN for short. As its predecessor, NA-SODINN is composed of the same three steps: producing the training set from an ADI sequence, training a detection model with this training set, and applying the model to find companions in the same ADI sequence.
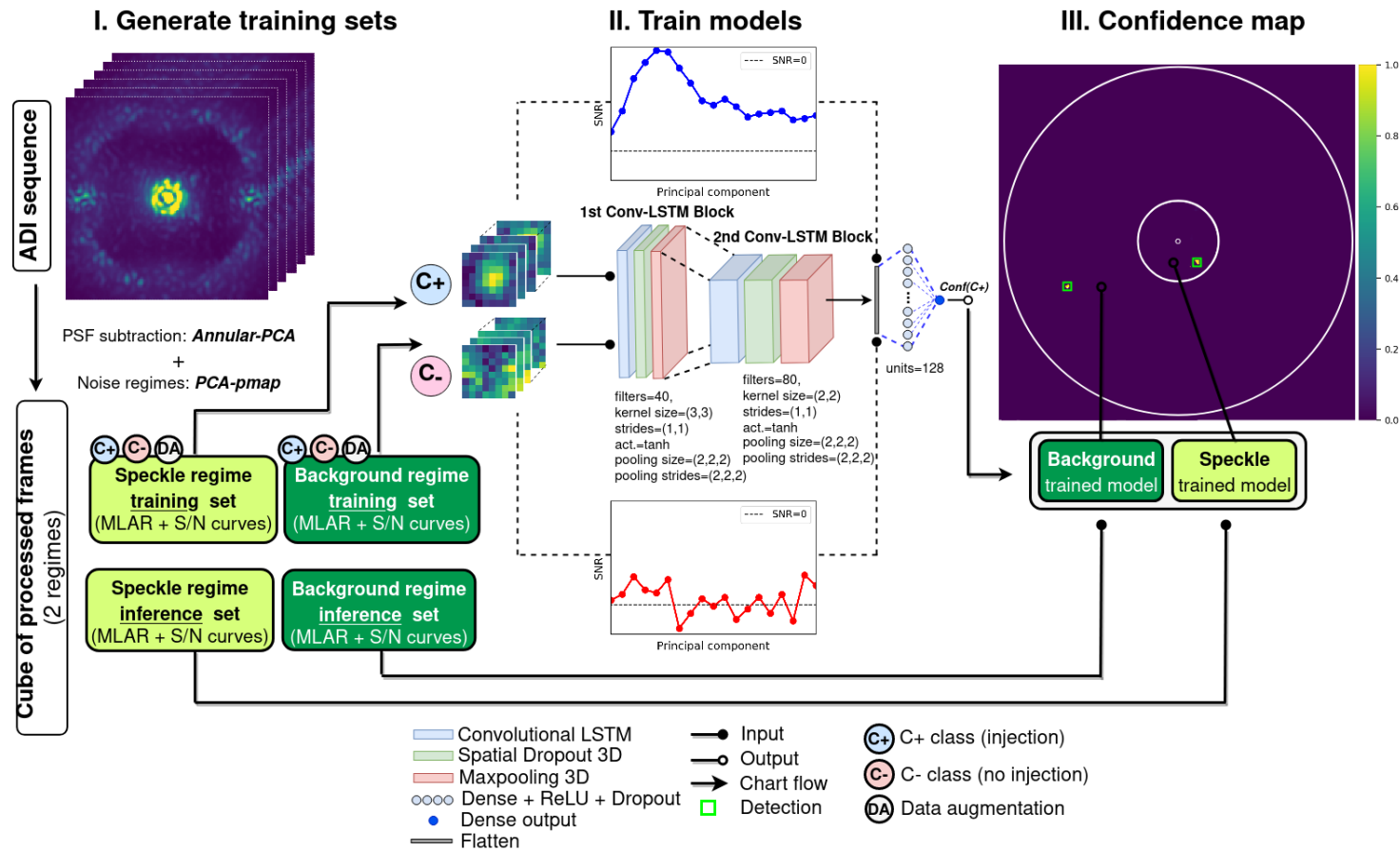
Figure 9.2: Illustration of the three steps within the NA-SODINN algorithm working flow. *Left: Generation of the training set.* NA-SODINN uses the annular-PCA algorithm to perform PSF-subtraction and produce the cube of processed frames. Then, it detects residual noise regimes by applying the PCA-pmap technique in this cube and build both the training, validation, and test (or inference) data sets (see Fig. 2.2-right) at each regime, which are composed of both MLAR samples and S/N curves. *Middle: Model training.* NA-SODINN trains as many detection models as detected noise regimes using their respective training and validation data sets (note that for the sake of simplicity, we have not duplicated the central deep neural network). This case contains two regimes, the speckle- and background-dominated noise regimes, so that two models are trained. *Right: Detection map.* Finally, NA-SODINN uses each trained model to assign a confidence value to belong to the c_+ class to each pixel of the corresponding noise regime field of view.

9.2   GENERATION OF THE TRAINING SET

NA-SODINN generates as many training sets as detected residual noise regimes. Each of these sets are composed of MLAR sequences and their corresponding S/N curves generated from the corresponding noise regime, including data augmentation.

Unlike SODINN, which makes use of the CEVR to define the appropriate range of principal components to generate the MLAR sequences (Gómez González et al., 2018), the selection of the principal components for producing both MLAR sequences and S/N curves in NA-SODINN is instead determined through a novel metric derived from the PCA-pmap. For each rolling annulus, the PCA-pmap can be used to estimate the principal component k_{opt} that maximizes the S/N for any planetary injection at any position within the annulus (see the peak on the blue curves of Fig. 9.1). The underlying motivation behind the identification of k_{opt} is that MLAR sequences and their S/N curves can then be defined around this principal component, thus maximizing the gap between planetary and noise signals in the training set.

To identify k_{opt} at a given angular separation and for a pre-defined S/N interval of injections, the PCA-pmap relies on two steps: (i) through the data-driven procedure of Appendix C, it pre-estimates the injection flux range that corresponds to the selected S/N range; (ii) once this flux range is estimated, it is used to randomly select fluxes within the range to inject many fake companions, within the annulus at random coordinates, and retrieve their S/N curves (e.g., Fig. 9.1). The k_{opt} can finally be estimated by averaging all these S/N curves. Here, we select the injected companion fluxes to produce an S/N ranging between 1 and 3 in the final PCA-processed map obtained with one single principal component, which was experimentally found to be appropriate for the NA-SODINN training as it generally produces companions close to the detection limit for a larger number of PCs. We indicate the k_{opt} obtained for this S/N range as white circles in Figs. 7.3 and 7.4. By comparing k_{opt} with the principal components where the 90% CEVR is reached in PCA-pmaps for both *sph2* and *nrc3* ADI sequences (Figs. 7.3 and 7.4), we observe that at some angular separations, k_{opt} is not well captured by the CEVR metric. This suggests that the use of CEVR as a figure of merit for choosing the principal components is not always optimal. The range of PCs around the value of k_{opt} can be chosen differently each time NA-SODINN is employed. A range between $15 - 30$ PCs is generally optimal.

9.3   TRAINING AND INFERENCE

NA-SODINN trains an independent detection model for each regime by using its corresponding training set. For each MLAR sequence in the training

set, the feature maps created through convolutional blocks are now concatenated with their respective S/N curves after the flattened layer (Fig. 9.2). NA-SODINN generally reaches a $\sim 99.9\%$ validation accuracy with $5 - 8$ epochs. In last step, NA-SODINN does inference in individual noise regimes. It applies the trained model of each regime to infer its corresponding confidence map of the same regime (Fig. 9.2). Finally, NA-SODINN builds the final confidence detection map by joining all confidence regime maps inferred with each detection model. Thus, our NA-SODINN algorithm is conceived to keep the main characteristics of the pioneering SODINN algorithm (Gómez González et al., 2018), such as its architecture, and adapt its optimization process to our local noise approach.

10

MODEL EVALUATION

Now that NA-SODINN has been introduced, we aim to thoroughly evaluate its performance. In the first part of this section, we explain the evaluation strategy and benchmark NA-SODINN with respect to its predecessor SODINN using the same *sph2* and *nrc3* ADI sequences. Then, in the second part, we apply NA-SODINN to the first phase of EIDC (Cantalloube et al., 2020), providing confidence maps for each ADI sequence in the data challenge and running the same statistical analysis to compare the NA-SODINN performance with the rest of HCI algorithms.

10.1 PERFORMANCE ASSESSMENT

The evaluation of HCI detection algorithms consists of minimizing the false positive rate (FPR) while maximizing the true positive rate (TPR) at different detection thresholds applied in the final detection map. This information is summarized by a curve in the Receiver Operating Characteristics (ROC) space, where each point in the curve captures both metrics at a given threshold value (Gómez González et al., 2018; Dahlqvist et al., 2020). In order to produce ROC curves for various versions of SODINN applied on a given ADI sequence D, we first build the evaluation set $\mathcal{D}_{\mathrm{eval}} = \{D_1, D_2, D_3, \ldots, D_s\}$ containing s synthetic data sets D_i, where each synthetic data set is a copy of D with one fake companion injection per noise regime. Here, we limit the number of injected companions per noise regime to one at a time to avoid any risk of cross-talk between companions in the detection algorithms themselves (e.g., because multiple companions can affect the PCA), or in their evaluation (e.g., if they get too close and merge in terms of confidence patch). The coordinates of these injections are randomly selected within the considered noise regime boundaries, and their fluxes are randomly set within a pre-defined range of fluxes that correspond to a S/N range between 0.5 and 2 in the ADI-PCA processed frame considering one PC. This pre-defined range of fluxes is estimated through the same data-driven method explained in Appendix C and illustrated in Fig. C.1. Hence, each algorithm provides s final detection maps, from which true positives (TPs), false positives (FPs), true negatives

(TNs) and false negatives (FNs) indicators are computed across the whole noise regime field of view at different detection thresholds. Then, all these indicators are averaged and the corresponding ROC curve for the considered noise regime is produced. Instead of using the FPR metrics as in standard ROC curves, here we use the mean number of FPs within the considered noise regime, which is more representative of the HCI detection task and facilitates the interpretation of our performance simulations.

We perform the proposed ROC curve analysis on both *sph2* and *nrc3* ADI sequences with $s = 100$ for each. For this assessment, a detection is defined as a blob in the final detection map with at least one pixel above the threshold inside a circular aperture of diameter equal to the FWHM centered at the position of each injection. With the aim to benchmark NA-SODINN, we include in this evaluation the annular-PCA algorithm (Absil et al., 2013) as implemented in the VIP Python package (Gómez González et al., 2017; Christiaens et al., 2023), the SODINN framework by Gómez González et al. (2018), and two hybrid detection models. These hybrid models are modifications of SODINN to include only one of the two additional features introduced in NA-SODINN: the adaptation to noise regimes, or the addition of S/N curves in the training. Hereafter, we refer to them respectively as *SODINN +Split* and *SODINN +S/N*. In the same spirit as an ablation study, these two hybrid models are included in our evaluation in order to provide information about the added value of each approach separately for the task of detection. It is worth mentioning that instead of re-training all considered SODINN-based models every time a different fake companion is injected into each evaluation set, we train them once per ADI sequence. While re-training would be more accurate, as the presence of an injected fake companion could slightly perturb the c_- class, we assume that our augmentation strategy (Sect. 8.1) mitigates this perturbation and does not significantly impact the training process and the model performance. Using the same model to detect all fake companion injections in a single ADI sequence saves computation time.

An important aspect to consider when comparing algorithms in ROC space is to optimally choose their model parameters. In the case of annular-PCA, we use 1, 5 and 10 principal components for each annulus as a good compromise to analyze its performance. For the various versions of SODINN, we need to define two main parameters: the list of principal components $\mathcal{PC} = (pc_1, pc_2, \ldots, pc_m)$ that are used to produce each sample in both the MLAR sequence and S/N curve, and the level of injected fluxes used for making c_+ class samples (see Sect. 8.1). For SODINN, we used the criterion based on the cumulative explained variance ratio (CEVR), as proposed by Gómez González et al. (2018), to define the range of $\mathcal{PC}$. For NA-SODINN and the hybrid models, we instead rely on the novel PCA-pmaps technique presented in Sect. 7.3, and we choose a list of $m = 15$ principal components centered around k_{opt} (Section 9.1). Regarding the injected fake companion

fluxes, we choose for all SODINN-based models a range of fluxes that correspond to an S/N between 1 and 3 in the ADI-PCA processed frame with one PC(Appendix C). This range of fluxes does generally not lead to class overlapping, where c_+ and c_- class samples would look too similar. However, in order to avoid FPs in the final detection map, the user may consider higher flux ranges. Finally, to build the ROC curve, we consider a list of S/N thresholds ranging from 0.1 to 4.5 in steps of 0.05 for annular PCA, while for the SODINN-based models we use a list of confidence thresholds from 0.09 to 0.99 in steps of 0.1. All SODINN-based models are trained on balanced training sets containing around 10^5 samples for each class using a NVIDIA GeForce RTX 3070 graphics processing unit (GPU).

Figures 10.1 and 10.2 display a series of ROC spaces –one for each detected noise regime–, respectively for the *sph2* and *nrc3* ADI sequences. For the sake of simplicity, note that we do not consider the detected regime comprised between $17 - 19\lambda/D$ in *sph2* (Fig. 7.3) in this analysis. Each of these ROC spaces displays one ROC curve per algorithm, which informs about its detection performance on that specific noise regime for different thresholds. We observe from both figures that NA-SODINN outperforms its predecessor, the hybrid models, and the annular-PCA technique for each noise regime. This behavior is further illustrated in Appendix D, with Figs. D.1,D.2 and D.3 for the case of *sph2*, and Figs. D.4,D.5 for *nrc3*, where the confidence maps from each algorithm are compared at different threshold levels. Regarding hybrid models, we generally observe that they land between the SODINN and NA-SODINN detection performance, with SODINN+S/N generally being the best hybrid model. It can also be observed that annular-PCA with $PC = 5$ and $PC = 10$ perform better than with $PC = 1$ for all regimes. We associate this behavior to the fact that for $PC = 5$ and $PC = 10$, we are closer to the principal component k_{opt} where the S/N is maximized, and therefore, the star-planet contrast is improved.

Based on these results and on additional experiments, we observe a general trend for both approaches separately. While splitting the field of view in noise regimes tends to reduce the number of false positives, especially when residual speckle noise is significant, adding a S/N curve for each MLAR sequence tends to enhance the algorithm's sensitivity to detect signals. These findings imply that both techniques, when combined in the neural network, considerably improve the SODINN detection performance.

10.2 NA-SODINN IN THE EIDC

By design, the first phase of the Exoplanet Imaging Data Challenge (EIDC, Cantalloube et al., 2020), presented in Chapter 4, can be used as a laboratory to compare and evaluate new detection algorithms against other state-of-the-art HCI detection algorithms. For instance, Dahlqvist et al. (2021a) used the
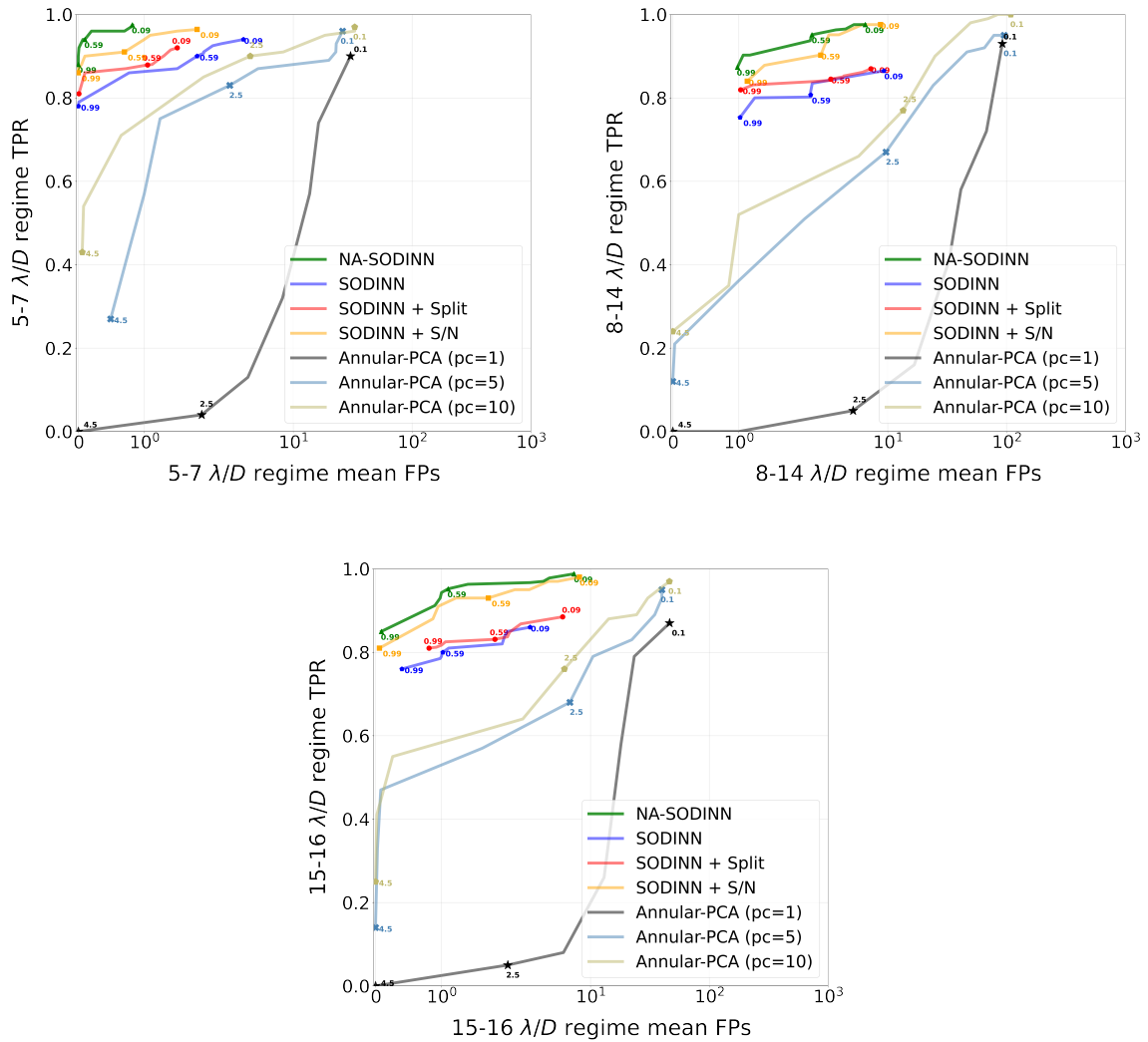
Figure 10.1: ROC analysis per noise regime for the *sph2* data set showing the performance of SODINN, NA-SODINN, annular-PCA, and hybrid SODINN models. The values plotted alongside each curve highlight some of the selected thresholds.
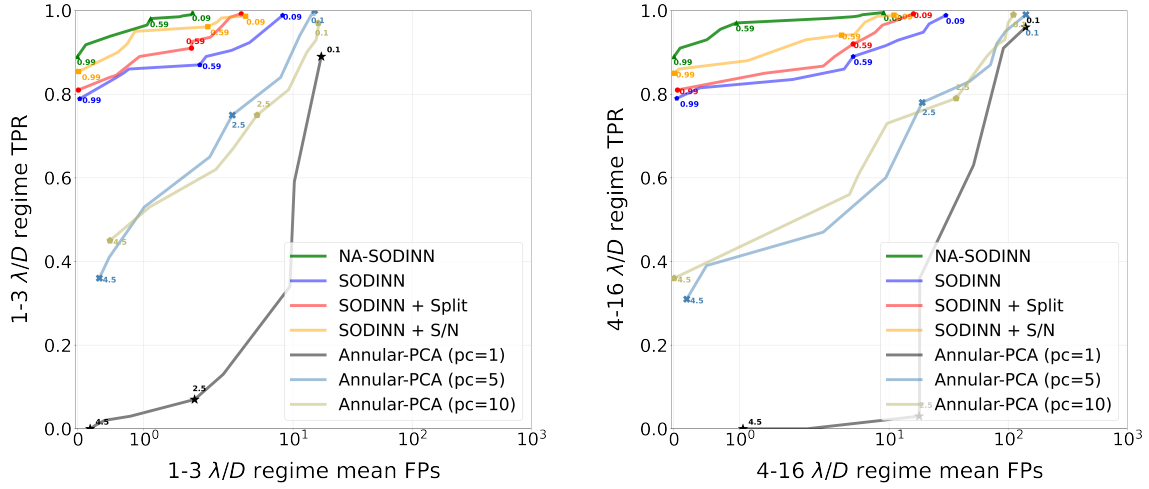
Figure 10.2: Same as Fig. 10.1 for the *nrc3* data set.

EIDC to highlight the improvement of the automated version of their RSM algorithm. Here, we use the ADI sub-challenge of the EIDC (Section 4.1) to generalize the ROC analysis, and evaluate how NA-SODINN performs with respect to the state-of-the-art HCI algorithms that entered the data challenge.

We apply our NA-SODINN framework to the EIDC, and as in the ROC analysis, we use PCA-pmaps as a tool for both estimating residual noise regimes and choosing the list of principal components $\mathcal{PC}$ at each angular separation. For the injection flux ranges, we use an S/N range between two and four times[1] the level of noise in the ADI-PCA processed frame with one PC. Each model is trained with balanced training sets that contain around 10^5 samples per class. Because all three LMIRCam cubes contain more than 3000 frames (Table 1), we decided to reduce this number to around $250-300$ frames to limit the computational time. To do that, we average a certain number of consecutive frames along the time axis in the sequence. Figure 10.3 shows a grid of all resulting NA-SODINN confidence maps from EIDC ADI sequences where we observe, by visual inspection, that NA-SODINN finds most of the injected fake companions, while producing only faint false positives that all fall below our default detection threshold $\tau = 0.9$. In order to quantify this information, we follow the same approach as in Cantalloube et al. (2020) by considering the area under the curve (AUC) for the TPR, FPR, and FDR as a function of the threshold, which allows

---

1 The choice for using a range $S/N = [2, 4]$ instead of the range $S/N = [1, 3]$ to produce c_+ samples in NA-SODINN for the EIDC is due to we know, as the rest of participants, that the contrast of EIDC planetary injections cover a wide range. In the end, this is a parameter that users can control.

sph1 - 1/1 **detections**   *sph2* - 0/0 **detections**   *sph3* - 5/5 **detections**

nrc1 - 3/4 **detections**   *nrc2* - 1/3 **detections**   *nrc3* - 0/0 **detections**

lmi1 - 1/2 **detections**   *lmi2* - 2/2 **detections**   *lmi3* - 2/3 **detections**
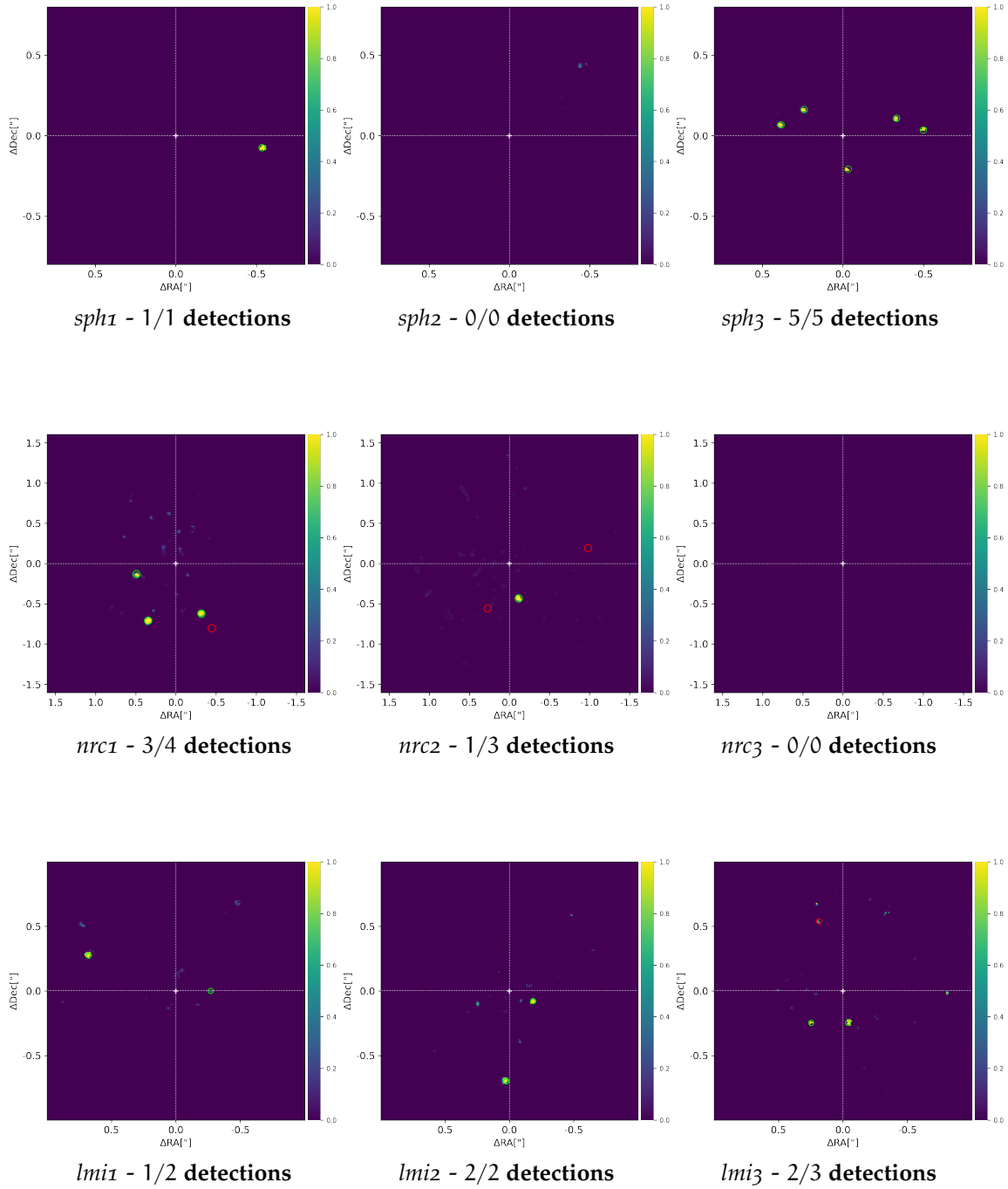
Figure 10.3: NA-SODINN confidence maps obtained on the whole set of EIDC ADI sequences (Table 1). For the submitted confidence threshold $\tau = 0.90$, we highlight with green circles the correct detection of injected companions (true positives), and with red circles the non-detection of injected companions (false negatives). The circles have a FWHM diameter. No false positive is reported in our maps, as all the remaining non-circled peaks in the confidence maps are below the threshold.

to mitigate the arbitrariness of the threshold selection by considering their evolution for a pre-defined range (see Section 4.1.2). The AUC_{TPR} should be as close as possible to one and the AUC_{FPR} and AUC_{FDR} as close as possible to zero. The F1-score ranges between zero and one, where one corresponds to a perfect algorithm, and is computed only on a single threshold τ_{sub} that is chosen by the participant.

Figure 10.4 shows the result of this analysis for all NA-SODINN confidence maps of Fig. 10.3, in which all TPR, FPR, and FDR metrics (and their respective AUCs) are computed for different confidence threshold values ranging from 0 to 1. Here, we mainly see that the AUC_{FDR} is generally higher along the range of thresholds for NIRC2 and LMIRCam than for SPHERE data sets, the AUC_{FPR} is close to zero for all data sets, and the AUC_{TPR} is almost perfect for SPHERE data sets. To compute the F1-score, we choose a $\tau_{sub} = 0.9$ confidence threshold. From our test with NA-SODINN, we consider this value as the minimum confidence threshold for which one can rely on the significance of detections, maximizing TPs while minimizing FPs. Thus, any pixel signal above this τ_{sub} on each confidence map of Fig. 10.3 is considered as a detection for the computation of the F1-score. Finally, through the AUC_{TPR}, AUC_{FDR} and F1-score metrics obtained with the NA-SODINN algorithm, we are able to update the general EIDC leader-board (Cantalloube et al., 2020). Figure 10.5 shows how NA-SODINN ranks compared to the algorithms originally submitted to the EIDC, for each considered metric. We clearly observe that NA-SODINN ranks at the top, or close to the top, for each of the EIDC metrics, with results generally on par with the RSM algorithm by Dahlqvist et al. (2020). In particular, NA-SODINN provides the highest area under the true positive curve, while preserving a low false discovery rate.
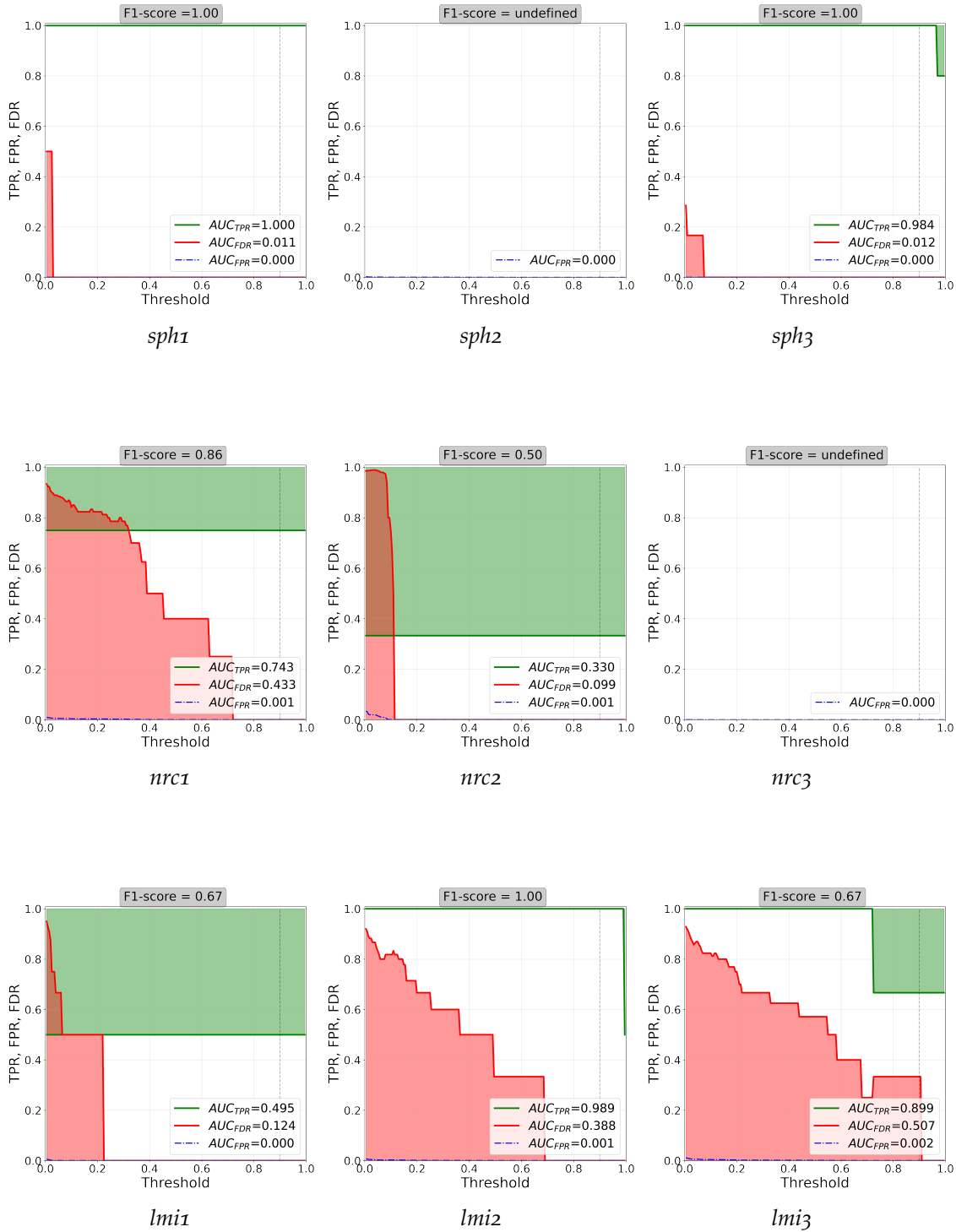
Figure 10.4: TPR, FDR and FPR metrics computed from the confidence maps of Fig. 10.3 for a range of confidence thresholds varying from zero to one. Their respective AUCs are showed in each legend. The F1-score is computed at the submitted threshold on the challenge $\tau_{\text{sub}} = 0.9$ (vertical dashed line) and it is showed in the top of each subplot.
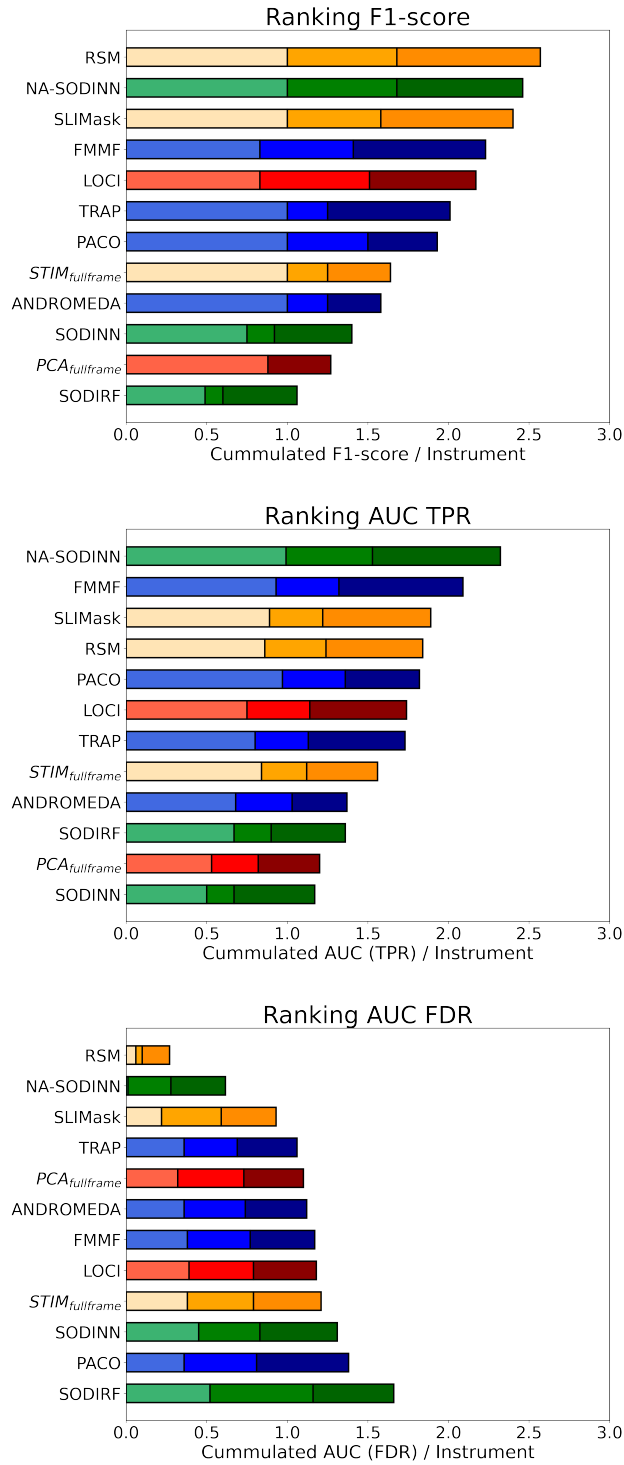
Figure 10.5: Updated EIDC leader-board after the NA-SODINN submission. Ranking based on the F1-score (on top), the AUC_{TPR} (on middle) and the AUC_{FDR} (on bottom). Colors refer to HCI detection algorithm families: PSF-based subtraction techniques providing residual maps (red) or detection maps (orange), inverse problems (blue) and supervised machine learning (green). The light, medium and dark tonalities correspond to SPHERE, NIRC2, and LMIRCam data sets respectively.

11

NA-SODINN ON THE SHINE SURVEY

The field of direct imaging has grown significantly over the last two decades, as evidenced by the design of numerous HCI surveys using various ground-based telescopes, instruments, and observing strategies. These surveys have resulted in the discovery of approximately 60 sub-stellar and planetary-mass companions orbiting young nearby stars, as documented in Wagner et al. (2019) and showed in Fig. 1.1. Initially, HCI surveys were relatively small, typically targeting samples of 50 to 100 stars. However, ongoing surveys are aiming to observe 500 to 600 stars. Among the most ambitious projects to date are the SHINE project conducted with SPHERE (Langlois et al., 2021) and the Gemini Planet Imager (GPI) Exoplanet Survey (GPIES, Macintosh et al., 2015). So far, SHINE and GPIES have collectively contributed three new exoplanet discoveries (Macintosh et al., 2015; Chauvin et al., 2017; Keppler et al., 2018b), along with several high-mass brown dwarfs (e.g. Konopacky et al., 2016; Cheetham et al., 2019). These surveys have also provided spectral and orbital characterization data for confirmed exoplanets (e.g., Nielsen et al., 2019; Rameau et al., 2013).

In this context, it is a logical progression to leverage advanced image post-processing algorithms to search for new planetary candidates. Thus, having successfully introduced and evaluated the NA-SODINN algorithm, our next step is its practical implementation within HCI surveys. In this chapter, we present preliminary results from applying NA-SODINN to the F150 sample of the SHINE survey. The complete set of results will be presented in a near future, including the upcoming *Conference on Machine Learning in Astronomical Surveys*, scheduled for November 27th to December 1st, 2023, jointly hosted at the IAP in Paris and the Flatiron Institute in New York. This concluding chapter is devoted to demonstrate the effectiveness of the novel NA-SODINN algorithm at detecting confirmed exoplanets in real HCI data from a survey and also observe whether it captures new potential candidates in the image field of view.

11.1 THE SHINE SURVEY

The *SpHere INfrared survey for Exoplanets* (SHINE) was designed to use 200 telescope nights of guaranteed time observations with the SPHERE instrument (Beuzit et al., 2019) at the VLT. SPHERE combines the use of the SAXO extreme adaptive optics system (Fusco et al., 2006, 2014; Petit et al., 2016) and a series of three scientific cameras (IRDIS, IFS, ZIMPOL), fed by an apodized pupil Lyot coronagraph (Soummer, 2005). This configuration allows for very high-quality imaging, achieving a SR of over 90% in the H-band under favorable observing conditions. The survey spanned from February 2015 to 2021 and aimed to observe $500 - 800$ nearby young stars. Observations were acquired in either IRDIFS or IRDIFS-EXT mode, that is, with both NIR cameras, (IFS and IRDIS) that were carrying out observations in parallel. The IFS covers a $1.7'' \times 1.7''$ FoV and IRDIS covers a nearly circular FoV of diameter $\sim 9''$. In IRDIS, all first epoch observations were performed with the DB-H23 or DB-K12 dual-band filter pairs (Vigan et al., 2010).

The primary objectives of the SHINE survey included: (i) the identification and characterization of new planetary and brown dwarf companions; (ii) the study of the architecture of planetary systems; (iii) the study of the link between the presence of planets and disks; (iv) the determination of the frequency of giant planets beyond 10 au; and (v) the investigation of the impact of stellar mass on the frequency and characteristics of planetary companions over the range $0.5 - 3$ solar masses. Detailed information about the survey concept and sample selection can be found in Desidera et al. (2021), while the observations and data reduction procedures are described in Langlois et al. (2021).

11.2 THE F150 SAMPLE

In order to apply NA-SODINN to the SHINE survey, we make use of the F150 sample (Vigan et al., 2021). This sub-sample consists of 150 targets, with first epoch observations obtained between February 2015 and February 2017, and second epoch observations extending until 2019. It is important to note that the sample was not optimized for completeness at this stage, as the scheduling favored the broader survey. Nevertheless, it is still representative of the overall data set well. The sample includes 53 *BA* stars, 77 *FGK* stars, and 20 *M* stars. The median age of stars in this sample is about 45 million years, with a median stellar mass of 1.15 times that of our Sun and a median distance of 48 parsecs. We refer to Vigan et al. (2021) for more information about the F150 sample, its analysis and conclusions.

11.2.1 *Data sets*

For this preliminary NA-SODINN analysis, we have chosen five representative ADI sequences from the F150 sample. This selection is made to encompass four distinct scenarios: (i) Sequences that do not contain confirmed exoplanets or disks, (ii) sequences that contain confirmed exoplanets but no disks, (iii) sequences that contain confirmed disks but no exoplanets, and (iv) sequences that contain both confirmed exoplanets and disks. The rationale for this selection criteria is as follows: firstly, we aim to rigorously test the efficacy of our NA-SODINN technique under various image noise configurations. These configurations include scenarios with the presence of extended sources in the image. Secondly, we intend to test the capability of our method to accurately recover confirmed targets in the field of view. Moreover, it is worth noting that each of these data sets was acquired under different observing conditions. Table 12 summarizes the properties of each ADI sequence, and Fig. 11.1 shows the median frames.

11.2.2 *Pre-processing*

In addition to the standard pre-processing (Langlois et al., 2021), we have performed two additional steps before applying the NA-SODINN algorithm. Making use of the open-source VIP Python package (Gómez González et al., 2017; Christiaens et al., 2023), our initial step consists in cropping the image's field of view to a dimension of 180×180 pixels. We also perform cropping and normalization of the stellar PSF for each data set. Finally, we conduct the Pearson distance correlation analysis to identify bad frames within the sequence. Ranging from zero (no-correlation) to one (maximum correlation), this metric measures the correlation of each frame in the sequence with a reference frame, which is the median frame of the sequence in our case. By applying a correlation threshold, frames that have correlations below this threshold are then removed. We apply a correlation threshold of 0.8 to each of our five ADI sequences. The final count of frames presented in Table 12 for each ADI sequence reflects the outcome of this pre-processing.

Star	RA	DEC	Dist	ST
	[h : min : sec]	[º:′:″]	[pc]	
HIP27321	05 : 47 : 17	−51 : 03 : 59	19.44 ± 0.05	A6V
HIP30030	06 : 19 : 08	−03 : 26 : 20	52.0 ± 1.3	G0V
HIP15457	03 : 19 : 21	+03 : 22 : 13	9.14 ± 0.02	G5V
HIP102409	20 : 45 : 09	−31 : 20 : 27	9.714 ± 0.002	M1V
HIP99742	20 : 14 : 16	+15 : 11 : 52	46.0 ± 0.5	A2V

Table 12: Summary of the main parameters of the five targeted stars from the F150 sample. RA and DEC columns correspond to the star coordinates right ascension and declination. The Dist column refers to the distance of the star with respect the Earth. Distances are derived from the Gaia-EDR3. ST stands as Spectral Type.

Star	Observation date	λ_{obs}	N_t	N_{img}	Δ_{rot}	Seeing	$\hat{\tau}_0$	Air mass
		[μm]		[px × px]	[º]	[″]	[ms]	
HIP27321	2015 − 12 − 26	1.667	472	180 × 180	37.3	1.443	2.16	1.120
HIP30030	2017 − 02 − 08	1.667	40	180 × 180	36.4	0.626	8.65	1.089
HIP15457	2015 − 12 − 26	1.667	480	180 × 180	33.2	1.043	2.91	1.141
HIP102409	2015 − 05 − 30	1.667	159	180 × 180	118.7	0.739	1.77	1.021
HIP99742	2016 − 06 − 11	1.667	159	180 × 180	35.7	0.639	4.66	1.316

Table 13: Properties of the SPHERE ADI sequence of each selected sample in Table 12. λ_{obs} is the observed wavelength, N_t denotes the number of frames within the sequence, N_{img} indicates the frame size, and Δ_{rot} the field of rotation. Both the seeing and $\hat{\tau}_0$ (coherence time) are averaged values along the observation. The air mass column also presents the average value.
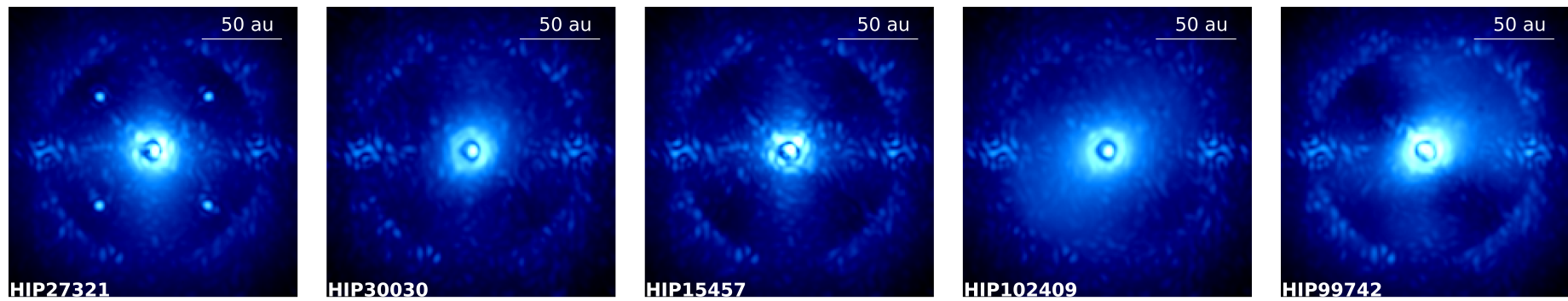
Figure 11.1: Median frame of each ADI data set from Table 13. The name of the star is written on the bottom of each frame. Various SPHERE structures can be observed in the images, such as satellite spots, strong wind-driven halos, and the corrected areas (Cantalloube et al., 2019).

11.3 MODEL CONFIGURATION

After pre-processing the five data sets of Table 12, NA-SODINN is used to search for potential companion candidates. As previously described in Chapter 9, NA-SODINN initiates the detection process by first identifying noise regimes in the annular PCA-processed frames through the PCA-pmap technique (Section 7.3). In the analysis of the five ADI sequences, we observed a noise pattern closely resembling that of the *sph2* dataset, which was used for testing. This pattern consisted of a speckle-dominated regime spanning $1 - 7\,\lambda/D$ (including the IWA), followed by a background-dominated regime from $8 - 14\,\lambda/D$, another speckle-dominated regime spanning $15 - 17\,\lambda/D$, and finally, a background-dominated regime extending beyond approximately $18\,\lambda/D$. Having identified these noise regimes, NA-SODINN generates a training set for each of them separately, including MLAR sequences and S/N curves for both the c_+ and c_- classes. For the c_+ samples, NA-SODINN initially estimates the injection fluxes at each annulus corresponding to a specified S/N range in the first processed frame (as detailed in Appendix C). In this analysis, we opted for injecting companions with a S/N range between 2 and 4. The selection of PCs used to generate each sample was customized to include roughly 20 PCs around k_{opt} (see Section 9.1). As for model training, we followed the optimization parameters used in Chapter 10.

11.4 DETECTION MAPS

The detection maps produced by NA-SODINN and various PSF subtraction techniques for each of the five ADI sequences are shown in Figures 11.2 to 11.6. In the case of NA-SODINN, we also included binary maps generated by applying different confidence thresholds, $\tau = [0.5, 0.7, 0.9, 0.99]$ to its confidence map.

Figure 11.2 depicts the case of the ADI sequence for the star HIP30030, also referred to as HD43989 or V1358 Ori. No exoplanets or disks have been confirmed around this star thus far. Nevertheless, NA-SODINN detects a faint point-like source at an angular separation of approximately $10\,\lambda/D$, with only a few pixels exceeding 99% confidence. Notably, this point-like source is challenging to discern in the detection maps generated by PSF subtraction techniques, as its S/N values are very close to the mean S/N of the image noise. This candidate needs to be confirmed with at least one additional epoch. NA-SODINN also identifies two more small candidates, but with confidence values in the range of $50 - 70\%$. Additionally, an over-density is observed in all the PCA-based S/N maps at the field's edge, with S/N values around $4 - 5$. NA-SODINN does not attribute any confidence to this feature as a potential candidate.

Figure 11.3 presents the case of HIP27321, commonly known as β Pictoris. In this system, two exoplanets, β Pictoris b (Lagrange et al., 2009) and β Pictoris c (Lagrange et al., 2019) have been confirmed, along with a young debris disk surrounding the star. NA-SODINN clearly detects the signature of planet b, with high confidence value s exceeding 99%. No other signals are identified within the field of view. All of the PSF subtraction techniques also detect the signature of planet b, with S/N values typically exceeding 7. The disk profile can be faintly observed in all of the PSF subtraction techniques, with median subtraction yielding the highest S/N values for the disk signals. However, the disk is not detected by NA-SODINN, which is expected as it relies on point-like sources.

Figure 11.4 illustrates the case of HIP15457, also known as HD20630 or κ^1 Ceti. Although no extra-solar planets have been confirmed to orbit this star, κ^1 Ceti is considered a strong candidate for the presence of terrestrial planets. The confidence map produced by NA-SODINN reveals three point-like sources with varying confidence levels. Two are at very small angular separations, with confidence levels reaching 90%, and a larger signature near the field of view limit attains confidence levels of 99%. None of these three signatures are clearly distinguishable in the S/N maps. These candidates need to be confirmed with at least one additional epoch.

Figure 11.5 shows the case of HIP102409, also known as HD197481 or AU Microscopii. This star features a large asymmetric circumstellar disk extending up to 210 au from the star (Kalas et al., 2004). Two transiting exoplanets, AU Mic b (Plavchan et al., 2020) and AU Mic c (Martioli et al., 2021), have been detected, and a third candidate, AU Mic d (Wittrock et al., 2023), was recently validated. In this data set, NA-SODINN clearly detects a point-like source with confidence levels exceeding 99%, even though it does not identify the circumstellar disk. When examining the S/N maps, we observe that the disk is fully recovered, especially for PCA-based techniques, which also faintly distinguish the signature detected by NA-SODINN. For median subtraction and NMF post-processing algorithms, we observe an unusual behavior close to the star. We associate this structure to the strong wind-driven halo (Fig. 11.1).

Finally, Figure 11.6 displays the case of HIP99742, also known as HD192425 or ρ Aquilae. No exoplanet or disk has been detected in this system thus far. NA-SODINN does not detect any potential signatures across the field of view. The S/N maps also fail to identify a clear circumstellar signal. NMF and median subtraction algorithms present the same unusual structure close to the star observed in HIP102409 Figure 11.5. We also associate this structure to the strong wind-driven halo (Fig. 11.1).
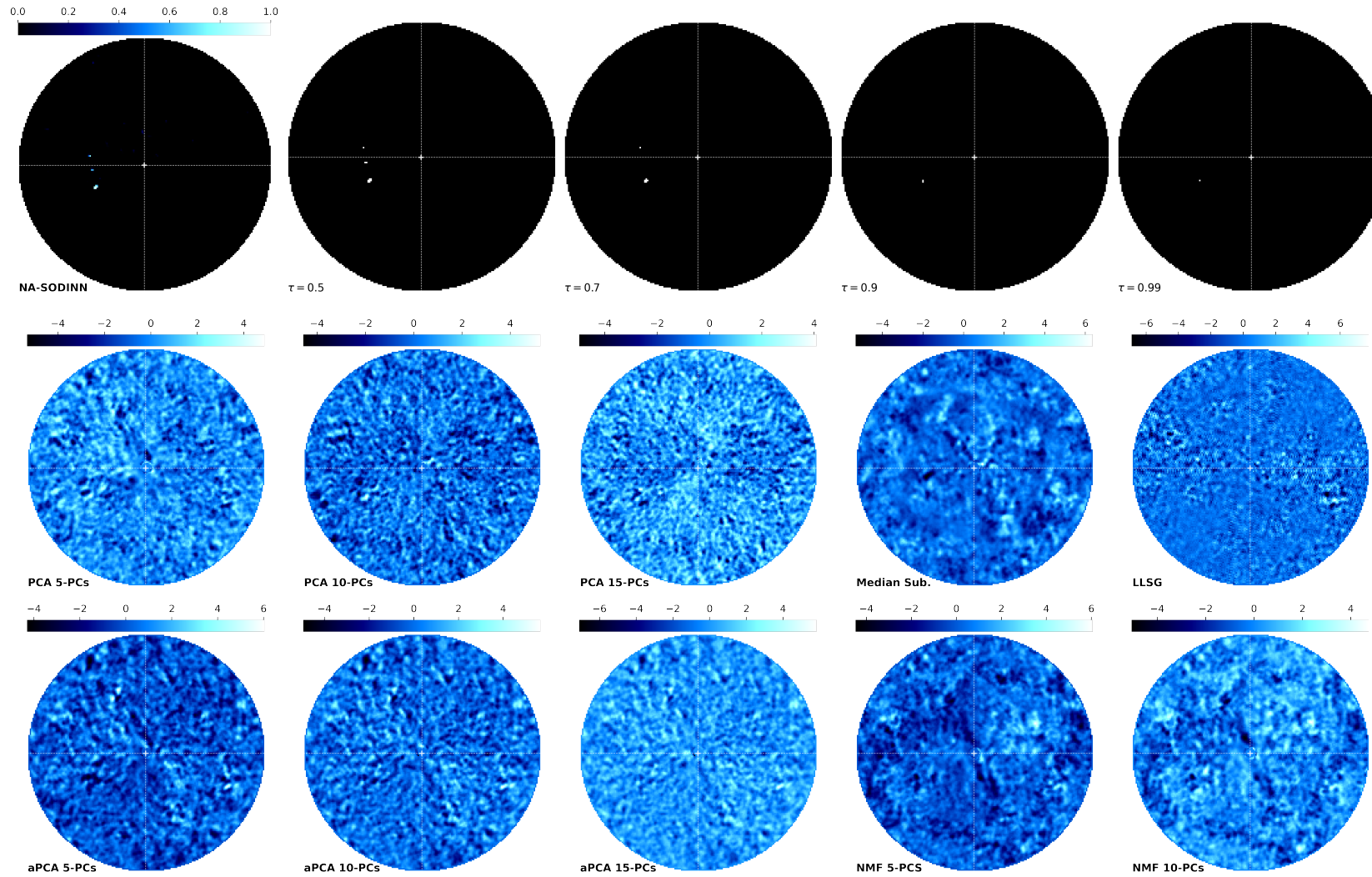
Figure 11.2: Detection maps for the HIP30030 star ADI sequence. The first row shows the NA-SODINN confidence map and its binary maps at a thresholds $\tau = [0.5, 0.7, 0.9, 0.99]$. The second and third row show the S/N maps of full-frame PCA, annular-PCA, Median subtraction, LLSG, and NMF post-processing algorithms. The dashed crossfair in white indicates the position of the obscured star (middle of the image).
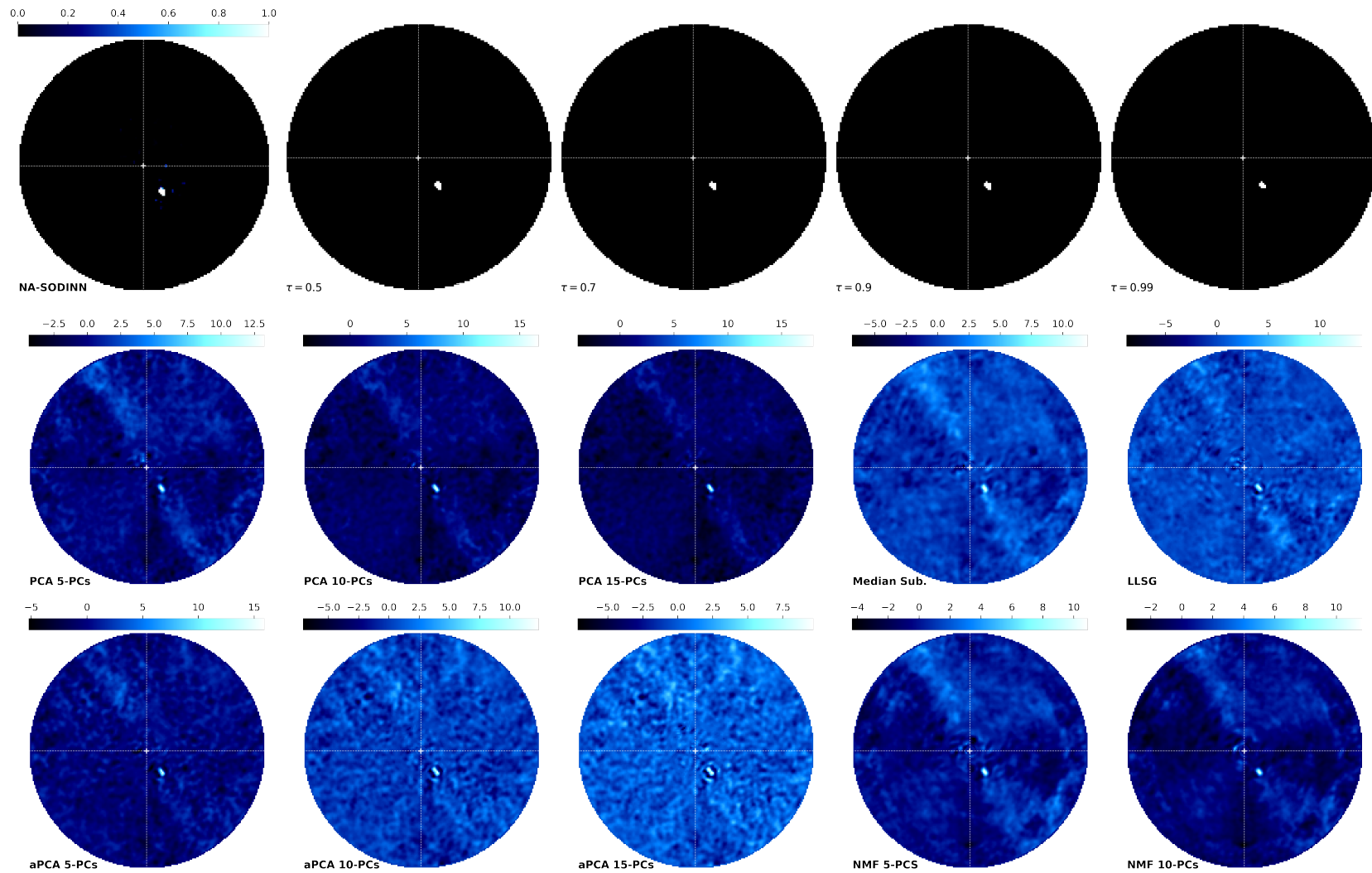
Figure 11.3: Same as Fig. 11.2 for the HIP27321 (β-pictoris) star ADI sequence.
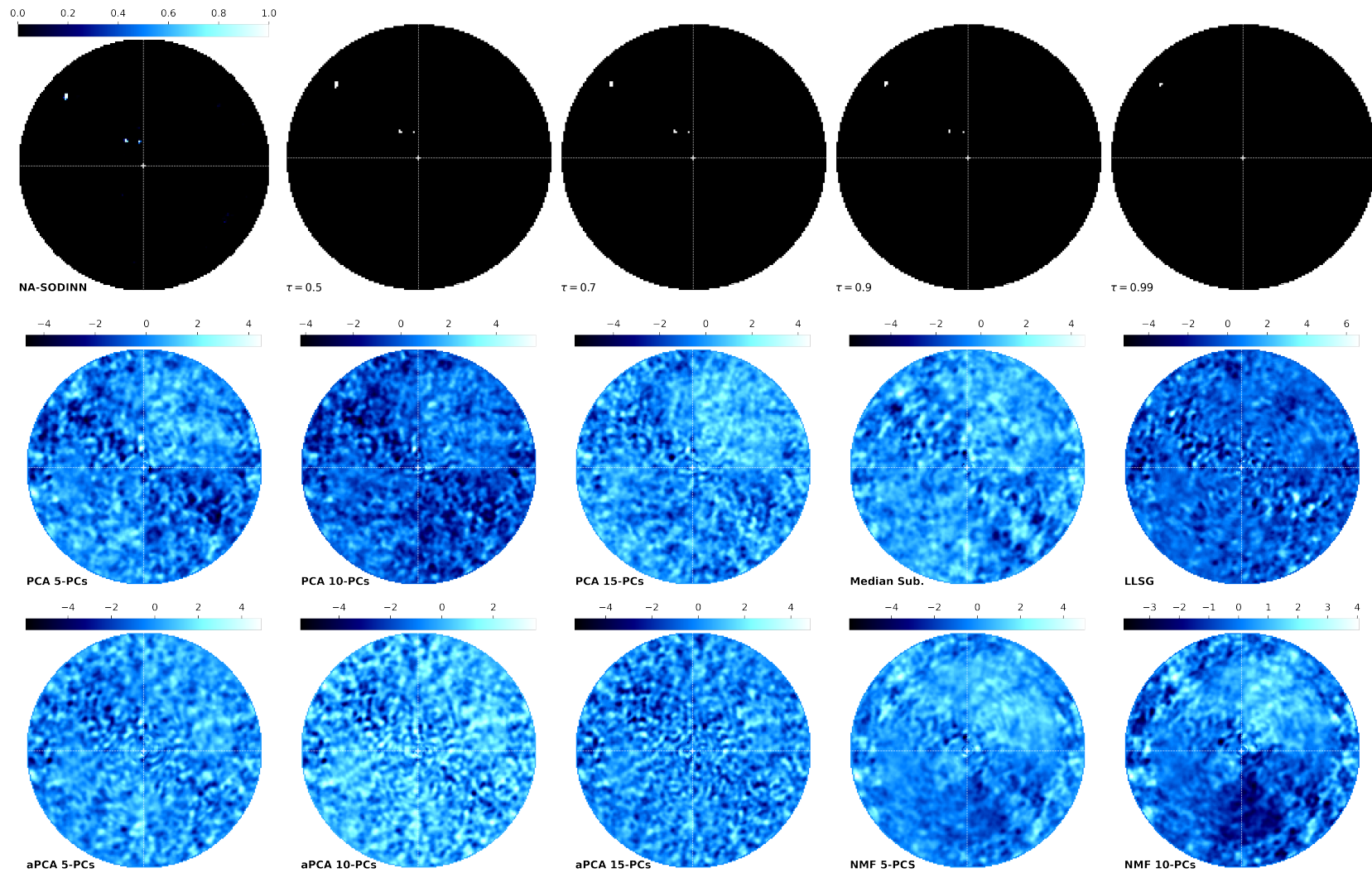
Figure 11.4: Same as Fig. 11.2 for the HIP15457 star ADI sequence.
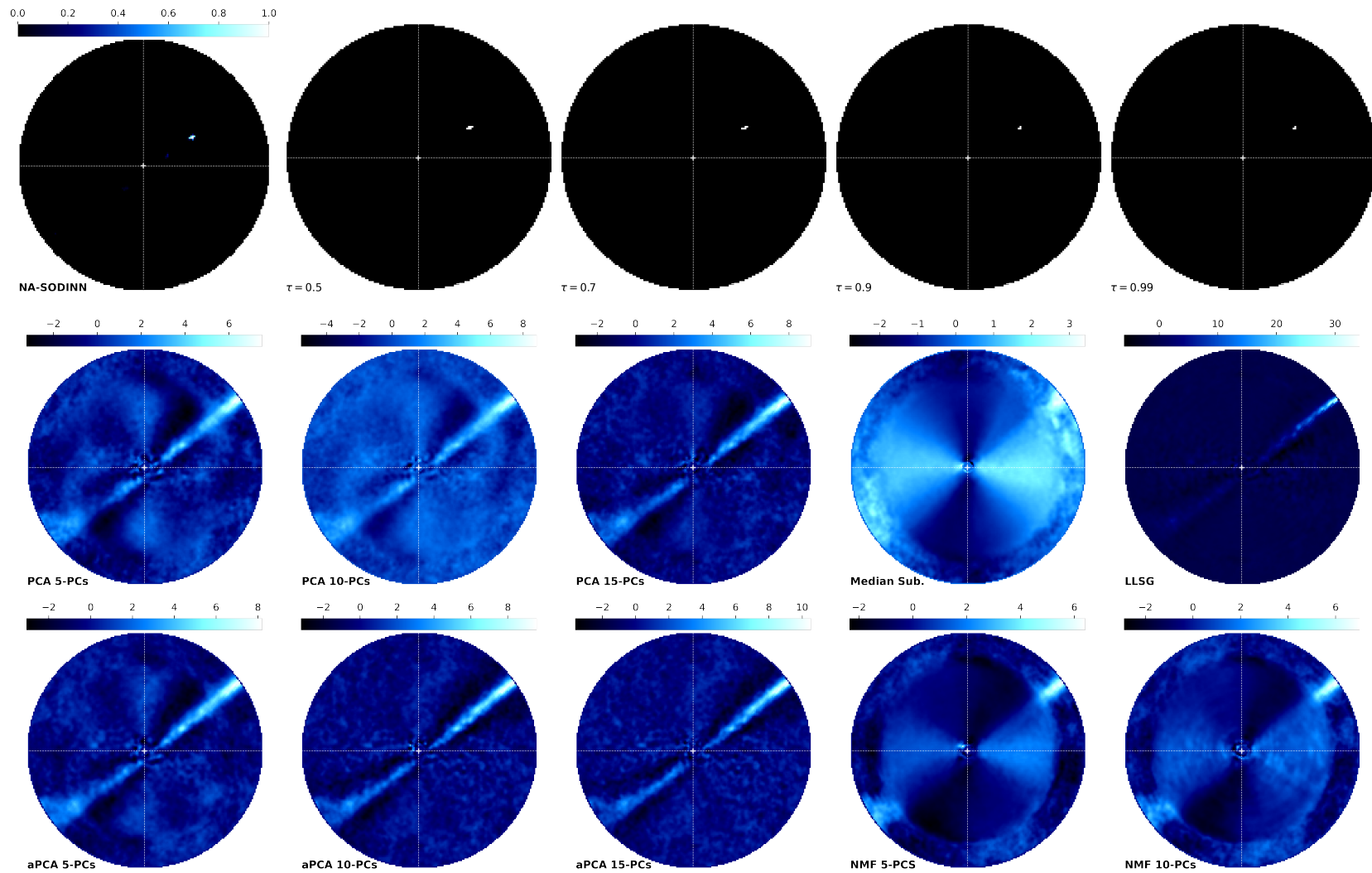
Figure 11.5: Same as Fig. 11.2 for the HIP102409 star ADI sequence.
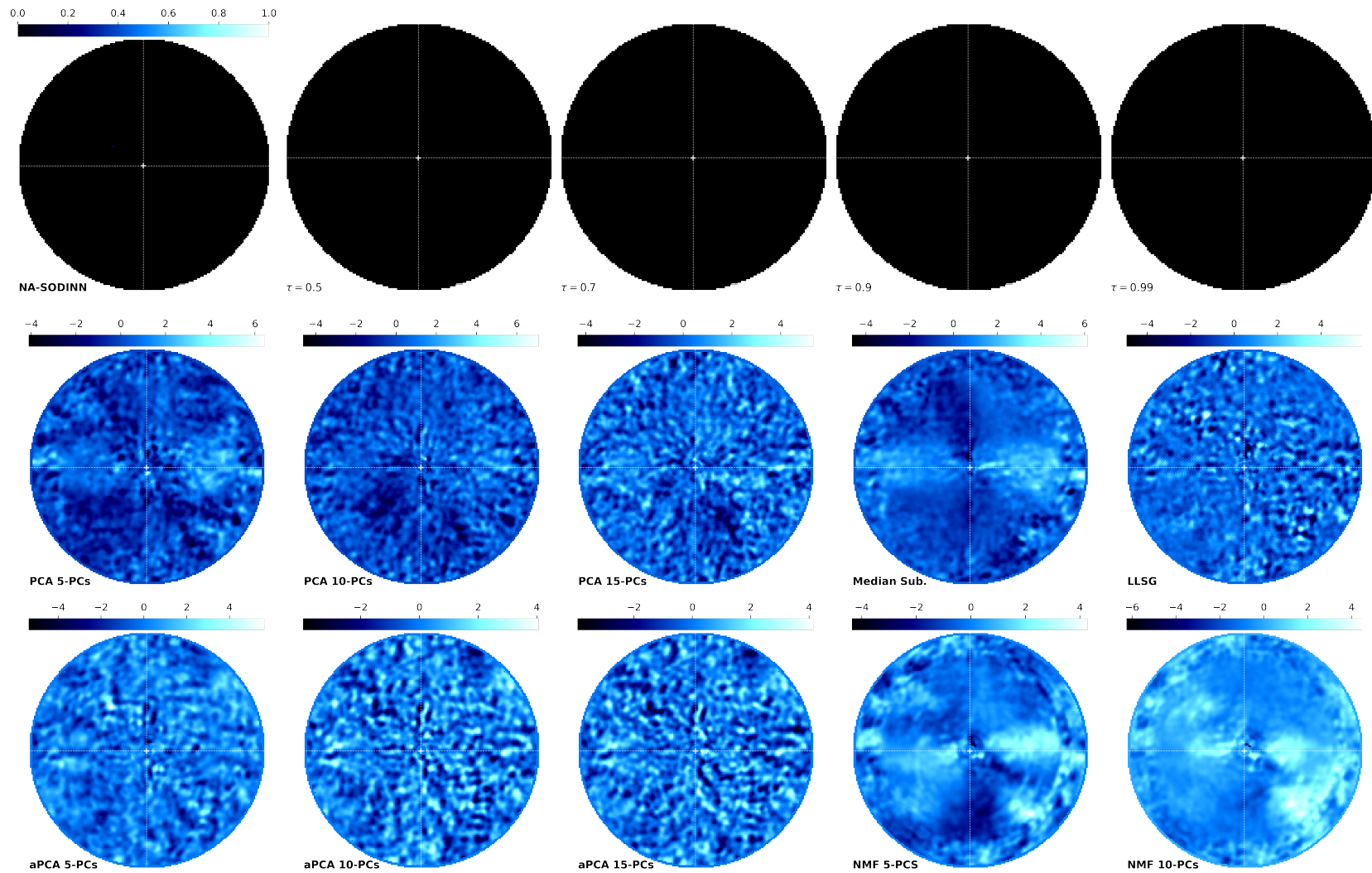
Figure 11.6: Same as Fig. 11.2 for the HIP99742 star ADI sequence.

CONCLUSIONS

In this part IV of the thesis, we presented and evaluated NA-SODINN, our novel exoplanet detection algorithm that combines the SODINN technique (Gómez González et al., 2018) with our noise regimes approach. NA-SODINN was evaluated through two distinct analyses. The first performance assessment was based on ROC curves using two ADI sequences provided by the VLT/SPHERE and Keck/NIRC2 instruments. In this analysis, NA-SODINN was evaluated with respect to the annular-PCA post-processing algorithm, the original SODINN, and two SODINN-based hybrid models that only used one of the two proposed approaches (the regime split or the addition of S/N curves). Results showed that hybrid models improve the detection performance of SODINN in all noise regimes, which demonstrated the interest of the local noise approaches considered in this thesis. Moreover, NA-SODINN reached even higher detection performance, by combining both approaches in the same framework. In order to benchmark NA-SODINN against other state-of-the-art HCI algorithms, it was then applied to the first phase of the EIDC. NA-SODINN ranks at the top (first or second position) of the challenge leaderboard for all considered evaluation metrics, providing in particular the highest TPR among all entries, while still keeping a low false detection rate. The NA-SODINN algorithm was finally applied to a small sample of the recent SHINE HCI survey. Results show that NA-SODINN identifies some potential candidates with strong confidence along the field of view. However, we acknowledge that this preliminary study does not conclude on the nature of the detections. More detection maps and analyses with different filters and epochs are necessary in order to really conclude on potential discoveries.

While NA-SODINN shows promise, we identified some limitations that could be addressed in future work. The algorithm relies on previous noise analyses, such as PCA-pmaps, to define these regime boundaries, limiting its independence. Future improvements could involve modifying the network architecture to enable the identification of noise regimes during training. Another limitation is the challenge of setting an appropriate detection threshold in the final detection map. This is typically based on the presence of obvious false positives, which may affect the application of NA-SODINN in certain contexts. However, this limitation can be mitigated by using dedicated metrics such as ROC-space to assess detection performance. We also note that NA-SODINN, and its predecessor, rely on data augmentation techniques to generate a diverse training set. While this methodology is used to prevent over-fitting during the training and lack of generalization, we believe that it is

not the most appropriate to really capture inherent relationships in HCI data. Exploring alternative methods such as generative deep learning models, such as latent diffusion models (Rombach et al., 2022) and generative adversarial networks (Goodfellow et al., 2014), may lead to more robust supervised models with better generalization. Lastly, extending the application of NA-SODINN to work on other observing strategies, such as SDI or even RDI, and detect extended sources, such as protoplanetary disks, would be a valuable avenue to increase the flexibility of the algorithm.

Part V

CONCLUSIONS

12

SUMMARY

The research conducted in this thesis focused on the development and testing of NA-SODINN (Cantero et al., 2023), a novel deep learning algorithm for exoplanet image detection using angular differential imaging (ADI). The thesis is divided into four main parts, comprising 11 chapters.

Part I served as an introduction to the thesis and consisted of three chapters. Chapter 1 provided insights into the current exoplanet census, explaining the indirect detection techniques employed in both ground- and space-based telescopes. The chapter then delved deeper into the direct imaging of exoplanets, which forms the cornerstone of the research in this work. Chapter 2 revisited the fundamentals of unsupervised and supervised machine learning, with a specific emphasis on neural networks, their intricate optimization processes, and their impact on exoplanet detection. Chapter 3 concluded this introduction by expanding on the scope of the thesis, highlighting its objectives, and providing a detailed explanation of its structure.

Part II, composed of two chapters, delved into the Exoplanet Imaging Data Challenge (EIDC) and my contribution to it. Chapter 4 addressed the inaugural phase of the EIDC (Cantalloube et al., 2020), dedicated to exoplanet detection. In this phase, various ADI and ADI+mSDI data sets from HCI instruments on different ground-based telescopes were used to inject a total of 20 planetary signals with different contrast levels. Participants were tasked with using their image post-processing algorithms to detect these signals. As a participant, I submitted supervised machine learning-based image post-processing algorithms, such as SODIRF and SODINN (Gómez González et al., 2018) and I modified their training procedures and architectures in order to test and improve them in the context of the EIDC. As a team member of the EIDC, I evaluated, in parallel with another team member, all the submissions according to the evaluation rules of the challenge. Chapter 5 explained the ongoing second phase of the EIDC, focused on exoplanet characterization (Cantalloube et al., 2022). In this phase, ADI+mSDI data sets are provided, and participants are tasked with accurately determining the positions of injected companions and retrieving their injected spectra. My contribution thus

far in this second phase has been the development of the challenge's evaluation back-end code for the metrics computation. In order to exemplify an algorithm submission, results for two well-known algorithms in the characterization tasks were presented.

Part III, consisting of two chapters, was dedicated to the development of a novel local image noise approach aimed at enhancing the detection performance of supervised machine learning exoplanet detection algorithms, such as SODINN (Gómez González et al., 2018). This approach relied on the identification of two different noise regimes along the processed frame: a residual speckle-dominated regime close to the star, and a background-dominated regime further away. Chapter 6 first revisited the theory of speckle noise and explained the origin of residual noise regimes after ADI processing. Chapter 7 addressed the challenge of identifying these noise regimes through developing two statistical techniques that rely on finding the best approximation of the radial distance from the star on the image at which the transition between both noise regimes occurs. The first method was based on the evolution study of different statistical moments with the angular separation and using different PCs for producing the ADI-PCA processed frame. The second method, called PCA-pmap, was instead based on a combination of normality test that, together with different arrangements of image non-correlated pixels, it achieved a higher noise diversity to decide about the null hypothesis. Both methods were tested through VLT/SPHERE and Keck/NIRC2 ADI sequences. Results showed consistent noise regime estimates.

Part IV, composed of four chapters, was finally devoted to explore the possibility of enhancing the detection performance of SODINN by adapting its labelling, training, and inference processes to the noise regimes approach. Chapter 8 first revisited the full SODINN framework. Chapter 9 explained the adaptation of the SODINN neural network to work under the presence of image noise regimes. This adaptation was further complemented by the integration of S/N curves, enhancing the model's ability to capture new local noise statistics in conjunction with MLAR patch sequences. As a result, a novel exoplanet imaging algorithm called *Noise-Adaptive SODINN*, NA-SODINN for short, was conceived. Chapter 10 evaluated the detection performance of NA-SODINN through two distinct analyses, a first performance assessment based on ROC curves using ADI sequences from the VLT/SPHERE and Keck/NIRC2 instruments, and a second analysis based on benchmarking NA-SODINN to the first phase of the EIDC. A clear message can be extracted from both evaluations: NA-SODINN significantly improves the detection performance of its predecessor, and is ranked at the top (first or second position) of the challenge leaderboard for all considered evaluation metrics. Finally, Chapter 11 presented the results of applying NA-SODINN to a small

sample of the recent SHINE exoplanet survey (Desidera et al., 2021), where the NA-SODINN detection maps revealed few point-like sources with exceptionally high confidence levels. While this presents promising initial findings, further analyses are imperative to establish the definitive potential of these signatures as exoplanet discoveries.

Concluding this Ph.D. research, I have learned two fundamental lessons. On one hand, the pursuit of training complex neural network architectures is not always imperative to significantly improve our model's performance. Instead, understanding the intricacies of the data itself can reveal powerful, previously unseen correlations. Leveraging these new-found insights and implementing innovative strategies can be the key to integrating these correlations into the model, ultimately enhancing its performance. In HCI, this entails a profound understanding of the underlying physics governing images and the dependencies of image noise during data acquisition. Image noise, in particular, exerts the most significant influence on the exoplanet detection task. However, different tasks or types of data might necessitate a diverse emphasis on aspects relevant to their specific nature. On the other hand, while deep learning stands as a remarkable tool reshaping our interaction with technology, it falls short when it comes to providing interpretability for its outcomes. As explained, neural networks execute non-linear transformations on input data, and the intricate interplay of numerous parameters and layers complicates our comprehension of how the model arrives at a specific output. Furthermore, neural networks learn high-dimensional feature representations of data, which are not readily interpretable since they might not correspond to easily discernible features or patterns. Although deep learning models offer accurate predictions, they lack the inherent capacity to explain the rationale behind a particular prediction. This limitation can pose challenges in applications where understanding the decision-making process is essential. In my opinion, these aforementioned challenges regarding the lack of interpretability underscore the need for further research in the field of deep learning, and they also emphasize the importance of continued exploration and understanding of data itself, particularly in the field of exoplanet direct imaging.

13

PERSPECTIVES

The NA-SODINN algorithm, introduced in this thesis, represents a significant step forward in the search for new and unconfirmed exoplanets and brown dwarfs in HCI data sets. Its ability to accurately identify point-like sources across all angular separations in ADI sequences outperforms the algorithms currently used in major surveys, as well as the majority of cutting-edge post-processing techniques. As a result, NA-SODINN is expected to be particularly well-suited for improving our understanding of the demographics of directly imaged exoplanets (Fig. 1.1).

In the near to mid-term future, our focus is directed towards reanalyzing ground-based HCI surveys in the search of potential candidates. As showcased in Chapter 11, we will first focus on the complete sample of the SHINE survey. However, other surveys like GPI-GPIES (Nielsen et al., 2019) or LEECHS (Stone et al., 2018) will be also considered for study. The emergence of upcoming $20 - 40$m ground-based telescopes (currently under construction), such as the ELT, coupled with dedicated HCI instruments like METIS (Brandl et al., 2021), holds the promise of groundbreaking observational capabilities. NA-SODINN has the potential of pushing the detection limits of such powerful instruments and thus of helping detect fainter exoplanets in their images.

Looking towards the long-term, the adaptability of NA-SODINN for processing data from space-based telescopes, such as the James Webb Space Telescope (JWST) and the planned Roman Space Telescope, is a promising avenue. Within the realm of HCI, the ultimate goal of these observatories is the direct imaging of Earth-like planets orbiting Sun-like stars, aiming to detect bio-signatures and explore planetary habitability. This ambitious objective demands achieving contrast levels of approximately 10^{-10} within the visible range, enabling the detection of cooler and older exoplanets through their reflected light. NASA is resolutely committed to achieving these detection limits, pioneering the use of HCI technology in space through JWST and, particularly, Roman, which will serve as a demonstrator for future space missions about exoplanet direct imaging, such as the Habitable Worlds Observatory (HWO, formerly known as LUVOIR-B/LuvEx) flagship mission. However, adapting the

NA-SODINN framework in this context comes with its challenges, particularly concerning the impact of low photon count rates on machine learning performance. For instance, Roman will use an Electron Multiplying Charge Coupled Device (EMCCD, Morrissey et al., 2023) detector optimized for low photon counting rates, providing only $1 - 10$ photons/pixel/minute. Consequently, the final Roman sequence may consist of approximately $10 - 100$ frames, significantly fewer than ground-based sequences. Operating in such conditions introduces uncertainty regarding the performance of machine learning models, given the shift into a distinct operational regime. Nonetheless, neural networks exhibit adaptability to varying conditions and complex scenarios. Hence, a concerted effort is imperative to design optimal training strategies that maximize exoplanet imaging performance in this low photon regime.

Part VI

APPENDIX

<div style="text-align: right; font-size: 4em;">A</div>

DETECTION MAPS FOR ADI SUBCHALLENGE

In this appendix, we display the detection maps of the 22 submissions for the nine data sets of the **EIDC subchallenge-**1 **(ADI)**. Each detection map is shown with a color-bar ranging from 0 to the submitted threshold by the participant. The yellow circles indicate true positives at the given threshold, while red squares indicate false positives. The first image (top left) shows the detection map for the chosen baseline algorithm (annular PCA). The last image (bottom right) shows the mask used to conduct the analysis of each map, with blue circles indicating the location of the injected synthetic planetary signals.
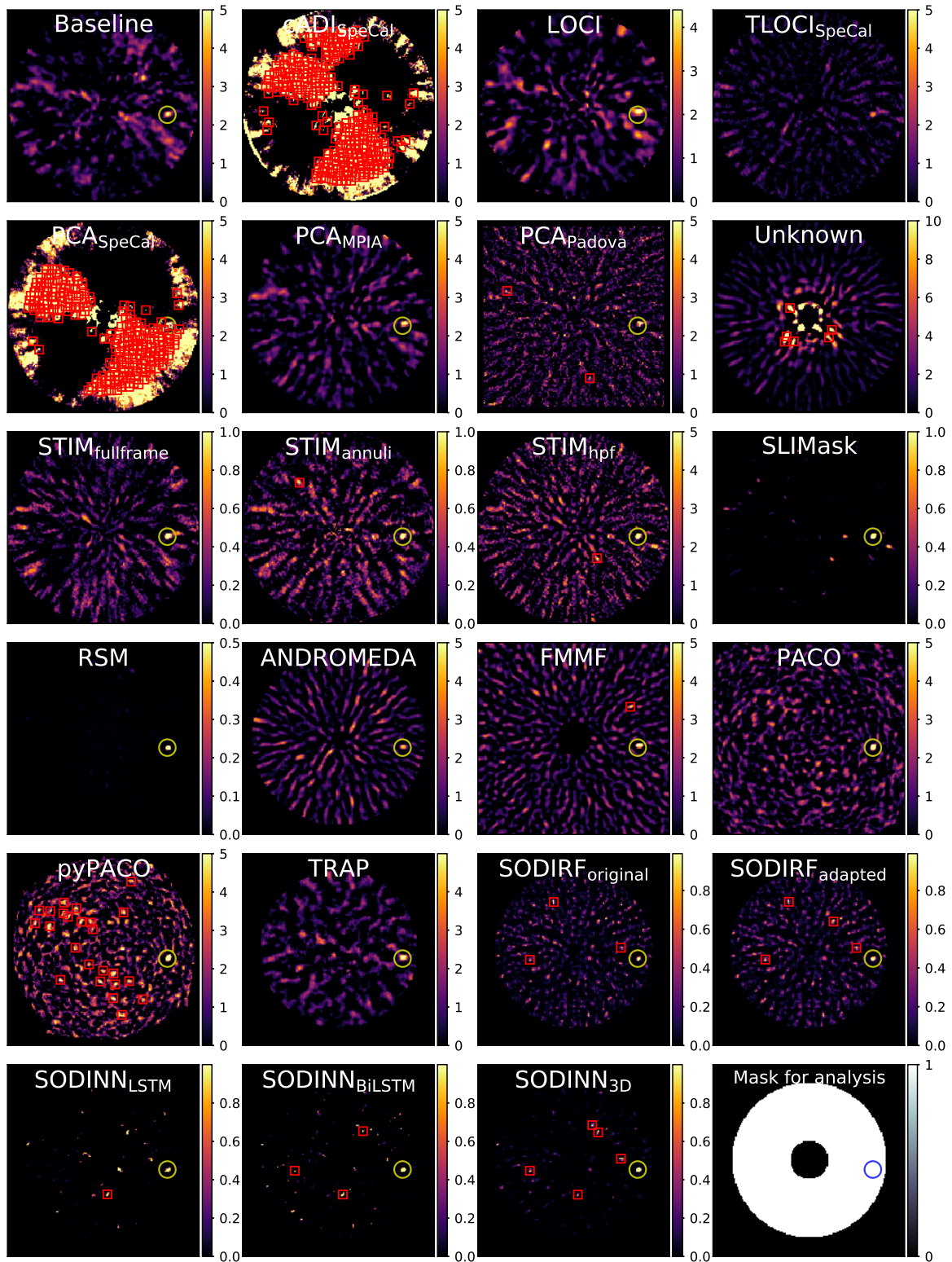
Figure A.1: Detection maps for the *sph1* data set. Figure from Cantalloube et al. (2020).
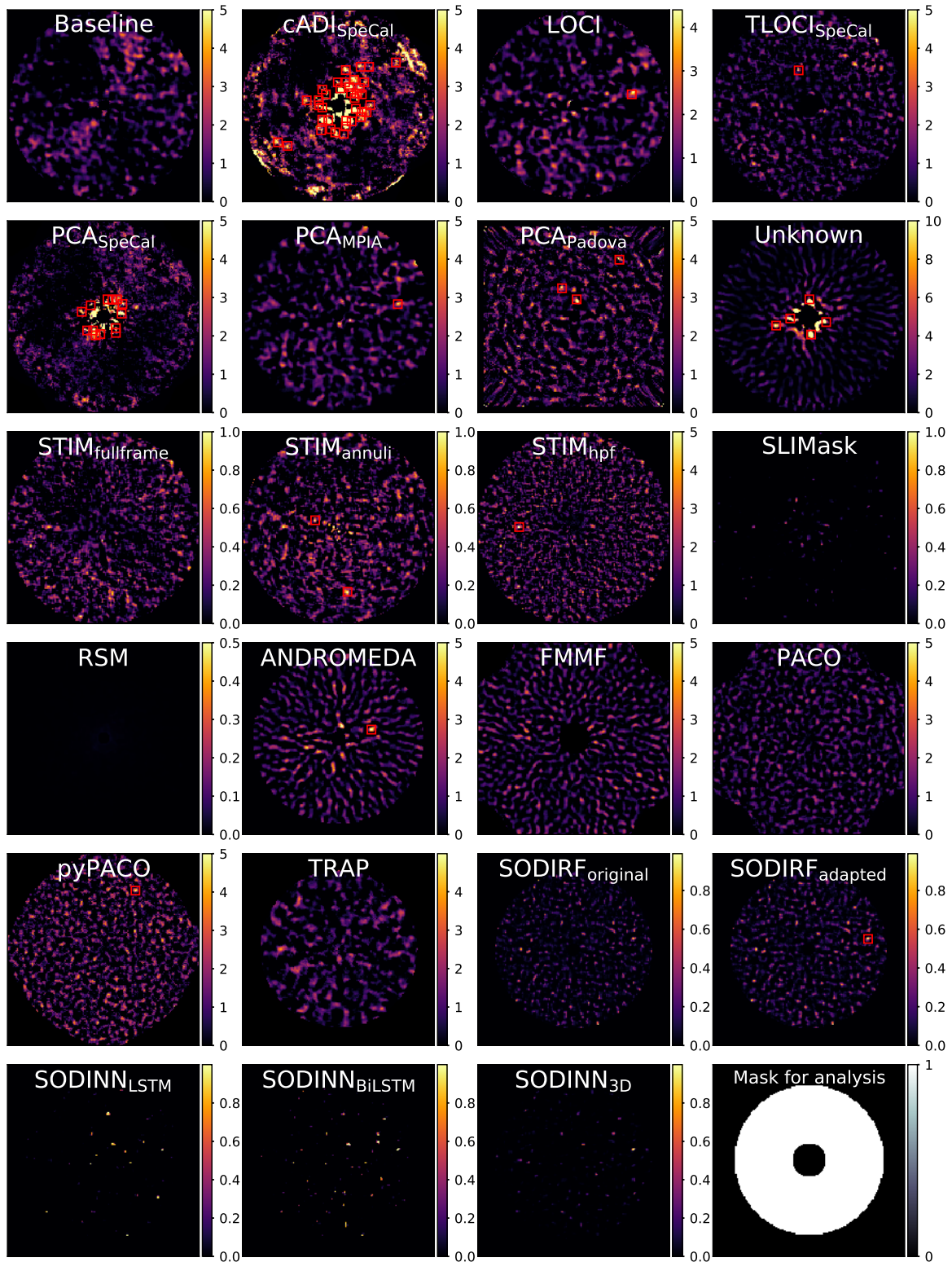
Figure A.2: Detection maps for the *sph2* data set. Figure from Cantalloube et al. (2020).
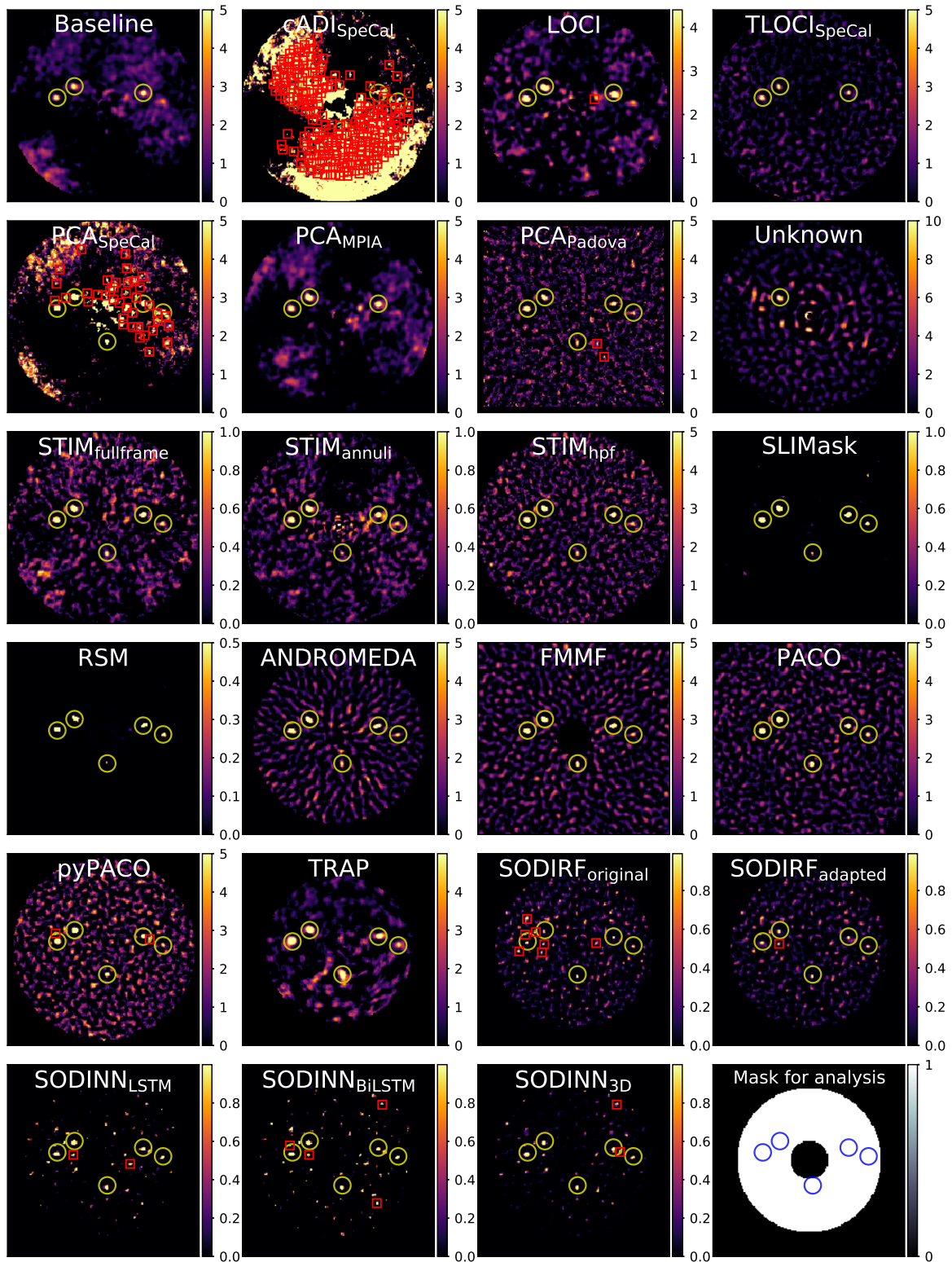
Figure A.3: Detection maps for the *sph3* data set. Figure from Cantalloube et al. (2020).
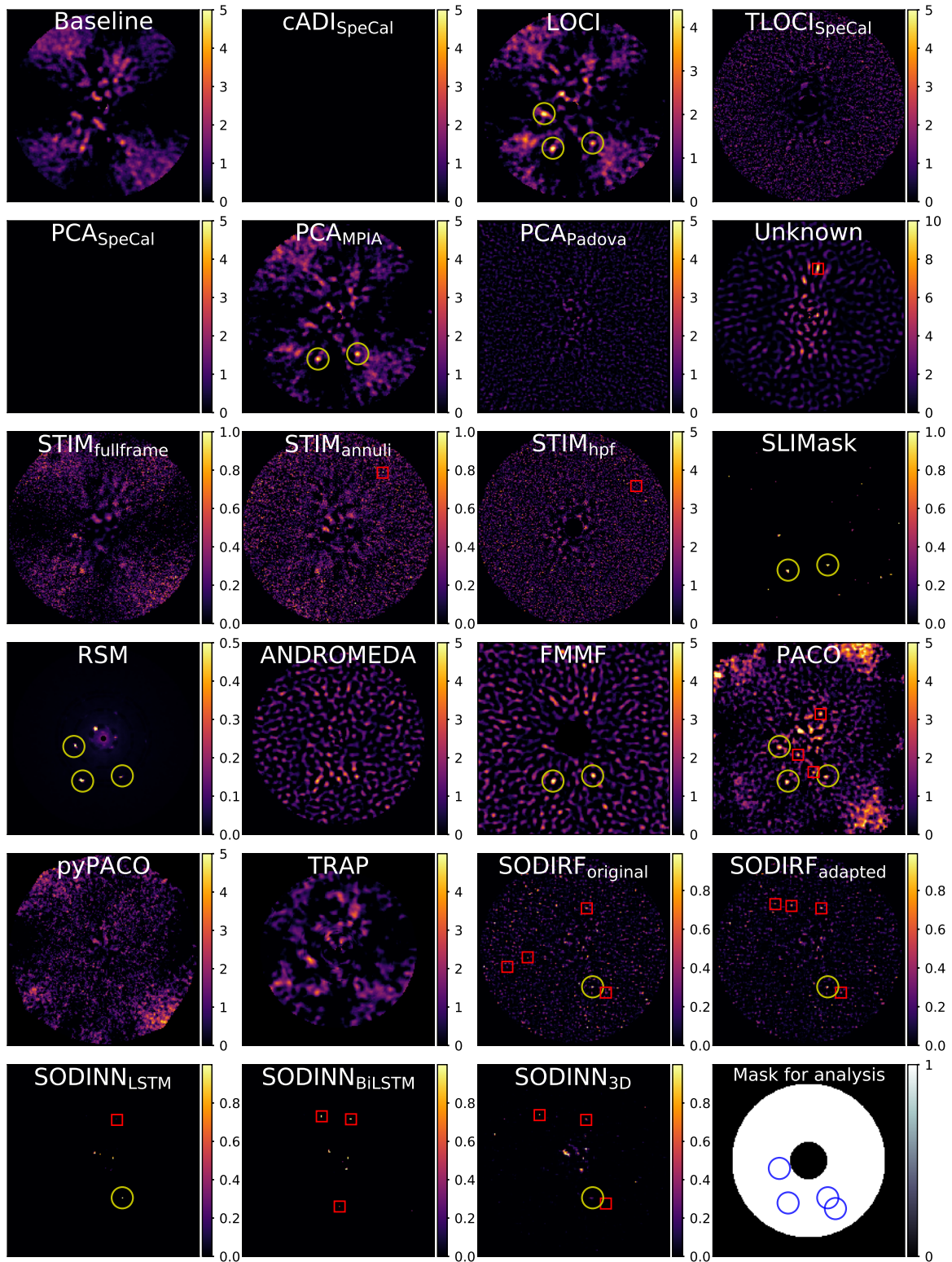
Figure A.4: Detection maps for the *nrc1* data set. Figure from Cantalloube et al. (2020).
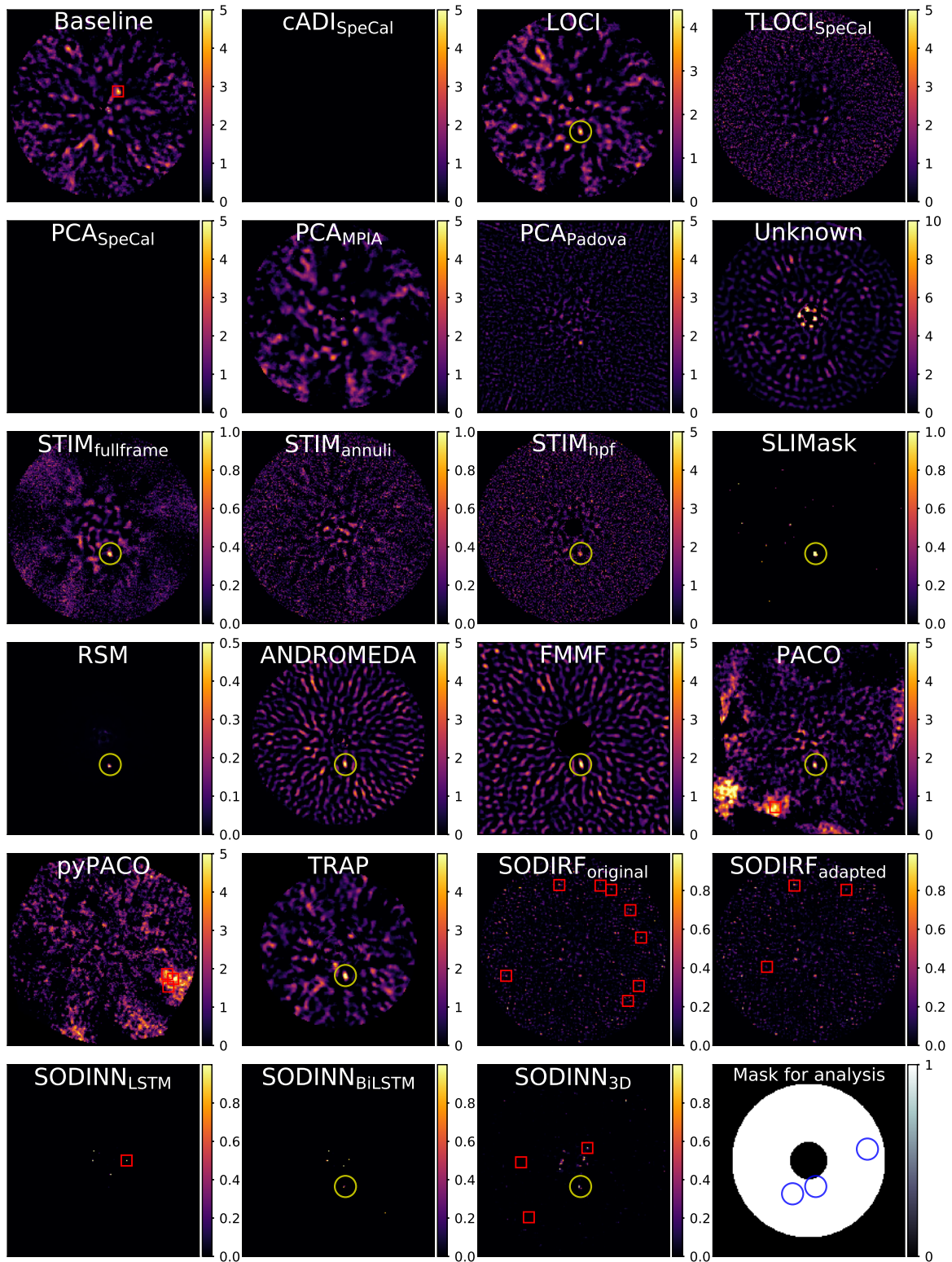
Figure A.5: Detection maps for the *nrc2* data set. Figure from Cantalloube et al. (2020).
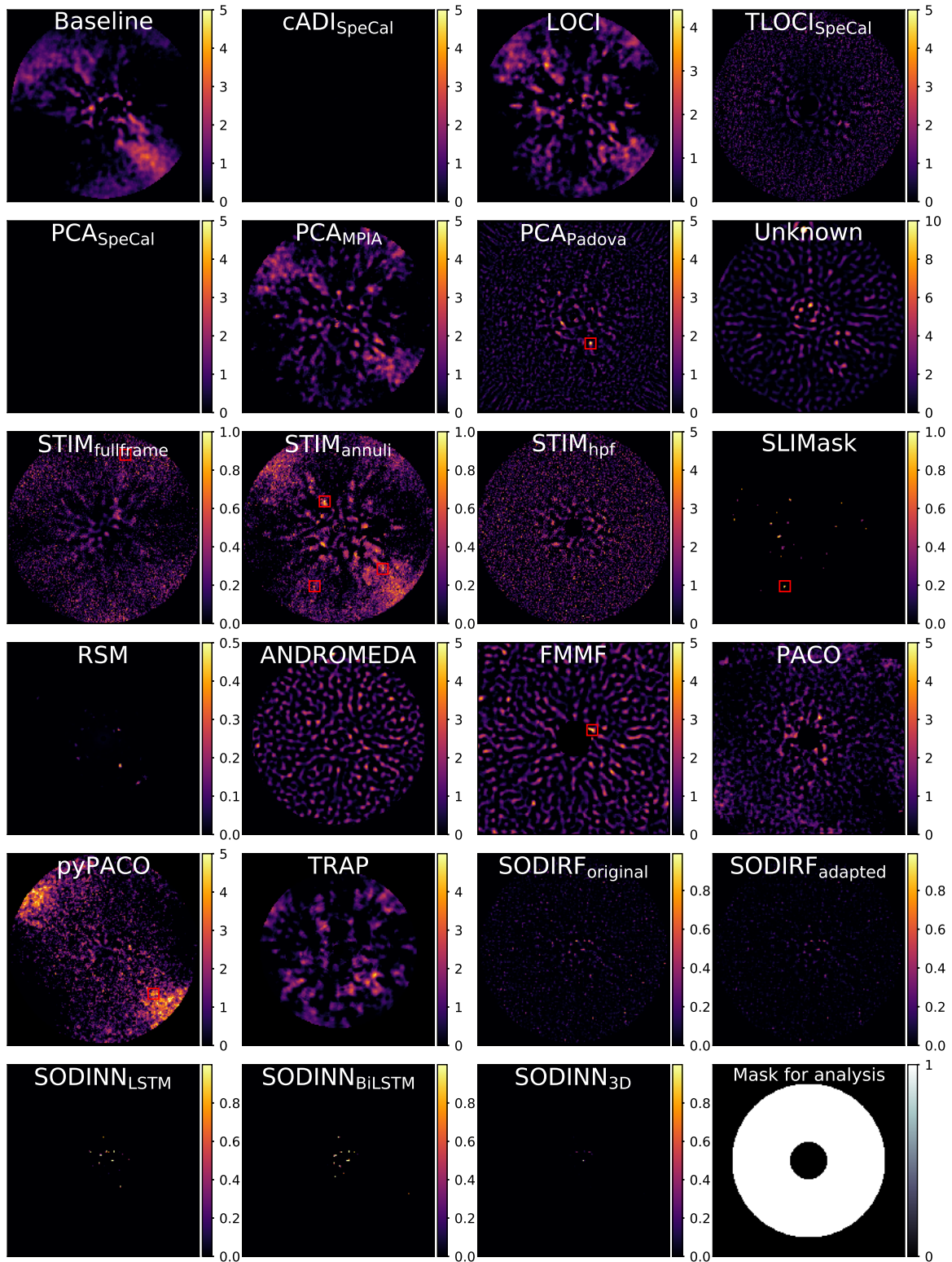
Figure A.6: Detection maps for the *nrc3* data set. Figure from Cantalloube et al. (2020).
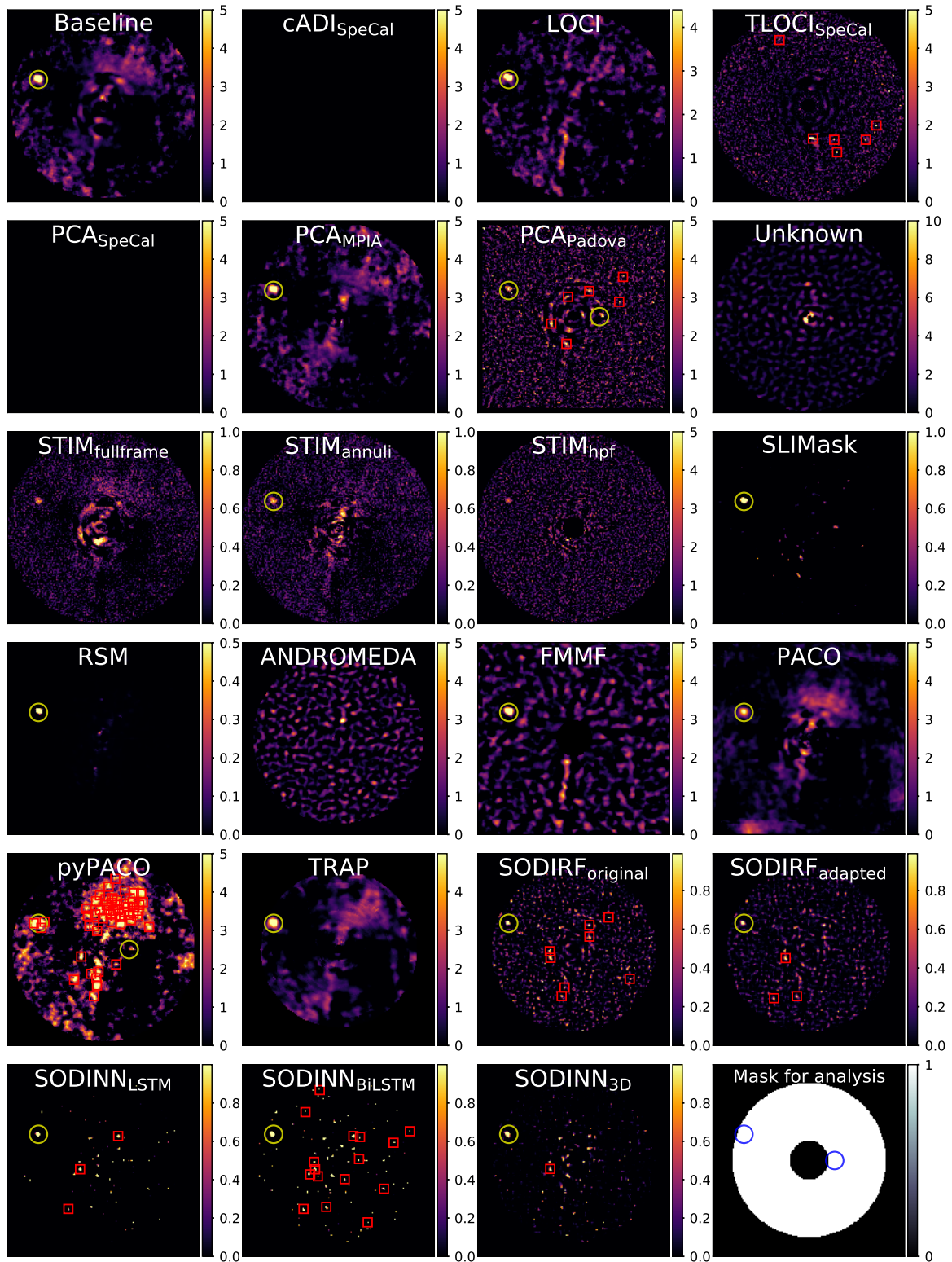
Figure A.7: Detection maps for the *lmr1* data set. Figure from Cantalloube et al. (2020).
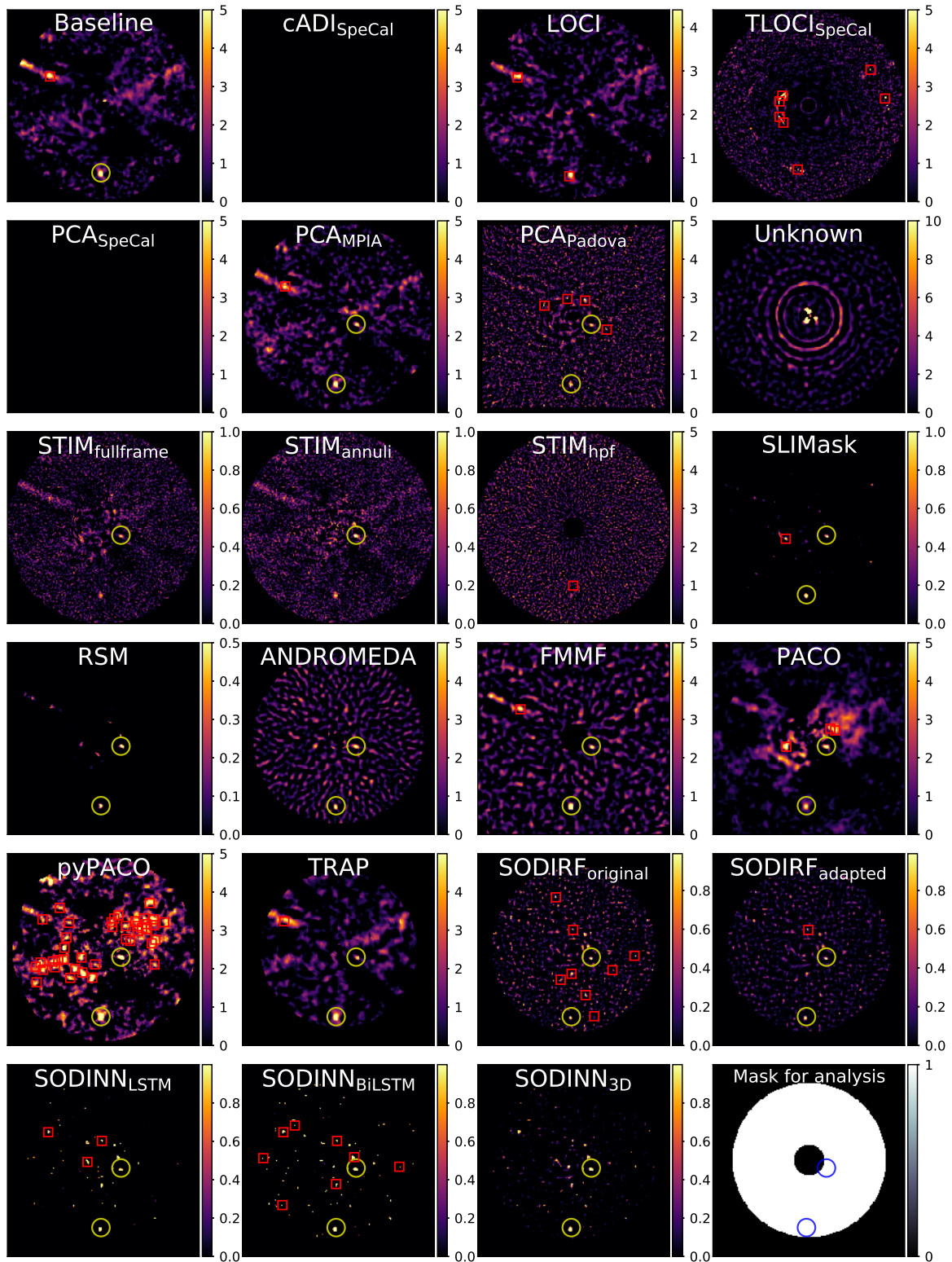
Figure A.8: Detection maps for the *lmr2* data set. Figure from Cantalloube et al. (2020).
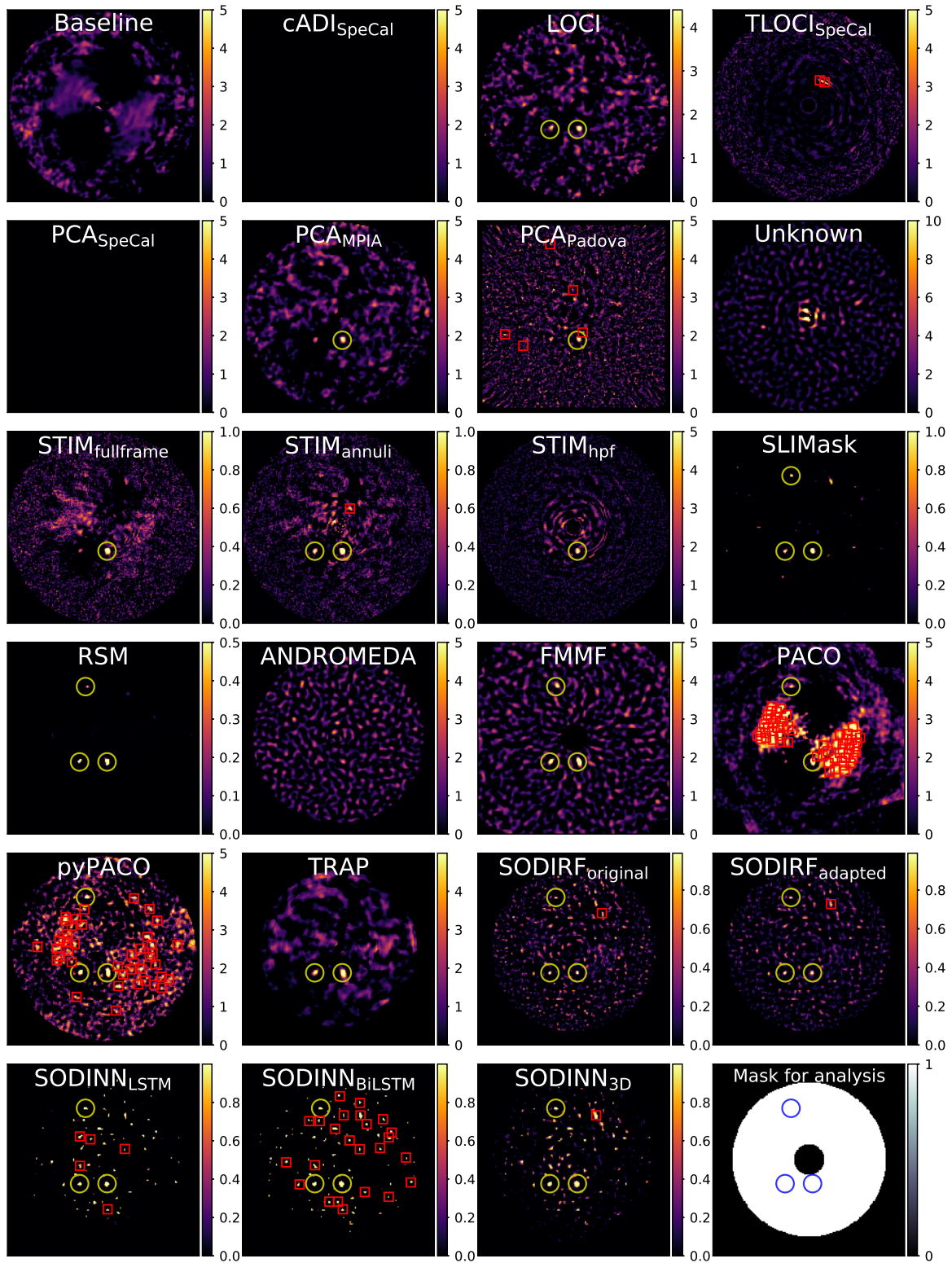
Figure A.9: Detection maps for the *lmr3* data set. Figure from Cantalloube et al. (2020).

B

DETECTION MAPS FOR ADI+MSDI SUBCHALLENGE

In this appendix, we display the detection maps of the 6 submissions for the ten data sets of the **EIDC subchallenge-**2 **(ADI+mSDI)**. Each detection map is shown with a color-bar ranging from 0 to the submitted threshold by the participant. The yellow circles indicate true positives at the given threshold, while red squares indicate false positives. The first image (top left) shows the detection map for the chosen baseline algorithm (annular PCA). The last image (bottom right) shows the mask used to conduct the analysis of each map, with blue circles indicating the location of the injected synthetic planetary signals.
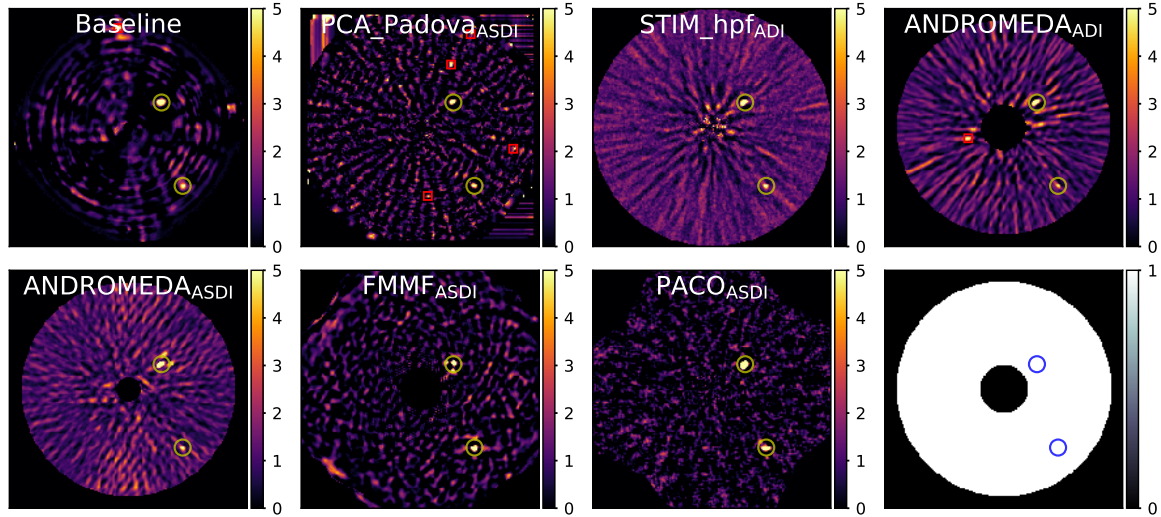
Figure B.1: Detection maps for the *ifs1* data set. Figure from Cantalloube et al. (2020).
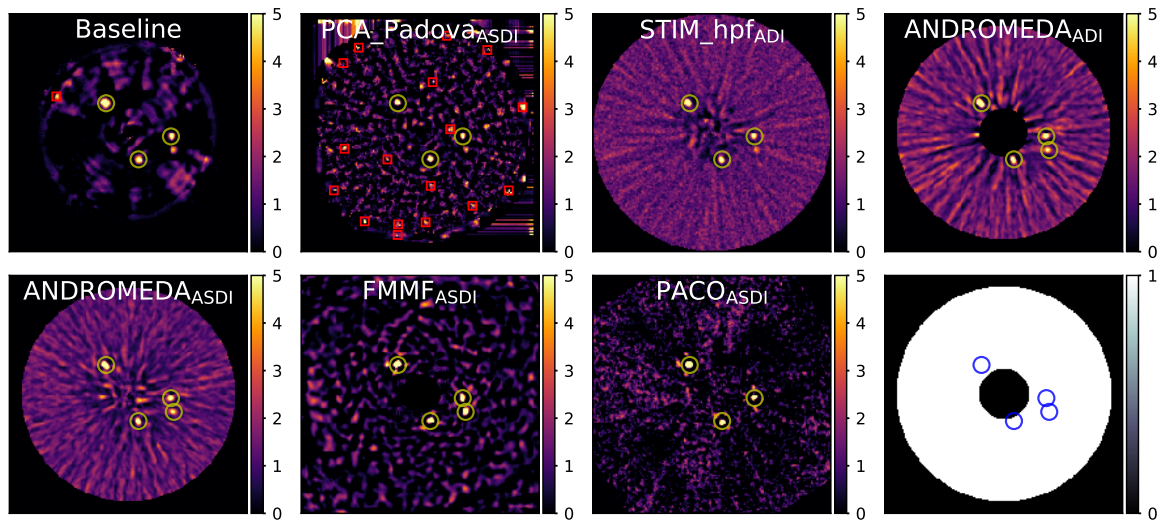
Figure B.2: Detection maps for the *ifs2* data set. Figure from Cantalloube et al. (2020).
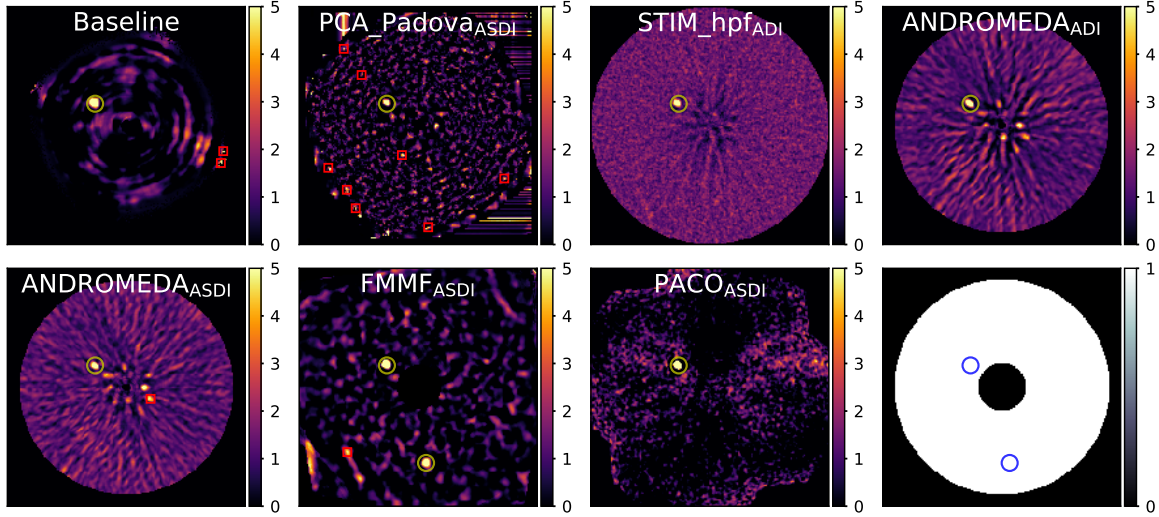
Figure B.3: Detection maps for the *ifs3* data set. Figure from Cantalloube et al. (2020).
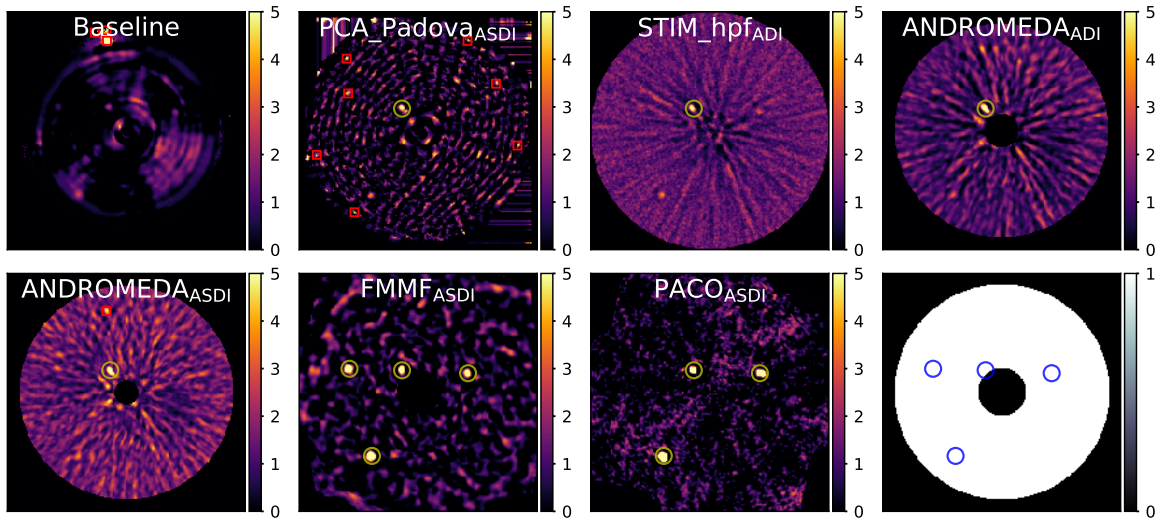
Figure B.4: Detection maps for the *ifs4* data set. Figure from Cantalloube et al. (2020).
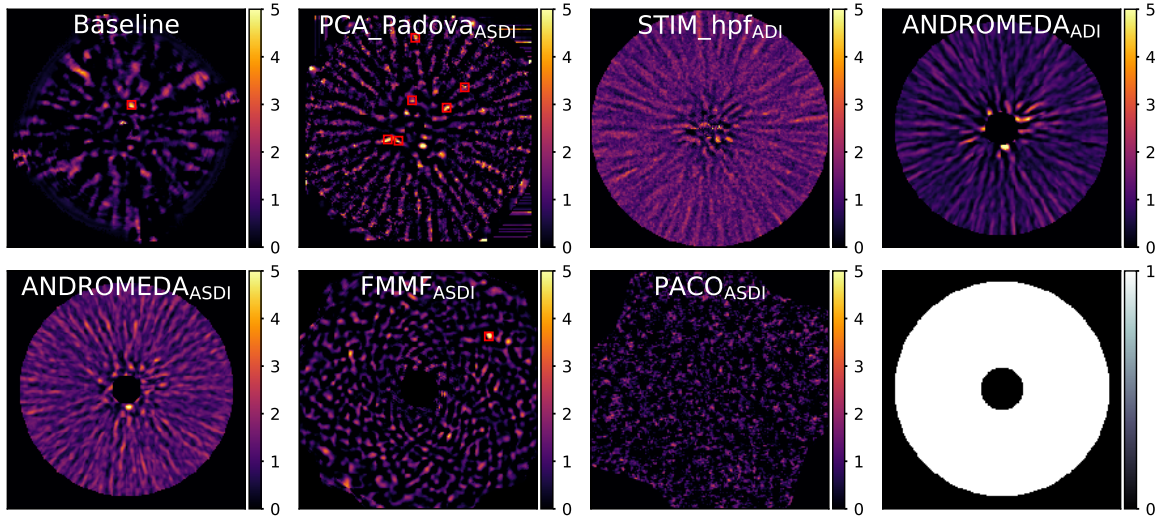
Figure B.5: Detection maps for the *ifs5* data set. Figure from Cantalloube et al. (2020).
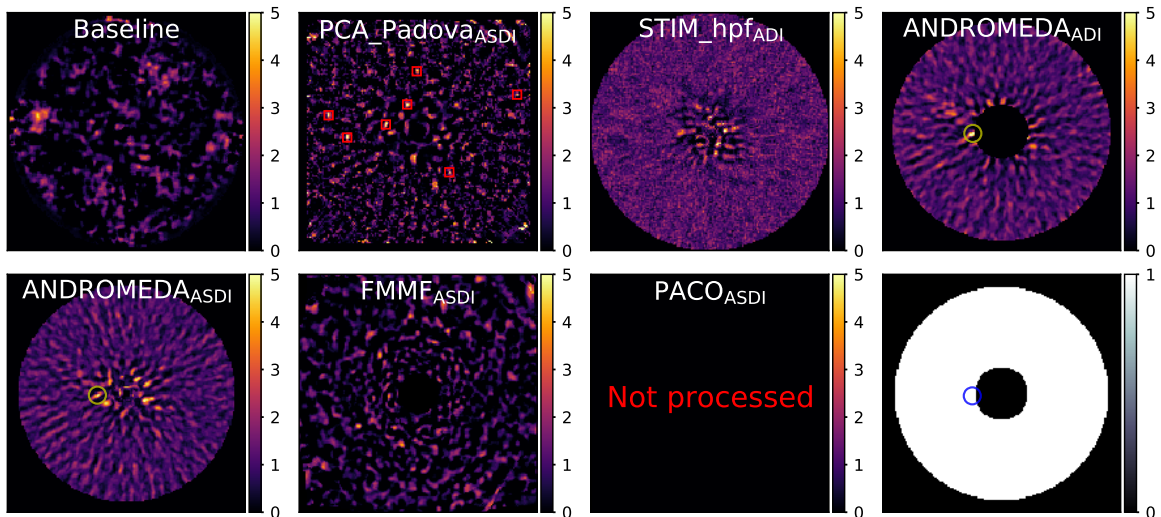
Figure B.6: Detection maps for the *gpi1* data set. Figure from Cantalloube et al. (2020).
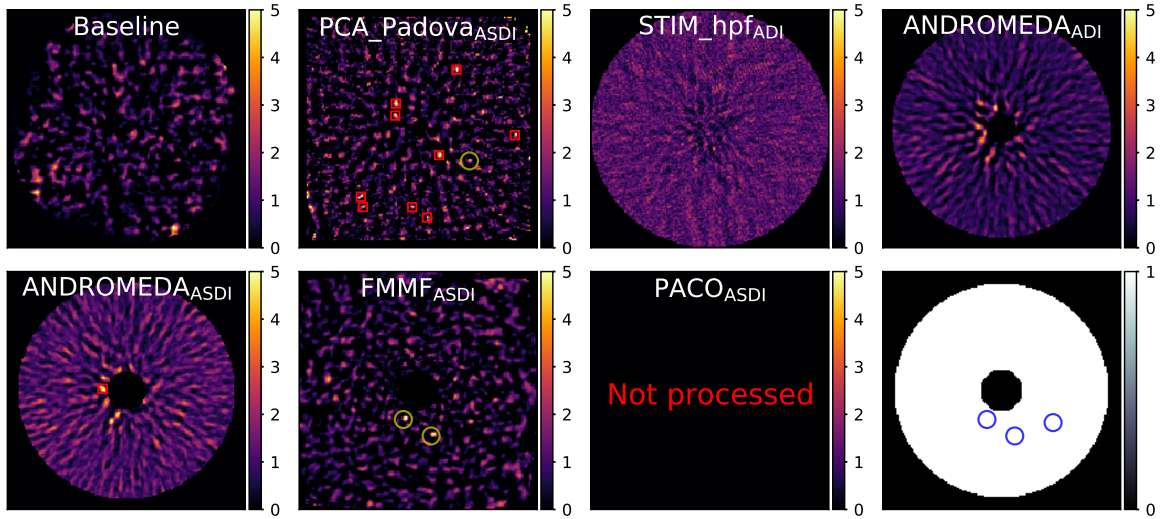
Figure B.7: Detection maps for the *gpi2* data set. Figure from Cantalloube et al. (2020).
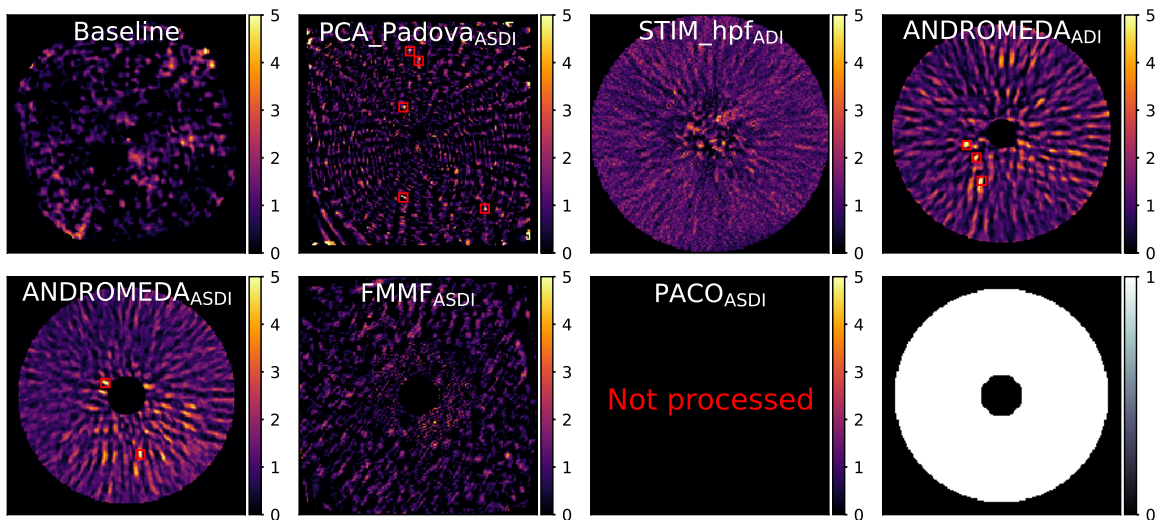
Figure B.8: Detection maps for the *gpi3* data set. Figure from Cantalloube et al. (2020).
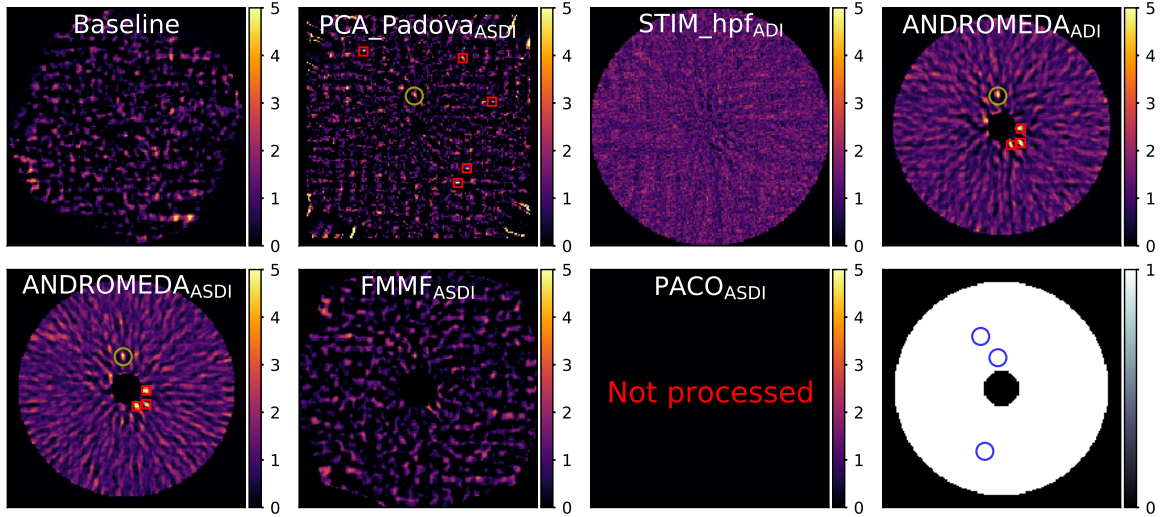
Figure B.9: Detection maps for the *gpi4* data set. Figure from Cantalloube et al. (2020).
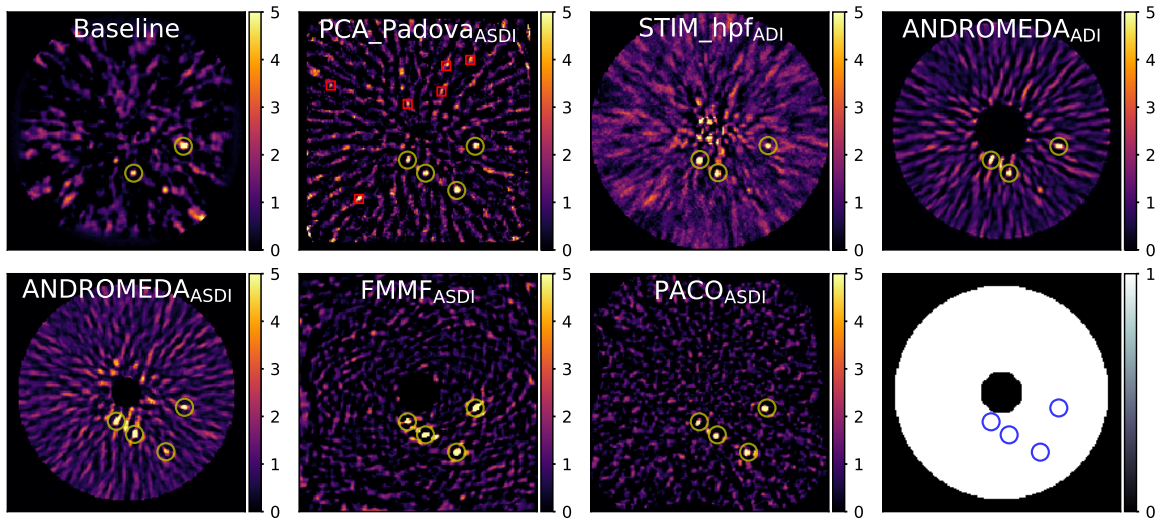
Figure B.10: Detection maps for the *gpi5* data set. Figure from Cantalloube et al. (2020).

C

PLANETARY INJECTION AND FLUX ESTIMATION

In this appendix, we describe the concept of planetary injection in HCI and its current limitations, as implemented in the open-source `VIP` package (Gómez González et al., 2017). In addition, we explain the methodology used in this dissertation to estimate injection flux according to a given S/N value. This flux estimation is performed multiple times along the presented work.

C.1 PLANETARY INJECTION

Given a HCI data set, i.e. an ADI sequence, a synthetic planetary injection is defined as the process to past the AO-corrected instrumental PSF (centered, cropped and normalized) to every frame in the image sequence at specific coordinates (r, θ) following field rotation. To control the flux of this injection, the standard procedure is to multiply the normalized PSF by a flux scale factor, denoted as α.

C.1.1 *Injection limitations*

This injection procedure has some limitations:

- The flux of each exoplanet injection is constant throughout the observing sequence (same flux for each frame).

- The center of the image (position of the host star) is fixed when injecting the signals, that is to say potential mis-centering of the star throughout the sequence is not taken into account.

- We do not consider the azimuthal smearing of the signal that could appear for long exposure times and/or at large angular separation from the star.

C.2 FLUX ESTIMATION FOR A GIVEN S/N RANGE

A common metric to assess exoplanet detection is the Signal-to-Noise ratio (S/N, Mawet et al., 2014). Unlike the planetary flux, a S/N measurement

sets a qualitative reference between the planetary signal and the noise at its position within the annuli in the field of view. Estimating an injection flux range that corresponds to a given S/N range in the post-processed frame implies estimating its respective flux scale factor range $\alpha_R = [\alpha_{min}, \alpha_{max}]$. Given a desired S/N range and an angular separation, α_{min} and α_{max} are estimated through the following data-driven procedure:

1. inject a companion in the raw image sequence at random coordinates (r, θ) within the annuli and with a random scale factor α;

2. compute the ADI-PCA processed frame for this synthetic image sequence using one single principal component in the PCA approximation of the speckle field;

3. apply Eq. 20 on the processed frame at the injection coordinates (r, θ), retrieving the companion S/N value;

4. Repeat $1-3$ steps N_{inj} times.

5. plot all S/N values retrieved from all N_{inj} injections of step 4 as a function of their corresponding scale factor;

6. linearly fit the data plotted in step 5, and define α_{min} and α_{max} as the intersection between the linear fit and the corresponding S/N range boundaries.

This process is repeated for each angular separation in the field of view in such a way that a different flux scale factor range α_R is estimated for each annulus. Fig. C.1 illustrates this data-driven procedure for the case of the *sph2* data set, showing the plots of step 5 for different annuli, each with $N_{inj} = 3000$ injections (step 4). From Fig. C.1, we observe a general trend: the estimated scale factor range decreases as the angular distance increases. This observation aligns with our expectations, given that the spatial component of speckle noise intensity displays a radial dependency in the raw HCI data, a characteristic that persists even after the ADI processing. However, for this *sph2* data set, a notable departure from this trend occurs between 15-16 λ/D separations. In this specific interval, we observe in Fig. C.1 an anomalous increase in the estimated scale factors instead. We associate this behavior with the fact that, at these angular separations for *sph2*, speckle dominates over background noise, as concluded in Chapter 7.
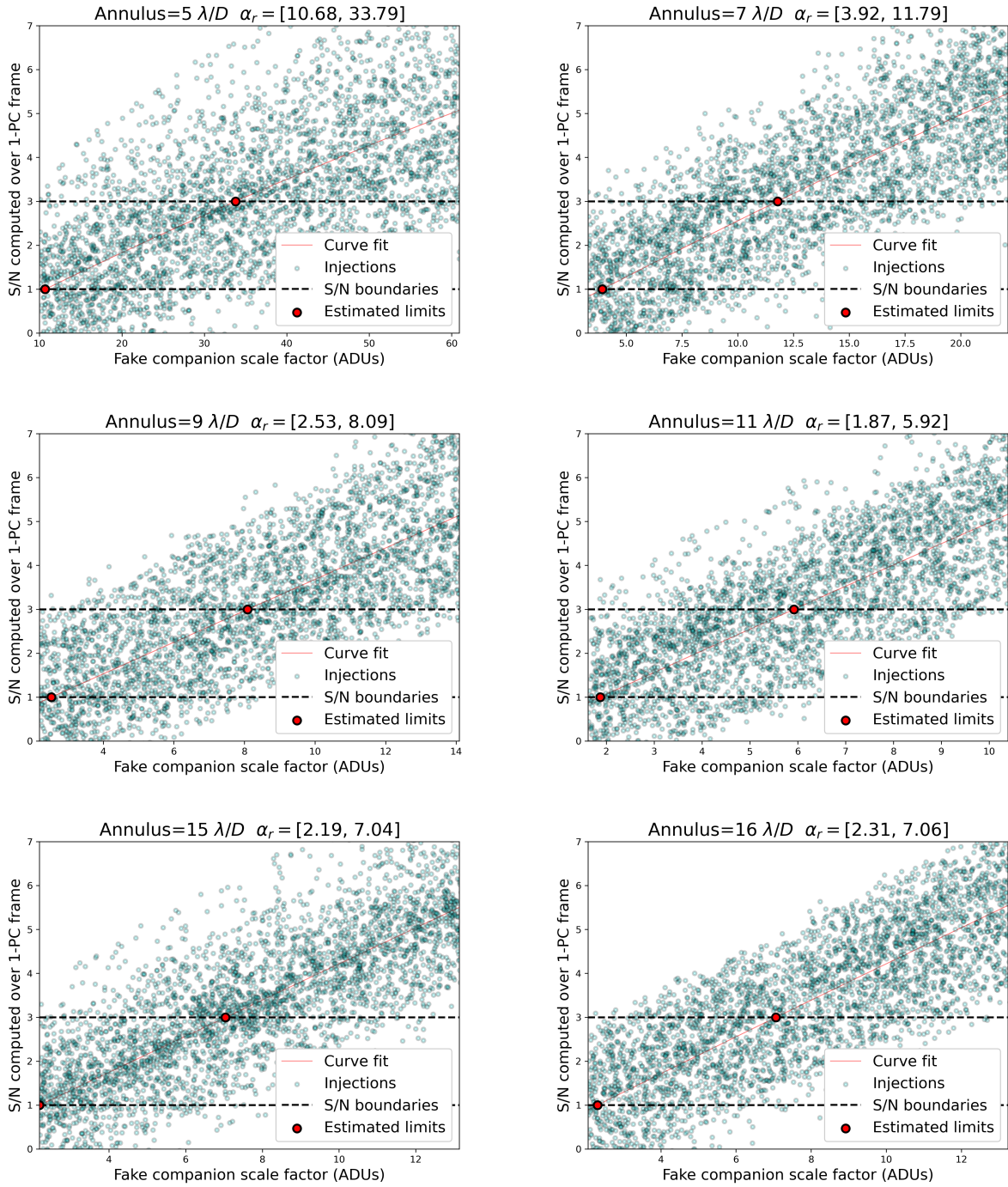
Figure C.1: Example of the data-driven flux estimation method for the case of the *sph2* sequence for $S/N_R = [1, 3]$. Each subplot refers to a different angular distance, and shows the S/N of injections (y axis), retrieved from the ADI-PCA processed frame ($PC = 1$), as a function of their scale factor (x axis). Each point in cyan color represents an injection, the thin red line is the curve fit, and dashed horizontal curves in black delimit the S/N_R. The two red dots show the intersection between the curve fit and the S/N range, delimiting the corresponding range of scale factors.

D

PERFORMANCE ASSESSMENT DETECTION MAPS

In this final appendix, we show a comparison example between the detection maps of NA-SODINN, SODINN, hybrid models, and annular PCA for each noise regime of *sph2* and *nrc3* data sets.
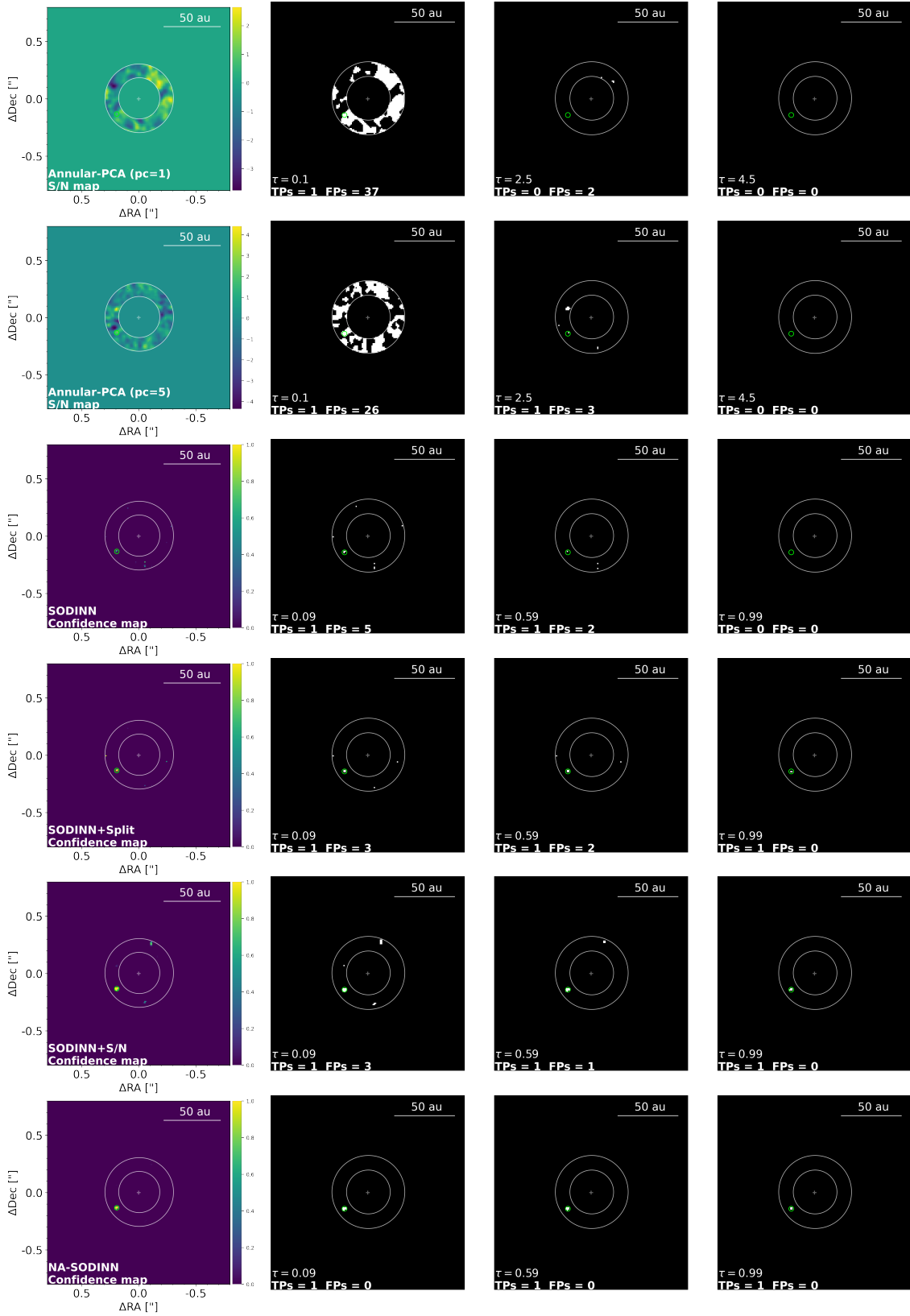
Figure D.1: Performance assessment example used for the ROC analysis of Fig.10.1 top-left (5 − 7 λ/D regime of *sph2*). The injection has S/N=0.75.
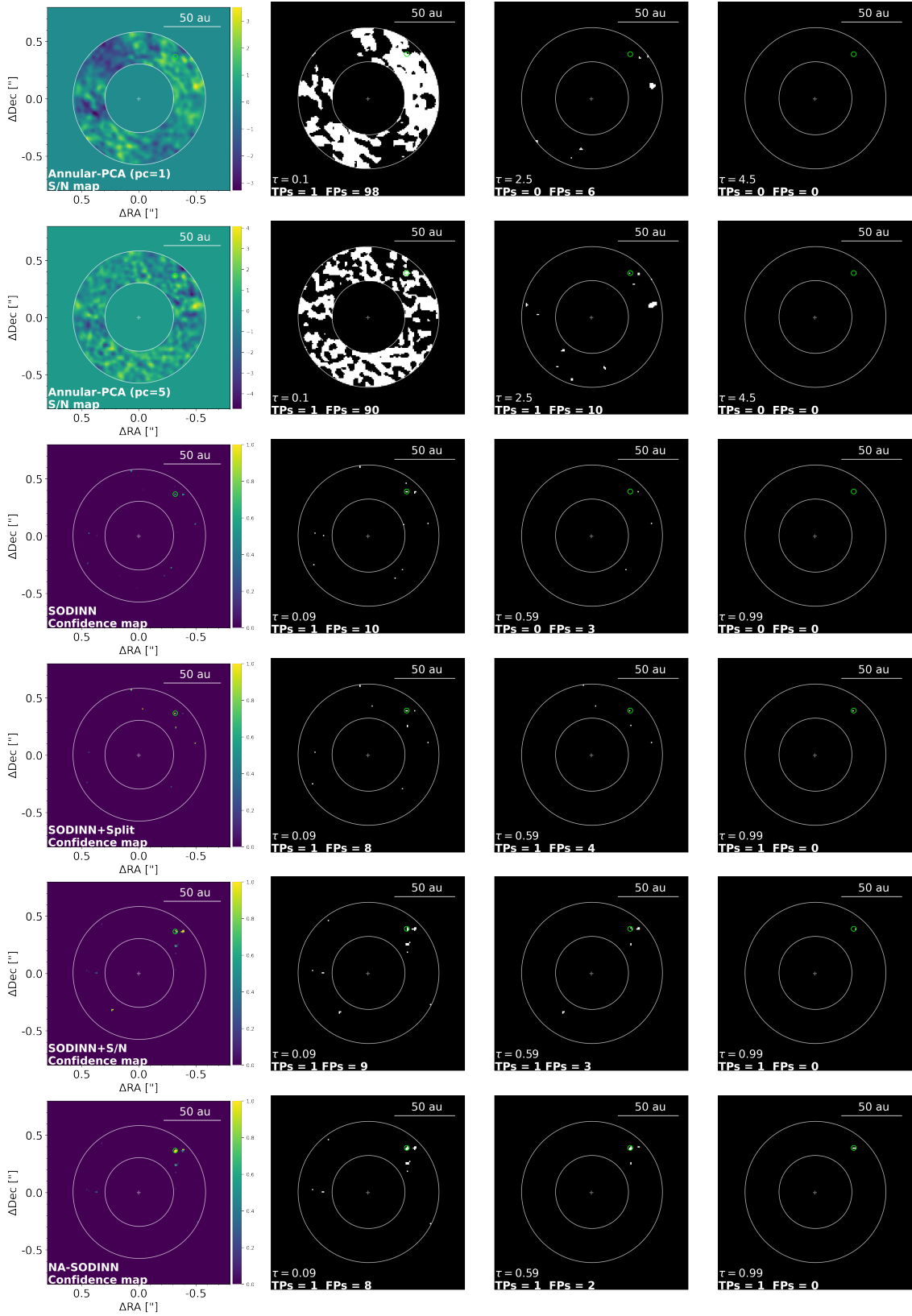
Figure D.2: Performance assessment example used for the ROC analysis of Fig.10.1 top-right ($8 - 14 \, \lambda/D$ regime of *sph2*). The injection has S/N=0.89.
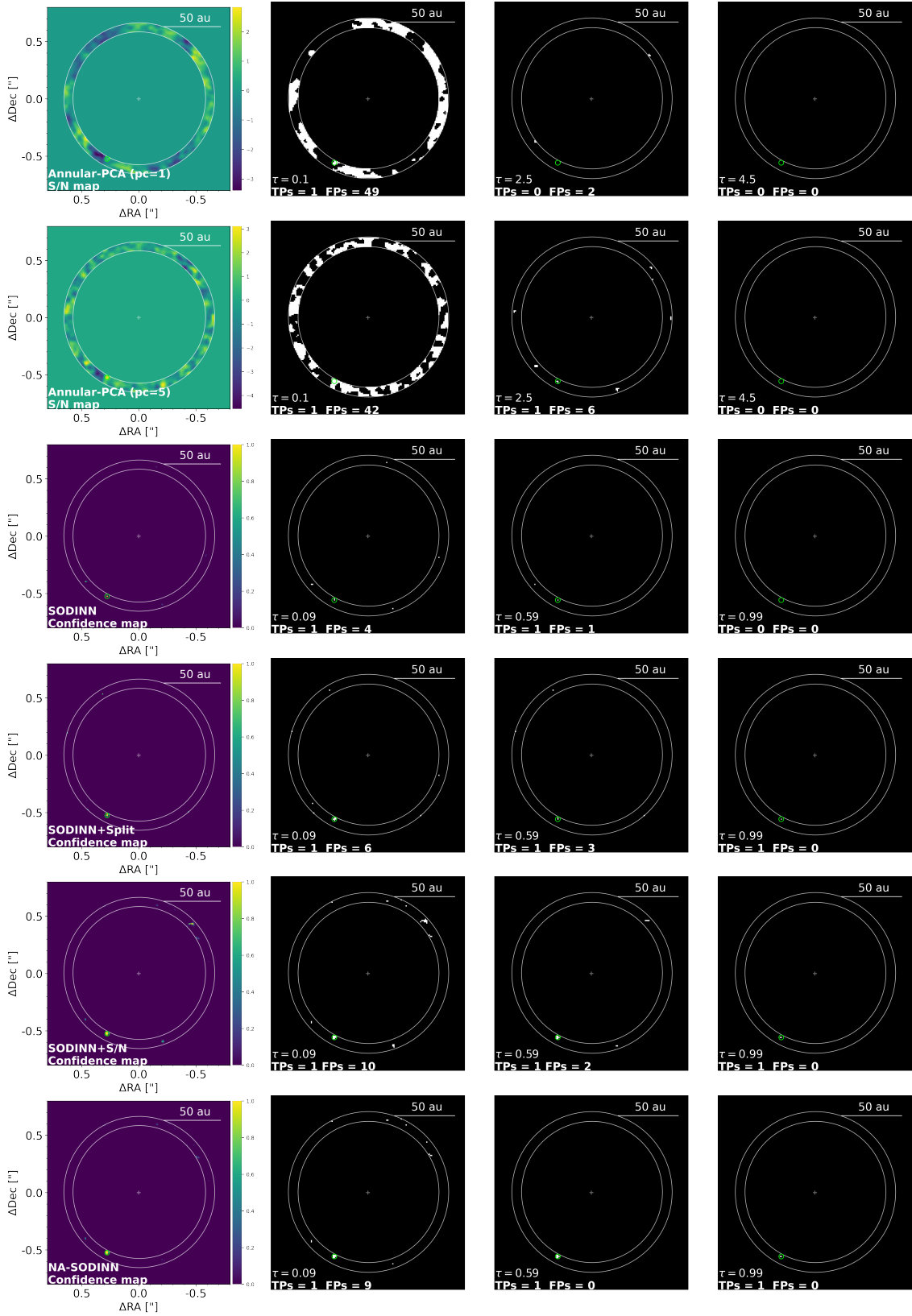
Figure D.3: Performance assessment example used for the ROC analysis of Fig.10.1 bottom ($15 - 16 \, \lambda/D$ regime of *sph2*). The injection has S/N=0.78.
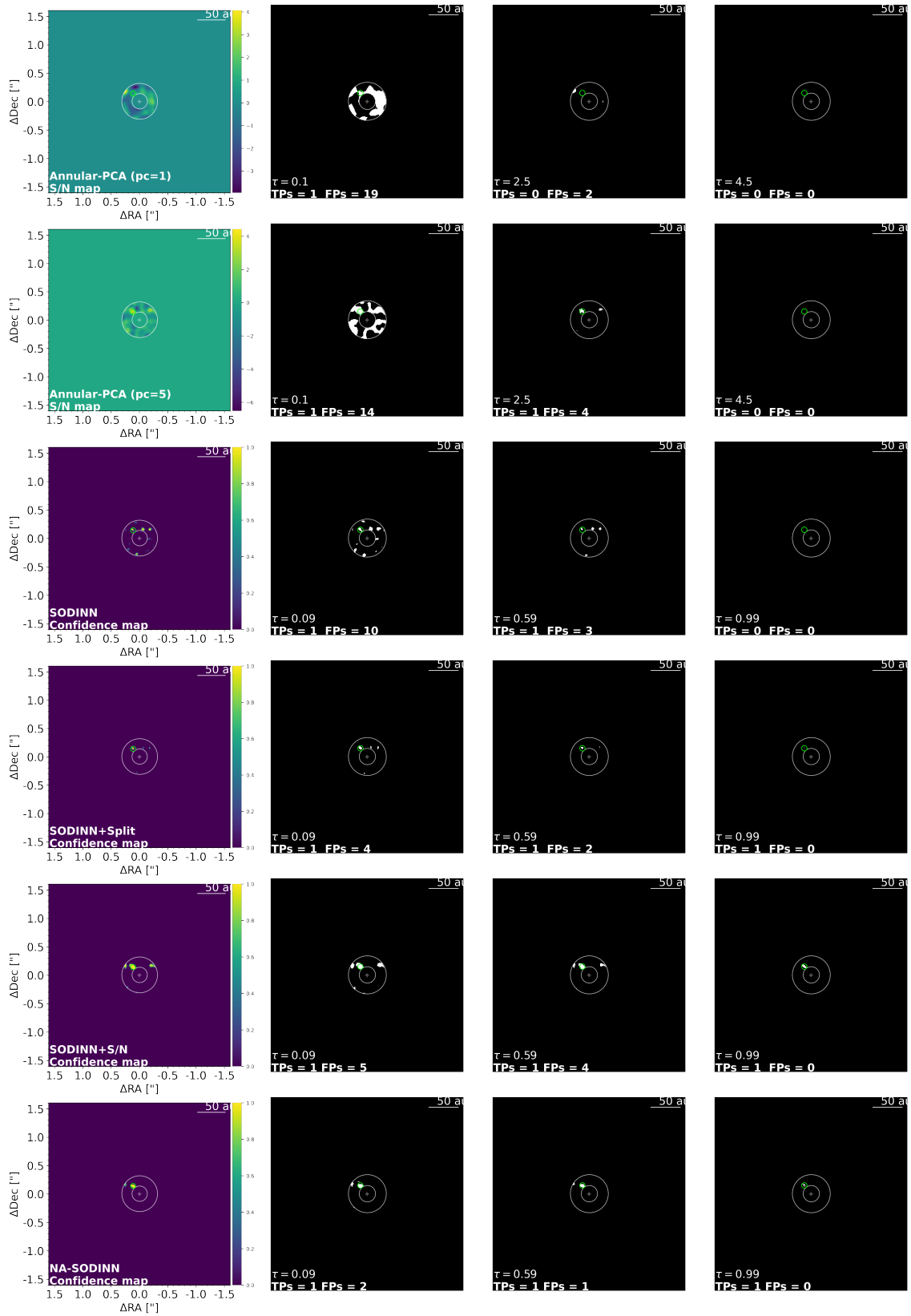
Figure D.4: Performance assessment example used for the ROC analysis of Fig.10.2-left ($2-3$ λ/D regime of *nrc3*). The injection has S/N=0.78.
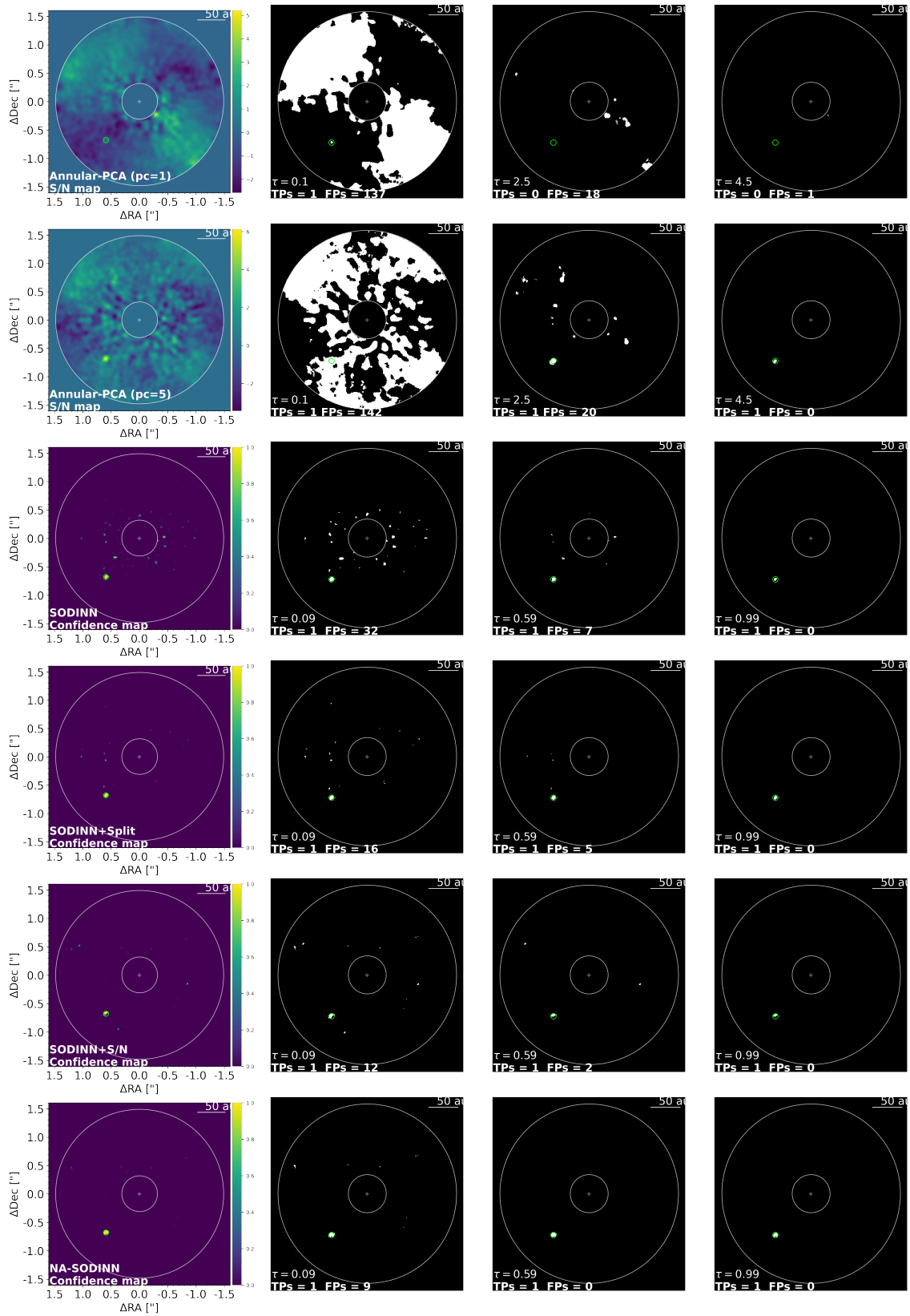
Figure D.5: Performance assessment example used for the ROC analysis of Fig.10.2-right ($4-16\ \lambda/D$ regime of *nrc3*). The injection has S/N=0.84.

BIBLIOGRAPHY

Abiodun, O. I., Jantan, A., Omolara, A. E., et al. 2019, IEEE Access, 7, doi: 10.1109/ACCESS.2019.2945545

Absil, O., Milli, J., Mawet, D., et al. 2013, Astronomy & Astrophysics, 559, doi: 10.1051/0004-6361/201322748

Ahmad, F., & Khan, R. A. 2015, Pakistan Journal of Statistics and Operation Research, 11, doi: 10.18187/pjsor.v11i3.845

Aimé, C., & Soummer, R. 2004, The Astrophysical Journal, 612, doi: 10.1086/424381

Amara, A., & Quanz, S. P. 2012, Monthly Notices of the Royal Astronomical Society, 427, doi: 10.1111/j.1365-2966.2012.21918.x

Anderson, T. W., & Darling, D. A. 1952, The Annals of Mathematical Statistics, 23, doi: 10.1214/aoms/1177729437

Ansdell, M., Ioannou, Y., Osborn, H. P., et al. 2018, The Astrophysical Journal Letters, 869, doi: 10.3847/2041-8213/aaf23b

Babcock, H. W. 1953, Publications of the Astronomical Society of the Pacific, 65, doi: 10.1086/126606

Bacon, R., Accardo, M., Adjali, L., et al. 2010, in SPIE Proceedings, Vol. 7735, doi: 10.1117/12.856027

Baqui, P. O., Marra, V., Casarini, L., et al. 2021, Astronomy & Astrophysics, 645, doi: 10.1051/0004-6361/202038986

Beuzit, J.-L., Vigan, A., Mouillet, D., et al. 2019, Astronomy & Astrophysics, 631, doi: 10.1051/0004-6361/201935251

Bond, I. A., Udalski, A., Jaroszyński, M., et al. 2004, The Astrophysical Journal, 606, doi: 10.1086/420928

Bonse, M. J., Garvin, E. O., Gebhard, T. D., et al. 2023, The Astronomical Journal, 166, doi: 10.3847/1538-3881/acc93c

Borucki, W. J., Koch, D., Basri, G., et al. 2010, Science, 327, doi: 10.1126/science.1185402

Boser, B., Guyon, I., & Vapnik, V. 1992, in Proceedings of the Fifth Annual Workshop on Computational Learning Theory, doi: 10.1145/130385.130401

Boss, A., Butler, R., Hubbard, W., et al. 2005, Proceedings of the International Astronomical Union, 1, doi: 10.1017/S1743921306004509

Boureau, Y.-L., Ponce, J., & LeCun, Y. 2010, Proceedings of the 27th International Conference on International Conference on Machine Learning, doi: 10.5555/3104322.3104338

Brandl, B., Bettonvil, F., Van Boekel, R., et al. 2021, Published in The Messenger, 182, doi: 10.18727/0722-6691/5218

Breiman, L. 2001, Machine Learning, 45, doi: 10.1023/A:1010933404324

Brescia, M., Cavuoti, S., Razim, O., et al. 2021, Frontiers in Astronomy and Space Sciences, 8, doi: 10.3389/fspas.2021.658229

Bulmer, M. G. 1979, Principles of statistics

Cantalloube, F., Dohlen, K., Milli, J., Brandner, W., & Vigan, A. 2019, The Messenger, 176, doi: 10.18727/0722-6691/5138

Cantalloube, F., Mouillet, D., Mugnier, L. M., et al. 2015, Astronomy & Astrophysics, 582, doi: 10.1051/0004-6361/201425571

Cantalloube, F., Gonzalez, C. A. G., Absil, O., et al. 2020, in Proceedings of SPIE, Vol. 11448, Adaptive Optics Systems VII (SPIE), doi: 10.1117/12.2574803

Cantalloube, F., Christiaens, V., Cantero, C., et al. 2022, in Proceedings of SPIE, Vol. 12185, Adaptive Optics Systems VIII, ed. D. Schmidt, L. Schreiber, & E. Vernet (SPIE), doi: 10.1117/12.2627968

Cantero, C., Absil, O., Dahlqvist, C.-H., & Van Droogenbroeck, M. 2023, Astronomy & Astrophysics, doi: 10.1051/0004-6361/202346085

Charbonneau, D., Brown, T. M., Latham, D. W., & Mayor, M. 2000, The Astrophysical Journal Letters, 529, doi: 10.1086/312457

Chauvin, G., Lagrange, A.-M., Dumas, C., et al. 2004, Astronomy & Astrophysics, 425, doi: 10.1051/0004-6361:200400056

Chauvin, G., Desidera, S., Lagrange, A. M., et al. 2017, in Proceedings of the Annual meeting of the French Society of Astronomy and Astrophysics. https://ui.adsabs.harvard.edu/abs/2017sf2a.conf..331C

Cheetham, A. C., Samland, M., Brems, S. S., et al. 2019, Astronomy & Astrophysics, 622, doi: 10.1051/0004-6361/201834112

Cho, K., Merrienboer, B., Gulcehre, C., et al. 2014, in Proceedings of the 2014 Conference on Empirical Methods in Natural Language Processing (EMNLP), doi: 10.3115/v1/D14-1179

Christiaens, V. 2022, Journal of Open Source Software, 7, doi: 10.21105/joss.04456

Christiaens, V., Gonzalez, C. A. G., Farkas, R., et al. 2023, Journal of Open Source Software, 8, doi: 10.21105/joss.04774

Curiel, S., Ortiz-León, G. N., Mioduszewski, A. J., & Sanchez-Bermudez, J. 2022, , 164, doi: 10.3847/1538-3881/ac7c66

D'Agostino, R., & Pearson, E. S. 1973, Biometrika, 60, doi: 10.2307/2335012

Dahlqvist, C.-H., Cantalloube, F., & Absil, O. 2020, Astronomy & Astrophysics, 633, doi: 10.1051/0004-6361/201936421

—. 2021a, Astronomy & Astrophysics, 656, doi: 10.1051/0004-6361/202141446

Dahlqvist, C.-H., Louppe, G., & Absil, O. 2021b, Astronomy & Astrophysics, 646, doi: 10.1051/0004-6361/202039597

Davies, R., Absil, O., Agapito, G., et al. 2023, Astronomy & Astrophysics, 674, doi: 10.1051/0004-6361/202346559

de Beurs, Z. L., Vanderburg, A., Shallue, C. J., et al. 2022, The Astronomical Journal, 164, doi: 10.3847/1538-3881/ac738e

Delorme, P., Meunier, N., Albert, D., et al. 2017, arXiv, doi: 10.48550/arXiv.1712.06948

Desidera, S., Chauvin, G., Bonavita, M., et al. 2021, Astronomy & Astrophysics, 651, doi: 10.1051/0004-6361/202038806

Dieleman, S., Willett, K. W., & Dambre, J. 2015, Monthly Notices of the Royal Astronomical Society, 450, doi: 10.1093/mnras/stv632

Dubey, S. R., Singh, S. K., & Chaudhuri, B. B. 2022, Neurocomputing, 503, doi: https://doi.org/10.1016/j.neucom.2022.06.111

Duchi, J., Hazan, E., & Singer, Y. 2011, Journal of Machine Learning Research, 12. http://jmlr.org/papers/v12/duchi11a.html

Dumoulin, V., & Visin, F. 2016, ArXiv, doi: 10.48550/arXiv.1603.07285

Esposito, S., Riccardi, A., Fini, L., et al. 2010, in Proceedings of SPIE, Vol. 7736, doi: 10.1117/12.858194

Fergus, R., Hogg, D. W., Oppenheimer, R., Brenner, D., & Pueyo, L. 2014, The Astrophysical Journal, 794, doi: 10.1088/0004-637x/794/2/161

Fitzgerald, M. P., & Graham, J. R. 2006, The Astrophysical Journal, 637, doi: 10.1086/498339

Flamary, R. 2017, in 25th European Signal Processing Conference (EUSIPCO), doi: 10.23919/EUSIPCO.2017.8081654

Flasseur, O., Bodrito, T., Mairal, J., et al. 2023, Monthly Notices of the Royal Astronomical Society, doi: 10.1093/mnras/stad3143

Flasseur, O., Denis, L., Thiébaut, É., & Langlois, M. 2018, Astronomy & Astrophysics, 618, doi: 10.1051/0004-6361/201832745

—. 2020, Astronomy & Astrophysics, 637, doi: 10.1051/0004-6361/201937239

Flasseur, O., Thé, S., Denis, L., Thiebaut, E., & Langlois, M. 2021, Astronomy & Astrophysics, 651, doi: 10.1051/0004-6361/202038957

Follert, R., Dorn, R. J., Oliva, E., et al. 2014, in Proceedings of SPIE, Vol. 9147, doi: 10.1117/12.2054197

Fusco, T., Rousset, G., Sauvage, J-.F annd Petit, C., et al. 2006, Optics Express, 14, doi: 10.1364/OE.14.007515

Fusco, T., Sauvage, J.-F., Petit, C., et al. 2014, in Proceeding of SPIE, Vol. 9148, doi: 10.1117/12.2055423

Galicher, R., & Mazoyer, J. 2023, Comptes Rendus. Physique, 24, doi: 10.5802/crphys.133

Galicher, R., Boccaletti, A., Mesa, D., et al. 2018, Astronomy & Astrophysics, 615, doi: 10.1051/0004-6361/201832973

Gebhard, T. D., Bonse, M. J., Quanz, S. P., & Schölkopf, B. 2022, Astronomy & Astrophysics, 666, doi: 10.1051/0004-6361/202142529

Gneiting, T. 1997, Journal of Statistical Computation and Simulation, 59, doi: 10.1080/00949659708811867

Goebel, S. B., Guyon, O., Hall, D. N. B., Jovanovic, N., & Atkinson, D. E. 2016, in Proceedings of SPIE, Vol. 9909, doi: 10.1117/12.2231926

Goodfellow, I., Bengio, Y., & Courville, A. 2016, Deep learning (MIT Press)

Goodfellow, I., Pouget-Abadie, J., Mirza, M., et al. 2014, in Advances in Neural Information Processing Systems (NeurIPS)

Goodman, J. 1975, Laser Speckle and Related Phenomena, doi: 10.1007/BFb0111436

Gómez González, C. September 2017, PhD thesis, ULiège - Université de Liège

Gómez González, C. A., Absil, O., Absil, P.-A., et al. 2016, Astronomy & Astrophysics, 589, doi: 10.1051/0004-6361/201527387

Gómez González, C. A., Absil, O., & Van Droogenbroeck, M. 2018, Astronomy & Astrophysics, 613, doi: 10.1051/0004-6361/201731961

Gómez González, C. A., Wertz, O., Absil, O., et al. 2017, The Astronomical Journal, 154, doi: 10.3847/1538-3881/aa73d7

Halko, N., Martinsson, P.-G., Shkolnisky, & Tygert, M. 2011, SIAM Journal on Scientific Computing, 33, doi: 10.1137/100804139

Hastie, T., Tibshirani, R., & Friedman, J. 2009, The elements of statistical learning: data mining, inference, and prediction, 2nd edn., Springer Series in Statistics (Springer)

Henry, G. W., Marcy, G. W., Butler, R. P., & Vogt, S. S. 1999, The Astrophysical Journal, 529, doi: 10.1086/312458

Hinkley, S., Oppenheimer, B. R., Soummer, R., et al. 2007, The Astrophysical Journal, 654, doi: 10.1086/509063

Hochreiter, S., & Schmidhuber, J. 1997, Neural Computation, 9, doi: 10.1162/neco.1997.9.8.1735

Houllé, M., Vigan, A., Carlotti, A., et al. 2021, Astronomy & Astrophysics, 652, doi: 10.1051/0004-6361/202140479

Hoyle, B. 2016, Astronomy and Computing, 16, doi:).10.1016/j.ascom.2016.03.006

Ioffe, S., & Szegedy, C. 2015, in International Conference on Machine Learning (ICML), Lille, France

Jensen-Clem, R., Mawet, D., Gomez Gonzalez, C. A., et al. 2017, The Astronomical Journal, 155, doi: 10.3847/1538-3881/aa97e4

Juillard, S., Christiaens, V., & Absil, O. 2023, Astronomy & Astrophysics, 679, doi: 10.1051/0004-6361/202347259

Kalas, P., Liu, M. C., & Matthews, B. C. 2004, Science, 303, doi: `10.1126/science.1093420`

Keppler, M., Benisty, M., Müller, A., et al. 2018a, Astronomy & Astrophysics, 617, doi: `10.1051/0004-6361/201832957`

—. 2018b, Astronomy & Astrophysics, 617, doi: `10.1051/0004-6361/201832957`

Kim, E. J., & Brunner, R. J. 2016, Monthly Notices of the Royal Astronomical Society, 464, doi: `10.1093/mnras/stw2672`

Kingma, D., & Ba, J. 2015, in International Conference on Learning Representations (ICLR), San Diego, California, USA

Konopacky, Q. M., Rameau, J., Duchêne, G., et al. 2016, The Astrophysical Journal Letters, 829, doi: `10.3847/2041-8205/829/1/L4`

Krizhevsky, A., Sutskever, I., & Hinton, G. 2012, in Advances in Neural Information Processing Systems (NeurIPS), Vol. 25, doi: `10.1145/3065386`

Lafreniere, D., Marois, C., Doyon, R., Nadeau, D., & Artigau, E. 2007, The Astrophysical Journal, 660, doi: `10.1086/513180`

Lagrange, A.-M., Gratadour, D., Chauvin, G., et al. 2009, Astronomy & Astrophysics, 493, doi: `10.1051/0004-6361:200811325`

Lagrange, A.-M., Meunier, N., Rubini, P., et al. 2019, Nature Astronomy, 3, doi: `10.1038/s41550-019-0857-1`

Langlois, M., Gratton, R., Lagrange, A.-M., et al. 2021, Astronomy & Astrophysics, 651, doi: `10.1051/0004-6361/202039753`

Larkin, K. G., Oldfield, M. A., & Klemm, H. 1997, Optics Communications, 139, doi: `10.1016/S0030-4018(97)00097-7`

Launhardt, R., Henning, Th., Quirrenbach, A., et al. 2020, Astronomy & Astrophysics, 635, doi: `10.1051/0004-6361/201937000`

Lee, D. D., & Seung, H. S. 1999, Nature, 401, doi: `10.1038/44565`

Lilliefors, H. W. 1967, Journal of the American Statistical Association, 62, doi: `10.1080/01621459.1967.10482916`

Lyot, B. 1939, Monthly Notices of the Royal Astronomical Society, 99, doi: `10.1093/mnras/99.8.580`

Macintosh, B., Ab, J., Graham, et al. 2008, in Proceedings of SPIE, doi: `10.1117/12.788083`

Macintosh, B., Graham, J. R., Barman, T., et al. 2015, Science, 350, doi: 10.1126/science.aac5891

Maire, J., Perrin, M. D., Doyon, R., et al. 2010, in Proceeding of SPIE, Vol. 7735, doi: 10.1117/12.858028

Males, J. R., Fitzgerald, M. P., Belikov, R., & Guyon, O. 2021, Publications of the Astronomical Society of the Pacific, 133, doi: 10.1088/1538-3873/ac0f0c

Malik, A., Moster, B. P., & Obermeier, C. 2021, Monthly Notices of the Royal Astronomical Society, 513, doi: 10.1093/mnras/stab3692

Margot, J.-L. 2015, The Astronomical Journal, 150, doi: 10.1088/0004-6256/150/6/185

Marmolejo-Ramos, F., & González-Burgos, J. 2013, Methodology, 9, doi: 10.1027/1614-2241/a000059

Marois, C., Correia, C., Galicher, R., et al. 2014, in Proceedings of SPIE, Vol. 9148, doi: 10.1117/12.2055245

Marois, C., Lafreniere, D., Doyon, R., Macintosh, B., & Nadeau, D. 2006, The Astrophysical Journal, 641, doi: 10.1086/500401

Marois, C., Lafreniere, D., Macintosh, B., & Doyon, R. 2008a, The Astrophysical Journal, 673, doi: 10.1086/523839

Marois, C., Macintosh, B., Barman, T., et al. 2008b, Science, 322, doi: 10.1126/science.1166585

Marois, C., Zuckerman, B., Konopacky, Q. M., Macintosh, B., & Barman, T. 2010, Nature, 468, doi: 10.1038/nature09684

Martioli, E., Hébrard, G., Correia, A. C. M., Laskar, J., & Lecavelier des Etangs, A. 2021, Astronomy & Astrophysics, 649, doi: 10.1051/0004-6361/202040235

Mawet, D., Riaud, P., Absil, O., & Surdej, J. 2005, The Astrophysical Journal, 633, doi: 10.1086/462409

Mawet, D., Serabyn, E., Liewer, K., et al. 2009, The Astrophysical Journal, 709, doi: 10.1088/0004-637x/709/1/53

Mawet, D., Milli, J., Wahhaj, Z., et al. 2014, The Astrophysical Journal, 792, doi: 10.1088/0004-637x/792/2/97

Mayor, M., & Queloz, D. 1995, Nature, 378, doi: 10.1038/378355a0

McInnes, L., Healy, J., Saul, N., & Großberger, L. 2018, Journal of Open Source Software, 3, doi: `10.21105/joss.00861`

McLean, I. S., Becklin, E. E., Bendiksen, O., et al. 1998, in Proceedings of SPIE, Vol. 3354, doi: `10.1117/12.317283`

Milli, J., Banas, T., Mouillet, D., et al. 2016, in Proceedings of SPIE, doi: `10.1117/12.2231703`

Mollière, P., Wardenier, J. P., van Boekel, R., et al. 2019, Astronomy & Astrophysics, 627, doi: `10.1051/0004-6361/201935470`

Morrissey, P., Harding, L. K., Bush, N. L., et al. 2023, Journal of Astronomical Telescopes, Instruments, and Systems, 9, doi: `10.1117/1.JATIS.9.1.016003`

Müller, A., Keppler, M., Henning, T., et al. 2018, Astronomy & Astrophysics, 617, doi: `10.1051/0004-6361/201833584`

Nair, V., & Hinton, G. 2010, in Proceedings of the 27th International Conference on International Conference on Machine Learning

Nielsen, E. L., De Rosa, R. J., Macintosh, B., et al. 2019, The Astronomical Journal, 158, doi: `10.3847/1538-3881/ab16e9`

Nieto, L. A., & Díaz, R. F. 2023, Astronomy & Astrophysics, 677, doi: `10.1051/0004-6361/202346417`

Pairet, B., Cantalloube, F., Gomez Gonzalez, C. A., Absil, O., & Jacques, L. 2019, Monthly Notices of the Royal Astronomical Society, 487, doi: `10.1093/mnras/stz1350`

Pairet, B., Cantalloube, F., & Jacques, L. 2021, Monthly Notices of the Royal Astronomical Society, 503, doi: `10.1093/mnras/stab607`

Pairet, B., Gonzalez, C. G., & Jacques, L. 2018, in Proc. Int. Traveling Workshop Interact. Between Sparse Models Technol.(iTWIST)

Patrício, M., Ferreira, F., Oliveiros, B., & Caramelo, F. 2017, Communications in Statistics - Simulation and Computation, 46, doi: `10.1080/03610918.2016.1241410`

Pavlov, A., Moeller-Nilsson, O., Feldt, M., et al. 2008, in Proceedings of SPIE, doi: `10.1117/12.789110`

Perger, M., Anglada-Escudé, G., Baroch, D., et al. 2023, Astronomy & Astrophysics, 672, doi: `10.1051/0004-6361/202245092`

Perrin, M., Ingraham, P., Follette, K., et al. 2016, in Proceeding of SPIE, Vol. 9908, doi: 10.1117/12.2233197

Perrin, M. D., Sivaramakrishnan, A., Makidon, R. B., Oppenheimer, B. R., & Graham, J. R. 2003, The Astrophysical Journal, 596, doi: 10.1086/377689

Petit, C., Sauvage, J.-F., Costille, A., et al. 2016, in Proceedings of SPIE, Vol. 2, doi: 10.1117/1.JATIS.2.2.025003

Plavchan, P., Barclay, T., Gagné, J., et al. 2020, Nature, 582, doi: 10.1038/s41586-020-2400-z

Pueyo, L. 2016, The Astrophysical Journal, 824, doi: 10.3847/0004-637X/824/2/117

Pueyo, L., Crepp, J. R., Vasisht, G., et al. 2012, The Astrophysical Journal Supplement Series, 199, doi: 10.1088/0067-0049/199/1/6

Quesnel, M., Orban de Xivry, G., Louppe, G., & Absil, O. 2022, Astronomy & Astrophysics, 668, doi: 10.1051/0004-6361/202143001

Racine, R. 1996, Publications of the Astronomical Society of the Pacific, 108, doi: 10.1086/133788

Ragazzoni, R., & Farinato, J. 1999, Astronomy & Astrophysics, 350

Rameau, J., Chanussot, J., Carlotti, A., Bonnefoy, M., & Delorme, P. 2021, Astronomy & Astrophysics, 649, doi: 10.1051/0004-6361/202140337

Rameau, J., Chauvin, G., Lagrange, A.-M., et al. 2013, The Astrophysical Journal, 772, doi: 10.1088/2041-8205/772/2/l15

Ren, B., Pueyo, L., Zhu, G. B., Debes, J., & Duchêne, G. 2018, The Astrophysical Journal, 852, doi: 10.3847/1538-4357/aaa1f2

Ricker, G. R., Winn, J. N., Vanderspek, R., et al. 2015, Journal of Astronomical Telescopes, Instruments, and Systems, 1, doi: 10.1117/1.JATIS.1.1.014003

Rombach, R., Blattmann, A., Lorenz, D., Esser, P., & Ommer, B. 2022, in 2022 IEEE/CVF Conference on Computer Vision and Pattern Recognition (CVPR), doi: 10.1109/CVPR52688.2022.01042

Rosenblatt, F. 1958, Psychological review, 65, doi: 10.1037/h0042519

Rouan, D., Riaud, P., Boccaletti, A., Clénet, Y., & Labeyrie, A. 2000, Publications of the Astronomical Society of the Pacific, 112, doi: 10.1086/317707

Rousset, G., Fontanella, J. C., Kern, P., Gigan, P., & Rigaut, F. 1990, Astronomy & Astrophysics, 230

Ruane, G., Ngo, H., Mawet, D., et al. 2019, The Astronomical Journal, 157, doi: `10.3847/1538-3881/aafee2`

Ruder, S. 2016, ArXiv, doi: `10.48550/arXiv.1609.04747`

Ruffio, J.-B., Macintosh, B., Wang, J. J., et al. 2017, The Astrophysical Journal, 842, doi: `10.3847/1538-4357/aa72dd`

Rumelhart, D. E., Hinton, G. E., & Williams, R. J. 1986, Nature, 323, doi: `10.1038/323533a0`

Sahlmann, J., Lazorenko, P. F., Ségransan, D., et al. 2013, Astronomy & Astrophysics, 556, doi: `10.1051/0004-6361/201321871`

Samland, M., Bouwman, J., Hogg, D. W., et al. 2021, Astronomy & Astrophysics, 646, doi: `10.1051/0004-6361/201937308`

Sauvage, J.-F., Fusco, T., Petit, C., et al. 2016, Journal of Astronomical Telescopes Instruments and Systems, 2, doi: `10.1117/1.JATIS.2.2.025003`

Schmidt, K., Geyer, F., Fröse, S., et al. 2022, Astronomy & Astrophysics, 664, doi: `10.1051/0004-6361/202142113`

Schneider, J., Dedieu, C., Le Sidaner, P., Savalle, R., & Zolotukhin, I. 2011, Astronomy & Astrophysics, 532, doi: `10.1051/0004-6361/201116713`

Schölkopf, B., Hogg, D. W., Wang, D., et al. 2016, Proceedings of the National Academy of Sciences (PNAS), 113, doi: `10.1073/pnas.1511656113`

Schuster, M., & Paliwal, K. 1997, IEEE Transactions on Signal Processing, 45, doi: `10.1109/78.650093`

Serabyn, E., Huby, E., Matthews, K., et al. 2017, The Astronomical Journal, 153, doi: `10.3847/1538-3881/153/1/43`

Shack, R. B., & Platt, B. C. 1971, J. Opt.Soc. Am., 61

Shapiro, S. S., & Wilk, M. B. 1965, Biometrika, 52, doi: `10.2307/2333709`

Shi, X., Chen, Z., Wang, H., et al. 2015, in Advances in Neural Information Processing Systems (NeurIPS), Vol. 1

Simić, M. 2021, Neural Computing and Applications, 33, doi: `10.1007/s00521-021-06229-7`

Skaf, N., Guyon, Olivier, Gendron, Éric, et al. 2022, Astronomy & Astrophysics, 659, doi: `10.1051/0004-6361/202141514`

Skrutskie, M. F., Jones, T., Hinz, P., et al. 2010, in Proceedings of SPIE, Vol. 7735, doi: `10.1117/12.857724`

Soummer, R. 2005, The Astrophysical Journal Letters, 618, doi: 10.1086/427923

Soummer, R., Ferrari, A., Aime, C., & Jolissaint, L. 2007, The Astrophysical Journal, 669, doi: 10.1086/520913

Soummer, R., Pueyo, L., & Larkin, J. 2012, The Astrophysical Journal Letters, 755, doi: 10.1088/2041-8205/755/2/l28

Sparks, W. B., & Ford, H. C. 2002, The Astrophysical Journal, 578, doi: 10.1086/342401

Srivastava, N., Hinton, G., Krizhevsky, A., Sutskever, I., & Salakhutdinov, R. 2014, Journal of Machine Learning Research, 15

Stone, J. M., Skemer, A. J., Hinz, P. M., et al. 2018, The Astronomical Journal, 156, doi: 10.3847/1538-3881/aaec00

Sumi, T., Kamiya, K., Bennett, D. P., et al. 2011, Nature, 473, doi: 10.1038/nature10092

Sutskever, I., Martens, J., Dahl, G. E., & Hinton, G. E. 2013, in International Conference on Machine Learning, Vol. 28

Uhm, T., & Yi, S. 2021, Communications in Statistics - Simulation and Computation, 1, doi: 10.1080/03610918.2021.1963450

Valizadegan, H., Martinho, M. J. S., Wilkens, L. S., et al. 2022, The Astrophysical Journal, 926, doi: 10.3847/1538-4357/ac4399

Van der Maaten, L., & Hinton, G. 2008, Journal of Machine Learning Research, 9

Vavilova, I. B., Dobrycheva, D. V., Vasylenko, M. Yu., et al. 2021, Astronomy & Astrophysics, 648, doi: 10.1051/0004-6361/202038981

Vigan, A., Moutou, C., Langlois, M., et al. 2010, Monthly Notices of the Royal Astronomical Society, 407, doi: 10.1111/j.1365-2966.2010.16916.x

Vigan, A., Fontanive, C., Meyer, M., et al. 2021, Astronomy & Astrophysics, 651, doi: 10.1051/0004-6361/202038107

Vovk, V., & Wang, R. 2020, Biometrika, 107, doi: 10.1093/biomet/asaa027

Wagner, K., Apai, D., & Kratter, K. M. 2019, The Astrophysical Journal, 877, doi: 10.3847/1538-4357/ab1904

Wahhaj, Z., Cieza, L. A., Mawet, D., et al. 2015, Astronomy & Astrophysics, 581, doi: 10.1051/0004-6361/201525837

Wang, J. J., Perrin, M. D., Savransky, D., et al. 2018, Journal of Astronomical Telescopes, Instruments, and Systems, 4, doi: `10.1117/1.jatis.4.1.018002`

Waterman, B. 2019, Honors College, 563

Wijekularathna, D. K., Manage, A. B. W., & Scariano, S. M. 2019, Communications in Statistics - Simulation and Computation, 51, doi: `10.1080/03610918.2019.1658780`

Wittrock, J. M., Plavchan, P., Cale, B. L., et al. 2023, Validating AU Microscopii d with Transit Timing Variations, doi: `10.48550/arXiv.2302.04922`

Wizinowich, P., Acton, D., Shelton, C., et al. 2000, Publications of the Astronomical Society of the Pacific, 112, doi: `10.1086/316543`

Wolszczan, A., & Frail, D. A. 1992, Nature, 355, doi: `10.1038/355145a0`

Xu, D., & Tian, Y. 2015, Annals of Data Science, 2, doi: `10.1051/0004-6361/202038957`

Xuan, W. J., Mawet, D., Ngo, H., et al. 2018, The Astronomical Journal, 156, doi: `10.3847/1538-3881/aadae6`

Yap, B. W., & Sim, C. H. 2011, Journal of Statistical Computation and Simulation, 81, doi: `10.1080/00949655.2010.520163`

Yip, K. H., Nikolaou, N., Coronica, P., et al. 2020, in Joint European Conference on Machine Learning and Knowledge Discovery in Databases, Vol. 11908, doi: `10.1007/978-3-030-46133-1_20`

Yu, L., Lai, K. K., Wang, S., & Huang, W. 2006, in Computational Science and Its Applications, doi: `10.1007/11751540_55`

Zhang, K., Gaudi, B. S., & Bloom, J. S. 2022, Nature Astronomy, 6, doi: `10.1038/s41550-022-01671-6`

Zhou, T., & Tao, D. 2011, in Proceedings of the 28th International Conference on International Conference on Machine Learning

Application of deep learning techniques for exoplanet detection in high contrast imaging

Carles Cantero Mitjans

Carles was born in Barcelona, Spain, in 1992. He grew very curious about the understanding of life and why something so beautiful and delicate is possible in a place such as the Earth, our planet. This curiosity motivated his desire to become an astronomer, and he thus pursued a bachelor's degree in Physics at the University of Barcelona, Spain. Afterwards, he continued his academic journey by obtaining a master's degree in Aerospace Science and Technology from the Polytechnic University of Catalonia (UPC), Spain. During the master's program, Carles realized the immense potential of artificial intelligence in processing big data surveys, particularly in the realm of astronomy. This revelation inspired him to delve into machine learning. He then started to collaborate with the UPC astronomy and astrophysics group, where he applied machine learning algorithms to classify white dwarfs in the Milky Way through precise data from the Gaia space mission. Later, he was selected for a traineeship in the European Space Agency (ESA). During his time at the European Space Astronomy Centre (ESAC-ESA, Madrid), he worked on the analysis of astrometry data from Gaia and applied machine learning techniques to identify new star candidates in the ρ-Oph star-forming region, leading to the identification of a few young stars surrounded by protoplanetary discs. After this traineeship, Carles firmly decided to dedicate his research on the detection of new worlds, and leverage his expertise in machine learning to improve standard detection techniques. In October 2019, he started a Ph.D. fellowship in exoplanet direct imaging using deep learning techniques at the University of Liège, Belgium. This thesis presents his Ph.D. research.

In January 2024, Carles is set to join the Observatory of Geneva in Switzerland for a Postdoctoral position. He will continue his research on exoplanet and brown dwarf detection using large high contrast imaging surveys, as well as leverage the Gaia precise data to complement exoplanet direct imaging with astrometry measurements.

erc

European Research Council
Established by the European Commission